Hydroxy Acids and Related Organic Linkers for the Synthesis of Functional Metal-organic Frameworks and Nanomaterials

A thesis submitted for the degree of

Doctor of Philosophy

By

Sudip Mohapatra

Chemistry and Physics of Materials Unit

Jawaharlal Nehru Centre for Advanced Scientific Research

(A Deemed University)

Jakkur, Bangalore-560064, India

August, 2012

Dedicated to Ma and Baba

TABLE OF CONTENTS

Chapter1: Introduction

1.1 Brief History of Metal-organic Frameworks (MOFs)

Until mid of 1990s there were two kind of porous materials, namely inorganic materials and carbon based materials. In case of microporous inorganic solids, the largest two subclasses of porous inorganic solids are aluminosilicates and aluminophosphates. Zeolites are 3D crystalline, hydrated alkaline or alkaline earth- alumina silicates with the general formula $M^{n+}_{x/n}$ $[(AlO_2)x(SiO_2)y]^{x-} \cdot wH_2O$.[1,2] Their structure built from corner sharing TO_4 tetrahedra (T = Al, Si), defines interconnected tunnels or cages in which water molecules or M^{n+} ions are present. The porosity is generated after removal of the water molecules, without affecting its structure. The cavities were extensively exploited for the molecular sieving and catalytic activity. Synthetic zeolites, aluminophosphates ($AlPO_4$s) were first observed in 1862 which consist of Al^{3+} and P^{5+} ion linked by corner sharing oxygen atoms.[3] These are 3D neutral framework with channel and/or pores of molecular dimension. The first publication of crystalline microporous alumina phosphate appeared in 1982. Since 1982 not only crystalline oxide materials, silicoaluminophosphates, metallosilicates, metalloaluminophosphates, metallophosphates but also porous chalcogenides, nitrides, halides phosphates have also been observed. Another porous inorganic solid, activated carbon has high open porosity and high specific surface area, but have a disordered amorphous structure. The structural feature of activated carbon is a twisted network of defective hexagonal carbon layer, cross linked by aliphatic bridging groups.

Since 1990 a new kind of porous material has been developed which is called porous coordination polymer or metal-organic framework. Metal-organic frameworks (MOFs) or porous coordination polymers (PCPs) are the crystalline compound of various dimensionalities, constructed from metal ion as a node and multidentate ligand as a linker. A brief history of progress in the field of metal-organic framework is as follows. The field was initiated by Robson *et al.* in 1990 after synthesizing such compound having anion exchange capability.[4] In 1992 Fujita *et al.* reported one 2D coordination polymer of cadmium(II) which exhibits catalytic activity[5] and in 1995 the adsorption of guest molecules were studied by Yaghi[6] and Moore.[7] In 1997 kitagawa *et al.* reported gas adsorption of PCP or MOF at ambient temperature.[8] Afterwards within two decades MOFs have emerged as promising hybrid materials in the areas of gas sorption, luminescent, catalysis, separation, magnetism, drug delivery and biological imaging. In recent years the chemistry of metal-organic framework is developing at extraordinary

pace with exponential growth in chemical literature. The enormous growth has been reflected in the increasing number of publications in various chemistry and material science journals year by year.

1.2 Fabrication and classifications of MOFs

There are two central components for the construction of metal-organic framework *viz* connector and linker. Connectors are inorganic metal ions and linkers are organic bridging ligands which are assembled together to form metal-organic frameworks (MOFs). The important characteristics of connectors are the number and orientation of their coordination sites. Linkers are multidentate organic ligand which can bind to various metal ions to form structures of various dimensionalities depending on synthetic conditions. Kitagawa has classified porous MOFs into three different categories *viz* 1st, 2nd

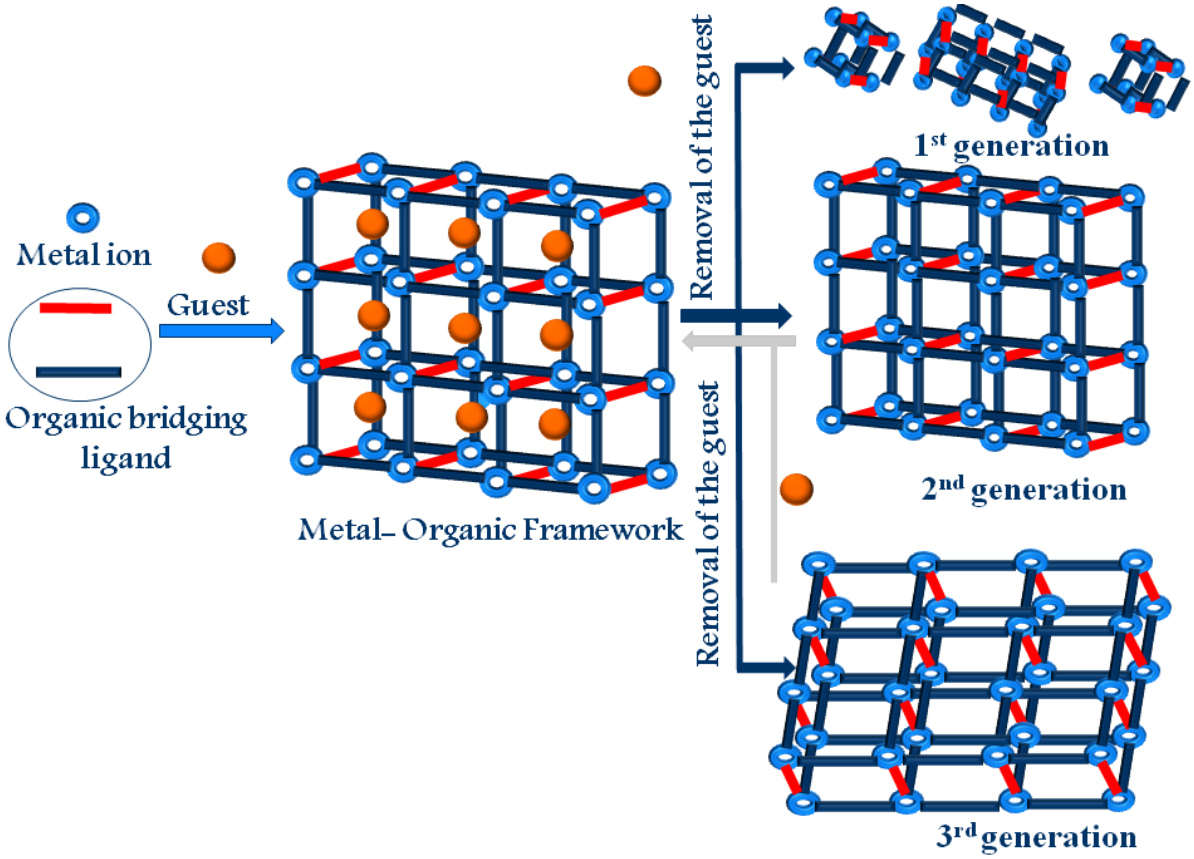

Figure 1. Schematic representation of fabrication of porous MOF and their classification

and 3rd generation frameworks.[9] 1st generation frameworks irreversibly collapse after guest molecule removal. 2nd generation compounds are rigid and robust can show permanent porosity without any guest molecule and 3rd generation MOF are flexible and dynamic frameworks, which responds to external stimuli such as light, electrical field,

guest molecules etc and change their channel and pore reversibly. Third generation compounds are further classified into different categories on the basis of different types of structural transformations.

1.3 Synthetic methods of MOFs

Two most common methods which I have used for the synthesis of metal-organic frameworks in this thesis are solvothermal and slow diffusion. In solvothermal technique MOFs are synthesized by combining metal salts and organic linker in a solvent by heating at high temperature and autogenous pressure and the resultant structure depends on both the nature of linker as well as on coordination geometry of the metal ion. The nucleation occurs near the walls or on the dust particle in this method therefore the growth process is very slow and crystal's dimension is bigger. In contrast microwave-assisted synthesis leads to the homogeneous nucleation throughout the bulk of the solution because local heating of the solvents generate hot spots which nucleate crystal growth.[11] The second method is advantageous for scaling up the product because crystal size is smaller and uniform.[10, 11] Slow diffusion method was used for the crystallization of framework obtained at room temperature because of very fast reaction between metal ions and ligand. Powder form of the compounds is obtained by simple mixing of the ligand and metal at room temperature in appropriate stoichiometry.

1.4 Properties of MOFs

MOFs are consisting of metal ion and organic linker, it exhibit versatile functionality from synergistic effect of both organic and inorganic part. Because of the separation of metaloxygen cluster or metal ions by organic bridging ligands, MOFs are often porous and have high surface area with regular and tunable channels, therefore those can be recognized as promising materials for exhibiting properties like gas storage, heterogeneous catalysis, gas/ solvent vapor separation, drug delivery, sensing of metal ions and solvent vapors, a template for nanomaterial synthesis, magnetic material with slow magnetic relaxation, a spin cross over materials and many others. Recent report suggests MOFs in conjunction with nanoparticle serves as a visible light driven photocatalytic hydrogen evolution system, promises it's near future application in clean fuel technology because hydrogen is a clean fuel with high energy density. Yaghi *et al.* synthesized various framework based on Zn^{II} metal which prognosticating possibility of achieving the target of DOE regarding hydrogen storage in near future by these material. The other potential applications of metal-organic materials (MOMs) are in catalysis,

emission property (ligand and metal based), metal ion sensing, spin cross over magnetic materials and single molecular magnet. All the properties mentioned above either comes from the metal or ligand or both metal ions and ligand simultaneously. In this thesis the discussion is based on MOF's useful application as a gas (H_2, CO_2 and methane) storage material, its emissive properties (based on metal as well as ligands) and luminescence quenching and sensing phenomenon for different solvent vapour and metal ions. Below is a schematic diagram of possible applications of MOF materials in various directions.

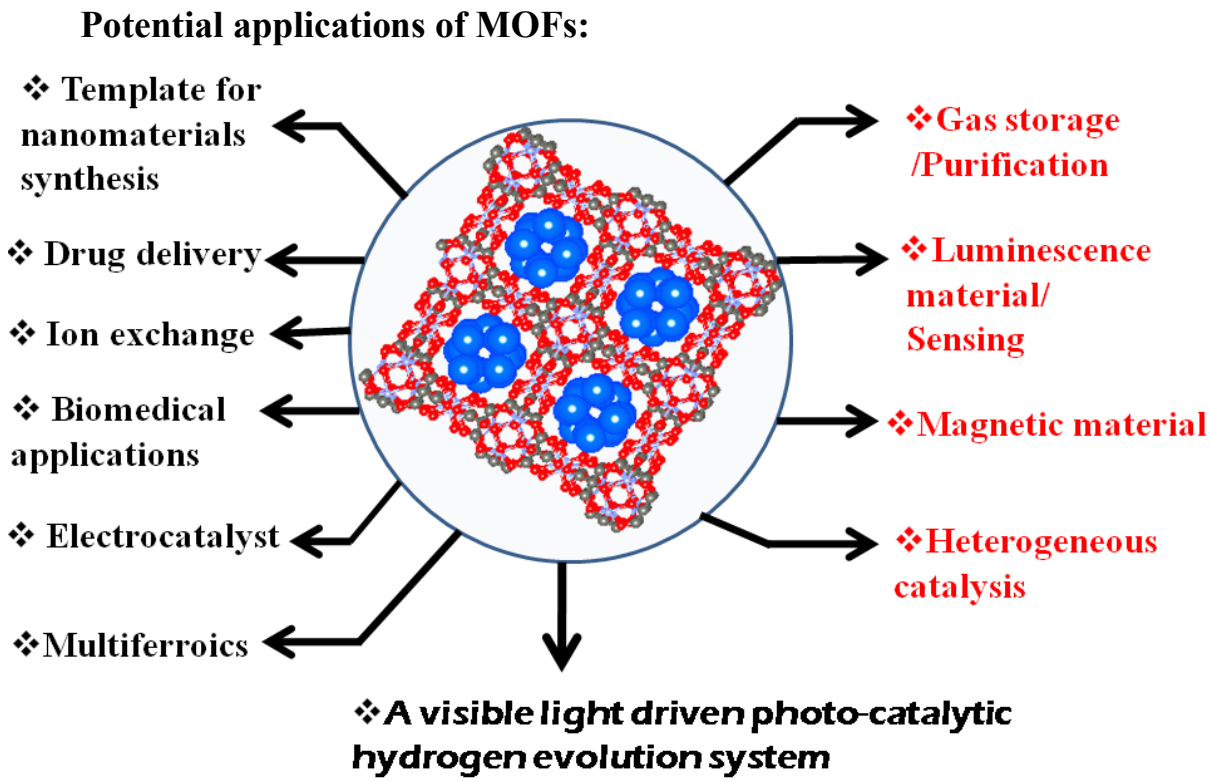

Figure 2. A scheme representing multiple applications of MOF.

1.4.1 Hydrogen and methane storage

In relation to the energy and environmental issues the most promising alternative for fossil fuel is hydrogen gas because it is clean and has high energy density (33.3 $kWhkg^{-1}$) and abundance. To use hydrogen as a fuel for automobile, 5-13 kg of the gas is required per day to drive 300 mile . Therefore fuel cell and automobile industries are eagerly looking for an efficient hydrogen storage material to manufacture vehicle operated with hydrogen fuel. U.S department of energy (DOE) has set up 2017 hydrogen storage target of 5.5 wt% in gravimetric capacity and 40 g L^{-1} volumetric capacity at an operating

temperature -40 to 60˚C under a maximum delivery pressure of 100 atm.[12] There are three different kind of hydrogen storage materials *viz* ‘‘physiosorption material’’, ‘‘on board reversible hydrides’’, and ‘off board reversible hydrides’. It is expected that hydrogen storage capacity of MOF mainly depends on the surface area and pore volume. MOF 210 synthesized by Yaghi *et al.*, exhibits the highest reported surface of 6240 m^2g^{-1} till date[13] and largest (in terms of pore volume) mesoporous MOF *viz* bio-MOF 100 was synthesized by Rosi *et al*.[14] Although MOF-210 has highest surface area but it is not promising as a hydrogen storage material, MOF-210 has excess and total uptake capacity of 8.6 wt% and 17.7 wt% at 77 K and 80 bar pressure but no report is available for its hydrogen uptake at room temperature. Probably because of the mesoporous nature, bio MOF-100 was not subjected for hydrogen adsorption study. A number of MOFs exhibit hydrogen storage capacity more than DOE target at 77 K, but unfortunately very few of them has storage capability at ambient condition. However the problem of storing hydrogen gas at ambient condition can be solved not only by increasing surface area and volume of the framework but also we need to increase the enthalpy of hydrogen adsorption by the framework by adopting various strategies. It is worth mentioning here that most of frameworks which can exhibit hydrogen storage capability at room temperature are less than 1 wt% at ambient condition. The highest adsorbing MOF is MOF 5, synthesized by Yaghi *et al.*, has storage capacity of 1.65 wt% at 298 K and 48 bar pressure.[15, 16] Strategies adopted by various group to enhance the enthalpy of hydrogen adsorption are as follows [17]

(a) Introduction of open metal coordination site on the surface
(b) Reducing the large void *via* catenation or interpenetration
(c) Tuning the pore size
(d) Doping alkali metal ions
(e) Impregnation

The highest enthalpy of hydrogen adsorption was observed in a cobalt-organic framework (SNU 15) of 15.1 kJ mol^{-1} because of the presence of vacant coordination sites in the MOF which increase the interaction energy between H_2 molecule and host framework. Unfortunately the framework exhibit very low uptake due to low surface area (356 m^2 g^{-1}). Therefore the DOE target can be achieved by the optimization of both the surface area

and interaction energy of the framework with hydrogen molecule. In this thesis chapter 3 is related to a strategy to increase the enthalpy of hydrogen adsorption in a MOF.

Methane storage: Natural gas is another good candidate as onboard fuel. The main component of natural gas is mostly methane (95%) and remaining 5% composed of other hydrocarbons, carbon dioxide, nitrogen, *etc*. Methane has comparable gravimetric heat of combustion as gasoline (50.0 MJ /kg *vs* 44.5 MJ /kg) therefore liquefied natural gas can provide about 72 % of the volumetric energy density of gasoline and it requires cryogenic conditions (112K). Compressed natural gas can provide 26 % of the volumetric energy density of gasoline when operating pressure is 200 bar. Adsorbed natural gas provides another storage method when natural gas is adsorbed in the porous adsorbent and the volumetric storage energy density for adsorbed natural gas has been reported up to 80% (35.5 bar) of compressed natural gas (at 208 bar). Therefore MOF is a potential candidate to store methane gas at ambient condition. DOE has set a methane storage target: 180 *v/v* at ambient temperature and pressure less than equal to 35 bar. Few carbon materials already reach the this target but they have limited packing density. In 1997 kondo *et al.* reported the first methane sorption study using MOF. In 2008 Ma *et al.* synthesized copper-organic framework known as PCN-14, which exhibit methane storage capacity of 230 *v/v* at ambient temperature (290 K), about 28 % higher than the DOE target. [18,19]

1.4.2 CO_2 sequestration by MOF

With rapid increase of the global population and industrialization of more and more countries, the consumption of energy is increasing enormously.[20] The majority of the energy demand (85%) has been satisfied with the burning fossil fuel . Fossil fuel will continue to play an important role in foreseeable energy, mainly in the power generation and industrial manufacturing. The burning of fossil fuels releases large amount of CO_2 into atmosphere. Since the beginning of the industrial age in 1750 the CO_2 concentration in atmosphere has enormously increased from 280 to 390 ppm in 2010. The increase of the CO_2 concentration in atmosphere imbalances the incoming and outgoing solar energy in the atmosphere system, leading to the raise in the average temperature of the surface of the earth's surface. Thus CO_2 has been considered as primary anthropogenic green house gas and leading culprit for the climate change therefore reduction of CO_2 emission is urgently required to control abnormal climate change. The ultimate goal of reaching a green society only be achieved after relinquishing our dependence over fossil fuel and use

some other alternatives like H_2 fuels or solar energy. The survey from the Intergovernmental Panel on Climate Change (IPCC) has shown that CO_2 emission could be reduced by 80-90 % for a modern power plant equipped with suitable CO_2 capture and storage (CCS) technologies. [20, 21] CCS is a three step process; CO_2 capture, transportation to a storage site and its permanent storage. However the considerable cost of capture approximately 2/3 of the total cost for CCS (primarily separating CO_2 gas from other gases) is slowing down the deployment of CCS project for commercial CCS project. Thus discovery of new material with high efficiency of sequestration of CO_2 gas is required very urgently. Up to date three commercially viable approach have been developed namely post combustion CO_2 capture based on chemical adsorption using amine solvents, oxyfuel combustion and calcium looping. The membrane based separation and adsorption of CO_2 into advanced sorbents like zeolite and metal-organic framework is now a day's an intensed area of research. Tuning the properties of traditional adsorbents are quite difficult therefore the advanced sorbent such as MOFs become hot topic of research regarding CO_2 sequestration. Separation is a combination of kinetic (diffusion selective) and thermodynamic (adsorption) properties therefore a material scientist or chemist has to consider both the size and electronic properties of the gas molecules. There are very small difference in kinetic diameter of CO_2 (3.30 Å), CH_4 (3.76 Å) and N_2 (3.64 Å) therefore it is difficult to separate CO_2 from other gases exclusively based on the size therefore difference in the electronic properties namely quadrupolar moment and polarization can also be used to accomplish the task at hand. MOFs can be designed and synthesized conceptually based on how the building blocks are coming together to form a net therefore the structure and property of MOFs can be tuned by judicious choice of building blocks. Moreover besides the pre-design in synthesis postsynthetic modification is also possible in MOFs for tuning the pore properties. Facile optimization of pore structure, surface function and other properties allow it for specific application as a porous material.

1.4.3 Photoluminescence property

Luminescence is the term used to describe a process in which light is produced after absorption of energy. If the adsorbed energy is a photon it is called photoluminescence. Luminescence has two basic forms fluorescence and phosphorescence depending on the multiplicity of the spin states of higher and lower energy states between which electronic transitions occurs during emission. In excited singlet states, the electron in the excited orbitals are paired to the second electron to the ground state, consequently return to the

ground state is spin allowed and occurs very rapidly (10^8 S^{-1}) by emission of a photon. Typical lifetime of fluorescence is near 10 ns. Phosphorescence is the emission of light from triplet excited state, in which the electron in the excited orbital has same spin orientation as the ground-state electron. Transition to the ground state is spin forbidden and emission rate are slow (10^3 to 10^{10} S^{-1}) so that phosphorescence lifetime is millisecond to second. Processes that occur between absorption and emission of light generally described in the form of Jablonski diagram (These diagrams named after Professor Alexander Jablonski because of his extraordinary contribution to this field).

1.4.3.1 Origin of luminescence in MOFs

MOFs are consisting of metal ions as well as organic linkers and luminescence property of a MOF can exist in several forms. Luminescence may arise because of organic ligand, direct metal center emission and charge transfer emission such as metal to ligand charge transfer emission (MLCT) and ligand to metal charge transfer emission (LMCT). Furthermore luminescence property can be introduced into MOFs by guest molecules *viz* guest induced luminescent property of MOFs. Emission from direct organic ligand occurs basically from a highly conjugated organic linker whereas metal based emission for lanthanides generally occurs through the so called antenna effect. Charge transfer luminescence is generated from the allowed transition from charge transfer excited state to the ground state. Guest induced luminescent MOFs are generated by using MOFs as a host for luminescent guest. Based on the type of metal ions used, luminescent MOFs are classified into four categories (1) lanthanide based MOFs (2) Transition metal Based MOFs (3) heterometal-organic frameworks (4) main group metal MOFs. Here I will dicuss about lanthanide based MOF as a photoluminescence material. [22, 23]

1.4.3.2 Lanthanide luminescence and antenna effect

Trivalent lanthanide ions such as Eu^{III}, Tb^{III} and Dy^{III} are attractive luminophores because they show spectrally narrow emission with longer lifetime in both solid and solution phase. The 4f orbital is shielded by filled $5S^25P^6$ sub-shell thus screening the inner-shell 4f-4f electronic transitions which generate well defined electronic energy states and allowing for the line like emission spectrum. Unfortunately electronic transition in lanthanides is formally forbidden according to Laporte selection rule leading to the weak absorbance and emission. A common way of overcoming this problem is by complexation of the Ln^{III} with a strongly absorbing organic linker. In the presence of strong vibronic coupling between linkers and metals, energy transfer from more readily

accessible linker excited state to the metal's elevated states is possible. (Figure 1b)This coupling was first identified by Weissman in 1942, leading to the drastic increase in the emission intensity and is widely known as antenna effect or in other words 'Luminescence Sensitization'. For Ln^{III} ions, the electronic dipole transitions are same order of magnitude of magnetic dipolar transitions and therefore both are readily seen in the optical spectra.[24, 25]

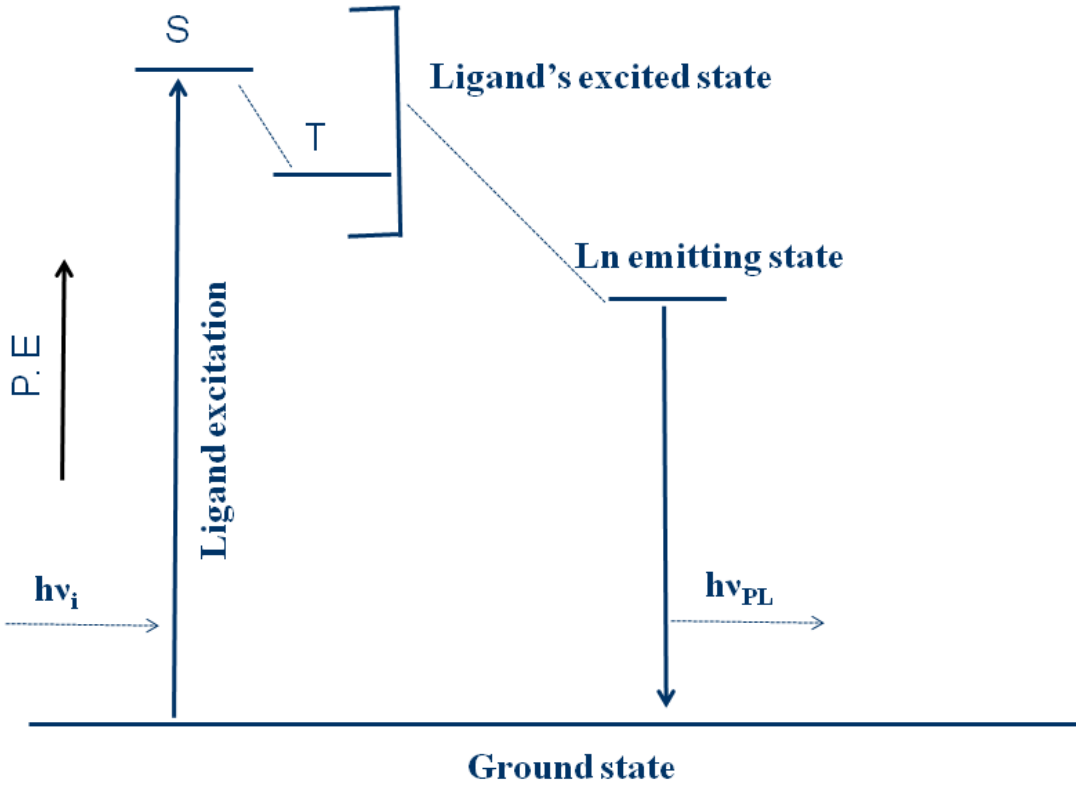

Figure 3. A schematic of antenna effect in lanthanide complexes.

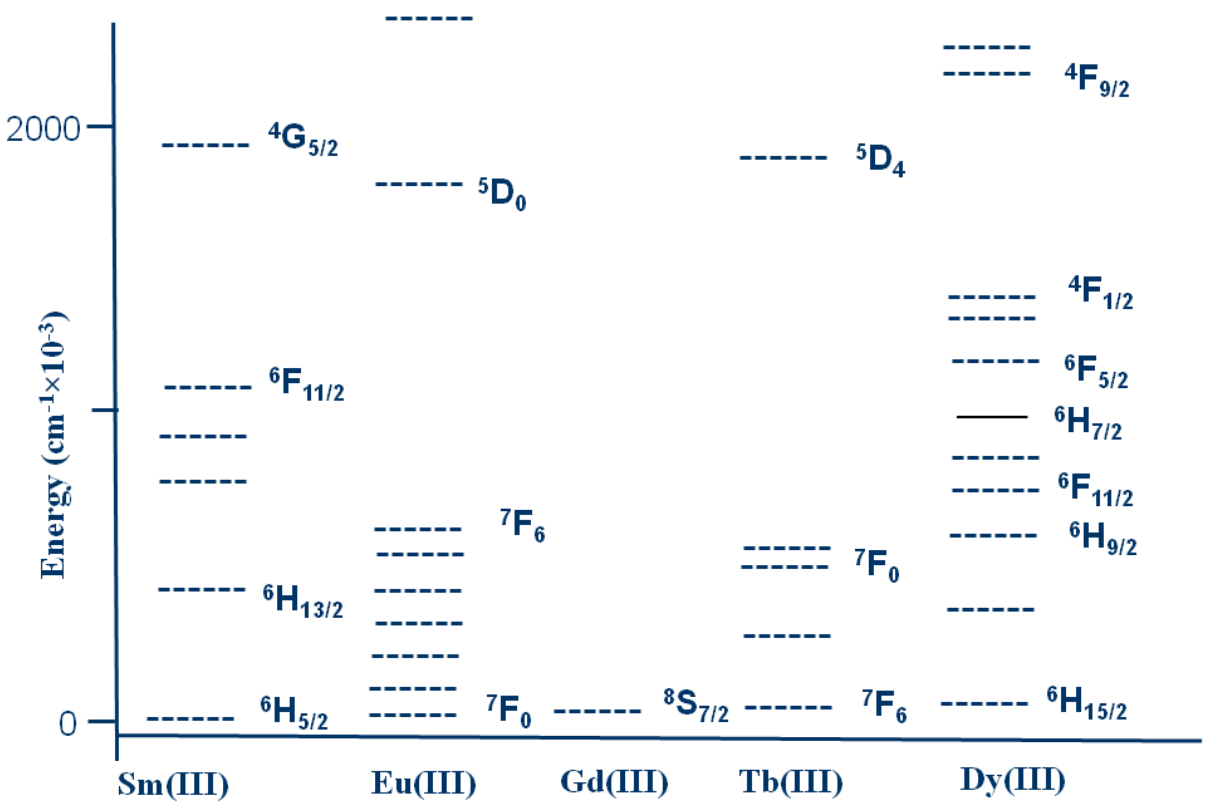

Figure 4. (a) Energy level diagram of the emissive states for commonly used lanthanides.

1.4.3.3 Energy transfer

The theory of resonance energy transfer (RET) was first derived by Theodor Förster in 1949 and also named as Förster resonance energy transfer (FRET). FRET can be defined as the non radiative transfer of energy from excited state of donor to the acceptor. RET and FRET has several other abbreviations like Fluorescence Resonance Energy Transfer, Luminescence (LRET), and Bioluminescence (BRET). All the processes has same resonance mechanism of inducing a dipole oscillation in acceptor by excited donor via coulombic interaction. The necessary condition to occur this process is emission spectrum of donor has to overlap with absorption spectrum of acceptor.

$$\Delta E\ (D \rightarrow D^*) = \Delta E\ (A \rightarrow A^*)$$

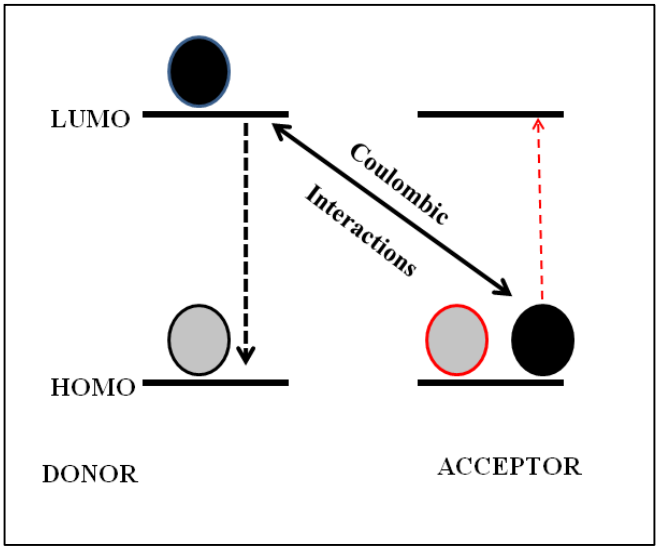

Figure 5. Schemetic of energy transfer between donor acceptor pair.

The energy transfer rate between donor and acceptor pair is given by

$k_T(r) = (1/\tau_D)*(R_0/ r)^6$

Another very important factor of FRET is the distance between donor and acceptor. Efficiency of energy transfer between single donor–acceptor pair at distance r is

$E = R_0^6/(R_0^6+ r^6)$

Where R_0 is Förster distance, the distance at which FRET is 50% efficient. From this equation it is obvious that the rate and efficiency of energy transfer are inversely proportional to the sixth order of the distance between the donor and acceptor.[25]

1.4.3.4 Quantification of energy transfer

The lifetime measurement for Ln^{III} emissions in the mixed lanthanide system is an important tool for understanding the energy transfer between Ln^{III} ions. Due to the presence of enegy transfer there are changes in the lifetime of the donor and acceptor. If efficient energy transfer occurs the lifetime of the donor will decrease and lifetime of the acceptor will increase. The probability (P) and efficiency (E) of energy transfer can be calculated by using the following two equations.[25]

$P_{Ln\rightarrow Ln} = (1/\tau)-(1/\tau_0)$

$E_{Ln\rightarrow Ln} = (1-\tau/\tau_0)$

Where τ = donor lifetime in the presence of an acceptor, τ_0 = donor lifetime in the absence of acceptor

Energy transfer may happen between various pairs of lanthanide ions based on their electronic energy levels.

As MOFs are crystalline materials the distance between donor and acceptor pair can be easily determined from X-ray diffraction study of a single crystal and a clear idea about the possible energy transfer can be obtained and it is possible to modulate the distance by changing the ligand system. In this context energy transfer in MOF system is not well explored. Recently few examples in nanoscale MOFs shows the energy transfer where chromophoric linker acts as a donor. In this thesis I have also focused energy transfer phenomena in lanthanide based system by dopping different % of acceptor in a donor host.

1.4.3.5 Electronic configuration and energy states of Ln^{III} ions

The energy of a given electronic state is determined by the n, L, S and J which are combined together to form a term symbol, $n(^{2S+1}L_J)$. The energy levels of lantahanides are highly degenerate and calculation of spectroscopic coefficient for f^n configuration suggests $Eu^{III}(4f^6)$ and $Tb^{III}(4f^8)$ can be splitted into 119 ^{2S+1}L terms by interelectronic repulsions . Each term further split into 2S+1 (if S≤L) and 2L+1 (if S>L) sublevels, leading to 295 $^{2S+1}L_J$ spectroscopic levels by spin orbit coupling. The final maximum degeneracy into D energy level is caused by the ligand field where every electronic level is degenerated into maximum 2J+1 stark level

D= (4L+2)!/ N!(4L+2-N)!, where N is the number of electron in 4f shell. The D values for Tb^{III} ($^7F_0$) and Eu^{III} ($^7F_6$) is 3003. For schematic view of this result a partial energy level diagram is shown below.[24]

1.4.3.6 Optical Transition and selection rule

Optical transition can be defined as a process in which an atom or molecule changes its energy states by absorbing or emitting electromagnetic radiation of ultraviolet, visible or infrared regions. Absorption process describes resonant energy transfer from radiation to matter whereas emission or luminescence describes resonant energy transfer from matter to radiation. Electronic absorption spectra are produced when electromagnetic radiation promotes the ions from their ground state to excited states. In case of lanthanide the most common of such transition involve excited state which are either component of the ground term or else belong to the excited term which arises from same $4f^n$ configuration. Lanthanide ion shows narrow absorption or emission bands because 4f orbitals are effectively shielded by the filled 5S and 5P shells. Because 4f electron of the lanthanide is largely buried in the inner core they are effectively shielded from their chemical

environment as a result spin-orbit coupling is much larger than the crystal field splitting (2000 cm^{-1} compared to 100 cm^{-1}). According to Broer *et al.* J is a good quantum number but L and S are not. There are two spectroscopic selection rules about the possibility of electronic transition between two given electronic states. The Laporte rule tells that if a molecule has a center of symmetry, transitions within a given set of *p* or *d* orbitals (i.e., those that only involve a redistribution of electrons within a given sub shell) are forbidden and permits the transitions only between opposite parity (g→u). Intra configurational f-f electronic transition only become possible due to interaction with ligand field and vibrational states, which mix electronic state of different pairity into the 4f wave function. Spin multiplicity rule forbids the transition between states of different spin multiplicity (2S+1). In the case of Tb^{3+} and Eu^{3+} the transition occurs between states of quintate and septate multiplicity, a spin forbidden transition therefore a more general term luminescence rather than fluorescence is used.[24]

1.4.4 Porous lanthanide MOF as a sensor

There are various limitations to develop a lanthanide based MOF as a sensor. The primary requirement for developing a sensor is porosity in the system but combining the porosity and Ln^{III} luminescence is challenging because high coordination number of Ln^{III} centers often forms the non porous solids. After removal of the coordinated solvent molecule structure usually collapse. The third limitation is very few ligands are able to form porous architectures as well as an efficient antenna. Chendler *et al*. has reported how they circumvented these issues by adopting stepwise approach and synthesized a series of mixed-metal porous solids Chen *et al.* has reported a number of MOFs exhibiting molecular recognition and sensing of various small molecule, cations and anions.[22]

1.4.4.1 Cation sensing

An intelligent way to fabricate MOFs for sensing metal ion is immobilization of Lewis basic center in the porous MOFs. These types of MOFs are very difficult to prepare because Lewis basic sites often bind to the metal ions to form condensed structure. However Ln^{III} preferentially binds to the carboxylate oxygen over hydroxo oxygen's and pyridyl nitrogen. Exploiting the weaker binding capability of pyridyl nitrogen to Ln^{III} center Chen *et al.* has synthesized a Eu^{III}-pyridine dicarboxylate framework where pyridyl nitrogen remains un coordinated in MOF and Lewis basic site lined in the interior of the channel.[26] After incorporating different cations into the pore they found the antenna effect

significantly changes and consequently the emission of lanthanide significantly changes based on the interaction of metal ions with the Lewis basic site.

1.4.4.2 Anion sensing

The study of sensing of anions by MOFs is very scanty in literature. Chen *et al.* pointed out that N-H and O-H group containing linker and terminal solvent within MOFs, which can participate in hydrogen bonding interaction with anions will be promising material for recognition and sensing of anions. Chen *et al.* has reported luminescent MOF of terbium whose luminescent intensity increases upon incorporation of different amounts of sodium halides in methanol. F^- has strongest enhancement effect compared to other halides in methanol and DMF. The possible mechanism of enhancement of luminescence intensity is due to the hydrogen bonding interaction between the F^- and MeOH ($F^- \cdots H\text{-}OCH_3$) that modifies the energy of the O-H bond stretching, leading to the observed change in the intensity.[27] Wong *et al.* has synthesized a terbium–mucicate MOFs and investigated their anion sensing property and the mechanism of luminescence intensity change in this compound is different from the previous one. It is well known fact that the O-H oscillation of water molecule acts as a efficient quencher of f- f emission of lanthanide therefore the intensity of hydrated lanthanide compounds is lesser than its dehydrated counterpart. Leung *et al.* suggested that rather than removing the quencher filling the channels with suitable guest ions, which can reduce the vibrational movement of the channel *via* intermolecular hydrogen bonding interaction between the OH group of the organic skeleton and anion.[28]

1.4.4.3 Molecular sensing

Unsaturated Ln^{III}center within MOF can act as a sensing site for small molecules (like methanol, water, ethanol, DMF) has been explained by Chen *et al*.[29] They synthesized a MOF of molecular formula,$\{[\ Eu(btc)(H_2O)]\cdot 1.5\ H_2O\}_n$, contains both coordinated and free water molecules, after calcinations at 140˚C, coordinatively unsaturated Eu^{III} centers are generated in the framework. The dehydrated frameworks were subjected for the emission property study after dispersing in various solvents and it was observed that the emission intensity strongly depends on the solvent. Among various solvents DMF and acetone exhibit maximum enhancing and quenching effect respectively and binding interaction of the luminescent metal site playing the important role. In another report with MOF-76, ,$\{[\ Tb\ (btc)(H_2O)]\cdot DMF\cdot H_2O\}_n$, the fluorescence intensity of emulsion in *n*-propanol increased and decreased significantly with addition of DMF

and acetone solvents respectively. This is due to the energy transfer between solvent molecule and the btc^{3-} ligands resulting from the absorption property of the solvent molecule and interaction of solvents and organic ligand. Water is used in many synthetic systems and significant effect in photoluminescence quenching is of particular of interest in this context.[30] Zhu *et al.* reported the family of porous framework of Ln^{III} where H_2O molecule enhances the luminescence intensity rather acts as a quencher. The as-synthesized compound was crystalline but after dehydration it becomes amorphous. The process is reversible upon rehydration. This interesting reverse nature might relate to the amorphous feature of the dehydrated phases, where the surrounding of the Ln^{III} ion becomes soft probably due to (a) the existence of a large number of defects or hanging bonds in the dehydrated materials and (b) the loss of the secondary coordination sphere around Ln^{III} ion, thus greatly enhancing the radiation less process. When rehydrated the materials recover their crystalline, and the surrounding of Ln^{III} becomes stiff again, and thus recovery of the luminescence is observed.[31]

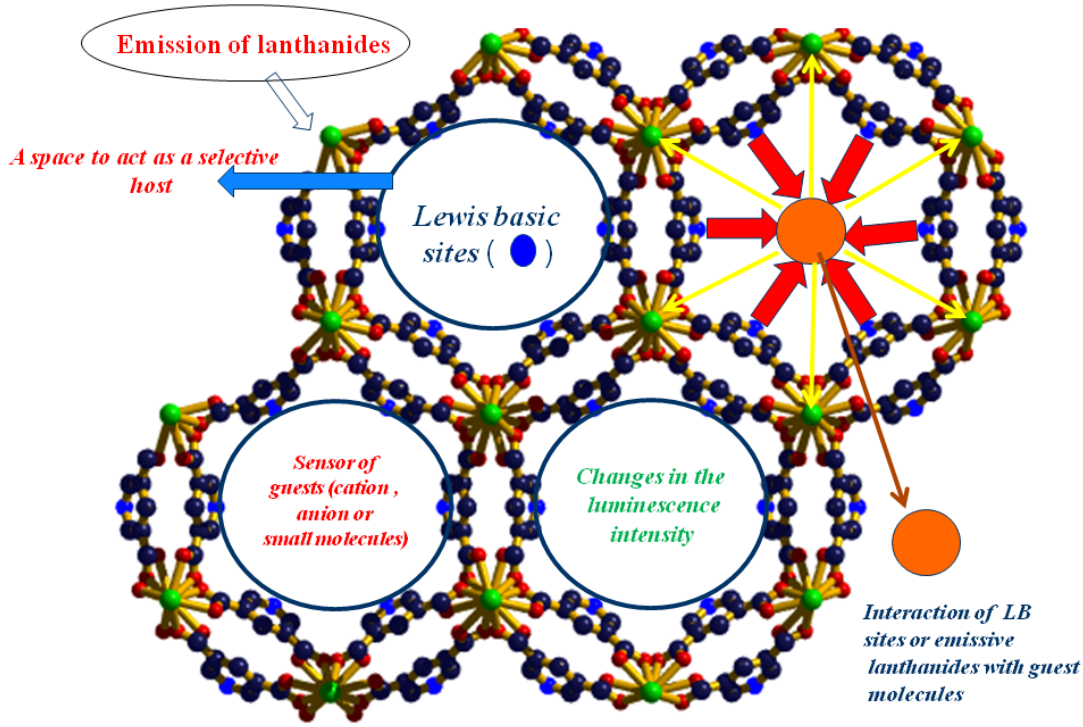

Figure 6. Schematics of sensing property by lanthanide MOFs for solvents and metal ions.

1.4.5 Ligand based emission and ESPT phenomena

When an organic molecule absorbs a photon of appropriate energy, a chain of photophysical event occurs *viz* fluorescence, phosphorescence, internal conversion, intersystem crossing and vibrational relaxation. In MOFs many π conjugated organic molecule are commonly used as a linker. Usually ligand based emission property of MOF is similar to the emission behavior of the ligand in the solution, corresponds to the transition from singlet excited state to the singlet ground state and the transitions are either π to π* or n to π* in nature. However the fluorescence properties such as λ_{max} and lifetime differs in solid MOF compared to the free molecules because of the stabilization of organic ligand in the MOF and step- down the non radiative decay leading to the increase in the fluorescence intensity, lifetime and quantum yield. A luminescent MOF formulated as $Zn_5(\mu_5\text{-pta})_2(\mu_2\text{-}H_2O)_2$ (pta= 2, 4, 6 pyridine tricarboxylate) shows emission peak at 467 nm whereas the free ligand exhibit the emission at 415 nm when excitation wavelength (λ_{ex}) is 338 nm at room temperature. The fluorescence enhancement and red shifted emission in the framework structure suggesting decrease in the HOMO–LUMO energy gap in the ligand of the MOF. The decrease in the energy gap in the framework attributed to the formation of framework structure and rigidity of the backbone stronger intermolecular/intramolecular intreractions among the organic linkers.

Fluorescence in organic molecule can be affected by reversible change in electron distribution occurring in the excited state. The two important processes are excited state proton transfer (ESPT) and excited state electron transfer (ESET). In ESET process the electron in the excited state transfer from electron rich donor to the electron acceptor upon excitation whereas in the ESPT process the proton in the excited state removed or join the molecule at different rate from that of in the ground state. ESPT is faster than the fluorescence emission and intramolecular proton transfer is faster than the intermolecular. The luminescence change induced by excited state intramolecular proton transfer has been observed by the Maji *et al.* in both the free dihydroxyterephthalate (dhta) ligand and in magnesium MOF , $Mg(dhta)(dmf)_2$.[32] Let us see the schematic diagram of excited state intramolecular proton transfer process.

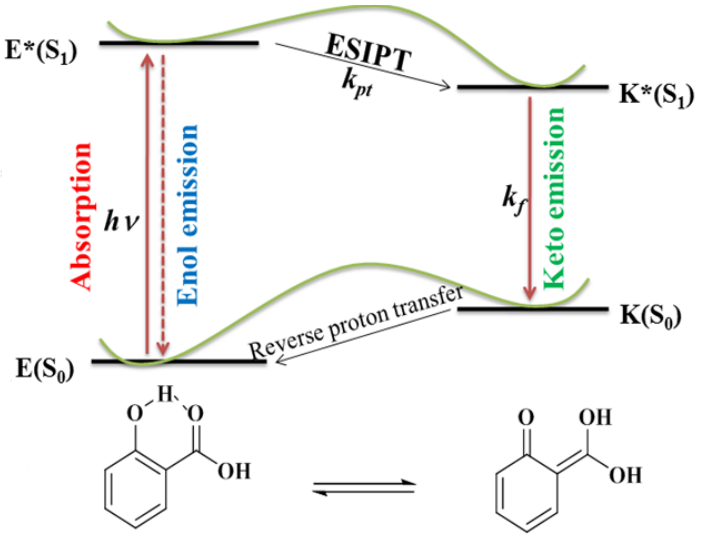

Figure 7. Schematic representation and energy diagram in ESIPT process.

1.4.6 Magnetic properties of MOFs

One of the many properties of MOF is magnetism. Magnetic property in a MOF can be implemented by incorporating either paramagnetic metal ions and/or open-shell organic ligands but this is not sufficient to render a material magnetic as magnetism is a cooperative phenomena and some kind of interaction between moment carrier is required.[33,34] Therefore a linker which can provide the distance between the moment carrier in the range of interaction and can mediate the exchange interaction process is essential. There are two fundamental series of magnetic elements which play an essential role in magnetism namely 3d transition metals and 4f rare earth metals. [35]

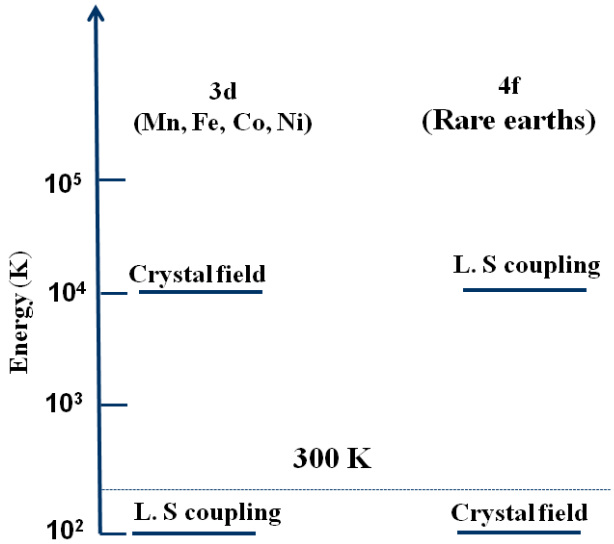

Figure 8. Orders of magnitude of the different interaction acting on 3d and 4f atoms in materials

The crystal field interaction is much weaker in the 4f element than in the case of 3d element because 4f shells are much better shielded by the outer shell than the 3d shell consequently 4f elements are less affected by bonding than that of 3d elements. Majority of the magnetic MOFs are consisting of 3d transition metal ion but rare earth can also give rise some interesting magnetic material. As mentioned magnetic property is a cooperative phenomena and the 'cooperative' word has several meaning but in the context of magnetism this word primarily refers to interaction of valence electron of neighboring atoms in a molecule or extended framework. The magnetic moments of rare earth elements are associated both with the spin and the orbital angular momentum of f electrons. Their spatial extension of small magnitude makes them weakly sensitive to their local environment. The trivalent ions are characterized by f^n configuration which give rise to ^{2S+1}L multiplet, splitted by spin orbit coupling to give J state and crystal field is considered as a perturbation acting on each J multiplet . Rare earth element carry large magnetic moment because of the presence of a large number of unpaired but transition temperature is less than that of the transition metal. Many of the lanthanides have very large magneto crystalline anisotropy, an important feature for some technological applications as well as anisotropy in magnetic moment. All these features boosted the material scientist to synthesize magnetic material based on the lanthanides. Therefore mixed lanthanide-transition metal framework is an important class of materials to exhibit interesting magnetic property arises from both the lanthanide and transition metal. The interesting aspect of magnetism is guest induced magnetic property change which can be exhibited by a porous magnet.

1.4.6.1 Porous Magnet

Porous magnet is a class of molecular materials where synergism of porous and magnetic properties has been observed.[35]There are various kind of porous magnet such as Prussian blue analogue and inorganic-organic hybrid material. Some fascinating properties of porous magnets are guest dependent spin crossover, guest dependent magnetic ordering and different magnetic behavior due to the reversible solvent induced structural change. Slight change of the coordination sphere around the metal ion expected to exhibit significant change in magnetic exchange coupling. Therefore structural determination of the material at various states after guest exchange or removal is very important to elucidate the structure-property relationship. However crystals which can retain its single crystallinity at solvent removed/ exchanged state are very scanty in the literature

especially those accompany the changes in the coordination environment therefore it is a great challenge to fabricate and understand the dynamic magnetic property in a porous magnet. Although two functionalities namely porosity and magnetism are mutually exclusive to each other but there are several reports of porous magnet. Solvent molecule induced magnetic property change requires the presence of porosity as well as long range magnetic ordering or structural reversibility via solvation and desolvation. The existence of porosity requires longer linker whereas long range magnetic ordering requires relatively short exchange pathways. The other possibility and most important applications of magnetism is development of materials exhibiting high anisotropic barrier.

1.4.6.2 Slow magnetic relaxation and anisotropic barrier

The first observed single molecular magnet (SMM), Mn_{12} -ac was synthesized by Lis *et al.* in 1980. If a metal cluster with very large ground state spin and magnetic anisotropy exhibits slow magnetic relaxation we call it as single molecular magnet. When the slow magnetic relaxation phenomena is observed in a 1d chain the terminology become single chain magnet (SCM). This indicates that slow magnetic relaxation phenomena is independent of the dimensionality of the compound and can be exhibited by any compound if it possesses both the large ground state spin and axial magnetic anisotropy. Lanthanide based polynuclear magnet are an important avenue to explore in the pursuit of slow magnetic relaxation with higher anisotropic barrier because of the strong spin orbit coupling commonly observed in 4f system. However lanthanide only compounds exhibiting slow magnetic relaxation are very rare. The scarcity of lanthanides only SMM results from the difficulty in promoting magnetic interactions between lanthanide ions however the interactions can be enhanced by overlapping bridging ligand orbital. In addition quantum tunneling of magnetization (QTM) which is common for lanthanide system generally prevents to isolate SMM with high anisotropic barrier. Although magnetic study of lanthanide based ferromagnet are well documented, it was hardly observed that ferromagnetic coupling and slow magnetic relaxation coexists in lanthanide based 3D frameworks.

1.4.7 Dual magneto –photoluminescent system

In the last few years there is a tremendous interest in developing multi functional material combining micro porosity, ferromagnetism, and optical properties. An interesting object is to synthesize a material where magnetic or luminescence property can be switched by some external perturbation. There are few lanthanide MOFs system reported in the

literature where the same material exhibit ferro-magnetism and emission properties. The general approach of synthesizing dual MOF is to assemble transition metal and lantahnides ions by polydentate nitrogen or oxygen containing linkers. Recently a 3d-4f (Dy-Mn) system of molecular formula $[Dy(hpd)_3(Mn)_{1.5}(H_2O)_6]\cdot 8.25\ H_2O$, which has honeycomb like 2D structure with cavity of 14.4 Å in diameter exhibits ferrromagnetic interaction and Dy^{III} based emission property. Most interestingly the emission peak intensities ($^4F_{9/2} \rightarrow {}^6H_{13/2}$ and $^4F_{9/2} \rightarrow {}^6H_{15/2}$ transitions) of the material increases drastically in DMF after adding Mg^{2+} ion, suggesting the compound can be used for sensing Mg^{2+}. The increase in the emission attributed to the coordination of Mg^{2+} to the hydroxo group of the ligand (hpd^{2-}) and changes the energy level of the excited state of the ligand consequently the energy level matches with the lanthanide leading to the decrease in the nonradioactive energy loss due the thermal vibration of -OH group.[38] An example of 4d-4f (Tb- Mo) system exhibits dual property was reported by Chelebaeva *et al*.[39] Many *n*d-4f system was synthesized earlier but their photoluminescence properties were overlooked. Another example of 4d-4f system reported by Zhao *et al.* where Ag^+ is used but a very weak magnetic interaction was observed in the case of Gd^{III}.[40] Few monometallic Ln^{III} systems also exhibit such dual property namely $[Tb_2(tdc)_3(H_2O)_4]$ reported by Huang *et al.* and $[Er(pza)(OH)(H_2O)]$ reported by Weng *et al*.[41,42]

1.5 Effect of process parameters for *in situ* ligand synthesis

Traditionally single-crystal of MOF or coordination polymers is obtained by the reaction of pre-synthesized or commercially available ligand and metal ion via evaporation of solvents, slow diffusion reaction and solvothermal reactions. Hydro (solvo) thermal reaction are typically carried out in sealed Teflon bombs and in the temperature range 120-200 ˚C under autogenous pressure(10-30 atm), exploit self assembled product from the precursors. The reduced viscosity of solvent under these conditions enhances the diffusion processes so that crystal growth from the solution is favoured. Under such non-equilibrium crystallizations conditions, metastable kinetic phases rather than thermodynamic phases can be isolated. Small changes in one or more variable of the hydrothermal reaction space like temperature, reaction duration, pH, solvent, and stoichiometry can have profound influence on the fate of the reaction. Recent research has revealed that the hydrothermal reaction is a promising technique in preparing complexes with novel structure and special properties especially in growing crystals of complexes involving *in situ* ligand synthesis. The vast majority of work on MOFs has used

transition metals. However the chemistry of rare earth metals till date has been largely an undeveloped area. Transition metal ions are more popular choice because of their well defined coordination geometry and low cost. Compared to this the reluctance of using lanthanides is due to their unpredictable coordination numbers and higher cost. Lanthanides trivalent ions are hard acceptor have strong affinity to coordinate with oxygen donors ligands than with nitrogen donor ligands. We used lanthanide ions to produce MOFs by using DHFA as a precursor. In this point I will also introduce another hydroxyacid 2,5-dihydroxyterephthalic (H_4DHTA) acid to have a comparative study. A series of compound which has been synthesized using DHFA, and DHTA as precursor of oxalate and /or carbonate ligand. Here we will see that DHFA at high temperature for 3 days will produce one type of compound whereas it will produce another kind of compound after eight days. It is worth mentioning here the product obtained after 8 days are not pure and only few crystal we could able to separate, the structure determination from the X-ray diffraction of a single-crystal provides an idea about synthesizing mixed metal MOFs which are very scanty in literature.

1.6 General Introduction of metal nanoparticles

The physical and chemical properties of materials are determined by the type of motion of electrons allowed to execute. Unconfined electrons have motion that is not quantized can thus absorb any amount of energy. Once an electron is bound in an atom or a molecule, its motion becomes highly confined and quantization begins. Smaller the space in which motion is bound stronger is the confinement and larger is the separation between allowed energies of different type of motion. In a metal electrons are least confined as they are highly delocalized over a large space and separation between valence and conduction band vanishes. As we decreases the size the separation between valence and conduction band increases and become comparable or larger than the kT and the metal becomes a semiconductor or an insulator. A new type of properties is expected to be observed which are neither possessed by the metal nor by the atom forming the metal due to increase in the size domain at which metal to insulator transition occurs. Mean free path of an electron is defined as the distance the electron travels between scattering collision with the lattice center. In nobel metal the decrease in size below mean free path of an electron give rise to intense absorption band at Visible- near-UV range. These results from the coherent oscillation of an electron from one surface of the particle to another and is called the surface plasmon absorption. Such strong absorption induces

stronger coupling with the electromagnetic radiation of light. This gives brilliant colour in colloidal solution that discovered by the scientists in 17th century. Chemical reduction of metal salts dissolved in appropriate solvents produces small nanoparticle with varying size distribution. Since colloidal particles prepared in solvent has a strong tendency to agglomerate it is necessary to inhibit their growth by using capping agent. A variety of reducing agent like different alcohols, glycerol, $NaBH_4$ etc has been used. With enormous growth in the multidisciplinary nanoscience research now material scientist, biologist, and engineers are trying to develop easy, sustainable, and 'green' method for the synthesis of metal nanostructures, having multiple functionalities. Such 'green chemistry' environment viable approach would be beneficial for application into biologically relevant systems and hence more practicable. There are various applications of small metal nanoparticle technology to a number of areas like heterogeneous catalysis, surface enhanced Raman scattering (SERS) and fields of research where surface and interface properties are important such as in heat exchangers, thermometers at ultra low temperatures, magnetic devices, superconductivity etc. Recent theoretical and experimental development of magnetic property of coinage metal at its nanometer size range has attracted considerable interest although the exact reason of showing ferromagnetic behaviour of a magnetically innocent metal at its nanometer size regime is a matter of contradiction.[43]

1.7 Surface Enhanced Raman Scattering (SERS)

The 'gas of free electrons' can be driven to perform collective oscillations that are known as *plasma oscillation* or *Plasmon.* These are simply quanta of the oscillation of surface charges produced by the external electric field. Plasmon modes can be observed in thin films, called surface Plasmon, in nanoparticle called localised surface Plasmon or particle Plasmons (PPs). SPs on flat surface are non radiative because interaction between light and SPs cannot simultaneously satisfy energy and momentum conservation. The restriction can be overcome by roughening the metal surface. Plasmon plays the key role in the explanation of SERS electromagnetic mechanism when they are excited in nanoscopic metal particles. Metal particle has better absorbance to electromagnetic radiation compared to smooth metal surface. There are three basic components involved in SERS; a molecule, a metal nano structure and an electromagnetic radiation. The molecule interacts with metal nanostructure either by physisorption or chemisorptions processes. Physisorption refers to weak interaction comes from Vander walls forces and

chemisorptions refers to strong interaction, almost comparable to a chemical bond. The absorption of light by nanostructure creates strong (enhanced) local electric fields at the position of the adsorbates. The new local electric field strongly affects the optical properties of the adsorbate species and exhibit SERS effect. The most commonly used metal in SERS is silver. The enhancement in SERS is not equal for all frequencies. The frequencies for which the Raman signal is shifted slightly from the incident light, both the incident light and the Raman signal can be in resonance with the plasmon frequency, leading to the E^4 enhancement. On the other hand when the frequency shift is large, the incident light and the Raman signal cannot both be in resonance, thus the enhancement at both stages cannot be maximal. The choice of surface metal is dictated by plasmon resonance frequency. To excite the Raman modes visible or NIR lights were used. Silver and gold are used for this purpose because their plasmon frequencies are falling within this wavelength range, providing maximum enhancement for visible and NIR light. In chapter 3 newly synthesized silver nanorods were used for SERS.[44]

1.8 Catalysis by gold

Catalysis is one of the most important applications of metal nanoparticle. Gold is known to be very popular because of its chemical inertness. However in 1970s Parravano's group investigated the catalytic activity of gold in oxygen/hydrogen transfer reactions and the reduction of NO by dihydrogen. Recently catalysis by gold nanoparticle as well as oxide supported gold nanoparticles is an interesting area of research. The reactions where gold nanoparticle taking part as a catalyst are oxidation of CO and alcohols, hydrogenation of unsaturated hydrocarbons, three component coupling reaction etc. It is believed that positively charged gold nanoparticles are more catalytically active and different oxide supported gold nanocatalyst systems are already been developed by various group to carry out different type of gold catalysed reaction. Furthermore recent reports suggests without oxide support gold can also exhibit catalytic activity in its colloidal form and with decrease in the size of the particle catalytic activity increases.[45]

1.9 Introduction of hydroxy acids

This thesis deals with the investigation of hydroxy acids and some other related organic compound for the fabrication of MOFs and coinage metal nanostructures. The various functionalities of MOFs and metal nanostructures have already been discussed in the previous sections. Let us define what hydroxyacids (HA) are and their possible different applications. HA are a class of compounds containing both hydroxyl group and acid

groups. HA plays an important role in cosmetic formulation as well as in many dermatologic applications, such as in treating photoaging, acne, ichthyosis, rosacea, pigmentation disorders, and psoriasis. Some of the hydroxy acids are non toxic. Since MOF has possible future applications in biology, use of nontoxic reagent for the synthesis of MOF may have better applications compared to other toxic chemicals.[46] The members of hydroxyacids which are included in this thesis are 2,3 dihydroxyfumaric acid (DHFA), mucic acids (2,3,4,5-tetrahydroxohexanedioic acid) and 2,5 dihydroxyterephthalic acid (H_4dhta). These three hydroxy acids are different with respect to its source, structure and functionality. Let us begin the discussion about DHFA.

1.9.1 2, 3-dihydroxyfumaric acid (DHFA)

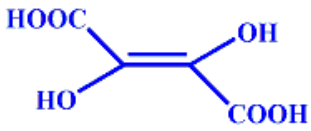

2,3 dihydroxyfumaric acid (DHFA)

DHFA has a long history since the days of its synthesis and extensive study by Fenton in the year 1890s.[47,48] The compound has been synthesized by oxidizing tartaric acid by hydrogen peroxide in presence of ferrous sulphate. The chemistry of DHFA and that of its ester derivative has been investigated in non aqueous solvent however studies of the aqueous chemistry is rarely explored due to its inherent instability in aqueous solution owing to its oxidative transformation into diketosuccinic acid (DKSA). In 2005 Robson *et al.* first reported synthesis of highly symmetric MOFs of divalent metal ion by using DHFA as a precursor of trisubstituted metahanol, $HOC(COOH)_3$. They have established the details mechanism of this conversion because of the aerial oxidation of DHFA. From the above mentioned chemistry of DHFA we believe that the DHFA has very high tendency to be oxidized, in other words it can act as a reducing agent.[49]

To understand the fact that DHFA can act as a reducing agent we performed a simple reaction to prove the reducing capability of DHFA. 0.1(M) aqueous solution of copper^{II} chloride was added to the aqueous DHFA solution of neutral pH under constant stirring and instantaneous colour change (blue to colorless) with white color precipitation at the bottom of the beaker was observed in end. The PXRD pattern of the white color

precipitation was found to have similar PXRD pattern as Cu_2Cl_2 (Figure 9). This observation motivated us to use it as a reducing agent for various purposes like synthesis of Cu^I or mixed-valence Cu^I/Cu^{II} MOFs and functional metal nanostructures

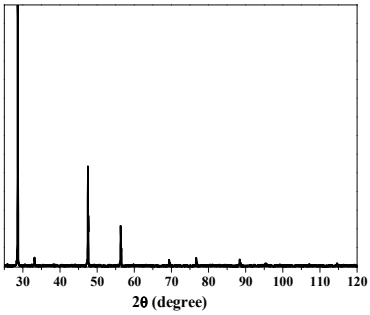

Figure 9. PXRD pattern of the solid after reaction of DHFA and $CuCl_2$ in aqueous medium.

1.9.1.1 Synthesis of cuprous compound in aqueous medium

As a researcher of MOF my first aim was to use this interesting compound for the fabrication of MOFs. Among various metal ions we have used copper as a targeted metal ion because monovalent coinage metal ions are attractive candidate as a soft Lewis acid. They can adopt diverse coordination geometries such as linear, trigonal planar, tetrahedral *etc*. Moreover coordinatively unsaturated Cu^I is a fundamental component of biological system. In porous coordination polymer coordinatively unsaturated metal centres plays crucial role as interacting sites for the guest molecules. It has been observed that Ag^I and Cu(I) exchanged zeolites shows higher activity towards adsorption of different gases like nitrogen, hydrogen, carbondioxide, and other hydrocarbons. Considering the density and price copper is more useful than silver in common sense. Synthesizing porous Cu^I compound with coordinatively unsaturated Cu^I sites supposed to be a potential candidate for gas storage materials. Acetylene is known to form metal$\cdots\pi$ complexes with Cu^I with low coordination number. Separation of acetylene from CO_2 is highly challenging since they are similar in the equilibrium sorption parameter and molecular size and shape and hence Cu^I compounds have potential to fulfill this purpose. [50] On the other hand mixed-valent compounds of copper are of paramount importance because of their interesting optical and electronic properties. Since synthesizing such compound requires appropriate linker for stabilization of Cu^I and fulfillment of coordination geometry of Cu^I as well as Cu^{II}. There are two major problems to fabricate Cu^I compounds in aqueous medium. Cu^I

has tremendously high tendency to be oxidized to cupric state and cuprous salts are insoluble in water. We solved both the problems by generating Cu^{I} *in situ* by using DHFA as reducing agent and stabilizing Cu^{I} state by soft organic linker. Controlling the stoichiometry of the reaction and judicious choice of the ligand it is possible to isolate mixed-valent Cu^{I}/Cu^{II} MOFs also.

The history of mixed valence compound begins with the synthesis of Prussian blue in 1704 later on various kind of mixed valence compounds were synthesized but they had not been treated as a different class of materials . In 1967 Robin and Day has classified these new class of compounds into three different classes based on their structure and property.[51] The brief theory of classifications of mixed-valenced compounds are as follows. Considering the set of seven metal ions having the geometrical arrangement shown in Figure 1 . The metal ion in site A differs from those of site B not only because of their relative geometrical arrangement but also because of the field of the ligand According to the classifications of Robins and Day the three different class of compounds has following distinguishable criteria.From above table one may easily distinguish different class mixed valenced compound by taking a close look at the structures. In the mixed valenced compound of copper where Cu^{I} has trigonal or tetrahedral coordination geometry whereas Cu^{II} is in octahedral coordination geometry we can classify the compound as a classI rather than class II or Class III because of the different symmetry and/or strength and we may guess mixing coefficient α^2 should have a negligibly small value.

Class I compounds has no interesting electronic or optical properties but these type of material with porous functionality may find some application as a gas storage, separation or guest responsive modulation of electronic ,magnetic or optical properties.

Class I	Class II	Class IIIA	Class IIIb
Metal ion in ligand fields of very different symmetry and/or strength i.e tetrahedral *vs.*	Metal ion in ligand fields of nearly identical symmetry differing from one another by distortion	metal ions indistinguishable but grouped into polynuclear clusters	all metal ions indistinguishable

Octahedral	of only a few tenths Å		
α=0; valences very firmly trapped	α > 0; Valences distinguishable, but with slight delocalization	α maximal locally	α maximal; complete delocalization over the cation sublattice
No mixed valence transition in the visible region	One or more mixed valence transition in the visible region	One or more mixed valence transition in the visible region	Absorption edge in the infrared, opaque with metallic reflectivity in the visible region

The second chapter explains novel synthesis, characterization and sorption properties of Cu^{I} and mixed-valent Cu^{I}/Cu^{II} MOFs.

1.9.1.2 Synthesis and properties of coinage metal nanostructures

A general approach to fabricate nanoparticle is reduction of metal ion in presence of organic capping agent. The reducing agent play the role of conversion of the metal ion to metal and capping agent inhibit the growth so that it is stabilized in nanometer size without the formation of bulk metal. This approach is generally known as bottom up chemical approach. DHFA is a reducing agent for Cu^{II} to Cu^{I} (E_0 =0.15V) obviously it is an efficient reducing agent for Ag^{I} to Ag^{0} (E_0 =0.80V) and Au(III) to Au(0) (E_0 =1.50V) conversion. Moreover DHFA after oxidation converted to diketosuccinicacid (DKSA), TSM and ester of DKSA all these derivatives are hydroxogroup and acid group enriched. Hence, DHFA may serve binary roles of reducing agent as well as capping agent (methyl ester of 2, 3-diketosuccinic acid (DKSA). Reducing capability and environmentally benign nature of DHFA inspired us to extend its use for the synthesis of nanoparticle at room temperature. In the chapter 3, I will introduce a new chemical into the world of nanoscience for the fabrication of coinage metal nanostructures and unveil their various interesting properties like SERS activity, catalytic activity and magnetic properties.

1.9.1.3 Synthesis of lanthanide-oxalate-carbonate and mixed metal-oxalate frameworks

In chapter 2 and 3 we observed DHFA acts as a reducing agent for the fabrication of low valent coinage metal MOF or nanostructures through *in situ* reduction of corresponding higher valent metal ions. In this chapter we will observe the same HA in different role, as a precursor of some symmetrical ligands, oxalate and carbonate. In chapter 4, DHFA is

used as a ligand precursor where it converted to oxalate and carbonate at high temperature in presence of La^{III} ions. Synthesis of a series of lanthanide-oxalate-carbonates, their characterization and interesting luminescence and magnetic properties are discussed in chapter 4. During the synthesis of a series of lanthanide-oxalate-carbonate, when a reaction was carried out with $Ho(NO_3)_3$ at high temperature in presence of KOH for longer time period once some beautiful crystal we could able to isolate from a product mixture. Structural determination of the crystal suggests that the compound is mixed metal (Ho-K)-oxalate framework with weakly coordinated solvent water molecule to K^I. The compound is expected to have interesting multiple functionality because of the presence of different kind of metal ions with different functionality in the system. Chapter 5 associated with the synthesis, characterization and details investigation of hydrogen gas and other solvent vapor sorption property whereas chapter 6 contains isostructural dysprosium compounds with interesting functionalities associated with the Dy^{III} ion. The framework exhibits highest ever reported value of anisotropic barrier of 418 K among lanthanide MOFs including single molecular magnet. The compound found to exhibit reversible water responsive magnetic and luminescent property change.

1.9.2 Mucic acid

The process parameters like temperature, pH, reaction time and solvents has significant role on the structure on the MOF materials and obviously to their properties. Such an example is a reaction of mucic acid with metal ions at different conditions. Mucic acid, an aliphatic, naturally occurring hydroxyacid can be isolated from various natural sources viz putrified blood, sugar beets, and fresh fruits.[52] This environmentally benign and naturally occurring hydroxyl acid is used very rarely for the synthesis of metal-organic framework although it has potential to obtain porous metal-organic for various applications like gas storage sensing, magnetism etc.

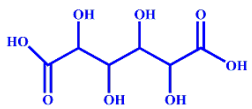

Mucic acid

In this chapter, I have discussed pH controlled synthesis of two different compounds under the same hydrothermal condition. The motivation behind choosing this compound as a linker is that it is a multifunctional ligand with two (-OH, -COOH) different type of chemically abstractable protons. After coordination with metal ions it may provide some

hydroxo group as a pendant site for interacting with guest molecule and polarity to the pore surface. This chapter deals with syntheses characterization, luminescent and magnetic properties of lanthanide mucicate framework. Tunable emission colour of mixed lanthanide with details study of energy transfer between terbium and europium has been discussed in this chapter. The another interesting aspect of this chapter is the study of sensing property of metal ions through the quenching of the emission intensity of lanthanide (Tb^{III}).

1.9.3 2,5 -dihydroxyterephthalic acid

In the final chapter, Chapter 8 2,5- dihydroxyterephthalic acid has been used as a linker. This chapter describes synthesis, structural characterization and adsorption properties of a number of lanthanide-organic frameworks has been demonstrated Furthermore H_4dhta is an excited state proton transfer (ESPT) responsive organic linker and based on this the tuneable emission properties of a lanthanide framework have been studied in different solvent system having different polarity. All the three different hydroxyacid at high temperature may act as a precursor of oxalate.

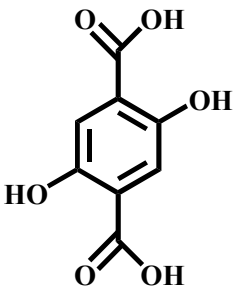

2,5-dihydroxyterephthalic acid (DHTA)

1.10 References

1. D. W Breck, *Zeolite molecular sieves: structure*, Chemistry and use, Willey, New York, 1974
2. W.M. Meier, D. H. Olsen and C, Baerlocher, *Atlas of zeolite structure types*, Elsevier, London, London, 1996.
3. J. V. Smith , *Chem Rev*., 1988, **88**, 149
4. B. F Hawkins and R. Robson , *J. Am. Chem. Soc*.,1990, **112**, 1546.

5. M. Fujita, Y. J. Kwon, S. Washizu and K. Ogura, *J. Am. Chem. Soc*., 1994, **116**, 1151.
6. O. M. Yaghi, G. Li and H. Li, *Nature,* 1995, **378**, 703.
7. D. Venkataraman, G. B. Gardner, S. Lee and J. S. Moore, *J. Am. Chem. Soc*.,1995, **117**, 11600.
8. M. Kondo, T. Yoshitomi, K. Seki, H. Matsuzaka and S. Kitagawa, *Angew. Chem. Int. Ed.,*1997, **36**, 1725.
9. S. Kitagawa, R. Kitaura and S-I. Noro, *Angew. Chem. Int. Ed.,*2004, **43**, 2334.
10. J. S. Choi, W. J. Son, J. kim and W. S. Ahn, *Micropororos and Mesoporos Materials*, 2008, **116**, 727.
11. Z. Ni and R. I. Masel, *J. Am. Chem. Soc*.,2006, **128**, 12394.
12. M. P. Suh, H. J. park, T. K. Prasad aand D. W. Lim, *Chem Rev*., 2012, **112**, 782
13. H. Furukawa, N. Ko, Y. B. Go, N. Aratani, S. B. Choi, E. Choi, A.Ö Yazaydin, R. Q. Snurr, M. O′Keefe, J. Kim and O. M. Yaghi, *Science*, 2010, **329**, 424.
14. J. An, O. K. Farha, J. T. Hupp, E. Pohl, J. I. Yeh and N. L. Rosi, *Nat. Commun.*2012, **3**, 604 , doi: 10.1038/ncomms1618 .
15. L. Pan, M. B. Sander, X. Huang, J. Li, M. Smith, E. Bittner, B. Bockrath, J. K. Johnson, *J. Am. Chem. Soc*., 2004, **126**, 1308.
16. M. Eddaoudi, J. Kim, N. Rosi, D. Vodak, J. Wachter, M. O′Keefe and and O. M. Yaghi, *Science*, 2002, **295**, 469.
17. L. J. Moore, M. Dinca and J. R. Long, *Chem. Soc. Rev.,* 2009, **38**, 1294.
18. R. J. Kuppler, D. J. Timmons, Q-R. Fang, J-R Li, T. A. Makal, M.D Young, D. Yuan, D. Zhao, W. Zhuang and H. C. Zhou, *Coord. Chem.Rev.,* 2009, **253**, 3042.
19. S. Ma, D. Sun, J. M. Simmons, C. D. Collier, D. Yuan and H. C. Zhau, *J. Am. Chem. Soc*.,2008, **130**, 1012.
20. J. R. Lee, Y. Ma, M. C McCarthy, J. Sculley, J. Yu, H. K. Jeong, P. B. Balbuena, H. C. Zhou, *Coord. Chem. Rev.,* 2011, **255**, 1791.
21. K. Sumida, D. L, Rogo, J. A. Mason, T. M. McDonald, E. D. bloch, Z. R. Harm, T. H. Bae and J. R. long, *Chem Rev*., 2012, **112**, 724.
22. J. Rocha, L. D. Carlos, F. M Almida paz and D. Ananias, *Chem. Soc. Rev.,* 2011, **40**, 926.
23. M. D. Allendorf, C. A. Bauer, R. K. Bhakta and R. J. t. Hout, *Chem. Soc. Rev.,* 2009, **38**, 1330.
24. N. Hildebrandt and H. G. Löhmannsröben, *Curr. Chem. Bio*. 2007, **1**, 2.

25. J. R. Lakowicz, *Principles of Fluorescence Spectroscopy,* Springer, 2006.
26. B. l. chen, l. B. Wang, Y. Q. Xiao, F. R. Fronczek, M. Xue, Y. J. cui, and G. D. Qian, *Angew. Chem. Int. Ed.,*2009, **48**, 500.
27. B. L. chen, L. B. Wang, F. Zapata, G. D. Qian and E. B. Lobkovsky, *J. Am. Chem. Soc*.,2008, **130**, 6718.
28. K. L. Wong, G. L. Law, Y. Y. Yang, and W. T. Wang, *Adv. Mater*., 2006, **18**, 1051.
29. B. L. Chen, Y. Yang, F. Zapata, G. D. Qian and E. B. Lobkovsky, *Adv. Mater.,* 2006, **18**, 1051.
30. Y. Q. Xiao, L. B. Wang, Y. J. Cui, B. L. Chen, F. Zapata, and G. D. Qian, *J. Alloys Compound*.,2009, **484**, 601.
31. W. H. Zhu, Z. M. Wang, and S. Gao, *Inorg. Chem*, 2007, **46**, 1337.
32. K. Jayaramulu, P. Kanoo, S. J. George and T. K. Maji, *Chem. Commun.*, 2010, **46**, 7906.
33. M. Kurmoo, *Chem. Soc. Rev.,* 2009, **38**, 1353.
34. E. Trémolet de, D. M. Schlenker, *Magnetism Fundamentals,* Springer, 2006.
35. X. N. Cheng, W. X. Zhang, Y. Y. Lin, y. Z. Zheng, and X. M. Chen, *Adv. Mater.,* 2007, **19**, 1494.
36. Z. Wang, B. Zhang, Y. Zhang, M. Kurmoo, T. Liu, S. Gao and H. Kobayashi, *Polyhedron*, 2007, **26**, 2207.
37. Y. G. Huang, F. L. Jiang and M.C. Hong, *Coord. Chem.Rev.,* 2009, **253**, 2814.
38. B. Zhao, H. L. Gao, X. Y. Chen, P. Cheng, W. Shi, D. Z. Liao, S. P. Yan, and Z. H. Jiang, *Chem- Eur. J.*, 2006, **12**, 149.
39. E. Chelebaeva, J. Larionova, Y. Guari, R. A. Sá Ferrieira, L. D. Carlos, F. A. A. Paz, A. Trifonov, and C. Guérnin, *Inorg. Chem*., 2009, **48**, 11048.
40. X. Q. Zhao, B. Zhao, S. Wei, and P. Cheng, *Inorg. Chem*., 2009, **48**, 11057.
41. W. Huang, D. Y. Wu, P. Zhou, W. B. Yan, D. Guo, C. Y. Duan, and Q. J. Meng, *Cryst. Growth. Des.,* 2009, 9, 1361.
42. D. F. Weng, X. J. Zheng, X. B. Chen, L. Li and L. P. Jin, *Eur. J. Inorg Chem.,*2007, 3410.
43. A. S. Edelstein,and R. C. Cammarata, *Nanomaterials: Synthesis,Properties and Applications* ,Institute of Physics , 1996.
44. Ricardo Aroca, *Surface enhanced vibrational spectroscopy*, Willey, 2006.
45. G. C. Bond, Catherine Louis, D. T. Thompson, *Catalysis by Gold,* Imperial College Press, 2006.

46. A. Kaurnhauser, S. G. Coelho, V. J. Hearing, *Clinical and Cosmetic Investigational Dirmetology*, 2010, **3**, 135.
47. H. J. H. Fenton, *J. Chem. Soc., Trans.*, 1894, **65**, 899.
48. H. J. H. Fenton, *J. Chem. Soc., Trans.*, 1896, **69**, 546.
49. B. F. Abrahams, T. A. Hudson and R. Robson, *J. Am. Chem. Soc.*, 2004, **126**, 8624.
50. J. P. Zhang and S. Kitagawa, *J. Am. Chem. Soc.*, 2008, **130**, 907.
51. M.B. Robin and P. Day *Adv. Inorg. Chem. Radiochem.,* 1967*,* **10***,* 247.
52. F. E. L. J. Anet and T. M. Reynolds, *Nature*, 1954, **174**, 930.

Chapter 2

Facile Synthesis of Functional Cu^{I} and Mixed-valent Cu^{I}/Cu^{II} Frameworks in Aqueous Medium and Aerobic Condition

Abstract 2,3-dihydroxyfumaric acid (DHFA) is a redox active hydroxyacid, can reduce Cu^{II} to Cu^{I} and oxidized to diketosuccinic acid (DKSA) in aqueous medium. The redox activity of DHFA has been utilized for the synthesis of versatile Cu^{I} MOFs using different Cu^{II} salts and stabilized by nitrogen containing linkers *viz* pyrazine (pyz), 1,2-bis(4-pyridyl)ethylene (bpee) and 2,3-pyrazine-dicarboxylate (pyzdc). Four novel Cu^{I}-frameworks, $\{Cu(pyz)_{1.5}(ClO_4)\}_n$ (**1**), $\{Cu(pyz)(NO_3)\}_n$ (**2**), and $\{[Cu(bpee)Cl]\cdot 2H_2O\}_n$ (**3**) and $\{[Cu_2(pyzdc)]\cdot 0.83H_2O\}_n$ (**4**) and other previously reported frameworks have been synthesized and structurally characterized. When the linker is same, only the copper salts are different, different structures are formed due to coordination of corresponding anion to the metal center. Inversely using same Cu^{II} source but changing the linkers various structures are obtained. This is a one step green method for the synthesis of Cu^{I} coordination frameworks from Cu^{II} state where DHFA acts as two electron donor to reduce Cu^{II} to Cu^{I}. Interestingly the compound **4,** synthesized by using 2,3-pyrazine dicarboxylate linker is unique from other reported frameworks because of its unusual coordination geometry, extraordinary thermal stabilty and porous property. Compound **4** exhibits single-crystal-to-single-crystal structural transformation via dehydration and rehydration. To demonstrate the control over the oxidation state of copper in the product, we changed the concentration of DHFA to isolate mixed valence compound. Two mixed-valent porous Cu^{I}/Cu^{II} frameworks, $[Cu^{II}Cu^{I}_2(2,4\text{-pyrdc})_2(pyz)_3]\cdot 2H_2O\}_n$ **(5)** and $\{[Cu^{II}Cu^{I}_2(2,4\text{-pyrdc})_2(bpy)_2]\cdot 4H_2O\}_n$ (**6**) have been synthesized using mixed ligand system. The mixed-valent state of the compounds has been established from X-ray diffraction study of single-crystal, X-ray photoelectron spectroscopy (XPS), magnetic measurement and bond valence calculations. Compound **3, 4, 5** and **6** exhibit interesting gas and solvent adsorption properties.

(1) A Paper related to this chapter has been published, S. Mohapatra and T. K. Maji, ***Dalton Trans.***, 2010, **39**, 3412.
(2) Another paper related to this chapter has been published, S. Mohapatra, H. Sato, R. Matsuda, S. Kitagawa and T. K. Maji, ***CrystEnggComm***, 2012, **14**, 4153.
(3) A paper related to this chapter has been submitted for publication.

2.1 Introduction

2,3-dihydroxyfumaric acid (DHFA) was first synthesized by Fenton in the 1890s from tatartaric acid, a naturally occuring hydroxyacid, afterwards it has been used for various purposes.[1] The chemistry of DHFA and that of its ester derivative has been investigated extensively in non aqueous solvents; moreover the aqueous chemistry is rarely explored due to its inherent instability in aqueous solution owing to its oxidative transformation into diketosuccinic acid (DKSA) and subsequent products.[2] The conversion of DHFA to DKSA in aqueous solution clearly demonstartes that it can act as a reducing agent for a redox couple with high reduction potential. On the otherhand coordination chemistry of Cu^{I} has paramount importance due to its role in biological processes,[3] catalysis,[4] solar energy sensing,[5] photophysics,[6] gas adsorption etc. Synthesis and stabilization of Cu^{I} compounds at open aerial atmosphere is a great challenge due to its intrinsic instability and facile oxidation to Cu^{II}.[2] Here, to establish a facile method for the synthesis of cuprous compound from Cu^{II} salt in a green way, we have exploited the $2e^{-}$ oxidation of DHFA (Scheme-1). However Mixed-valent Cu^{I}/Cu^{II} coordination compounds have great biological importance for their versatile coordination geometry, structural relevances in certian metallo-enzymes and interesting electronic properties.[7] Since the stoichiometry behind the reduction of Cu^{II} to Cu^{I} by DHFA has been understood properly, it is possible to synthesize different Cu^{I} and mixed-valent Cu^{I}/Cu^{II} compounds. Small literature of mixed-valent copper coordination frameworks[8] witness the difficulties of synthesizing this kind of compounds. Most of the reported mixed-valent copper coordination frameworks were prepared in hydrothermal conditions with pyridine derivatives and occurences were largely serendipitious.[9] Here we have chosen pyrazine based linker for the stabilization of Cu^{I} state. We have stabilized the mixed valence state by intutively adopting a mixed ligand system of pyridinedicarboxylate a chelating ligand and a soft linker pyrazine (pyz), 1,2-bis(4-pyridyl)ethylene (bpee) or 4,4′ bipyridine (bpy).[10] Pyrazine and its derivative have been extensively used for the fabrication of verstaile metal-organic frameworks of Cu^{I}.[11,12] This chapter deals with the one step facile synthesis of Cu^{I} and Cu^{I}/Cu^{II} mixed-valent coordination frameworks by using various pyridine or pyrazine based linker from different Cu^{II}-salts in aqueous solution under

open atmosphere (details in Scheme 1). During the synthesis of various Cu^{I} MOFs we could able to isolate a unique porous MOF of Cu^{I}, $\{[Cu_2(pyzdc)]\cdot 0.83H_2O\}_n$ exhibiting high thermal stability, rigidity and single-crystal-to-single-crystal structural transformation upon dehydration and rehydration. Two mixed-valent compounds, $[Cu^{II}Cu^{I}_2(2,4\text{-pyrdc})_2(pyz)_3]\cdot 2H_2O\}_n$ and $\{[Cu^{II}Cu^{I}_2(2,4\text{-pyrdc})_2(bpy)_2]\cdot 4H_2O\}_n$ of different dimensionality exhibit solvent and gas adsorption properties.

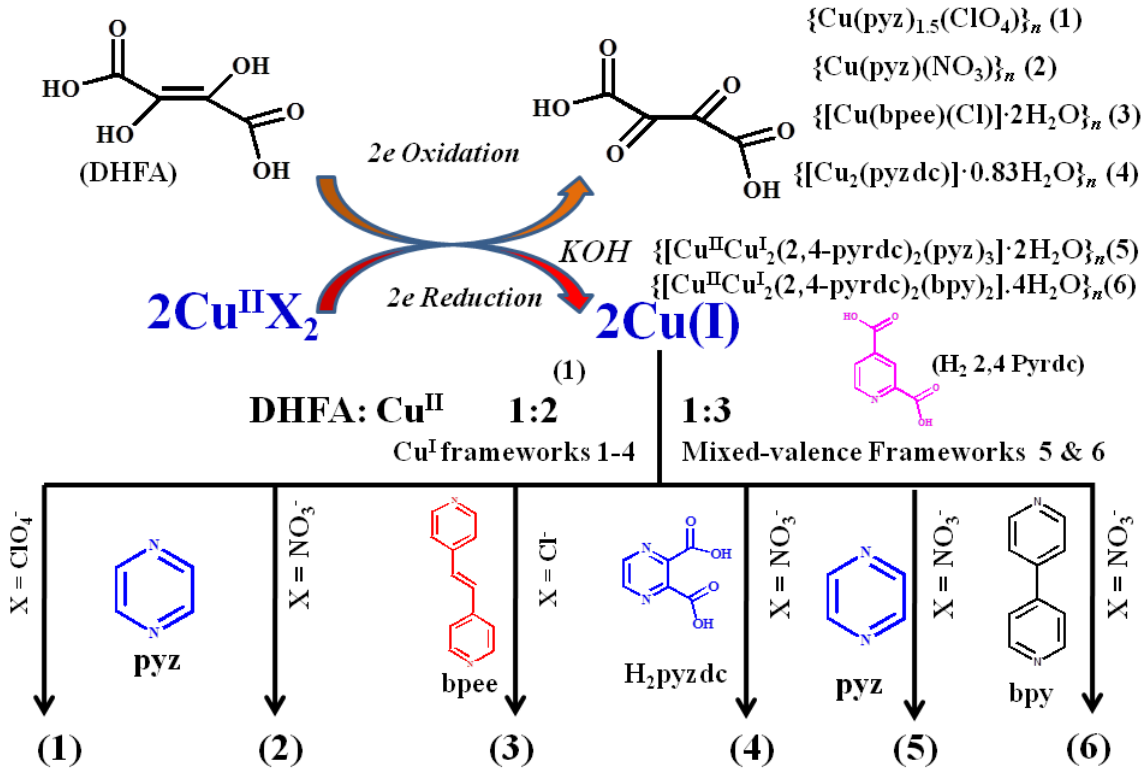

Scheme 1. *In situ* redox reaction of Cu^{II} salt and DHFA for the synthesis of different Cu^{I} and mixed-valent Cu^{I} / Cu^{II} MOFs.

2.2 Experimental section

2.2.1 Materials. All the reagents and solvents employed were commercially available and used as supplied without further purification. $Cu(ClO_4)_2\cdot 6H_2O$, $CuSO_4\cdot 5H_2O$, $Cu(NO_3)_2\cdot 2.5H_2O$, $CuCl_2\cdot 2H_2O$, 2,3-dihyroxyfumaric acid, 2,4-pyridinedicarboxylic acid and pyrazine, 2,3- pyrazinedicarboxylic acid, 4,4′-bipyridine (bpy) were obtained from Sigma Aldrich Chemical Company.

2.2.2 General synthesis of $[CuI(pyz)x(X)y]_n$

5 mL aqueous solution of $Cu^{II}X_2$ ($X = ClO_4^-, NO_3^-, 0.5SO_4^{2-}, Cl^-$) (1 mmol) was drop wise added to the basic aqueous solution (10 mL) of 2,3-dihydroxyfumaric acid (DHFA) (0.5 mmol) and pyrazine (pyz) (1 mmol). The pH of the ligand solution was adjusted by using aqueous KOH solution. Instantaneously red / yellow coloured precipitate was formed. The whole reaction mixture was stirred for 20 min. The precipitate was filtered, washed with water and dried under vacuum. All the compounds were characterized by elemental analysis, IR spectroscopy, PXRD and single-crystal structural determination. The details of the synthesis of single-crystals and powder are given below.

2.2.3 Synthesis of $\{Cu(pyz)_{1.5}(ClO_4)\}_n$ (1)

An aqueous solution (10 mL) of DHFA (0.5 mmol; 0.074 g) was mixed with an aqueous solution (10 mL) of pyrazine (pyz) (1 mmol; 0.80 g) with constant stirring. Then 5 mL aqueous KOH solution was drop wise added to the above solution and pH was adjusted to slightly alkaline condition. $Cu(ClO_4)_2 \cdot 6H_2O$ (1 mmol; 0.370 g) was dissolved in 25 mL of MeOH and 2 mL of this solution was slowly and carefully layered on the top of the above mixed ligand solution using the 1 mL buffer solution (H_2O and MeOH; 2 : 1 (= V/V)). Yellow needle-like crystals were obtained after one week. The crystals were separated and washed with water and dried.

Purity of the compound was confirmed by the elemental analysis, IR spectra and PXRD pattern Yield: 70%.(relative to metal ion), Anal Calcd for $CuC_6H_6ClN_3O_4$ **(1)** : C, 25.42; H, 2.12; N,14.83. Found: C, 25.10; H, 2.29; N, 14.32. IR spectra (cm^{-1}, KBr pellet): ν(pyz), 3085, 3026w (b_{1u}, b_{3u}); 1475m (b_{1u}); 1415s (b_{3u}); 1110m (b_{2g}); 800m (b_{2u}) 447s (b_{2u}); $\nu_3(ClO_4^-)$ 1114vs; $\nu_4(ClO_4^-)$ 941w.

2.2.4 Synthesis of $\{Cu(pyz)(NO_3)\}_n$ (2) and $\{Cu(bpee)(H_2O)_2\}_n$ (3)

Red colored single-crystals of the compound **2**, **3** and **4** were prepared adopting the same procedure as of the compound **1** by using the $Cu(NO_3)_2 \cdot 2.5H_2O$ for **2** and **4** and $CuCl_2 \cdot 2H_2O$, for **3** respectively instead of $Cu(ClO_4)_2.6H_2O$. For **3**, bpee was used instead of pyz. For $\{Cu(pyz)(NO_3)\}_n$ (**2**): Yield 80%. Anal Calcd for $CuC_4H_4N_3O_3$ (**2**): C, 23.34; H, 1.95; N, 20.42. Found: C, 23.67; H, 2.11; N, 20.06. IR (cm^{-1}, KBr Pellet): ν(pyz),

3085, 3026w (b_{1u}, b_{3u}); 1477m (b_{1u}); 1155s (b_{1u}); 1112m (b_{2g}); 800s (b_{2u}) 447s (b_{2u}); $\nu(NO_3)$: ν_1(NO) 1385(s); ν_5 (NO) 1514 (vw)

For complex $\{Cu(bpee)(Cl)\}_n$ (3): Yield 80%. Anal Calcd for $CuC_{12}H_{14}ClN_2O_2$ (4): C, 45.43%; H, 4.42%; N, 8.83%. Found: C, 45.49%; H, 4.46%; N, 8.86%. IR (cm^{-1}, KBr pellet): ν(pyz), 3085, 3026w (b_{1u}, b_{3u}); 1477m (b_{1u}); 1408s (b_{3u}); 1110w (b_{2g}); 800s (b_{2u}); 446s(b_{2u});

2.2.5 Synthesis of $\{[Cu_2(pyzdc)]\cdot H_2O\}_n$ (4)

An aqueous solution (10 mL) of DHFA (1 mmol; 0.184 g) was mixed with an aqueous solution (10 mL) containing 2,3-pyrazinedicarboxylic acid (pyzdc) (1 mmol; 0.168g) with constant stirring. Then aqueous KOH (0.4 M) solution was drop wise added to the above solution and pH was adjusted to ≈ 6.0. and 25 mL aqueous ligand solution was prepared. $Cu(NO_3)_2\cdot 2.5H_2O$ (2 mmol; 0.465 g) was dissolved in 25 mL of MeOH and 2 mL of this solution was slowly and carefully layered on the top of the 2 mL above mixed ligand solution using 1 mL buffer (H_2O and MeOH: 1 : 1 (= V/V)). Dark red block shaped crystals were obtained after one week, were washed with MeOH and water and dried. Bulk amount of the compound was obtained by direct mixing of the respective reagents using the same molar ratio as indicated above in aqueous medium. Yield: 0.558 g (70% based on Cu). Anal Calcd for $Cu_2C_6H_4O_5N_2$ (**4**): C 23.15, H 1.28, N 8.99%. Found: C 23.05, H 1.37, N 9.06%. IR (KBr pellet, cm^{-1}): 3420 s ν(O-H); 1653s $\nu_a(COO_{unidentate})$, 1598 s $\nu_a(COO_{bridging})$, 1358 m ν_s(COO);

Compounds **1-3** were synthesized in bulk adopting same procedure as of compound **4**

2.2.6 Synthesis of $\{[Cu^{II}Cu^{I}_2(2,4\text{-pyrdc})_2(pyz)_3]\cdot 2H_2O\}_n$ (5)

An aqueous solution (10 mL) of DHFA (1 mmol; 0.148 g) was mixed with an aqueous solution (10 mL) containing pyrazine (pyz) (3 mmol; 0.240 g) and 2,4-pyrdc (2 mmol, 0.334 g) with constant stirring. Then 5 mL aqueous KOH solution was drop wise added to the above solution and pH was adjusted to slightly alkaline condition. $Cu(NO_3)_2.2.5H_2O$ (3 mmol; 0.696 g) was dissolved in 25 mL of MeOH and 2 mL of this solution was slowly and carefully layered on the top of the above mixed ligand solution using the 1 mL buffer solution (H_2O and MeOH: 2 : 1 (= V/V)). Red block shaped

crystals were obtained after one week which was collected and washed with MeOH and water and dried. Bulk amount of the compound was obtained by direct mixing of the respective reagents using the same molar ratio as indicated above in aqueous medium. The phase purity was confirmed by the elemental analysis and PXRD pattern. Yield: 70 %. Anal Calcd for $Cu_3C_{26}H_{22}O_{10}N_8$ (**5**): C, 39.14; H, 2.76; N, 14.05. Found : C, 39.05.; H, 2.67; N, 14.20. IR (cm^{-1}, KBr pellet): *ν*(pyz); 3085, 3026, vw (b_{1u}, b_{3u}); 1475w (b_{1u}); 1415s (b_{3u}); 1110m (b_{2g}); 1046m (b_{1u}) 800s (b_{2u}); 580 446s(b_{2u}); *ν*(COO^- $_{unidentate}$) 1653 b (ν_a), 1333 m (ν_s); *ν*(COO^- $_{bridging}$) 1613 s (ν_a).

2.2.7 Synthesis of $\{[Cu^{II}Cu^{I}_2(2,4\text{-pyrdc})_2(bpy)_2]\cdot 4H_2O\}_n$ (6)

Single-crystal of the compound was grown by slow diffusion reaction. 25 mL aqueous ligand solution was prepared by dissolving DHFA (1 mmol; 0.148 g); pyridine dicarboxylic acid (2 mmol, 0.334 g) and bpy (2 mmol; 0.312g) with constant stirring in 20 mL water. Then 5 mL aqueous KOH solution was dropwise added to the above solution and pH was adjusted to slightly acidic condition ≈ 6.5. $Cu(NO_3)_2\cdot 2.5H_2O$ (3 mmol; 0.696 g) was dissolved in 25 mL of MeOH and 2 mL of this solution was slowly and carefully layered on the top of the 2mL of above mixed ligand solution using the 1 mL buffer solution (H_2O and MeOH: 2 : 1 (= V/V)). Yellow block shaped crystals were obtained after one week which was collected and used for single-crystal X-ray diffraction study. Bulk amount of the compound was obtained by direct mixing of the respective reagents using the same molar ratio as indicated above in aqueous MeOH medium. The phase purity was confirmed by the elemental analysis and PXRD pattern. Yield: 50 %. Anal Calcd for $Cu_3C_{34}H_{30}O_{12}N_6$ (**6**): C, 45.08; H, 3.31; N, 12.38. Found : C, 45.15.; H, 3.19; N, 12.50. IR (cm^{-1}, KBr pellet): *ν*(bpy) 3095, 3020, vw (b_{1u}, b_{3u}); 1410s (b_{3u}); 1105m (b_{2g}); 1040m (b_{1u}) 805s (b_{2u}); 575 440s(b_{2u}); *ν*(COO^- $_{unidentate}$) 1657 b (ν_a), 1333 m (ν_s); *ν*(COO^- $_{bridging}$) 1610 s (ν_a)

2.2.8 Physical measurements

The elemental analyses were carried out on a Perkin Elmer 2400 CHN analyzer. IR spectra were recorded on a Bruker IFS 66v/S spectrophotometer with samples prepared in KBr pellets in the region 4000-400 cm^{-1}. X-ray powder diffraction (PXRD) pattern were

recorded on a Bruker D8 Discover instrument using Cu-$K\alpha$ radiation. Thermogravimetric analysis (TGA) were carried out on METTLER TOLEDO TGA850 instrument in the temperature range of 25 - 650 °C under nitrogen atmosphere (flow rate of 50 mL min^{-1}) at a heating rate of 5 °C/min.

2.2.9 X-ray crystallography

Suitable single-crystals of compound **1-6** were mounted on a thin glass fiber with commercially available super glue. X-ray single-crystal structural data were collected on a Bruker Smart–CCD diffractometer equipped with a normal focus, 2.4 kW sealed tube X-ray source with graphite monochromated Mo-$K\alpha$ radiation (λ = 0.71073 Å) operating at 50 kV and 30 mA, with ω scan mode. The programme SAINT [13]was used for integration of diffraction profiles and absorption correction were made with SADABS[14] programme. All the structures were solved by direct methods using SIR 92 and followed by successive Fourier and difference Fourier Syntheses. For all the compounds the non-hydrogen atoms were refined anisotropically. All hydrogen atoms were located by Fourier analysis. All calculations were carried out using SHELXL 97,[15] SHELXS 97,[16] PLATON 99[17] and WinGX system, ver. 1.70.01.[18] Crystal data and structure refinement parameters for **1-6** are summarized in Table 1. Selected bond distances and angles for **1-6** are given in Table 2-9, respectively.

2.2.10 Adsorption measurements

The adsorption isotherms of desolvated compounds of **3-6** (**3′-6′)** for different solvents (like H_2O, MeCN, EtOH, at 298 K and MeOH at 293 K) were measured in the vapour state by using BELSORP-aqua volumetric adsorption instrument from BEL, Japan. In the sample chamber (~12 mL) maintained at $T \pm 0.03$ K was placed the adsorbent sample (100-150 mg), which had been prepared at 373 K for **3, 5, 6** and 400K for **4** at 10^{-1} Pa for 18 hours prior to measurement of the isotherms. The adsorbate was charged into the sample tube, and then the change of the pressure was monitored and the degree of adsorption was determined by the decrease of the pressure at the equilibrium state. All operations were computer-controlled and automatic. N_2 (77 K), CO_2, Ar and H_2 (77 K) adsorption study of the dehydrated samples prepared at 373K (for **3, 5,** and **6)** and 400K

(for **4**) under high vacuum, were carried out using QUANTACHROME Quadrasorb- *SI* analyzer. The H_2, N_2, Ar and CO_2 used for the measurements are scientific / research grade with 99.999% purity. For the measurements, approximately 100 mg sample was taken in a sample holder and degassed for 18 hours under 0.1 Pa vacuum. Dead volume of the sample cell was measured with helium gas of 99.999% purity.

2.3 Results and discussion

DHFA acts as a two electron donor in the reaction to reduce two mole of Cu^{II} to Cu^{I} and various pyrazine or pyridine based soft organic bridging ligand acts as linker to form various structures (Scheme 1). In the case of compound **4** judicious choice of pyzdc, as a stabilizer and linker for fabricating a 3D Cu^{I} MOF is based on the following two facts. Firstly, it contains pyrazine ring which is a well-known heterocyclic ring for stabilizing Cu^{I} via coordination to softer nitrogen atoms.[8a] Secondly, two carboxylates are orthogonal to each other and consequently a higher dimensional structure based on oxygen coordination is expected compared to the linker where two carboxylate are present in the same plane. In the case of mixed-valenced compound synthesis along with pyrazine or bpy, 2,4-pyridinedicarboxylate was used because it is a good chelating ligand for Cu^{II}. The synthesis of various framework of Cu^{I} and Cu^{I}/Cu^{II} by using DHFA is shown in scheme 1. It was observed In both the mixed-valenced compounds that the coordination environment of Cu^{I} has higher number of nitrogen than oxygen whereas octahedral coordination geometry of Cu^{II} are formed by four oxygens and two nitrogen atoms.

2.3.1 Strcutural description of $\{Cu(pyz)_{1.5}(ClO_4)\}_n$ (1)

Compound $\{Cu(pyz)_{1.5}(ClO_4)\}_n$ (**1**) crystallizes in the monoclinic $P2_1/n$ space group and structural determination (Table 1) reveals a 2D coordination framework of Cu^{I} bridged by the two different pyz ligands (Figure 1a). Each Cu^{I} acts as a 3-connected node and attached to the three different Cu^{I} centres through pyz forming a 2D (6,3) connected honeycomb like network in the *bc* plane (Figure 1b). Each Cu^{I} centre is ligated to a monodentate ClO_4^- and form a distorted tetrahedral geometry with CuN_3O chromophore. The angles related to Cu^{I} are in the range of 89.54(13) – 144.11(14)°,

which reflect the degree of distortion from the ideal tetrahedral geometry. Cu1–N bond distances are in the range of 1.954(3) – 2.089(3) Å and the Cu1-O1_a (a = -1+x, y, z) bond distance is 2.564(4) Å, suggesting weak coordination of ClO_4^-anion. Both the pyz rings are involve in π···π interactions (cg···cg distances, 4.590 – 5.636 Å) resulting a 3D supramolecular framework (Figure 1c). In the 2D sheet nearest neighbour Cu···Cu separation through the two different pyz rings are 6.65 and 6.97 Å, respectively.

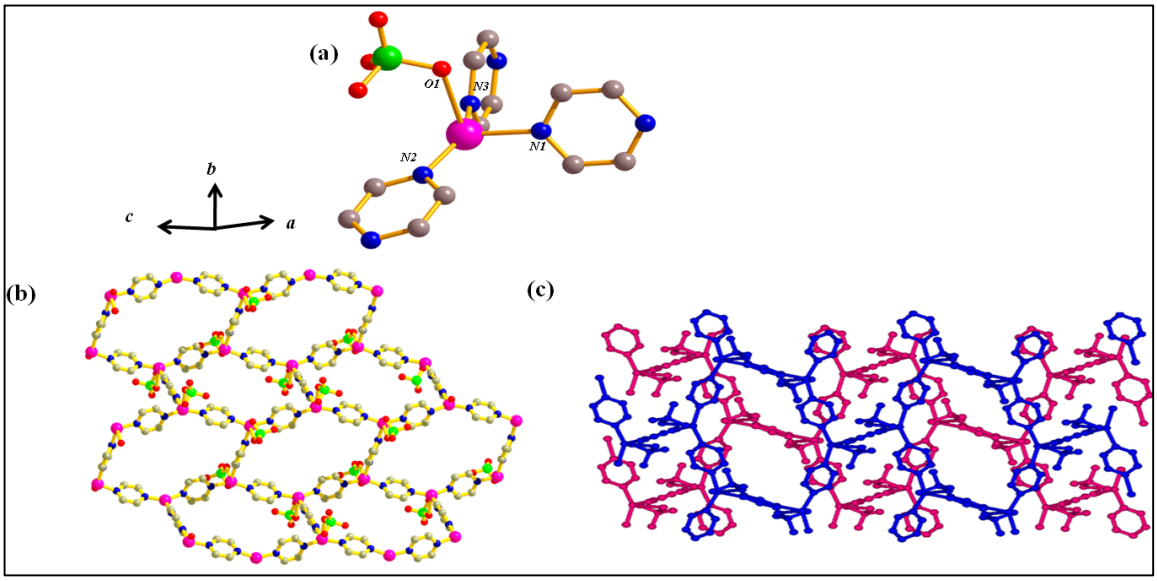

Figure 1. (a) Coordination environment of Cu^{I} in **1** (b) View of 2D (6, 3) corrugated sheet (c) Packing diagram between the 2D sheets.

2.3.2 Structural description of $\{Cu(pyz)(NO_3)\}_n$ (2)

Compound $\{Cu(pyz)(NO_3)\}_n$ (**2**) crystallizes in the orthorhombic *Pnma* space group and structural determination (Table 1) shows a 2D sheet of Cu^{I} bridged by the pyz and NO_3^- anions (Figure 2a). Each NO_3^- anion acts as a tridentate bridging ligand and chelates to a Cu^{I} via O1, O2 and connects to another Cu^{I} through μ_2-O2 bridge, forming a 1D zigzag chain of $[Cu(\mu\text{-}NO_3)]_n$ along the crystallographic *a*-axis. 1D chains are further pillared by the pyz ligands (N1, N1_e, e = x, -1/2-y, z) resulting a (4, 4) 2D sinusoidal sheet in the crystallographic *ab* plane (Figure 2a). In **2**, each Cu^{I} is in a distorted trigonal bipyramidal like geometry. Cu–O bond distances are in the range of 2.476(5) – 2.529(5) Å and Cu–N1 bond distance is 1.933(3) Å. N1–Cu1–

N1_e angle is 158.40(12)° suggesting the twist in connection with pyz ligand. The equatorial O–Cu1–O angles are in the range of 50.97(16) – 120.64(16)°, exhibiting the distortion around Cu1 geometry. Each 2D sheet stacks along the *c*-axis in a staggered conformation (Figure 2b). Cu···Cu distances along the NO_3^- and pyz bridges in 2D sheet are 4.594 and 6.580 Å, respectively and nearest neighbour intersheet Cu···Cu separation is about 5.079 Å.

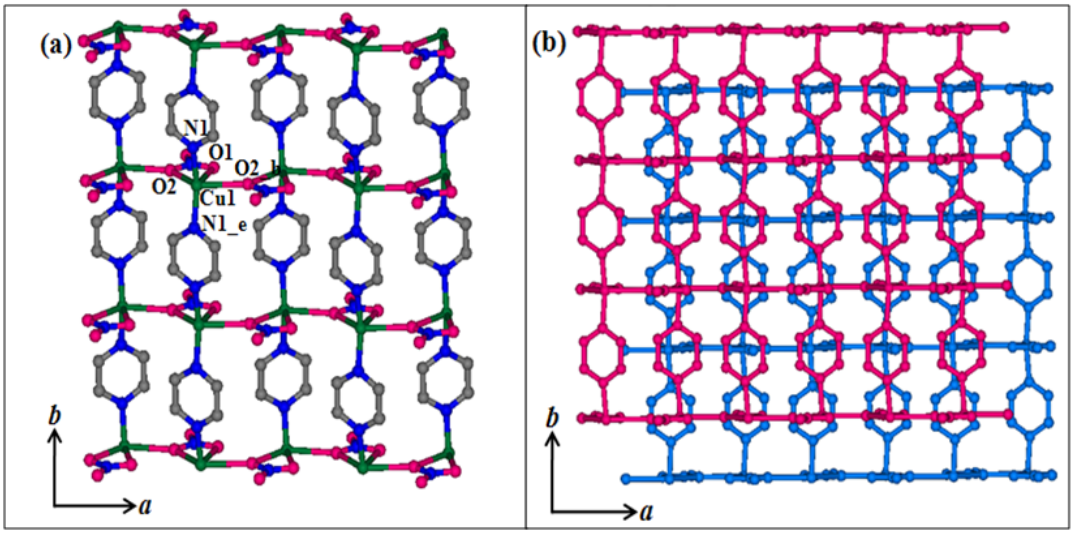

Figure 2. (a) View of the 2D sinusoidal sheet of $\{Cu(pyz)(NO_3)\}_n$ (**2**) in the crystallographic *ab* plane; (b) View of the packing diagram showing ABAB stacking (staggered type) between the 2D sheet.

2.3.3 Structural description of $\{[Cu(bpee)(Cl)]\cdot 2H_2O\}_n$ (3)

Compound **3** crystallizes in triclinic $P\bar{1}$ space group and structure determination reveals that a 2D coordination polymer of Cu^{I} brdiged by the Cl^- and bpee linker. Each Cu^{I} centre is connected to two different bpee linkers through nitrogen atoms (N1 and N2) and two Cl^- anions forming distorted tetrahedral geometry with CuN_2Cl_2 chromophore (Figure 3a). Therefore each Cu1 centre connected to three different Cu1 centre through two bpee linkers and doubly bridged Cl^- forming a 2D (6,3) net lying perpendicular to the (**01$\bar{1}$**) plane. In the framework Cu1-N1 bond distance (1.989(7) Å) is slightly larger than the Cu1-N2 bond distance (1.978(7) Å), whereas Cu1-Cl1 2.406(2) Å is smaller than the Cu1-Cl1_b 2.406(2) Å. The degree of distortion from the ideal tetrahedral geometry is reflected in the angles surrounding Cu1 is in the range of 85.70(7) – 132.1(2) ° (Table 4).

2D framework contains oval shaped channels with the dimension of 2.3 × 5.4 $Å^2$. It is worth mentioning that stacking of the 2D sheet along the crystallographic *b*-axis provides 1D water filled channels and the dimension of the square shaped channels is about 3.2 × 3.2 $Å^2$ (Figure 4). The framework contains 23.8% potential solvent accessible void volume to the total crystal volume as suggested by the PLATON[15]. Cu1···Cu1 separation along the bpee linker is about 13.325 Å and Cl^- bridged part is about 3.443 Å.

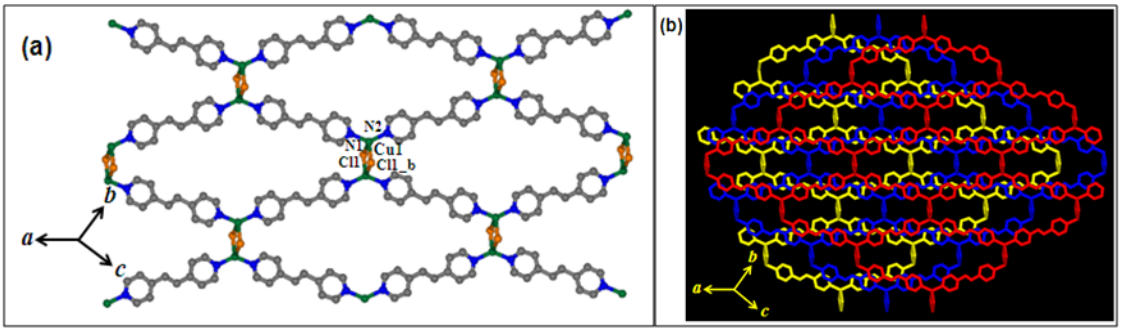

Figure 3. (a) View of the 2D (6,3) net of **3** showing coordination enevironemnt of Cu^{I} connected by the bpee linkers and Cl^- anions lying perpendicular to the crystallographic (**01**$\bar{1}$) plane; (b) Perspective view of the packing of 2D sheets.

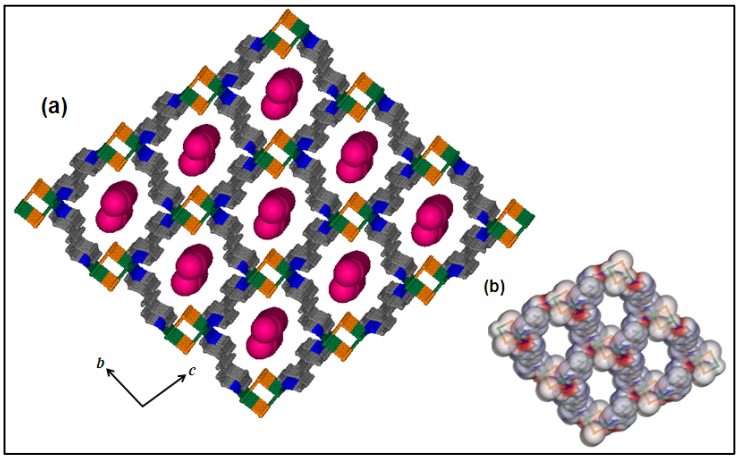

Figure 4. (a) 3D structure with 1D water filled channel along the *c*-axis formed by the AA stacking of 2D sheets in **3**; (b) View of the hexagonal pore in **3′**.

2.3.4 Structural description of $\{[Cu_2(pyzdc)]\cdot 0.83H_2O\}_n$ (4)

Compound **4** crystallizes in monoclinic crystal system with the space group *C*2/*c*. In

the asymmetric unit there are three crystallographically independent Cu^{I} centers (Cu1, Cu2 and Cu3), one pyzdc linker and 0.83 water molecule, where Cu2 and Cu3 atoms lie on the same two fold axis and Cu1 is at the general position (Figure 5). The highly distorted tetrahedral geometry around each Cu1 centre is formed by one chelated pyzdc (N1, O1), one carboxylate oxygen (O3) and one pyrazine nitrogen atom (N2) from another pyzdc linker. Two Cu1-O bond lengths are 2.096(6) and 2.194(6) Å whereas Cu1-N1/N2 bond lengths are 1.956(5) Å. The distortion around Cu1 is reflected in surrounding bond angles which are in the range of 80.7(2) – 140.7(3)°. Each Cu2 centre is connected to four bridging (μ_2-O) carboxylate oxygen atoms (O1, O1a, O4b and O4c) from the four different pyzdc linkers (Figure 5). The Cu2-O bond lengths are 2.728(6) and 2.789(5) Å for Cu2-O4 and Cu2-O1, respectively. The coordination geometry of Cu2 is neither tetrahedral nor trigonal pyramidal as the bond angles around Cu2 centre are in the range of 80.44(17) – 172.20(17)°. Such unusual coordination geometry of Cu2 is stabilized by the weak interaction with the bridging carboxylate oxygen atoms (O2, O2a) at a distance 2.880(5) Å. The most remarkable point is that Cu3 is connected to two carboxylate oxygen atoms (O2 and O2a) at a distance of 2.663(5) Å and the corresponding angle is about 88.20(17)°. However, Cu3 undergoes weak interaction with the crystalline water molecule O1w and its symmetry related counterpart at a distance of 2.95(2) Å (Figure5).

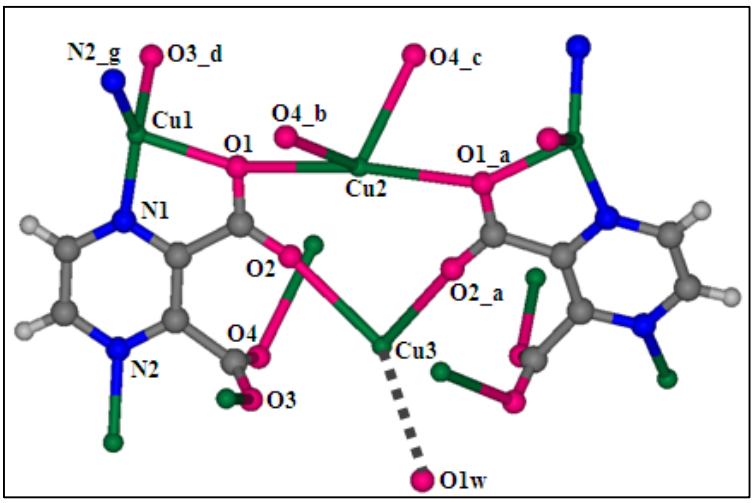

Figure 5. View of the coordination environment around different Cu^{I} centres connected by pyzdc in **4**. a =-x,y,-1/2-z, b =-x,1-y,-z, c =x,1-y,-1/2+z, d = x,1-y,1/2+z, g =1/2-x,1/2+y,1/2-z.

A 2D sheet is formed by the coordination of Cu^{I} to nitrogen atoms (N1, N2) and carboxylate oxygen atoms (O1, O2) which are present in the same plane of the pyrazine ring (Figure 5). Orthogonal carboxylate oxygens O3 and O4 (perpendicular to the plane containing pyrazine ring) and pyrazine nitrogen N2 act as connectors between 2D sheets to form a 3D framework (Figure 6A). This is clearly indicating orthogonal carboxylate group has significant role to extend the structure into 3D. The 3D framework contains a 1D water filled channels along the crystallographic *c*-axis (Figure 6B). Moreover, the water molecules present in the pore have an unusual coordination to Cu3 as its distance is 2.95Å and can be considered as semi-coordination. The dimension of the channels is about 2.54 × 3.05 $Å^2$. The void space of the desolvated framework is about 18.3 % to the total volume as suggested by PLATON.[15] In the 3D framework the nearest neighbour distances between the Cu1···Cu2, Cu1···Cu3 and Cu2···Cu3 is about 4.7999(10), 3.9325(10) and 3.8896(7) Å, respectively.

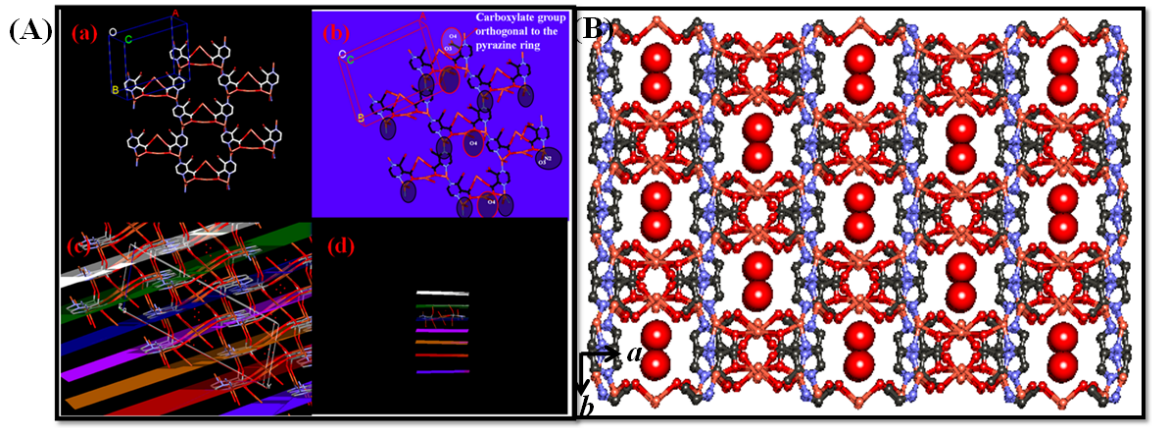

Figure 6. Formation of 3D framework structure: (A) (a) structure of 2D sheet, (b) red and black circles are the connecting sites of two adjacent 2D sheets, (c) and (d) showing the parallel equally spaced 2D sheets (B) 3D framework of **4** viewing along crystallographic *c* direction showing water filled channels.

2.3.5 Structural description of $\{[Cu^{II}Cu^{I}_2(2,4\text{-pyrdc})_2(pyz)_3]\cdot 2H_2O\}_n$ (5)

Compound **5** crystallizes in triclinic $P\bar{1}$ space group and structural determination reveals a 3D coordination framework of Cu^{I}/Cu^{II} bridged by the 2,4-pyrdc and pyz organic linkers. There are two crystallographically independent copper atoms (Cu1 and Cu2) in **5** as shown in Figure 7a. Each Cu1 atom is chelated to two 2,4-pyrdc in quatorial positions (N1, O1 and N1_g, O1_g; g = 4-x, -y, 2-z) and axial sites are occupied by the two oxygen atoms (O4_b and O4_f; b = 1+x, y, z; f = 3-x, -y, 2-z) from another two different 2,4-pyrdc ligands forming 4+2 coordination geometry. Each tetrahedral Cu2 atom is connected to three pyz ligands (N2, N3 and N4) and one oxygen atom (O3) from 2,4-pyrdc. The Cu1–O bond distances are in the range of 1.945(2) – 2.734(3) Å and Cu1–N1 bond distance is 1.966(2) Å. The degree of distortion of Cu1 from perfect octahedral geometry is reflected in *cisoid* angles which are in the range of 83.21(10) – 96.79(10)º. The Cu2-N bond distance is slightly higher and are in the range of 1.978(2) – 2.0507(19) Å and Cu2-O3 bond distance is 2.122(2) Å. In **5**, Cu1 and 2,4-pyrdc ligand form a $[Cu^{II}(2,4\text{-pyrdc})_2]^{2-}$ 'metallo ligand' and connect two $[Cu^{I}(pyz)_3]^{-}$ units through oxygen atoms (O3) and its symmetry related counterparts (O3*) and other two Cu^{II} through O4 and O4* atoms forming a 3D coordination framework with 1D water filled channels along the crystallographic *c*-axis (Figure 7b & c). The dimension of the rectangular channels (Figure 7c) is about 2.1 x 2.3 $Å^2$ [17] and calculation using PLATON[15] suggests framework contains 3.6 % void space to the total crystal volume. Each 2,4-pyrdc linker acts as a tridentate ligand leaving one oxygen atom (O2) free, which is aligned in the pore surfaces and connect with guest water molecule O1w through H-bond (O2···O1w, 2.830(2) Å). The pendent oxygen atoms O2 decrease the overall pore size of the framework and their periodic arrangment forms a 1D helical channels with highly polar pore surfaces (Figure 7c). The coordination geometry of Cu1 and Cu2 atoms in combination with charge balance and bond-valence calculation (Table 10)[18] indicates that Cu1 is divalent and Cu2 is in monovalent state.

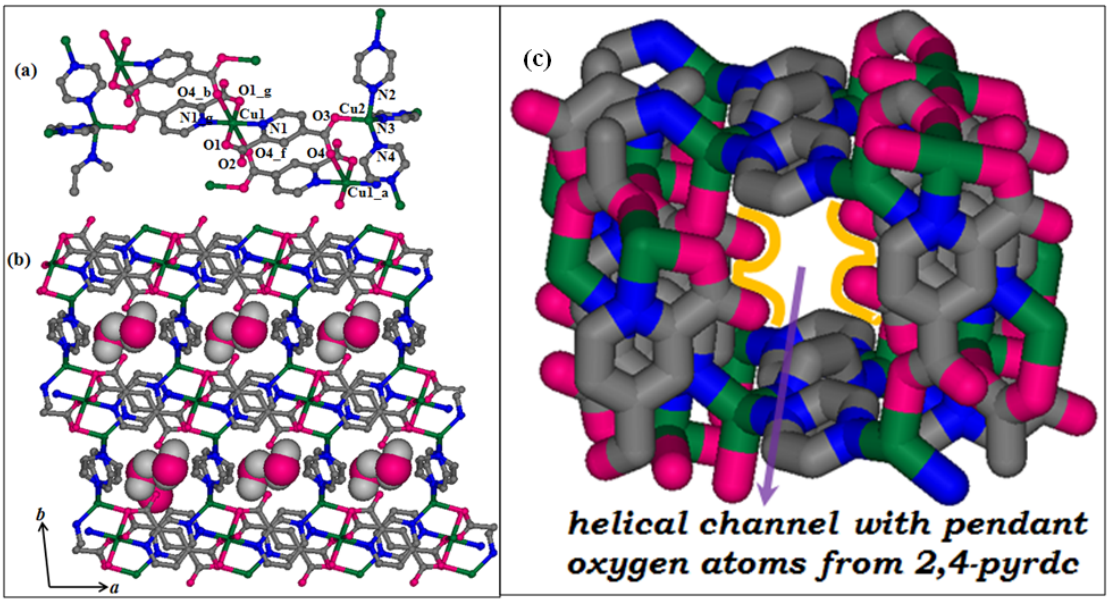

Figure 7. (a) View of the coordination environment around Cu^{II} (Cu1) and Cu^{I} (Cu2) in **5**; (b) View of the 3D coordination framework of 5 with 1D water filled channels along the *c*-axis. (c) View of the helical channel of **5** showing the pendent oxygen atoms from the 2,4-pyrdc are aligned in the pore surfaces.

2.3.6 Structural description of $\{[Cu^{II}Cu^{I}_2(2,4\text{-pyrdc})_2(bpy)_2]\cdot 4H_2O\}_n$ (6)

Compound **6** crystallizes in triclinic $P\bar{1}$ space group and structural determination reveals a 2D coordination framework of Cu^{I}/Cu^{II} bridged by the 2,4-pyrdc and bpy organic linkers. There are two crystallographically independent copper atoms (Cu1 and Cu2) in **1** as shown in Figure 8. Each divalent octahedral Cu2 centers are chelated to two 2,4-pyrdc in equatorial positions (N3, O1 and N3_e, O1_e; e =2-x,-y,2-z) and axial sites are occupied by the two oxygen atoms (O3 and O3_f; f = 3-x, -y, 2-z) from other two 2,4-pyrdc ligands. Each trigonal planar Cu1 centers are connected to two different nitrogen atoms (N1, N2) from two bpy and one oxygen atom (O2) of 2,4-pyrdc to form a trigonal planar coordination geometry. The Cu1–O and Cu1–N1 bond distances are 2.503(6) Å and 1.904(7) Å respectively Two different bond angles are 96.6° and 166.0°. In case of divalent copper (Cu2) two equivalent Cu2-N bond distance are 1.960Å. Cu2-O1 and Cu2-O3 bond lengths are 1.953Å and 2.653Å respectively. In this compound Cu2 and 2,4-pyrdc ligand form a $[Cu^{II}(2,4\text{-pyrdc})_2]^{2-}$ 'metallo ligand' and connected to two $[Cu^{I}(bipy)_2]$ linear chain through oxygen atoms

(O2) and form a 2D bilayer coordination framework. The linear chain of copper and bpy of two different sheets are involved in the non-covalent interaction to form a 3D structure with 1D water filled channel along the crystallographic *a*-axis (Figure 9). The 2D sheets are non covalently connected to each other by π···π stacking interaction along crystallographic *c* axis, where cg.. cg distances are of 3.902Å, and 3.673Å between two bpy rings (Figure 9). The 3D structure contains 1D dumbell shaped channels of about 2.3 × 4.5 $Å^2$ [19] along *a* axis and calculation using PLATON[15] suggests framework contains 13.2 % void space to the total crystal volume. Each 2,4-pyrdc linker acts as a pentadentate ligand leaving one oxygen atom (O4) uncoordinated, which is aligned in the pore surfaces and connected with guest water molecule O1w through H-bonding (O2...O1w, 2.830(2) Å). Topological analysis by TOPOS 4.0 suggest the structure is 4,6-c bi-nodal net structure with point symbol$\{\{3;6^4;8\}_2\{3^4;4^2;6^4;7^4;8\}$ where Cu1 and Cu2 has $\{3;6^4;8\}$ and $\{3^4;4^2;6^4;7^4;8\}$ point symbols respectively.

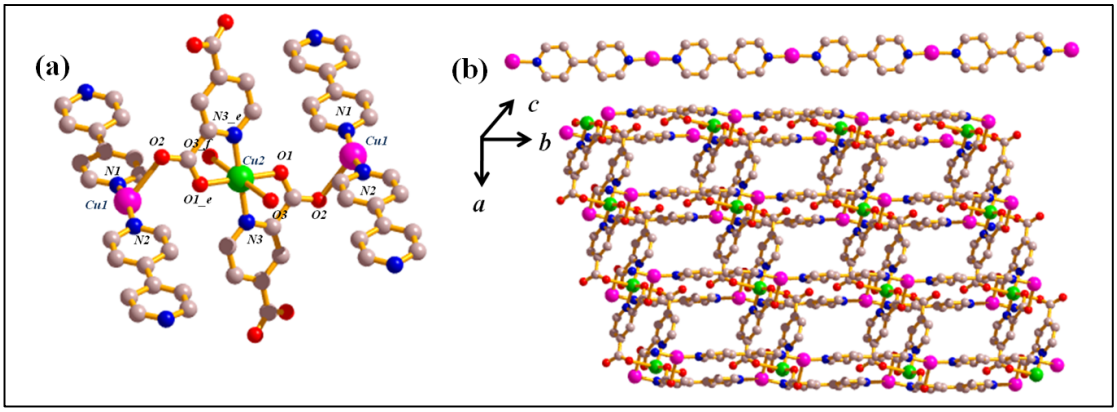

Figure 8. (a) Coordination environment of Cu1 and Cu2 (b) 2D bilayer structure of the mixed valent compound (**6**)

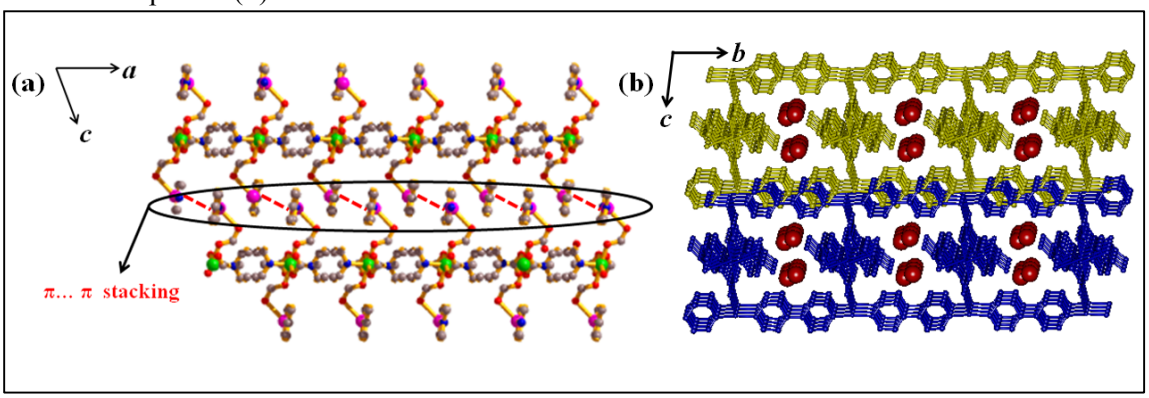

Figure 9. (a) View of the 3D structure formed by π···π stacking of bpy rings in **6** (b) Top: 1D Cu-bpy chain and bottom; view of 3D structure along crystallographic *a* direction with water

filled dumbell shaped channels.

2.3.7 Role of 2,3 dihydroxyfumaric acid

To understand the role of DHFA in the synthesis of Cu^{I} MOFs we performed a reaction at identical condition as of **1** and **2** by using $CuCl_2$ metal salt and pyz linker. The slow diffusion reaction provides green color block shaped crystal in the absence of DHFA and structural determination reveals that the compound, $\{Cu(pyz)(Cl)_2\}_n$ is same as previously reported by Fetzer and Pickardt *et. al*.[10b. 10e] The 2D structure is composed of copper in +2 oxidation state bridged by pyrazine and chloride (Figure 10a). When the same reaction was carried out in presence of DHFA a different compound, $\{Cu(pyz)(Cl)\}_n$ is formed. Structural determination reveals that copper is in +1 oxidation state which was reported earlier by Moreno *et al*[11d] (Figure 10b). This simple experiment firmly proves that DHFA is acting as reducing agent for Cu^{II}. As we have mentioned in the scheme that DHFA acts as two electron donor and by controlling the stochiometry of the reaction it is possible to obtain mixed valent compound in a facile way from Cu^{II} salt in aqueous medium. Two different mixed-valence compounds were synthesized adopting this strategy. The strategy needs the intuitive choice of ligand system which can provide the stability to Cu^{I} state as well as proper coordination environment of Cu^{II}. Mixed-valence compounds **5** and **6** has been synthesized employing this reagent.

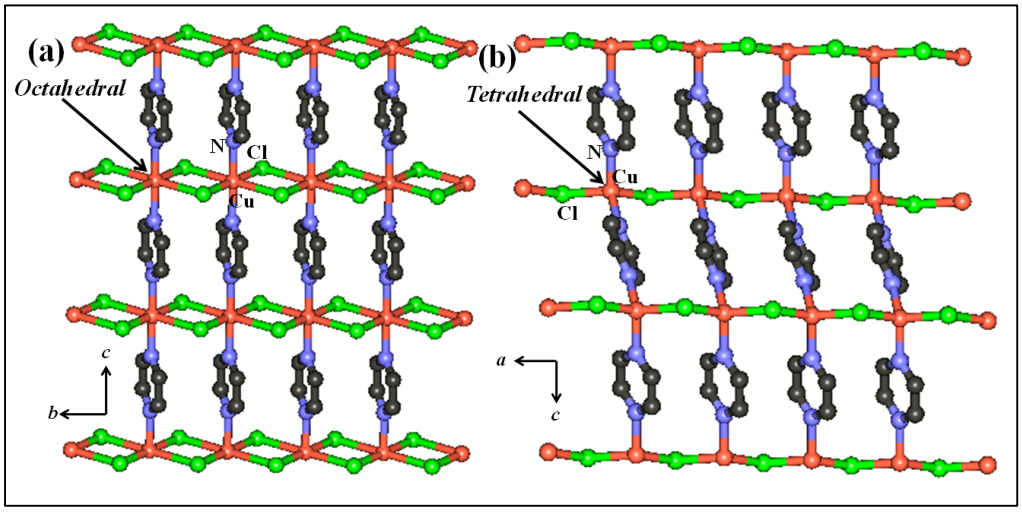

Figure 10. (a) Perspective view along crystallographic a direction of 2D rectangular grid-like framework of $\{Cu(pyz)(Cl)_2\}_n$ showing doubly bridge Cu^{II} with octahedral geometry (viewing

along crystallographic *a* direction) **(b)** Crystal structure of the compound obtained in presence of DHFA, where copper has tetrahedral coordination geometry (viewing along crystallographic *b* direction).

Table 1: Crystal data and structure refinement parameters for **1-6**

	1	**2**	**3**	**4**	**4′ (Dehydrated)**	**4″ (Rehydrated)**	**5**	**6**
Empirical formula	$C_6H_6ClCuN_3O_4$	$C_4H_4CuN_3O_3$	$C_{12}H_{14}ClCuN_2O_2$	$C_6H_2Cu_2N_2O_{4.83}$	$C_6H_2Cu_2N_2O_4$	$C_6H_2Cu_2N_2O_5$	$C_{26}H_{22}Cu_3N_8O_{10}$	$C_{34}H_{30}Cu_3N_6O_{12}$
M_r	283.14	205.65	317.22	308.48	293.2	311.2	797.17	905.29
crystal System	Monoclinic	Orthorhombic	Triclinic	Monoclinic	Monoclinic	Monoclinic	Triclinic	Triclinic
space group	$P2_1/c$	*Pnma*	$P\bar{1}$	$C2/c$	$C2/c$	$C2/c$	$P\bar{1}$	$P\bar{1}$
a (Å)	7.6851(10)	7.9915(5)	7.9239(6)	19.4082(4)	19.3848(4)	19.3929(10)	7.7849(4)	7.1189(10)
b (Å)	13.4524(17)	6.5796(4)	9.9549(9)	12.5929(2)	12.5209(3)	12.5914(6)	9.8480(5)	10.8416(14)
c (Å)	9.3010(13)	12.0511(8)	10.2041(9)	7.5885(2)	7.7134(2)	7.5890(3)	10.5585(6)	11.5089(15)
α (°)	90	90	98.014(6)	90	90	90	107.136(2)	86.263(9)
β (°)	97.565(7)	90	110.367(5)	107.034(1)	107.822(1)	107.013(2)	109.811(3)	75.333(10)
γ (°)	90	90	108.134(5)	90	90	90	96.066(2)	76.676(9)
V (Å^3)	953.2(2)	633.66(7)	688.83(11)	1773.31(7)	1782.32(7)	1772.02(14)	708.49(7)	836.2(2)
Z	4	4	2	8	8	8	1	1

T (K)	293	293	293	293	455	293	293	293
D_c (g cm^{-3})	1.973	2.156	1.510	2.296	2.185	2.318	1.868	1.798
μ (mm^{-1})	2.568	3.399	1.773	4.794	4.758	4.800	2.306	1.968
F (000)	564	408	316	1189	1136	4.800	401	459
θ_{max} (deg)	29.4	27.6	27.5	26.3	31.1	26.6	27.4	34.5
λ (Mo Kα)(Å)	0.71073	0.71073	13253	0.71073	0.71073	0.71073	0.71073	0.71073
tot. data	12240	3795	3151	7091	7189	7089	12400	13941
data [$I > 2\ \sigma(I)$]	1930	481	1518	1517	1785	1391	2526	1018
R^a	0.0585	0.0473	0.0783	0.0695	0.0764	0.0697	0.0331	0.0680
$R_w{}^b$	0.1781	0.0929	0.2626	0.1714	0.1834	0.1991	0.0900	0.1857
S	1.07	1.02	1.02	1.09	1.58	1.00	1.05	0.74

$R_a = \sum||Fo|-|Fc||/\sum|Fo|$; $^b R_w = [\sum\{w(Fo^2-Fc^2)^2\}/\sum\{w(Fo^2)^2\}]^{1/2}$

Table 2: Bond distances (Å) and angles (°) for $\{Cu(pyz)_{1.5}(ClO_4)\}_n$ (**1**)

Cu1-N1	1.958(3)	Cu1-N3	2.089(3)
Cu1-O1	2.564(4)	Cu1-N2	1.954(3)
N1-Cu1 -N3	101.44(13)	O1-Cu1-N1	99.32(14)
O1-Cu1-N3	89.54(13)	N3-Cu1-N2	112.31(13)
N2-Cu1-N1	144.11 (13)	O1-Cu1-N2	92.96(14)

Symmetry Code: a = -1+x, y, z

Table 3: Bond distances (Å) and angles (°) for $\{Cu_2(pyz)(NO_3)\}_n$ **(2)**

Cu1-O1	2.529(5)	Cu1-O2	2.476(5)
Cu1-N1	1.933(3)	Cu1-O2_b	2.500(5)
Cu1-N1_e	1.933(3)		
O1-Cu1-O2	50.97(16)	O1-Cu1-N1	100.71(8)
O1-Cu1-O2_b	69.67(16)	O1-Cu1-N1_e	100.71(8)
O2-Cu1-N1	95.67(10)	O2-Cu1-O2_b	120.64(16)
O2-Cu1-N1_e	95.67(10)	O2_b-Cu1-N1	94.97(12)
N1-Cu1-N1_e	158.40(12)	O2_b-Cu1-N1_e	94.97(12)
Cu1-O2-Cu1_a	134.8(2)	N1-Cu1-N3	101.44(13)
O1_a-Cu1-N1	99.32(14)	O1_a-Cu1-N3	89.54(13)

Symmetry Code: a = -1/2+x,-1/2-y,1/2-z; b = 1/2+x,-1/2-y,1/2-z; e = x,-1/2-y,z.

Table 4 : Bond distances (Å) and angles (°) for $\{[Cu(bpee)(Cl)]\cdot 2H_2O\}_n$ **(3)**

Cu1-N1	1.989(7)	Cu1-N2	1.978(7)
Cu1-Cl1	2.406(2)	Cu1-Cl1_b	2.649(2)
Cl1-Cu1-N1	108.3(2)	Cl1-Cu1-N2	109.05(18)
Cl1-Cu1-Cl1_b	94.30(7)	N1-Cu1-N2	132.1(2)
Cl1_b-Cu1-N1	98.37(17)	Cl1_b-Cu1-N2	107.55(19)
Cu1-Cl1-Cu1_b	85.70(7)		

Symmetry code: b =1-x,1-y,1-z

Table 5: Bond distances (Å) and angle **(˚)** for $\{[Cu_2(pyzdc)]\cdot H_2O\}_n$ **(4)**

Cu1-O1	2.194(6)	Cu1-N1	1.956(5)
Cu1-O3_d	2.096(6)	Cu1-N2_g	1.956(5)
Cu2-O1	2.789(5)	Cu2 -O2	2.880(5)
Cu2 -O1_a	2.789(5)	Cu2-O2_a	2.880(5)
Cu2-O4_b	2.729(6)	Cu2-O4_c	2.728(6)
Cu3-O1W	2.95(2)	Cu3-O2	2.663(5)

Cu3-O3	2.943(6)	Cu3-O1W_a	2.95(2)
Cu3-O2_a	2.663(5)	Cu3-O3_a	2.943(6)
O2 -Cu3-O2_a	88.20(17)	O2 -Cu3 -O3_a	138.92(17)
O1-Cu1-O3_d	95.4(2)	O1 -Cu1-N2_g	115.4(2)
O3_d-Cu1-N1	120.7(2)	O2_a -Cu3-O3	138.92(17)
N1 -Cu1-N2_g	140.7(3)	O3 -Cu3-O3_a	151.02(16)
O3_d-Cu1 -N2_g	94.5(2)	O1W_a-Cu3 -O2_a	111.2(4)
O1W_a -Cu3-O3_a	70.4(4)	O1 -Cu2-O1_a	172.20(17)
O2_a -Cu3-O3_a	66.77(16)	O1-Cu2-O4_b	104.32(18)
O1-Cu2 -O4_c	80.44(17)	O1_a-Cu2 -O2	126.14(16)
O1 -Cu1-N1	80.7(2)	O1_a-Cu2-O4_b	80.44(18)
O1_a -Cu2-O4_c	104.32(18)	O4_b-Cu2-O4_c	106.6(2)
O1W-Cu3-O2	111.2(4)	O1W -Cu3 -O3	70.4(4)
O1W -Cu3 -O2_a	150.6(5)	O1W-Cu3-O3_a	84.6(4)
O2 -Cu3-O3	66.77(16)	O1W_a -Cu3 -O2	150.6(5)

Symmetry code: a = x,y,-1/2-z, b = x,1-y,-z, c = x,1-y,-1/2+z, d =x,1-y,1/2+z, g =1/2-x,1/2+y,1/2-z

Table 6: Bond distances (Å) and angle **(°)** for $\{[Cu_2(pyzdc)]\cdot H_2O\}_n$ **(4′)**

Cu1-O1	2.211(4)	Cu1-N1	1.951(4)
Cu1-O3_d	2.074(4)	Cu1-N2_g	1.980(5)
Cu2-O1	2.777(4)	Cu2 -O1_a	2.777(4)
Cu2-O2_a	2.834(5)	Cu2-O4_b	2.692(6)
Cu2-O4_c	2.692(6)	Cu3-O2	2.643(5)
Cu3-O3	2.933(4)	Cu3-O2_a	2.643(5)
Cu3-O3_a	2.933(4)		
O2_a -Cu3-O3	138.08(17)	N1 -Cu1-N2_g	138.33(18)
O1 -Cu1-N1	80.67(16)	O3 -Cu3-O3_a	150.41(13)
O2 -Cu3-O2_a	84.46(17)	O2_a -Cu3-O3_a	68.54(14)
O1-Cu1-O3_d	96.07(16)	O1-Cu2-O4_b	99.12(15)
O2 -Cu3 -O3_a	138.08(15)	O1-Cu2 -O4_c	86.10(15)
O1 -Cu1-N2_g	111.27(17)	O1_a-Cu2 -O2	124.42(14)
O1_a-Cu2-O4_b	86.10(15)	O1_a -Cu2-O4_c	99.12(15)
O4_b-Cu2-O4_c	107.80(17)	O2 -Cu3-O3	68.54(14)
O3_d-Cu1-N1	124.17(17)		

Symmetry code: a = x,y,-1/2-z, b = x,1-y,-z, c = x,1-y,-1/2+z, d =x,1-y,1/2+z, g =1/2-x,1/2+y,1/2-z

Table 7: Bond distances (Å) and angle **(°)** for $\{[Cu_2(pyzdc)]\cdot H_2O\}_n$ **(4″)**

Cu1-O1	2.195(4)	Cu1-N1	1.950(5)
Cu1-O3_d	2.081(4)	Cu1-N2_g	1.965(5)
Cu2-O1	2.788(4)	Cu2 -O2	2.870(5)
Cu2 -O1_a	2.788(4)	Cu2-O2_a	2.870(5)
Cu2-O4_b	2.721(6)	Cu2-O4_c	2.721(6)
Cu3-O1W	2.930(12)	Cu3-O2	2.645(5)
Cu3-O3	2.943(4)	Cu3-O3_a	2.943(4)

Cu3-O2_a	2.645(5)	Cu3-O1W_a	2.930(12)
O2_a -Cu3-O3	139.06(13)	O1 -Cu1-N1	80.92(16)
O2 -Cu3-O2_a	87.96(16)	O1W-Cu3-O3_a	83.8(3)
N1 -Cu1-N2_g	140.2(2)	O3 -Cu3-O3_a	150.91(12)
O1-Cu1-O3_d	95.39(16)	O3_d-Cu1 -N2_g	94.77(19)
O2 -Cu3 -O3_a	139.06(13)	O1W_a-Cu3-O2_a	111.6(3)
O1 -Cu1-N2_g	114.91(18)	O1W_a-Cu3-O3_a	71.2(3)
O1 -Cu2-O1_a	172.42(13)	O2_a -Cu3-O3_a	66.80(12)
O1-Cu2-O4_b	104.62(14)	O1-Cu2 -O4_c	80.01(14)
O1_a-Cu2 -O2	126.00(14)	O1_a-Cu2-O4_b	80.04(14)
O1_a -Cu2-O4_c	104.62(14)	O4_b-Cu2-O4_c	106.20(17)
O1W_a-Cu3 -O3	83.8(3)	O1W-Cu3-O2	111.6(3)
O3_d-Cu1-N1	120.99(17)	O1W_a -Cu3 -O2	149.7(3)
O2 -Cu3-O3	66.80(12)	O1W -Cu3 -O2_a	149.7(3)

Symmetry code: a = x,y,-1/2-z, b = x,1-y,-z, c = x,1-y,-1/2+z, d =x,1-y,1/2+z, g =1/2-x,1/2+y,1/2-z

Table 8: Bond distances (Å) and angle **(°)** for $\{[Cu^{II}Cu^{I}_2(2,4\text{-pyrdc})_2(pyz)_3]\cdot 2H_2O\}_n$ **(5)**

Cu1-O1	1.945(2)	Cu2-N4	1.978(2)
Cu1-N1	1.966(2)	Cu2-N3	2.048(2)
Cu1-O4_b	2.734(3)	Cu2-N2	2.0507(19)
Cu1-O1_g	1.945(2)	Cu2-O3	2.122(2)
Cu1-N1_g	1.966(2)	Cu1-O4_b	2.734(3)
O1-Cu1-O4_f	96.79(10)	O1_g-Cu1-N1	96.46(12)
O1-Cu1-N1_g	96.46(9)	N1-Cu1-N1_g	180.00
O1-Cu1-O1_g	180.00	O4_b-Cu1-N1_g	86.11(8)
O1-Cu1-O4_b	83.21(10)	O1_g-Cu1-O4_b	96.79(10)
O3-Cu2-N2	96.49(8)	O4_b-Cu1-N1_g	86.11(10)
O3-Cu2-N3	99.33(9)	O4_b-Cu1-O4_f	180.00
O3-Cu2-N4	119.22(9)	O1_g-Cu1-N1_g	83.54(12)
N2-Cu2-N3	102.59(8)	O1_g-Cu1-O4_f	83.21(10)
N2-Cu2-N4	116.31(9)	O4_f-Cu1-N1_g	93.89(8)
N3-Cu2-N4	119.06(8)	O1-Cu1-N1	83.54(9)
O4_b-Cu1-N1	93.89(8)		

Symmetry code: b =1+x,y,z; g = 4-x,-y,2-z; f =3-x,-y,2-z

Table 9: Bond distances (Å) and angle **(°)** for $\{[Cu^{II}Cu^{I}_2(2,4\text{-pyrdc})_2(bpy)_2].4H_2O\}_n$ **(6)**

Cu1-O2	2.503(6)	Cu1-N1	1.904(7)
Cu1 -N2_c	1.891(6)	Cu2-O1	1.953(6)
Cu2-N3	1.960(7)	Cu2-O3_a	2.653(6)
Cu2-O1_e	1.953(6)	Cu2 -N3_e	1.960(7)
Cu2-O3_f	2.653(6)		
O2 -Cu1 -N1	96.6(2)	O2-Cu1-N2_c	96.6(3)
N1 -Cu1 -N2_c	166.0(3)	O1-Cu2-N3	82.9(3)
O1 -Cu2-O3_a	87.8(2)	O1_e-Cu2-N3	97.1(3)
O1-Cu2-O1_e	180.00	O3_a-Cu2-N3	78.6(2)
O1-Cu2-N3_e	97.1(3)	O1-Cu2-O3_f	92.3(2)

N3-Cu2-N3_e	180.00	O3_f-Cu2-N3	101.4(2)
O1_e-Cu2-O3_a	92.3(2)	O3_a-Cu2-N3_e	101.4(2)
O3_f -Cu2-N3_e	78.6(2)		

Symmetry code: a = -1+x,y,z; c = x,1+y,z; e =2-x,-y,2-z; f =3-x,-y,2-z

2.3.8 Additional evidence of mixed-valent state for 5 and 6

2.3.8.1 XPS study of 5 and 6

The XPS spectrum of the bulk sample of **5** shows a peak of $^{2}P_{3/2}$ at 932.0 eV, which is lower than that of a Cu^{II} complex (Figure 11a). It is because of the presence of Cu^{I} ions in this system. The weak satellite peak around 943 eV indicates that **5** also contains Cu^{II} ions. The XPS spectrum of the bulk sample of **6** shows a double humped curve in the region 928.5-938 eV(Figure 11b). This peak after deconvolution has been split into two different peaks of $^{2}P_{3/2}$ of binding energy 932.1 eV, and 934.2 eV. The peak at 932.1 eV corresponds to Cu^{I} and peak at 934.2 eV corresponds to Cu^{II}. The relative ratio of Cu^{I} and Cu^{II} is 2.03 which corroborates well with the molecular formula obtained from single-crystal X-ray diffraction study.

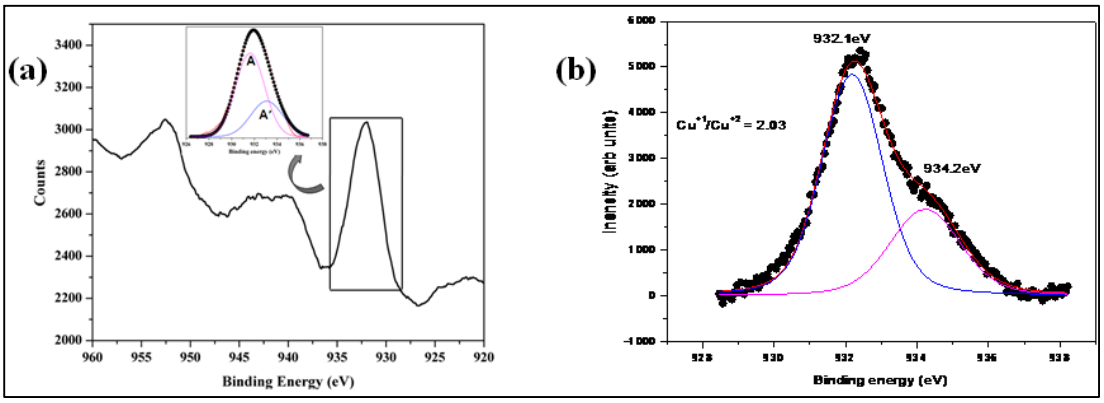

Figure11. XPS spectra for mixed-valent compounds **5** and **6.**

2.3.8.2 Magnetic Property of 5 and 6

The variable temperature susceptibility (2.5 – 300 K) of compound **5** was measured by a VSM magnetometer under the applied magnetic field of 1000 Oe. The temperature dependences of the χ_M versus T and $\chi_M T$ versus T is shown in Figure 12 and the observed $\chi_M T$ value for **5** at 300 K is 0.44 emu $mol^{-1}K$ (χ_M = 0.0018 cm^3mol^{-1}) and the values are close to the expected value for a magnetically 'isolated' Cu^{II} (with g = 2.1). Upon cooling, the $\chi_M T$ decreases continuously from 300 K and the value at 2.5 K is 0.27 emu

$mol^{-1}K$. There is no maxima in the χ_M versus T (Figure 12) and shape of the $\chi_M T$ versus T curve is characteristic of the occurrence of weak antiferromagnetic interaction. The χ_M^{-1} versus T is nearly a straight line above 25 K, which obeys the Curie-Weiss law. The Curie and Weiss constants, C and θ, are 0.39 emu mol^{-1} K and -4.83 K, respectively and Weiss constant suggests very weak antiferromagnetic interaction between the Cu^{II} centres, which is reasonable with a distance of 7.78 Å. From this magnetic data it also exclusively suggest the mixed valence state of Cu in the compound **5**. Compound **6** also exhibit similar magnetic behavior as of compound **5** and room temperature $\chi_M T$ value is 0.52 emu mol^{-1} K close to the value of one unpaired electron per formula unit (0.37 emu $mol^{-1}K$) the slightly higher value is attributed to the oxidation of small fraction of Cu^{I} state to Cu^{II}.

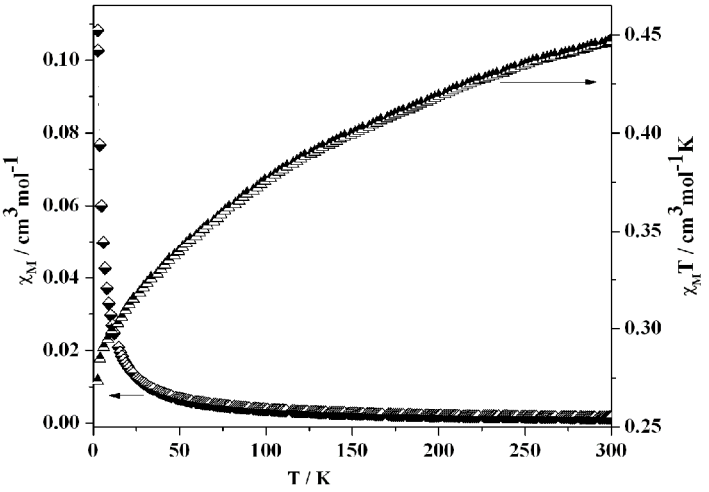

Figure 12. Plot of χ_M versus T and $\chi_M T$ versus T for **5.**

2.3.8.3 Bond valence calculation

Bond valence calculation suggests that Cu1 of compound **5** is in +2 oxidation state whereas two Cu2 per formula unit are in +1 oxidation state (Figure 7). In compound **6** Cu1 is in +1 and Cu2 is in +2 oxidation state (Figure 8).

The valence sum rule suggests that the valence of an atom is equal to the sum of the valences of all the bond it forms.[19] Where valence of a bond between atom i and atom j is given by

$S_{ij} = \exp((R_0 - R_{ij})/ B)$

$S = \Sigma S_{ij}$

R_{ij} = Experimental determined bond length between atom i and j

R_0 is constant for a specific bond and B is also constant and typical value of B is 0.37

Table 10: Result of Bond valence calculation for **5**

Cu^{I} (a)	Bond	Dist	R_0	B	BVal	Sum	Diff
1	Cu1 - O1	1.9410	1.6790	0.37	0.493	0.493	1.507
2	Cu(1) -O(1)c	1.9410	1.6790	0.37	0.493	0.985	1.015
3	Cu(1) -N(1)	1.9670	1.7510	0.37	0.558	1.543	0.457
4	Cu(1) -N(1)c	1.9670	1.7510	0.37	0.558	2.101	0.101
5	Cu(1) -O(4)a	2.7340	1.6790	0.37	0.058	2.159	0.159
6	Cu(1) -O(4)d	2.7340	1.6790	0.37	0.058	2.217	0.217
Cu^{II} 1	Cu(2) -N(4)	1.9770	1.5200	0.37	0.291	0.291	0.709
2	Cu(2) - N(2)	2.0480	1.5200	0.37	0.240	0.531	0.469
3	Cu(2) -N(3)	2.0510	1.5200	0.37	0.238	0.769	0.231
4	Cu(2) - O(3)	2.1230	1.6100	0.37	0.250	1.019	0.019

Table 11: Result of Bond valence calculation for **6**

Cu1 (I)	Bond	Dist	R_0	B	BVal	Sum	Diff
1	Cu(1) - N(2)c	1.8910	1.5200	0.37	0.367	0.367	0.633
2	Cu(1) - N(1)	1.9040	1.5200	0.37	0.354	0.721	0.279
3	Cu(1) -O(2)	2.5030	1.6100	0.37	0.090	0.811	0.189

Cu2 (II)	Bond	Dist	R_0	B	BVal	Sum	Diff .
1	Cu(2) - O(1)	1.9530	1.6790	0.37	0.477	0.477	1.523
2	Cu(2) - O(1)	1.9530	1.6790	0.37	0.477	0.954	1.046
3	Cu(2) -N(3)	1.9600	1.7510	0.37	0.568	1.522	0.478
4	Cu(2)- N(3)	1.9600	1.7510	0.37	0.568	2.091	0.091

2.3.9 Thermal stability of $\{[Cu(bpe)Cl]\cdot 2H_2O\}_n$ (3) and $\{[Cu_2(pyzdc)]\cdot H_2O\}_n$ (4)

Thermogravimetric analysis (Figure.13a) of **3** shows a weight loss (5.5 %) in the tempearture range of 45 – 85 °C, corresponding to the loss of one water molecule per formula unit (calc. 6 wt%). The dehydrated framework $\{[Cu(bpe)Cl]\}_n$ **(3′)** is stable upto 175 °C and then decomposes to unidentified product. Discrepancy in the TGA results arises due to the volatility of crystalline water molecules. The water molecules are present in the pores without any H-bonding interactions. Thermogravimetric analysis (TGA) of the framework **4** suggests the release of the water molecule in the temperature range of 100-130˚C and dehydrated framework is stable up to 225˚C

(Figure.13b). Such high temperature release of the water molecule also correlates the presence of interaction of water molecules with Cu3. PXRD pattern of the dehydrated framework **3′** shows a new peak at around 2θ = 6.2 and also changes in Bragg's intensity suggesting the structural transformation after removal of the water molecules (Figure. 14a). This may due to the sliding of the 2D sheets. The PXRD pattern of the dehydrated framework $\{[Cu_2(pyzdc)]\}_n$ (**4′**) shows no changes in terms of peak positions and Bragg's intensities compared to as-synthesized **4** suggesting the framework is highly rigid (Figure. 14b).

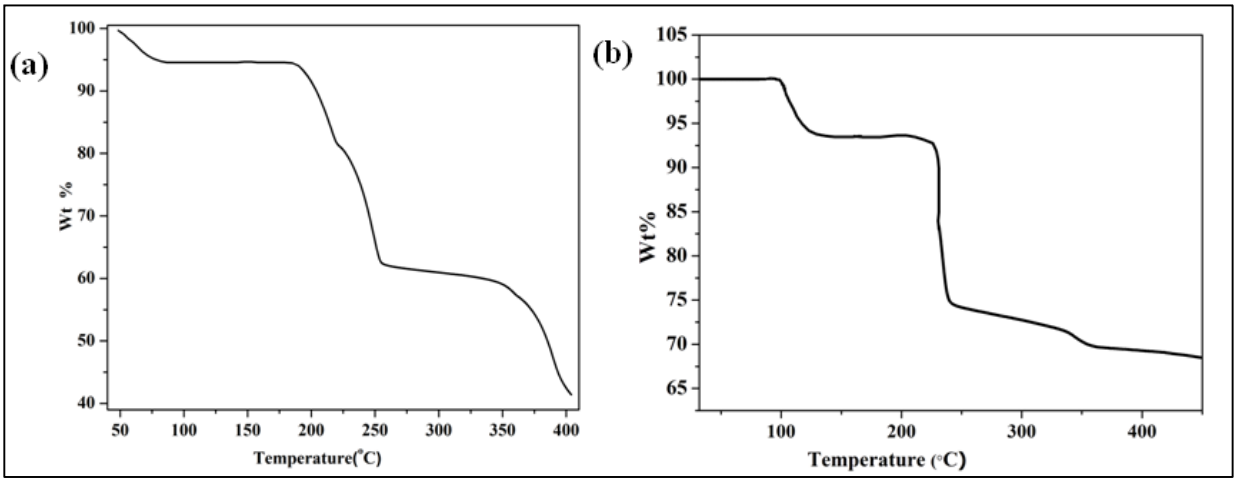

Figure 13. TGA profile of the compound **3** and **4**

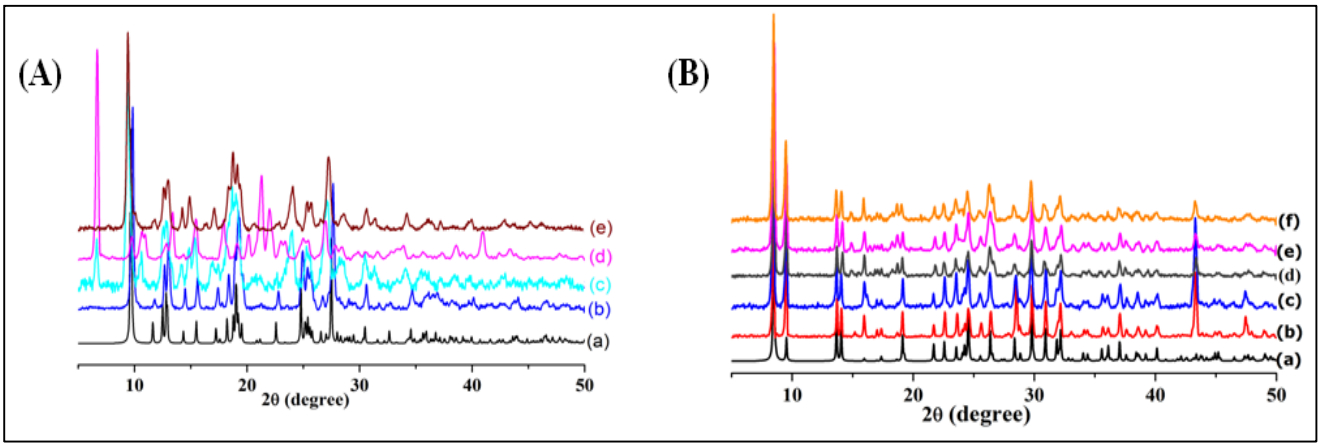

Figure 14. PXRD pattern for (a)$\{[Cu(bpee)(Cl)]\cdot 2H_2O\}_n$ (**3**) and (b) $\{[Cu_2(pyzdc)]\cdot 0.83H_2O\}_n$ (**4**) in different state: (a) simulated; (b) as-synthesized; (c) dehydrated (d) exposed to the water vapor; and (e) exposed to the MeOH vapor; (f) exposed to the MeCN vapor

2.3.10 Single-crystal-to-single-crystal structural transformation in $\{[Cu_2(pyzdc)]\cdot 0.83H_2O\}_n$ (4)

High thermal stabilitity and unchanged PXRD pattern after removal of the semicoordinated water molecule inspired us to detrmine the structure after dehydration. The structure determination from *in situ* X-ray diffraction study of a single-crystal after heating at 180˚C reveals that no water molecule is present inside the pore and 3D framework structure remain intact (Table 1,5 and 6, Figure 15). Moreover, when the same crystal was exposed to water vapour for 24 h a framework regenerated with water molecule inside the pore (Figure 15 and table7). The single-crystal data of the as-synthesized, dehydrated and rehydrated crystal shows similar cell parameter also suggesting the framework is highly rigid and robust (Table 1). We categorized this compound as second generation porous coordination polymer as classified by kitagawa *etal.*[8d] The single-crystal-to-single-crystal structural transformation upon dehydration and rehydration in porous Cu^{I} coordination polymer is rarely explored due to inherent instability of the cuprous state.

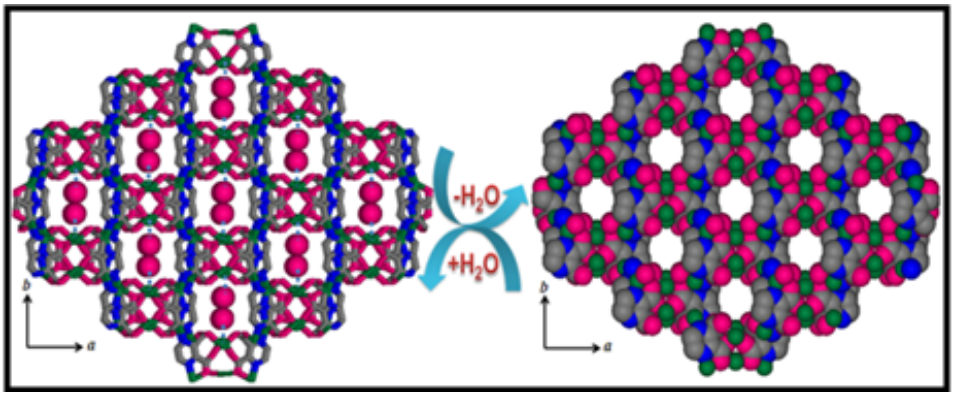

Figure 15. View of the 3D coordination framework of **4** and **4′**. Left side: 1D water filled channels along the crystallographic *c*-axis; Right side: CPK diagram of the dehydrated compound, $\{Cu_2(pyzdc)\}_n$ (**4′**) showing 1D channels with unsaturated Cu^{I} sites.

2.3.11 Thermal stability of $\{[Cu^{II}Cu^{I}_2(2,4\text{-pyrdc})_2(pyz)_3]\cdot 2H_2O\}_n$ (5) and $\{[Cu^{II}Cu^{I}_2(2,4\text{-pyrdc})_2(bpy)_2].4H_2O\}_n$ (6)

Compound **5** shows weight loss of 4.6% (calc. 4.5 %) in the temperature range of 30−75 °C, corresponding to the removal of two guest water molecules and the dehydrated framework $\{[Cu^{II}Cu^{I}_2(2,4\text{-pyrdc})_2(pyz)_3]\}_n$ (**5′**) is stable upto 150 °C

without further weight loss (Figure 16a). Above 150˚ C the framework decomposes to unidentified product. Thermogravimetric analysis (TGA) of the bulk powder sample of **6** suggests a gradual 4 % weight loss from room temperature to 100˚C . The molecular formula obtained from X-ray diffraction study of a single-crystal, suggests four water molecules per formula unit which corresponds about 7.95% weight loss (Figure 16b). The discrepancy in the TGA profile has been explained by considering water molecule present in the pore are loosely bound and when sample were filtered and dried under vacuum about 50% water molecule evaporated. PXRD pattern of the dried powder sample has significant difference from the simulated pattern supports the same. Because the framework is 2D bilayer and 3D structure has been formed via supramolecular non-covalent interactions like π…π stacking and hydrogen bonding interaction based on water molecules in the pore. The structure undergoes severe change after drying and heating at 100˚C. PXRD patterns of the sample at its partially dehydrated and completely dehydrated state are shown in the Figure17b which suggests the change of the as-synthesized and dehydrated sample from the simulated pattern after removal of the water molecules (Figure17b). It is worth mentioning here purity of the sample was confirmed from elemental analysis. Mixed valence state of **5** and **6** has been confirmed from magnetic and XPS measurements. The PXRD pattern of the as-synthesized **5** and the dehydrated **5′** are similar, indicating that the porous network is retained after the removal of the guest water molecules (Figure17a).

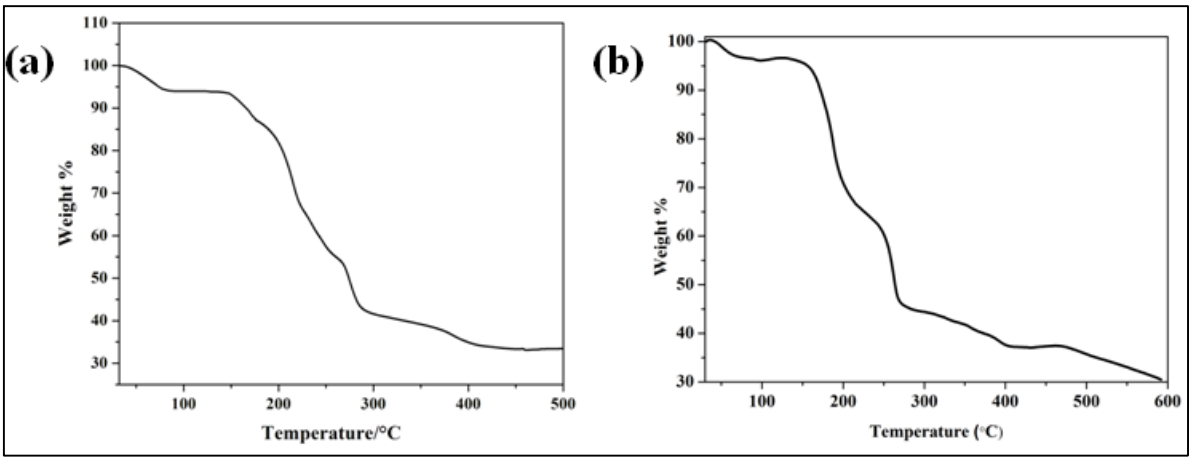

Figure 16. TGA profile (a) $\{[Cu^{II}Cu^{I}_2(2,4\text{-pyrdc})_2(pyz)_3]\cdot 2H_2O\}_n$ (**5**) (b) $\{[Cu^{II}Cu^{I}_2(2,4\text{-pyrdc})_2(bpy)_2].4H_2O\}_n$ (**6**).

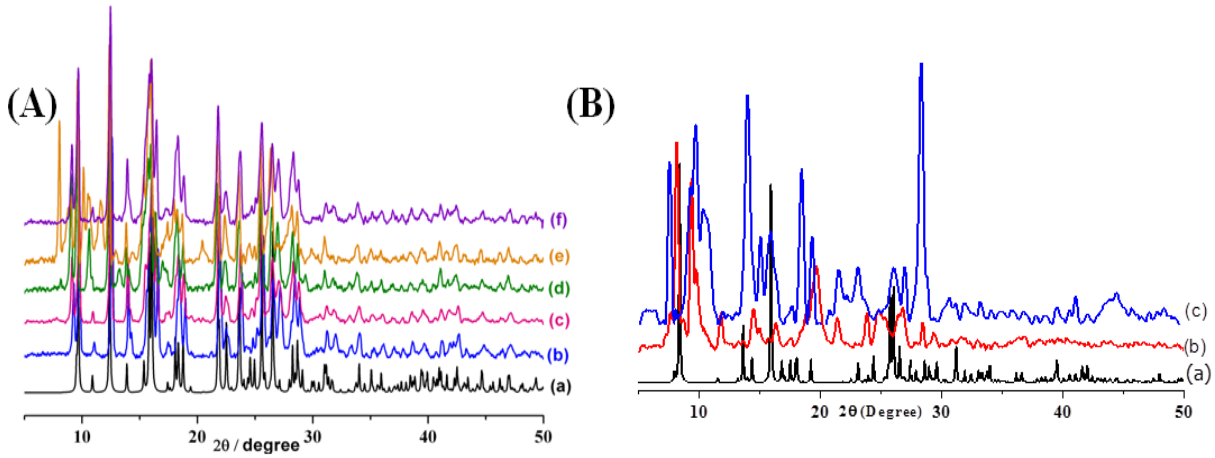

Figure 17. PXRD pattern for (a)$\{[Cu^{II}Cu^{I}_2(2,4\text{-pyrdc})_2(pyz)_3]\cdot 2H_2O\}_n$ **(5)** and (b) $\{[Cu^{II}Cu^{I}_2(2,4\text{-pyrdc})_2(bpy)_2].4H_2O\}_n$ (**6**) in different state: (a) simulated; (b) as-synthesized; (c) dehydrated (d) exposed to the water vapor; and (e) exposed to the MeOH vapor;(f) exposed to the MeCN vapor

2.3.12 Adsorption properties of $\{[Cu(bpe)(Cl)]\}_n$ (3') and $\{[Cu_2(pyzdc)]\}_n$ (4')

The framework **3′** exhibits type-II sorption profile with N_2 (kinetic diameter = 3.6 Å) at 77 K, suggesting the absence of micropore in the framework. We have also measured the sorption properties with H_2O (2.65 Å) and MeOH (4.0 Å) vapor at 298 K, and 293K respectively (Figure 18A). Framework **3** shows stepwise sorption of H_2O with large hysteresis suggesting structural transformation in the framework during the adsorption of H_2O. The maximum uptake of water at P/P_0 = 1.0 is 62 mL g^{-1} without saturation which correspond about 0.8 molecules per formula unit of **3′**(Figure 18A). Very low uptake of water at low pressure regions suggesting weak affinity toward water molecules, reflected in smaller βE_0 value (5.47 kJ/mol). MeOH sorption study reveal type-II profile, suggesting non-inclusion of MeOH molecules into the pore (Figure 18A (b)). Due to the sliding of the 2D sheets the pore was blocked for entering the MeOH molecules, however step wise sorption of smaller size and highly polar H_2O molecles results opening of the pore for entering the water molecules.

To examine the permanent porosity, **4′** was subjected to sorption studies with N_2 (kinetic diameter 3.6 Å) at 77 K and CO_2 (kinetic diameter 3.3 Å) at 195 K. Both the isotherm shows type-II profile according to the IUPAC classification. The adsorption amount at P/P_0 ~1 is 8 mL g^{-1} (for N_2) and 12 mL g^{-1} (for CO_2) suggesting occlusion of N_2 and CO_2 molecules into the pores and related to the surface adsorption. This can

be correlated to the smaller pore aperture of **4′** compared to the kinetic diameter of N_2 and CO_2. Inspired by the small pores with highly reactive unsaturated Cu^{I} sites, we anticipated that **4′** could selectively adsorb solvents molecules on the basis of size and polarity. H_2O (kinetic diameter 2.65 Å), MeOH (4.0 Å), MeCN (4.3 Å) and EtOH (4.5 Å) vapour sorption isotherms were measured at ambient condition. As shown in Figure 18b the sorption profile of H_2O shows typical type-I curve with steep uptake at low pressure regions indicating the strong interaction of H_2O molecules with the pore surface. The amount of final uptake is about 127 mL g^{-1} at P/P_0 ~1 which corresponds to 1.66 molecule of H_2O per formula unit of **4′.** The higher uptake of H_2O during adsorption may be rationalized to the strong adsorbate-adsorbate interaction after filling the specific unsaturated Cu^{I} adsorption site by one H_2O molecule. The strong interaction with unsaturated Cu^{I} site of H_2O is further supported by the hysteretic incomplete desorption profile of H_2O. It is worth mentioning that MeOH sorption profile also revealed type-I profile (0.5 molecule per formula unit), however MeCN and EtOH are not adsorbed by **4′** (Figure 18B (b, c, d).

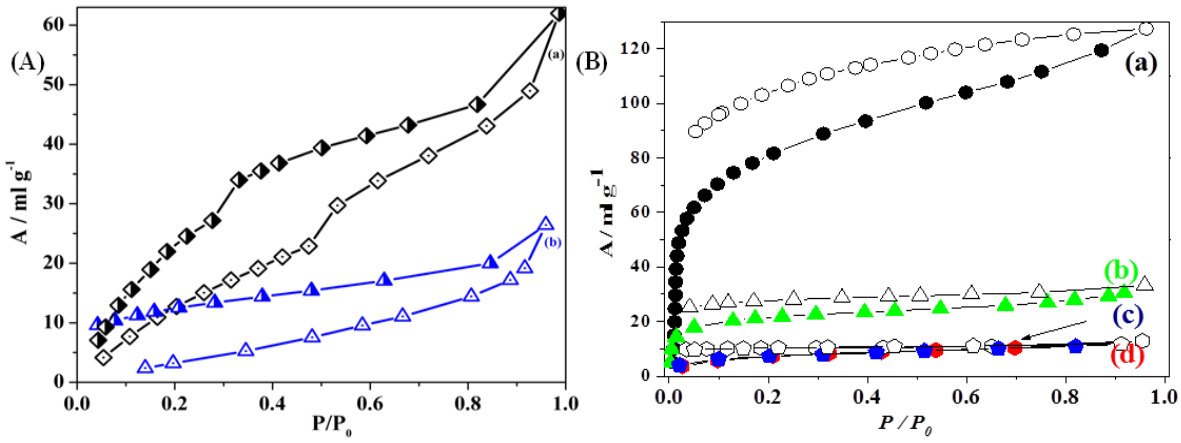

Figure. 18. (A) Vapor sorption Isotherms for **3′**(a) H_2O (298 K), (b) MeOH (293 K) vapor sorption of framework **3′**. (B) vapor sorption Isotherms for **4′** (a) H_2O (298 K), **(**b) MeOH (293 K) (c) EtOH (298 K) (d) MeCN (298K).

2.3.13 Solvent and gas sorption properties of $\{[Cu^{II}Cu^{I}_2(2,4\text{-}pyrdc)_2(pyz)_3]\cdot 2H_2O\}_n$ (5) $\{[Cu^{II}Cu^{I}_2(2,4\text{-}pyrdc)_2(bpy)_2]\cdot 4H_2O\}_n$ (6)

To examine the permanent porosity, the dehyrated framework of **5** (**5′**) was subjected to sorption studies with N_2 (kinetic diameter 3.6 Å) at 77 K and shows a type-II

profile for defined by the IUPAC (Figure 19a). The adsorption amount at P/P_0 =1 is 42 mL g^{-1} which corresponds to 1.4 N_2 molecule per formula unit of **5′**, suggesting the occlusion of N_2 molecules into the pores rather surface adsorption. Recently, Chen *et al*.,[18a] reported similar type of N_2 sorption (195 K) profile in a flexible Cu^{I} framework, MAF 2 with smaller pore aperture. They have also determined adsorbed N_2 molecules in the pores by X-ray crystallography. The pore size of **5′** is small compare to the kinetic diameter of N_2 and similar type-II profile is also documented in the porous frameworks containing small channels.[19c] Inspired by the small pores and chemical environement, we anticipated that **5′** could selectively adsorb solvents molecules on the basis of size and polarity. H_2O, MeOH and EtOH vapor sorption isotherms were measured (Figure 19B). As shown in, the sorption profiles of H_2O (kinetic diamater 2.8 Å),[19d] MeOH (4.0 Å) reveal uptake in the low P/P_0 regions and amount of adsorption increases gradually along with the increasing pressure (Figure 19A, B). However, EtOH (4.8 Å) molecules do not adsorb at low pressure region and at certain onset pressure (P/P_0 ~ 0.5), called gate-opeing pressure, sorption started and ended without saturation (Figure 19c). The desorption curve in all cases do not coincide with the adsorption curve and large hysteretic sorption in all cases suggest strong host-guest interaction realized by the H-bonding interaction between the solvent molecules and the pendent oxygen atoms (O2), decorated on the pore surfaces (Figure 7c). Calculations using the final sorption amount suggest 3.9, 1.6 and 1.0 molecule of H_2O, MeOH and EtOH, respectively were adsorbed per formula unit of **5′**. Steep uptake of H_2O at low pressure region compare to MeOH and EtOH suggests strong affinity of the H_2O molecules to the pore surfaces of **5′**. All the profiles were analyzed by the DR equation,[22] and the values of βE_0 are 7.35, 3.20 and 1.53 kJ/mol for H_2O, MeOH, and EtOH, respectively, also indicating the strong hydrophilic character of the pore surfaces. PXRD patterns of **5′** with expose to the different solvent vapors exhibit some changes in peak position and intensity and also appearance some new peaks at low angles correlating some structural rearrangement upon inclusion of the solvent molecules (Figure 17A, 19B). Different vapor exposed compounds of **5′** show low angle peak suggesting structural expansion for the accommodation of high amount of H_2O compare to the assyntheized framework and also explains the accommodation of oversize guests like water MeOH and EtOH molecules. To the best of our knowledge

this is the first mixed-valent Cu^{I}/Cu^{II} porous framework showing structural flexibility with interesting vapor sorption properties.

We measured gas sorption isotherm of the dehydrated compound of **6** (**6′**), which exhibit clear signature of selective adsorption of CO_2 (kinetic diameter = 3.3 Å) over other non polar gases like N_2, Ar and H_2 at 195K (figure 20). The N_2 sorption isotherm at 77K suggests a typical type-II profile indicating non inclusion of N_2 gas into pore and support the selectivity of CO_2 over other gases (Figure 20).

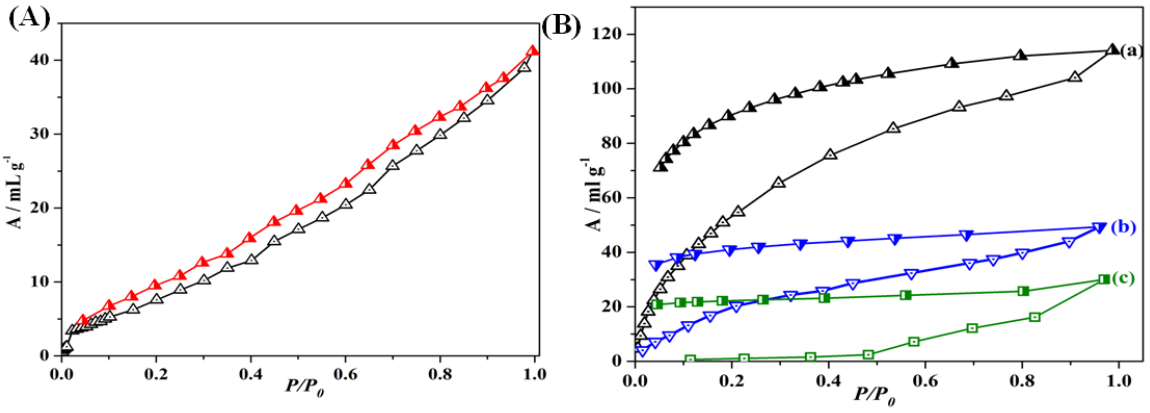

Figure 19. (A) N_2 sorption profile at 77K (B) Isotherms for (a) H_2O (298 K), (b) MeOH (293 K) (c) EtOH (298 K) vapor sorption of framework **5′**. P_0 is the saturated vapor pressure of the respective adsorbate at the corresponding temperature.

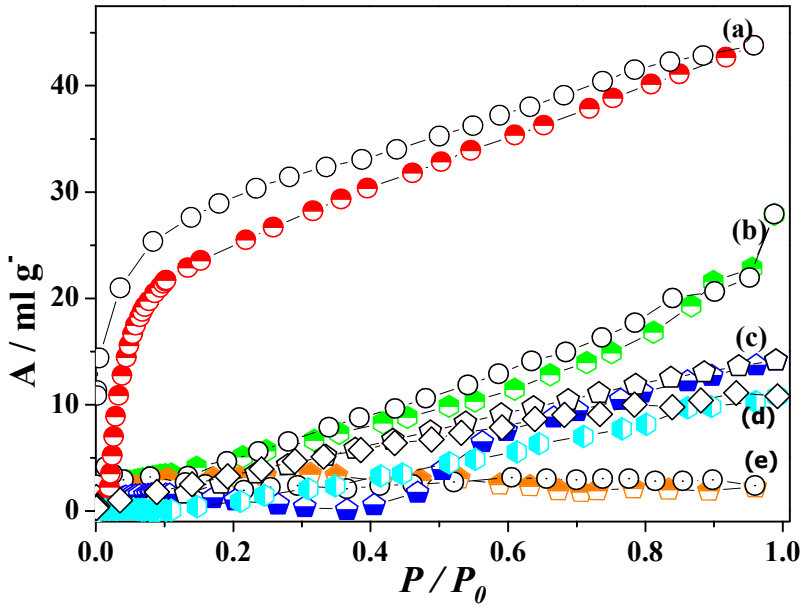

Figure 20: (a) CO_2 (at 195 K) and (b)N_2 (at 77 K) (c) N_2 at 195K (d) Ar at 195K (e) H_2 at 195K desorption (black) isotherms for dehydrated sample.

CO_2 adsorption profile shows a typical type-I profile with uptake amount of 44 mL g^{-1} is considerably higher compared to other gases at 195K. N_2 (kinetic diameter = 3.64 Å) sorption profile shows typical type-II isotherm with negligibly small amount of uptake of N_2. The surface area of the compound was determined from the CO_2 sorption profile at 195K and shows BET surface area of 117 m^2 g^{-1}. The selective CO_2 adsorption over other gases is attributed to the presence of highly polar pore surface and smaller pore aperture. Pore surface of **6′** contains pendant carboxylate oxygen which interact strongly with CO_2 (βE_0=6.24 kJ mol^{-1}) because of larger quadruple moment (-1.4 $\times 10^{-39}$ C m^2) compared to other gases providing extra potential energy for adsorption.

2.4 Summary

Exploiting the redox activity of DHFA we have developed a facile way of synthesizing Cu^{I} MOFs. The structure and dimensionality of the MOFs depends on the anion of the copper salt as well as the linker used. Apart from the four Cu^{I} compounds described in this chapter other reported Cu^{I} coordination polymer with SO_4^{2-} and Cl^{-} anion with pyz were also isolated adopting our method. The compound **4** is unique for its extraordinary stability, unusual coordination geometry and strong hydrophilic character. High thermal stability and framework rigidity has been understood from single-crystal-to-single-crystal-structural transformation upon dehydration and rehydration. Analogous Cu^{I} MOFs with larger pore dimension can be synthesized with potential application as storage materials for hydrocarbons (ethylene or acetylene) gases because of the presence of unsaturated Cu^{I} sites on the pore surface. Two novel mixed-valent porous frameworks (Cu^{I}/Cu^{II}) of different dimensionality have also been isolated by controlling reaction stoichiometry and using different organic linkers. This method presents a very simple and convenient way to construct Cu^{I} and mixed-valent porous Cu^{I}/Cu^{II} frameworks in aqueous solution and aerobic condition.

2.5 References

1. (a) H. J. H. Fenton, *J. Chem. Soc., Trans.*, 1894, **65**, 899 (b) H. J. H. Fenton, *J. Chem. Soc., Trans.*, 1896, **69**, 546 (c) B. F. Abrahams, T. A. Hudson and R. Robson, *J. Am. Chem. Soc.*, 2004, **126**, 8624.

2. (a) E. F. Hartree, *J. Am. Chem. Soc.*, 1953, **75**, 6244; (b) S. Goodwin and B. Witkop, *J. Am. Chem. Soc.*, 1954, **76**, 5599; (c) V. Naidu Sagi, P. Karri, F. Hu and R. Krishnamurthy, *Angew. Chem. Int. Ed.*, 2011, **50**, 8127; (c) D. S. Kemp and B. R. Bowen, *Tetrahedron Lett,* 1988, **29**, 5077.

3 (a) E. A. Lewis and W. B. Tolman, *Chem. Rev.,* 2004, **104**, 1057; (b) L. M. Mirica, X. Ottenwaelder and T. D. P. Stack, *Chem. Rev*., 2004, **104**, 1013; (c) N. W. Aboelella, A. M. Reynolds and W. M. Tolman, *Science*, 2004, **304**, 836.

4 (a) Y. I. Kim, S. Salim, M. J. Huq and T. E. Mallouk, *J. Am. Chem. Soc.,* 1991, **113**, 9561; (b) B. Zhao, H. Du and Y. Shi*, J. Am. Chem. Soc.*, 2008, **130**, 7220.

5 (a) C. W. Rogers and M. O. Wolf, *Coord. Chem. Rev*., 2002, **233**, 341; (b) B. O'Regan and M. Graetzel, *Nature*, 1991, **353**, 6346.

6 (a) D. V. Scaltrito, D. W. Thompson, J. A. O'Callaghan and G. J. Meyer, *Coord. Chem. Rev*., 2000, **208**, 243; (b) B. –C. Tzeng, T. –H. Chiu, B. –S. Chen and G. –H. Lee, *Chem. Eur. J.*, 2008, **14**, 5237; (c) M. T. Miller, P. K. Gantzel and T. B. Karpishin, *Inorg. Chem*., 1999, **38**, 3414; (d) S. Chowdhury, G. K. Patra, M. G. B. Drew, N. Chattopadhyay and D. Dutta, *J. Chem. Soc., Dalton Trans*., 2000, 235; (e) X. –C. Huang, J. –P. Zhang, Y. –Y. Lina and X. –M. Chen, *Chem. Commun*., 2005, 2232; (f) J. –P. Zhang, Y.-Y. Lin, X. –C. Huang and X. –M. Chen, *Cryst. Growth Des.*, 2006, **6**, 519

7 (a) D. D. LeCloux, R. Davydov and S. J. Lippard, *J. Am. Chem. Soc*., 1998, **120**, 6810; (b) S. Ferguson-Miller and G. T. Babcock, *Chem. Rev*., 1996, **96**, 2889; (c) S. Iwata, C. Ostermeier, B. Ludwig and H. Michel, *Nature*, 1995, **376**, 660; (d) K. D. Karlin, Q.-F Gan, Z. Tyeklár, *Chem. Commun.*, 1999, 2295; (e) J. Kuzelka, S. Mukhopadhyay, B. Spingler and S. J. Lippard, *Inorg. Chem.,* 2004, **43**, 1751; (f) J. A. Halfen, S. Mahapatra, M. M. Olmstead and W. B. Tolman, *J. Am. Chem. Soc.*, 1994, **116**, 2173.

8. (a) R. Gupta, Z. H. Zhang, D. Powell, M. P. Hendrich, and A. S. Borovik, *Inorg. Chem.,* 2002, **41**, 5100; (b) G. Dong, Q. Chun-qi, D. Chun-ying, P. Ke-liang and M. Qing-jin, *Inorg. Chem.,* 2003, **42,** 2024; (c) S. Jun-ichiro; Y. Tatsuo; M. Setsuo; H. Hong-

wei and S. Takeshi. *Angew. Chem., Int. Ed.,* 2000, **39**, 1115; (d) S. Kitagawa, R. Kitaura and S. Noro, *Angew. Chem. Int. Ed.*, 2004, **43**, 2334.

9. (a) T. K. Maji, D. Ghoshal, E. Zangrando, J. Ribas and N. R. Chaudhuri, *CrystEngComm,* 2004, **6**, 623; (b) S. M-F. Lo, S. S-Y.Chui, L. -Y. Shek, X. X. Zhang, Z. Xi. Zhenyang Lin, G. -H. Wen and I. D. Williams, *J. Am. Chem. Soc*., 2000, **26**, 6293; (c) X. –M. Zhang, X. –M. Chen, *Eur. J. Inorg. Chem*., 2003, **6**, 413; (d) M. M. Vincent, S. Franzen, A. P. Shreve, M. R. Ondrias, S. E. Wallace-Williams, M. E. Barr and W. H. Woodruff, *Inorg. Chem.,* 1999, **38,** 2546; (e) Y. L. Lu and K. A. Runnels, *Inorg. Chem. Commun*., 2001, **4**, 678; (f) L. –M. Zheng, X. Wang and A. J. Jacobson, *J. Solid State Chem*., 2000, **152**, 174; (g) X. –M. Zhang, Y. –F. Zhao, H –S. Wu, S. R. Batten and S. W. Ng, *Dalton Trans.*, 2006, 3170; (h) J. He, J.-X. Zhang, C. –K. Tsang, Z. Xu, Y. –G. Yin, D. Li and S.-W. Ng, *Inorg. Chem.* 2008, **47,** 7948; (i) M. -L. Tong, L. –J. Li, K. Mochizuki, H. –C. Chang, X. –M. Chen, Y. Li and S. Kitagawa, *Chem. Commun*., 2003, 428; (j) H. Zhao, Z. –R. Qu, Q. Ye, X.-S. Wang, J. Zhang, R. –G. Xiong and X. –Z. You, *Inorg. Chem.,* 2004, **43**, 1813; (k) J. Tao, Y. Zhang, M. -L. Tong, X. -M. Chen, T. Yuen, C. L. Lin, X. Huang and J. Li, *Chem. Commun*., 2002, 1342; (l) T. Okubo, R. Kawajiri, T. Mitani and T. Shimoda, *J. Am. Chem. Soc*., 2005, **127**, 17598; (m) Y. Cai, Y. Wang, Y. Li, X. Wang, X. Xin, C. Liu and H. Zheng, *Inorg. Chem*., 2005, **44**, 9128; (n) J.-P. Zhang, Y.-Y. Lin, X.-C. Huang and X.-M. Chen, *J. Am. Chem. Soc.*, 2005, **127,** 5495.

10. (a) C. J. O'Connor, C. L. Klein, R. J. Majeste and L. M. Trefonas, *Inorg. Chem*., 1982, **21**, 64; (b) J. Pickardt and B. Staub, *Z. Naturforsch., B: Chem. Sci,* 1997, **52**, 1456; (c) M. Henary, J. L. Wootton, S. I. Khan and J. I. Zink, *Inorg. Chem*., 1997, **36**, 796; (d) T. Liu, Y. –H. Chen, Y. –J. Zhang, Z. –M. Wang and S. Gao, *Inorg. Chem*., 2006, **45**, 9148; (e) T. Fetzer, A. Lentz and T. Debaerdemaeker, *Z. Naturforsch*., 1989, **B44**, 553.

11. (a) A. B. P. Lever, J. Lewis and R. S. Nyholm, *Nature*, 1961, **189**, 58; (b) M. M. Turnbill, G. Pon and R. D. Willett, *Polyhedron,* 1991, **10**, 1835; (c) T. Otieno, S. J. Rettig, R. C. Thompson and J. Trotter, *Inorg. Chem*., 1993, **32**, 1607; (d) J. M. Moreno, J. Suarez-Varela, E. Colacio, J. C. Avila-Rosón, M. A. Hidalgo and D. Martin-Ramos, *Can. J. Chem*., 1995, **73**, 1591; (e) T. Otieno, S. J. Rettig, R. C. Thompson and J. Trotter, *Can. J. Chem*., 1990, **68**, 1901; (f) P. Amo-Ochoa, G. Givaja, P. J. S. Miguel, O. Castillo and F. Zamora, *Inorg. Chem. Commun.*, 2007, **10**,

921.

12. (a) S. Hu, A.-J. Zhou, Y. –H. Zhang, S. Ding and M.-L. Tong, *Cryst. Growth Des.*, 2006, **6**, 2543; (b) M. Henary, J. L. Wootton, S. I. Khan and J. I. Zink, *Inorg. Chem.*, 1997, **36,** 796; (c) J. Lu, G. Crisci, T. Niu and A. J. Jacobson, *Inorg. Chem.,* 1997, **36**, 5140; (d) J. Y. Lu, B. R. Cabrera, R.-J. Wang and J. Li, *Inorg. Chem.*, 1999, **38**, 4608; (e) L. R. Hanton and K. Lee, *Dalton Trans.*, 2000, 1161; (f) H. Araki, K. Tsuge, Y. Sasaki, S. Ishizaka and N. Kitamura, *Inorg. Chem.*, 2005, **44**, 9667; (g) F. Thébault, S. A. Barnett, A. J. Blake, C. Wilson, N. R. Champness and M. Schröder, *Inorg. Chem.*, 2006, **45**, 6179; (h) P. M. Graham, R. D. Pike, M. Sabat, R. D. Bailey and W. T. Pennington, *Inorg. Chem.*, 2000, **39**, 5121; (i) H. K. Fun, S. S. S. Raj, R. –G. Xiong, J. –L. Zuo, Z. Yu, X.-L. Zhu and X. -Z. You, *Dalton Trans.*, 1999, 1711.

13. *SAINT*, 6.02 ed., Bruker AXS, Madison, WI, 1999**;**

14. G. M. Sheldrick, *SADABS, Empirical Absorption Correction Program*, University of Göttingen, Göttingen, Germany, 1997

15. G. M. Sheldrick, SHELXS 97, *Program for the Solution of Crystal Structure*, University of Gottingen, Germany, 1997.

16. G. M. Sheldrick, SHELXL 97*, Program for the Refinement of Crystal Structure*, University of Gottingen, Germany, 1997.

17. A. L. Spek, PLATON, *Molecular Geometry Program*, University of Utrecht, The Netherlands, 1999.

18. L. J. Farrugia*, WinGX - A Windows Program for Crystal Structure Analysis*. *J. Appl. Crystallogr*., 1999, **32**, 837.

19. (a) N. E. Brese and M. O. Keeffe, *Acta Cryst.* 1991, **B47**, 192; (b) I. D. Brown, (2002). *The Chemical Bond in Inorganic Chemistry: The Bond Valence Model*. Oxford University Press.

20. (a) Z. P. Zhang and X. –M. Chen, *J. Am. Chem. Soc*., 2008, **130**, 6010; (b) J. –P. Zhang and S. Kitagawa, *J. Am. Chem. Soc.* 2008, **130**, 907.

21. (a) K. Allan, A. Campion, J. Zhou and J. B. Goodenough, Phys. Rev. B., 1990, 41, 11572; (b) B. Balamurugan, B. R. Mehta and S. M. Shivprasad, *Appl. Phys. Lett.*, 2001, **79**, 3176 (c) R. –Q. Zou, L. Jiang, H. Senoh, N. Takeichi and Q. Xu, *Chem. Commun*., 2005, 3526; (d) D. W. Beck*, Zeolite Molecular Sieves:* Wiley & Sons: New York, 1974.

22. M.M. Dubinin and L.V. Radushkevich, *Dokl. Akad. Nauk. SSSR*.,1947, **55**, 331.

A Novel Method for the Synthesis of Silver and Gold Nanostructures: Studies of SERS, Magnetic and Catalytic Activities

Abstract: This chapter deals with synthesis of silver and gold nanostructures in a novel facile and eco-friendly way by simple chemical reduction of $AgNO_3$ and $HAuCl_4$. Silver nanorods with increased surface enhanced Raman scattering sensitivity and detection have been synthesized using 2,3-dihydroxyfumaric acid (DHFA) in aqueous medium under aerobic condition. The structure and composition of the silver nanorods were characterized by UV-vis spectroscopy, powder X-ray diffraction, transmission electron microscopy (TEM) and field emission scanning electron microscopic (FESEM) studies. Simple hard washing agglomerates the anisotropic silver nanorods and the agglomerated nanorods consist of several 'Hot Spots', easily replaceable capping agents, which are responsible for its high sensitivity and trace detection (picomolar level) of different adsorbate molecules (thiophenol, rhodamine 6G) in surface enhanced Raman scattering study. Rarely observed but theoretically established unpaired s-electron based ferromagnetism is the other interesting aspect of silver and gold nanostructure. PVP stabilized gold nanoparticles obtained using DHFA exhibit excellent catalytic activity for controlled and complete aerial oxidation of hydroxybenzylalcohols to hydroxybenzaldehydes. Uncapped gold nanoparticles are ferromagnetic in nature at room temperature.

(1) A Paper related to this chapter has been published, S. Mohapatra, S. Siddhanta, D.R. Kumar, C. Narayana and T. K. Maji, ***Eur.J. Inorg. Chem.***, 2010, 4969.
(2) Another paper related to this chapter has been published, S. Mohapatra, R. K. Kumar and T. K. Maji, ***Chem.Phys.Lett.***, 2011, **508**, 76.

3.1 Introduction

We anticipated from the method developed for the synthesis of Cu^{I} and Cu^{I}/Cu^{II} MOFs in chapter 2 that the same reagent can be used for the reduction of other coinage metal ions to their zero oxidation state based on the reduction potentials. On the other hand 2,3-dihydroxyfumaric acid (DHFA) and its oxidised products contain hydroxo and carboxylate groups which may help to play the role of capping agent. This chapter deals with a facile and new route for synthesis of the coinage metal nanostructures and their various interesting properties. Metal particles in nanometer size range have attracted much attention due to their size, shape and composition dependent phenomena.[1-4] Coinage metal nanomaterials show size dependent tuning of their electrical,[5] optical,[6-8] magnetic,[9,10] and catalytic properties,[11] which are related to the confinement of delocalized electrons. The novel properties are different from the isolated atom or in bulk phase due to the 'quantum size effect'.[12] However the challenge in the nano scale synthesis is the creation of pure and perfect nanometer scale materials with definite size and shape,[13,14] which can identically be replicated in unlimited quantities. Conventionally silver and gold nanoparticles are synthesized by citrate or borohydride reduction.[15,16] But stronger reducing power of the reductant and high temperature requirement imply one constraint in their application for *in situ* generation in a temperature sensitive mild system. Apart from these two methods there are several other methods like sol-gel technique, thermal decomposition, laser ablation have been reported in the literature.[17] With enormous growth in the multidisciplinary nanoscience research now material scientist, biologist, and engineers are trying to develop easy, sustainable, and 'green' method for synthesis of nanomaterials having multiple functionalities. Such 'green chemistry'[18] environment viable approach would be beneficial for application into biologically relevant systems and hence more practicable. In the previous chapter we exploited the 2-electron oxidation of DHFA for the synthesis of a number of Cu^{I} and mixed valent porous $Cu^{I/II}$ coordination frameworks in aqueous solution under aerobic condition.[19] This facile and green approach has been extended for the synthesis of nobel metal nanostructures in aqueous solution in open atmosphere. In this contribution we report a novel, environmentally benign, and more advantageous method for the synthesis of silver nanorods (NRs) and gold nanoparticles in aqueous solution without any external capping agent. Here, DHFA serves binary roles of reducing agent [20, 21] as well as capping agent. Among various probable applications, we have unveiled properties such as

increased SERS sensitivity and trace detection up to picomolar level of thiophenol (TP) and Rhodamine 6G (R6G) molecules, and ferromagnetism of the newly synthesized silver NRs. On the other hand gold nanoparticle has various interesting properties. Among various properties catalytic activity of gold nanostructure is most important and it is not well explored.[22] We are introducing a new reducing agent, DHFA into the nanoworld of gold. In absence of capping agent carboxylate group of DHFA and diketosuccinic acid (DKSA) acts as capping agent via electrostatic interaction.[23] We present the catalytic activity of PVP stabilized gold nanoparticle for the controlled and complete aerial oxidation of hydroxybenzylalcohol to aldehyde, which is a challenging task in the synthetic organic chemistry. We also report interesting ferromagnetic property of uncapped gold nanoparticle which supports recent theoretical findings.

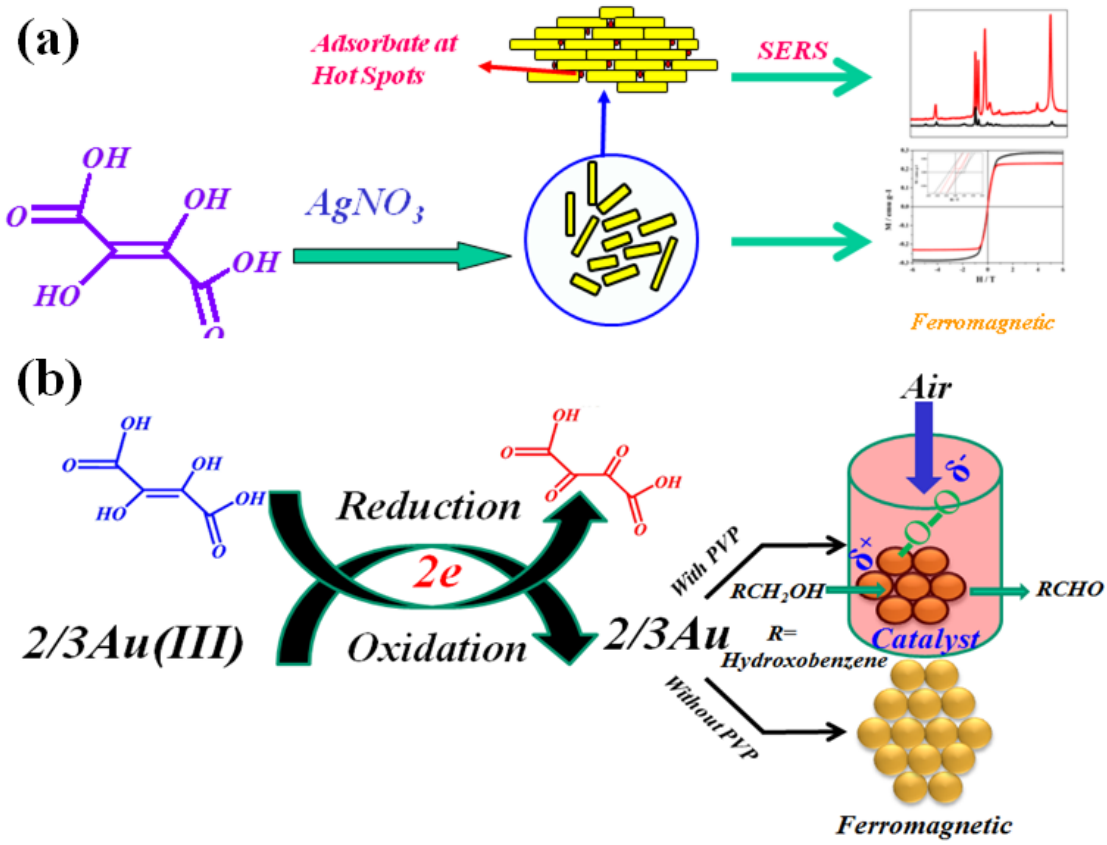

Scheme 1. Schematic representation of synthesis and properties of silver and gold nanostructures.

3.2. Experimental

3.2.1 Chemicals

$AgNO_3$, $HAuCl_4$, 2,3-dihydroxyfumaric acid, Thiophenol (TP), Rhodamine 6G (R6G), *o*-, *m*-, and *p*-hydroxybenzyl alcohols were obtained from Sigma-Aldrich Chemical Inc. and used without further purifications. Other reagents and solvents used were of AR grade.

3.2.2 Physical measurement

For transmission electron microscopy (TEM) analysis, the precipitate of silver nano rods and gold nanoparticles were dispersed on a carbon-coated copper grid. TEM images were recorded with a JEOL JEM 3010 instrument (Japan) operated at an accelerating voltage of 300 kV. Field emission scanning electron microscopic (FESEM) images were obtained by means of FEI (Nova-Nano SEM-600 Netherlands). UV-Vis absorption measurements were performed with a Perkin-Elmer Lambda 900 UV/Vis/NIR spectrometer. Magnetic measurements were carried out using 11.6 mg of the sample with vibrating sample magnetometer in physical properties measurement system (PPMS, Quantum Design, USA). IR spectra were recorded on a Bruker IFS 66v/S spectrophotometer with samples prepared in KBr pellets in the region 400-4000 cm^{-1}. X-ray powder diffraction (PXRD) pattern were recorded on a Bruker D8 Discover instrument using Cu-Kα radiation. The solid state NMR spectra were recorded on a Bruker Avance-III spectrometer using 2.5 mm triple resonance probe. The pulses and the spectra were calibrated using a commercially available sample adamantine without further purification. Mass spectra are measured on Bruker Ultraflex II MALDI/TOF spectrometers. GCMS spectra were recorded using GC-2010 plus SCHIMADZU instrument. The column Rtx-5ms of length 30m, thickness 0.25μm and diameter 0.25 mm. ^1H NMR spectrum were recorded on a Bruker AV-400 spectrometer with chemical shift reported as ppm (in $CDCl_3$ and TMS as internal standard).

3.2.3 SERS measurement

For micro Raman experiments, the 632.8 nm laser excitation from a He-Ne laser (Model 25-LHR-151-230, Melles-Griot, USA) was used, which traversed a band pass filter (XL 12-633NB4, Omega Optical Inc., USA) and then launched into an epifluorescent microscope (Nikon 50i, Japan; axial resolution ~ 1μm). A 50x dry objective (Nikon L Plan, NA 0.45) was used for focusing the laser beam and collecting the scattered light.

The microscope was coupled to a spectrometer (IHR320 Triax, Horiba Inc.) attached to a liquid nitrogen cooled CCD detector (Andor, UK) by a 100 μm multi-mode single optical fiber cable. A resolution of 4 cm^{-1} was achieved by a holographic grating (1800 grooves mm^{-1}) in combination with a 500 μm entrance slit. The laser power measured at the sample was 5 mW. 1 μL of the NRs was dropped on a clean glass slide. Molecules were adsorbed onto the NRs by dropping 1μL of 1 mM of TP in ethanol followed by drying. Excess unadsorbed molecules were washed off with ethanol. For concentrations of μM and pM, the NRs and the solution were mixed and sonicated for 15 minutes prior to dropping on to the glass substrate.

3.2.4 Synthesis of silver nanorods

The silver NRs were synthesized by the reduction of silver ions in the aqueous medium by DHFA and the approach is quite straightforward and novel. In a typical synthesis, an aqueous solution (50 mL) of $AgNO_3$ (0.5 mM, 0.085 g) was added drop wise (2 mL/minute) to an aqueous solution (30 mL) of DHFA (0.25 mM, 0.046 g) under constant stirring in a 250 mL conical flask. pH of the solution was maintained 5.0 by adding KOH solution (1M).Then the whole reaction mixture was stirred and sonicated for another 2 hours. The colour of the solution changes to grayish-yellow indicating the formation of silver nanoparticles. Greyish-yellow color suspension was centrifuged and the resultant as-synthesized product was characterized by the TEM, UV-vis spectroscopy and powder X-ray diffraction study. The as-synthesized greyish-yellow color product was washed several times with water and methanol to remove the excess capping agent and was employed for UV-vis, SERS, and magnetic property measurements.

3.2.5 Synthesis of gold nanoparticle without capping agent

In a 30 mL vial 0.010 g DHFA was dissolved in 15 mL water (pH ~ 4.5) and 1000 μL $HAuCl_4$ solution was added slowly under constant stirring and instantaneously a deep red colour solution appear indicating the formation of carboxylic group stabilized gold nanoparticles. The solution was employed for UV-visible study and TEM analysis. For the magnetic measurement as-synthesized gold nanoparticle was washed with water and ethanol for several times.

3.2.6 Synthesis of PVP stabilized gold nanoparticle for catalysis

In 25 mL water 0.008 g PVP and 0.010 g of DHFA were dissolved and 1 mL of $HAuCl_4$ solution was added slowly and kept reaction mixture for 30 minutes under constant stirring. A red colour solution appeared indicate the formation of PVP stabilized gold nanoparticle which is characterized by IR, UV-vis, PXRD and TEM analysis.

3.3 Results and discussion

3.3.1 Mechanism of the reaction

Determination of the stoichiometry

To determine the stoichiometry of the reaction we performed potentiometric titration individually for redox reactions related to silver and gold nanoparticle formation. For both the experiment standard calomel electrode was used as reference electrode and platinum electrode was used as measuring electrode. For potentiometric titration an aqueous solution was prepared by dissolving 0.33 mM $AgNO_3$ (0.056 g) in 30 ml water in a 100 mL beaker and two electrodes were inserted into the solution. Then aqueous solution (25 mL) of DHFA (0.93 mM, 0.171 g) was prepared in 25 mL volumetric flask. Voltage across the solution in milivolts were measured point by point after addition of a certain volume (µL) of DHFA solution. The second potentiometric titration was carried out in an aqueous solution (15 mL) of $HAuCl_4$ (0.0635 mM, 0.025 g) was prepared in 100 mL beaker and two electrodes were inserted into the solution. Then aqueous solution (25 mL) of DHFA (0.7004 mM, 0.129 g) was prepared in 25 mL volumetric flask. Voltage across the solution in milivolts was measured point by point after addition of a certain volume (µL) of DHFA solution. Abrupt decrease in the voltage was observed at the equivalence point. From the amount of DHFA solution required at the equivalence point suggests that one mole DHFA can reduce two equivalent Ag^I and 2/3 equivalent Au^{III} (Scheme 2).

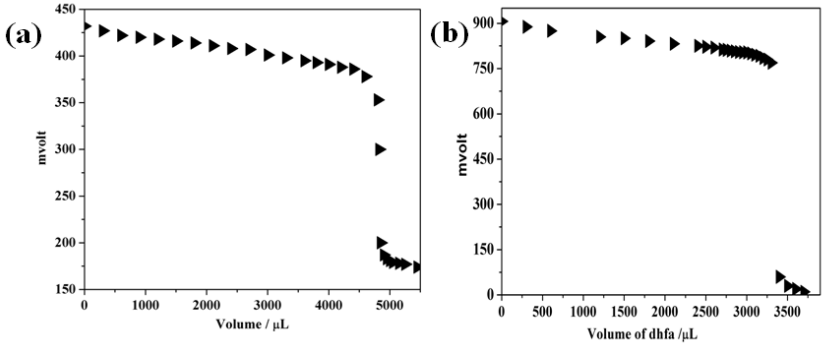

Figure 1. Potentiometric titration curve for the oxidation-reduction reaction of (a) $AgNO_3$ and (b) $HAuCl_4$ with DHFA in aqueous medium.

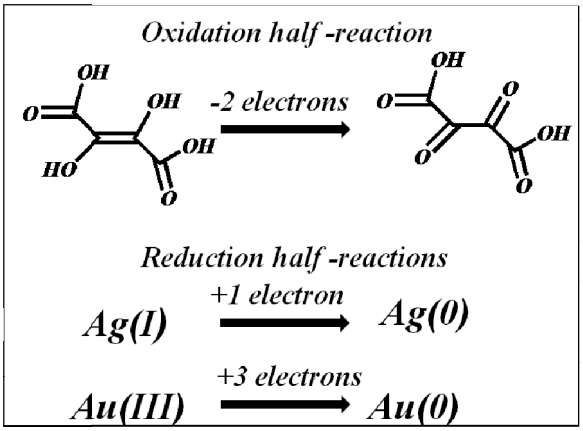

Scheme 2. Oxidation-reduction reaction equations for the formation of metallic silver and gold from Ag(I) and Au(III).

3.3.2 Characterization of capping agent

Mass spectrum (MALDI) of the solution obtained after reaction of $AgNO_3$and DHFA in 2:1 ratio in aqueous medium (Figure 2a) shows a peak at *m/z* 145.83 corresponds to the oxidized product of DHFA *i.e* DKSA (Calcd: 146.05). The rearranged product of DKSA *i.e.* tricarboxylic acid substituted methanol ($(HOOC)_3C$-OH) is also present in the solution phase[1] which corresponds to the peak at *m/z* 163.86 (Calcd: 164.06). The mass spectrum contain additional peak at *m/z* 174.58 (Calcd: 174.11) which corresponds to dimethyldiketosuccinate [$(H_3COOC\text{-}CO)_2$] in the aqueous medium. The formation of dimethyldiketosuccinate has been explained as follows; highly unstable tricarboxylic acid converted to methanol after decarboxylation which reacts with acid group of diketosuccinic acid (DKSA) to form dimethyldiketosuccinate as observed in the mass spectra. These results suggest dimethyldiketosuccinate is the ultimate product which acts as the capping agent with other organic reagents present in the system (Scheme 3).

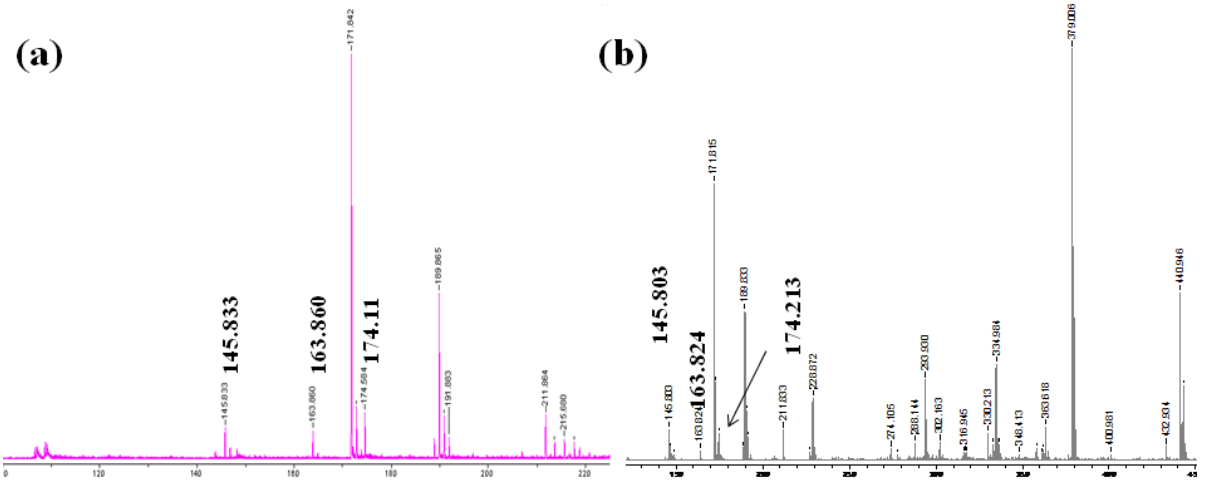

Figure 2. Mass spectrum (MALDI) of the solution obtained after stoichiometric reaction between (a) $AgNO_3$ (b) $HAuCl_4$ with DHFA.

The IR and NMR spectra further support the above conclusion. IR spectrum of silver NRs (see Figure 3a) show bands at 1592 cm^{-1} and 1306 cm^{-1} corresponding to ν_{as}(COO)(s) and ν_s(COO)(s), respectively of the carboxylate anion.[2] Although the capping agent is an ester when it binds to the surface atom of NRs methyl group distance from oxygen increases consequently ester group behave almost like carboxylate group. It is worth mentioning that IR spectrum of the solid NRs does not contain any peak corresponds to α-diketone which corroborates the existence of Ag…O interaction with carbonyl oxygen of C_2 and C_3. Further evidence of such interaction was supported by the Raman spectral band ($\nu_{Ag...O}$) at 220 cm^{-1} (Figure 4).[24] Gold nanoparticle with and without PVP has been synthesized by using the same reagent, DHFA at room temperature and in aqueous medium at pH~5.0. The procedure we are reporting here is expedient to synthesize particle both in presence and absence of PVP. A potentiometric titration suggest one mole of $HAuCl_4$ get reduced by 1.5 mole of DHFA (Scheme 1). DHFA after two electron oxidation converted to diketosuccinic acid (DKSA) and tricarboxylic acid substituted methanol (TSM) and simultaneously Au(III) get reduced to Au(0). Mass spectrum (MALDI) contains two peaks at 164 and 146 (Fig. 2b) corresponds to TSM and DKSA, respectively, which unequivocally suggests similar mechanism as for the synthesis of silver nanorods. It is worth mentioning that, this method is similar to the sodium citrate method reported by Turkevisch *et al*. The extra advantage of our method is nanoparticle of similar size can be obtained at room temperature. and size can be reduced by adding

extra capping agent like PVP. Gold nanoparticles without PVP are stabilized through electrostatic interaction from the carboxylic groups of unreacted DHFA, and oxidized products DKSA and TSM. However, these Au..O interactions are very weak due to softness of gold and therefore uncapped gold nanoparticles were easily obtained by simple washing with ethanol. IR spectrum of the washed nanoparticles do not contain any peak corresponding to carboxylic group indicating it is free from any capping agent (Figure 3b). The gold nanoparticles were characterized by UV-visible spectrum, transmission electron microscopy (TEM) and powder X-ray diffraction (PXRD). Solid state ^{13}C, ^{1}H NMR and solution phase ^{1}H NMR further supports the above observations.

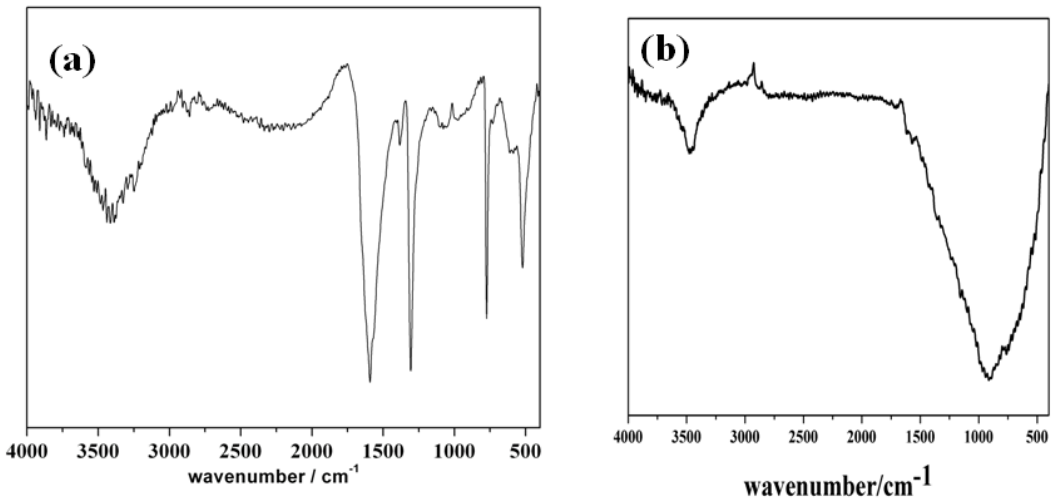

Figure 3. IR-spectrum for the (a) washed silver NRs, (b) washed gold nanoparticles.

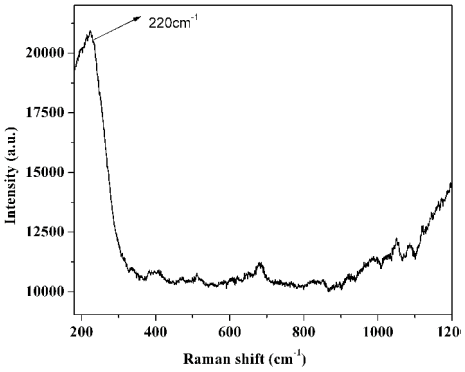

Figure 4. Raman spectra for silver NRs showing the presence of Ag…O band at 220 cm^{-1}.

Solid state ^{13}C NMR of silver NR's the peak at 27 ppm which corresponds to ester methyl group. The peak at 101 ppm and 190 ppm represents C_2/C_3 and C_1/C_4 carbon atoms respectively (see figure 5). The ester methyl group carbon of the NR's surface is more shielded compare to a normal ester because ester oxygen strongly interacts with surface

atom of silver NRs leading to increase in carbon oxygen bond distances. Similarly for C_2 and C_3 again the shielding effect arises due to interaction of silver with oxygen.

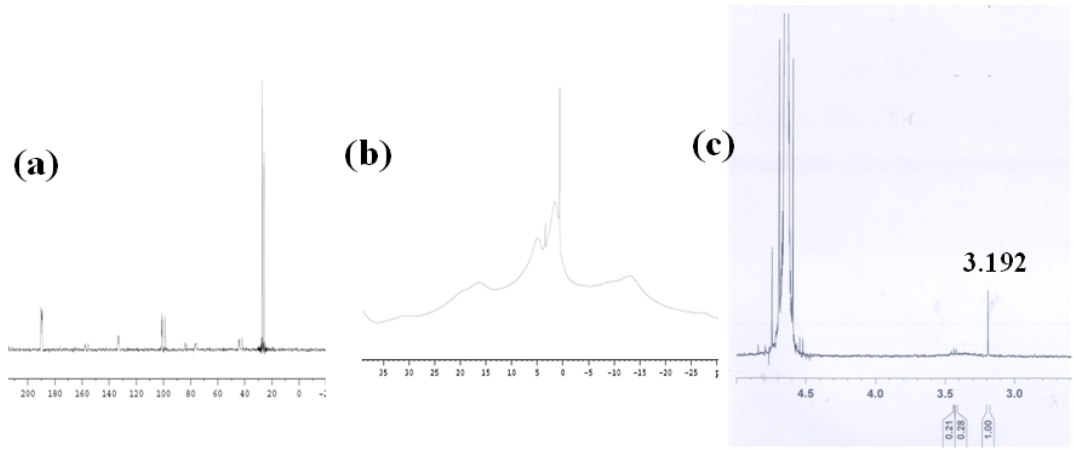

Figure 5. (a) Solid state ^{13}C NMR spectra of the NRs, (b) solid state ^{1}H NMR spectra, (c) ^{1}H NMR spectrum of the solution after reaction.

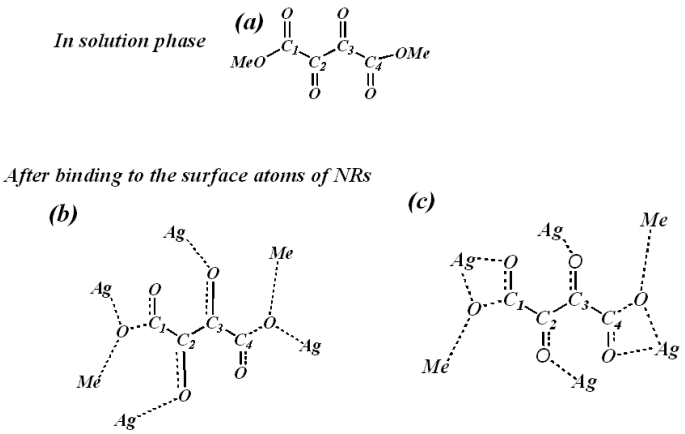

Figure 6. (a) Capping agent in solution phase; (b) Probable interactions of the capping agent with the silver NRs.

Therefore from the above observations, we can conclude that in solution phase we have the dimethyldiketosuccinate as shown in Figure 6 and in solid phase the dimethyldiketosuccinate binds to the surface silver atoms of the NRs as a capping agent. The overall scheme of the synthesis of silver (Scheme 3a) and gold (Scheme 3b) nanostructure are shown below.

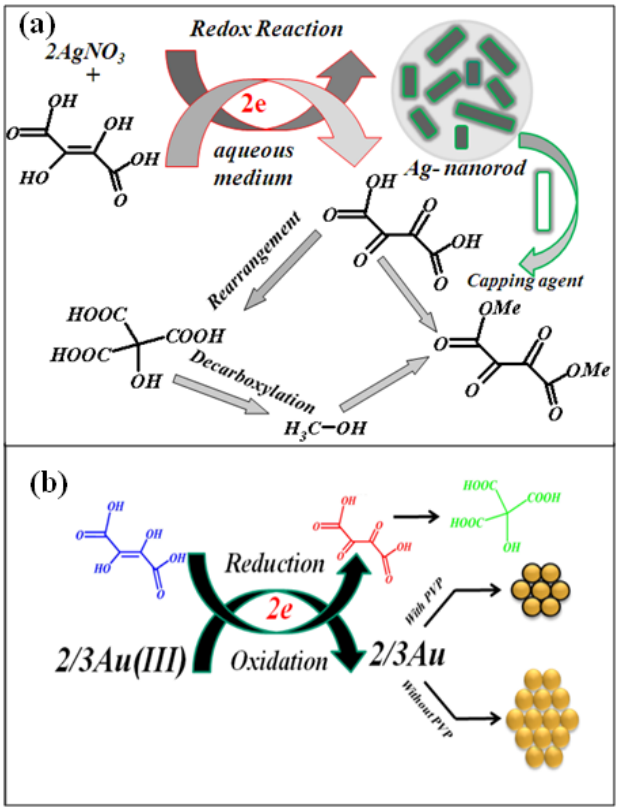

Scheme 3. Mechanism for the formation of (a) silver NRs and corresponding capping agent (b) gold NPs (both in the presence and absence of PVP).

3.3.3 Characterization of silver nanorods and gold nanostructures

3.3.3.1 TEM imaging

Morphology of the as-synthesized silver nanostructure is rod shaped as shown by TEM image (Figure 7a). The size distribution is found to be 20 - 80 nm. Most of the rod shaped nanostructures formed with an average length of 53 nm and a width of 25 nm. The distribution of the size with respect to its frequency of occurrence is calculated considering, 194 nanoparticles and the histogram is shown in Figure 7b. To clarify the crystallinity of the silver NRs, electron diffraction (ED) measurements were carried out. The diffraction rings of the silver NRs in ED pattern (Figure 7b) confirming the crystalline nature of these silver NRs.

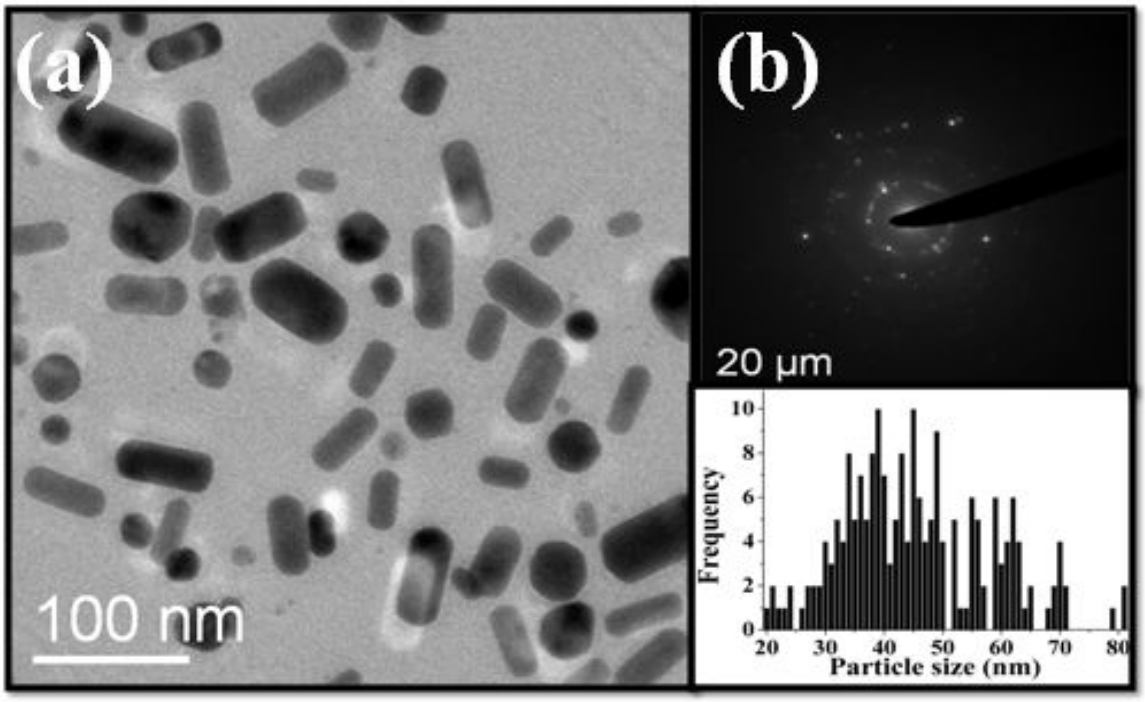

Figure 7. (a**)** TEM image for the as-synthesized silver NRs; (b) Electron diffraction (ED) pattern showing crystalline nature of the silver NRs and the histogram of particle size distribution.

TEM image of the carboxylic group stabilized gold nanoparticles is shown in Figure 8 indicating spherical particle and histogram obtained by considering 82 nanoparticles suggests there is a wide distribution of size from 20 to 70 nm with average particle size of 40 nm. The crystalline nature of particles was confirmed from electron diffraction (ED) pattern. The nanoparticle obtained after addition of aqueous $HAuCl_4$ solution into the reaction mixture containing, DHFA, and PVP is shown in Figure 9a. The particle sizes are smaller compared to particles obtained without PVP, having the size variation from 2 to 40 nm.

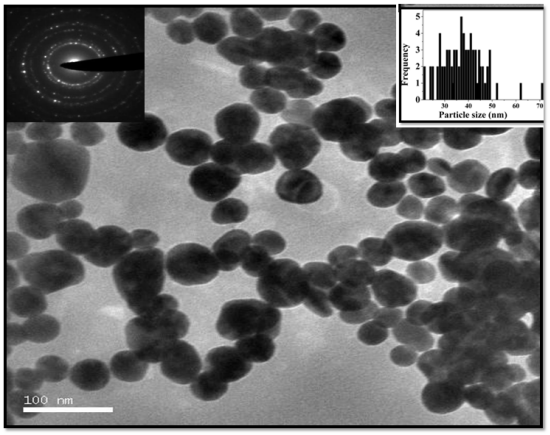

Figure 8. TEM image, histogram of gold nanoparticles.

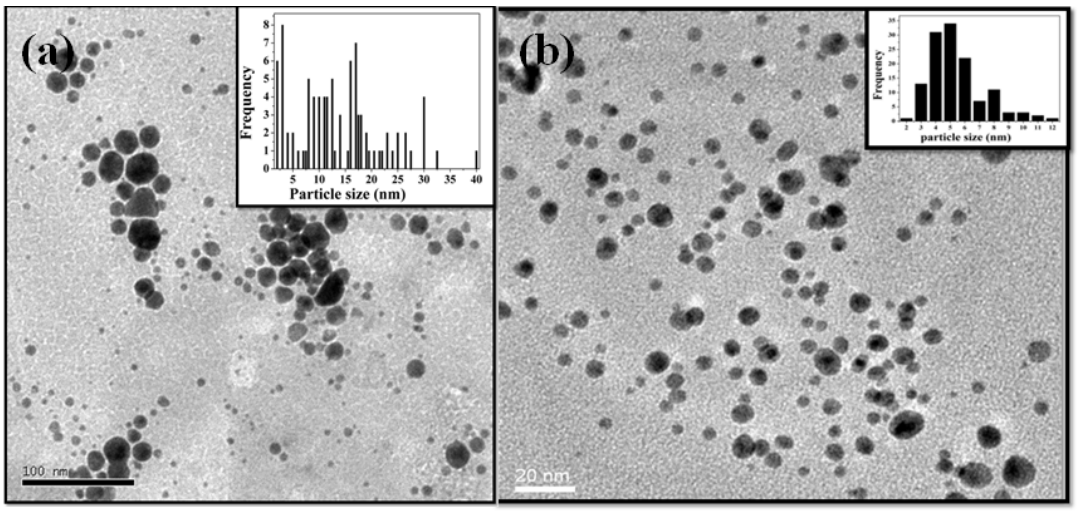

Figure 9. TEM image, histogram of PVP stabilized gold nanoparticles (a) before catalytic reaction (b) after catalytic reaction.

3.3.3.2 UV- Visible study

UV-vis spectrum (Figure 10a) of the silver NRs shows two surface plasmon resonance bands; (SPR) one at 420 nm and other at 582 nm. The first band at 420 nm corresponds to the transverse SPR band which is common for all silver nano structures. The band at 582 nm corresponds to the longitudinal SPR band. The UV-vis spectra of the colloids clearly supports that nanostructures are anisotropic in shape.[24] Since the as-synthesized silver NRs have very less zeta potential and capping agents have weak interaction with silver therefore they have very high tendency to agglomerate. The change of the solution's color with three hours interval is shown in Figure 11 and a clear layer of NRs at the bottom of the vial indicates the sedimentation, due to agglomeration or inefficient dispersion in aqueous medium. The UV-vis spectra of washed NRs show a broad band starting from 416 nm with the merging of the second SPR band (Figure 10b). This is due to the agglomerations and formation of nanocluster with different size and shape after removal of the capping agents. It is worth mentioning that particle size and shape depends on the concentration ratio of DHFA to silver nitrate.

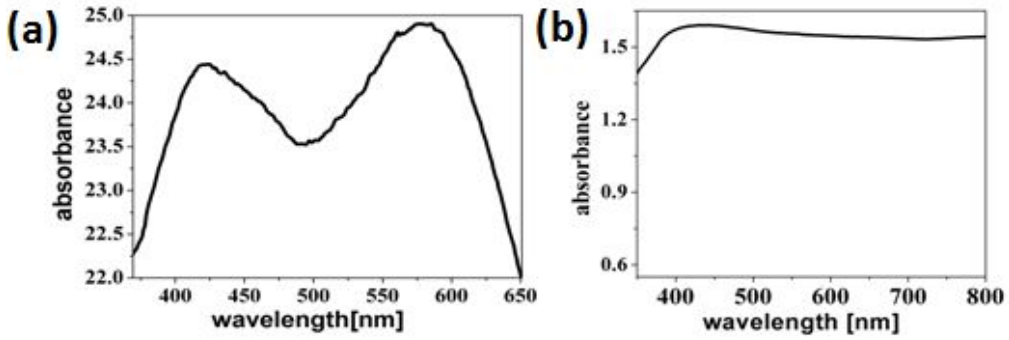

Figure 10. (a) Uv-vis spectra of as-synthesized silver (a) nanorods and (b) after washing with MeOH and water.

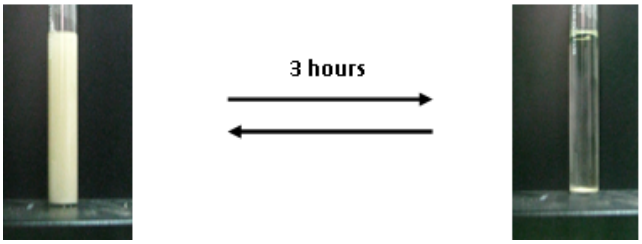

Figure 11. Photograph for the as-synthesized greyish-yellow color silver NRs in aqueous medium (left side) and after 3 hours NRs settled down with clear upper solution (right side).

The UV-visible spectrum of the gold nanoparticle synthesized in the absence of PVP shows only one characteristic surface plasmon resonance (SPR) band at 540 nm suggesting spherical shape of particle (Figure11a). The nanoparticles synthesized in presence of PVP exhibit blue shifted SPR band at 520 nm (Figure 11b) suggesting the average particle size are smaller compared to the particle synthesized in absence of PVP.

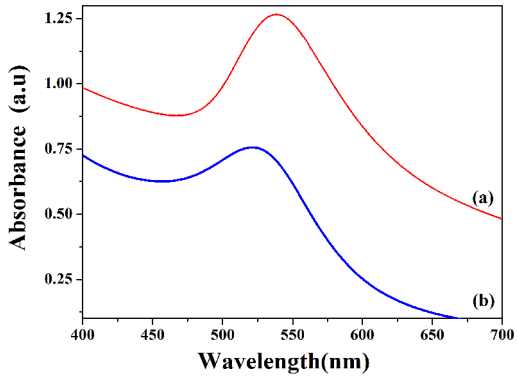

Figure 12. Uv-vis spectra of gold nanoparticle synthesized in (a) absence of PVP (b) in presence of PVP.

3.3.3.3 PXRD study

Furthermore the powder X-ray diffraction (PXRD) pattern (2θ = 30 – 80°) of silver NRs is presented in Figure 13a, in which the diffraction peaks for the (111), (200), (220), and (311) lattice planes appear clearly. The diffraction planes of the silver nanorods are corresponding well to the crystalline planes of the face-centered-cubic (fcc) structure of Ag, which is consistent with the ED pattern.[13] Gold nanopowder obtained after washing the carboxylic group stabilized nanocolloids, were characterized further from the PXRD pattern which shows the peak corresponds to (111), (220), (300), (311) crystal planes of an FCC structure (Figure13b).

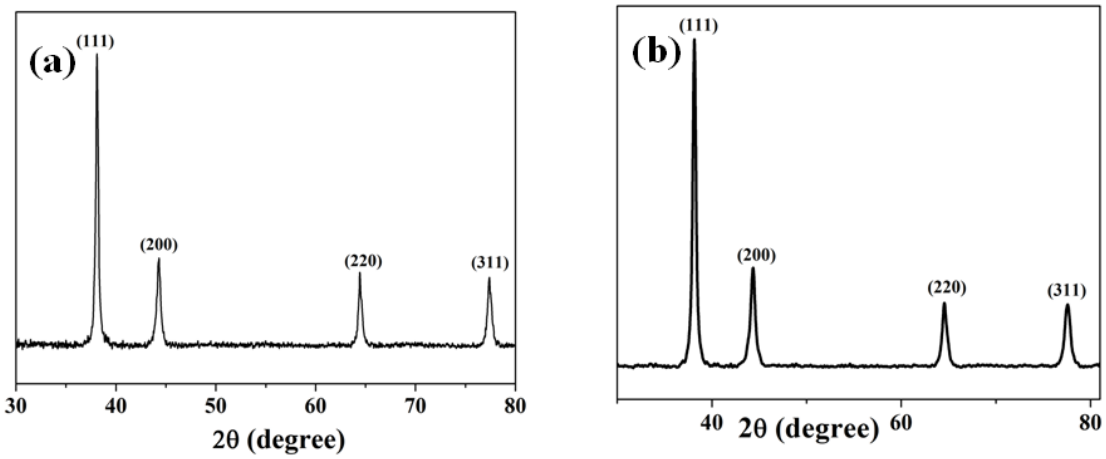

Figure 13. X-ray powder diffraction pattern (PXRD) for the as-synthesized (a)silver NRs and (b) gold NPs.

3.3.4 SERS activity of nanorods

One of the most common properties of silver nanoparticle is SERS and the possibility of trace detection of molecules makes it an important property. Due to a very broad UV-vis absorption and tendency to agglomeration (Figure 11) of these NRs encourage us to employ it for trace detection of different substrate molecules. The advantage of a nearly flat response of the washed NRs in UV-vis spectra (Figure 10b) is that there is no restriction on the excitation source to be used for SERS. To demonstrate this we have chosen an excitation source 632.8 nm, which is far away from the UV-vis absorption peak of 420 nm and 736 nm for single silver NR. In order to take advantage of agglomeration of NRs, the molecule could be incubated with NRs a prior, which would trap the molecules among the NR agglomerates leading to hot spot like environment (inset of Figure 15). In order to test this, we have taken thiophenol (TP) as the test molecule and incubated with washed silver NRs on a glass substrate. The SERS spectra of the incubated TP with NRs and free TP molecules have been shown in Figure 14. The spectral features agree well with the reported values. The enhancement factor G was calculated by the procedure given by Yu *et.al.*[25]

$$G = (I_{SERS}/I_{norm})(N_{bulk}/N_{surf})$$

where I_{SERS} and I_{norm} are the intensities of a specific band in SERS and normal Raman of test molecule, respectively. N_{bulk} and N_{surf} are the number of probe molecules under laser illumination in the bulk and SERS experiments, respectively. We have chosen two bands at 1069 cm^{-1} and 1572 cm^{-1} (ν_{c-c}) to calculate G factor for TP. N_{surf} is given by CA, where C and A are surface densities of TP (6.8×10^{14} molecules cm^{-2}) and area of the laser spot

on the sample, respectively.[26] On the other hand, N_{bulk} is given by A$h\rho/m$, where h, ρ and m are the penetration depth (100 μm), the density (1.079 g cm^{-1}), and the molecular weight (110.18 g mol^{-1}) of TP, respectively. In the present experiment, we obtained the G ~ 10^5 for TP.

The silver NRs were also employed for SERS of the Rhodamine 6G (R6G) and phenylalanine Raman probes as shown in Figure 14 (inset). It can be observed that NRs with both the adsorbates exhibit very strong SERS activity. The spectral features of TP, R6G and phenylalanine obtained are similar to earlier reports.[27-29] In the case of R6G some background fluorescence observed was subtracted for clarity. It is normally observed that R6G has a strong chemical interaction with metal nanoparticles which results in fluorescence quenching. In our case strong chemical binding is absent but R6G adsorbs to the NRs giving good SERS signal with some background fluorescence. In the case of TP, the thiol group helps in chemical binding leading to no residual background giving rise to stable SERS spectra. The large decrease of frequency of the in-plane breathing mode coupled to the $\upsilon_{(C-S)}$ mode from 1092 cm^{-1} to 1069 cm^{-1} in the SERS spectra show that the TP molecule is bonded to the metal surface.[30] The NRs as substrate can detect SERS of TP and R6G down to a concentration of 10^{-12} M is much lower than those reported, [31] where as in case of phenylalanine we could go down to only μM concentration (Figure 14, inset).

Sun *et. al.* have reported that dissolution of capping agents like CTAB in ethanol results in formation of aggregates.[32] Chen *et. al.* have shown that the electromagnetic enhancement depends strongly on the degree of aggregation of silver nanoparticles.[33] 3D aggregation of nanoparticles strongly influences the SERS enhancements as shown by Pignataro *et. al.*[34] Many a times for stronger SERS signals aggregating agents like NaCl, KCl, KNO_3 are used.[35] In our case washing with methanol reduces the density of capping agents on the NR surface facilitating the adsorbates to be adsorbed on to the surface. The reduction in the capping agents facilitates creation of 3D structures resembling hotspots (Figure 15).[36] Hence, the present NRs have a preference on the types of analytes having the groups containing sulphur, π electrons and nitrogen facilitates chemical binding or strong adsorption on these NRs resulting in its ability for trace detection.

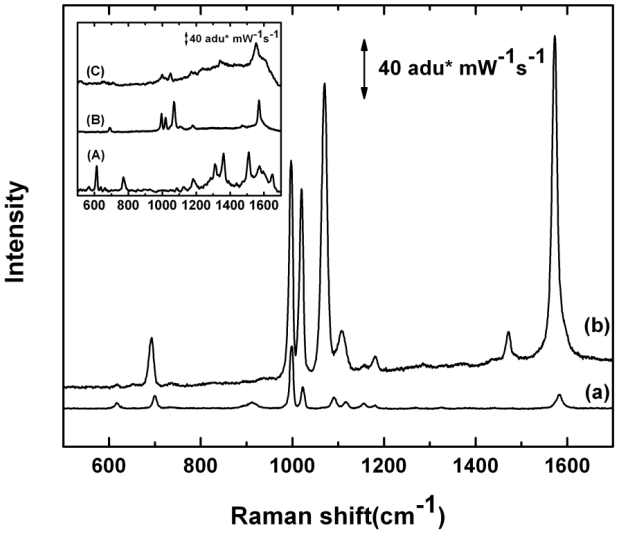

Figure 14. SERS spectra of Thiophenol (TP): (a) without and (b) with NRs. Inset: SERS spectra of (A) Rhodamine 6G (R6G, 1pM), (B) Thiophenol (TP, 1pM) and (C) L-Phenylalanine (1 μM).

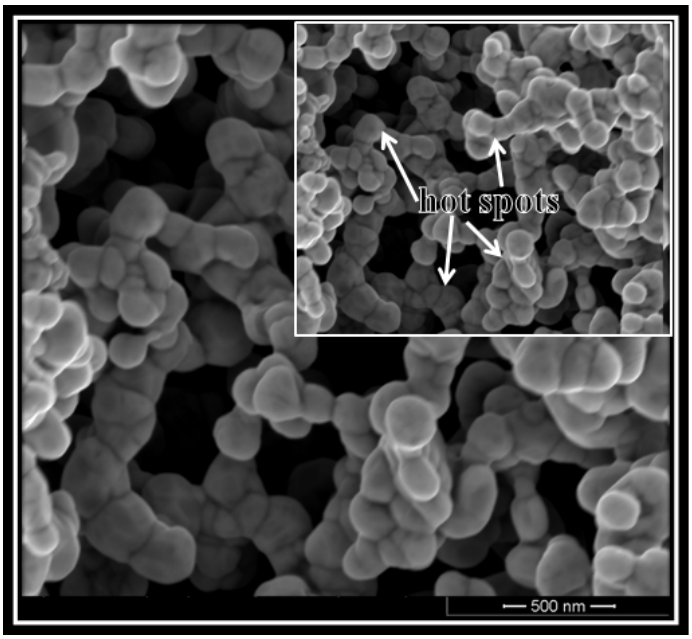

Figure 15. FESEM image for the agglomerated silver NRs after washing with water and methanol; inset showing the 'Hot Spots' in the agglomerated silver NRs.

3.3.5 Catalytic activity of PVP stabilized gold nanoparticle

To unveil the catalytic activity for oxidation of alcohol by gold nanoparticle, *o*-, *m*- and *p*-hydroxybenzylalcohols were chosen as the substrate molecule and reactions were carried out using PVP protected gold nanoparticle at two different temperature 300 and 333 K (Figure16). The results are summarized in the Table 1. The *o*-, *m*- and *p*-hydroxybenzylalcohols were converted to corresponding aldehyde at three, six and thirteen days, respectively at 300 K. However, when the same reactions were performed at 333 K the alcohols were selectively get converted to corresponding

aldehyde after few hours without the formation of any side product. Heating at 333 K for catalytic activity study the nanoparticle size get reduced to narrow size distribution following digestive ripening mechanism.[37] The bigger size particles were converted to smaller and corresponding size distribution is shown in Figure 9b. As the hydroxyl group position changes from *o*-, to *m*- to *p*- from the benzylic position the rate of the reation decreases suggesting inductive effect of hydroxo group is a major factor for controlling the reaction rate. The purity of the aldehydes were confirmed from NMR spectrum (Figure 17-19). It is worth mentioning here that the same gold nano catalyst solution can be used several times for the catalytic reaction after complete extraction of the product. We examined the reusability upto fifth cycle. Normally oxidation of hydroxybenzylalcohol by conventionally synthesized gold nanoparticles produce mixture of product rather than a single product because aldehyde is more susceptible to further oxidation.[38] Using this new strategy for the synthesis of gold nanoparticles, we could able to control the oxidation of alcohol at aldehyde stage.

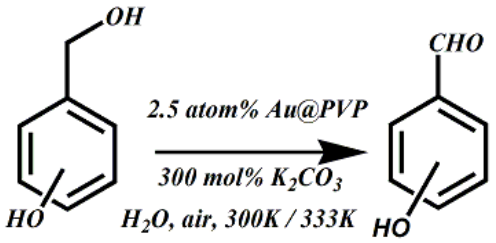

Figure16. Schematic showing catalytic reactions at 300 and 333 K.

substrate	Time (300K)	Conv*	Time (333K)	Conv.*
o-OH benzylalcohol	3days	100%	6hours	100%
m-OH benzylalcohol	6days	100%	10hours	100%
p-OH benzylalcohol	13days	100%	20hours	100%

Table 1. Catalytic reactions at 300K and 333K (*Estimated from GC analysis by using ethyl acetate as solvent)

The oxidation probably proceeds via the abstraction of hydrogen atom by superoxo like molecular oxygen adsorbed on Au@PVP as reported earlier.[38-45] Since catalytic activity inversely related to the size of the particle consequently the conversion rate is

lower at room temperature compared to the earlier report. In our case aldehyde is selectively forming without any other side product. Nanoparticle used for catalysis purpose were synthesized using DHFA little excess than the stoichiometrically required amount , that can discard the possibility of Au(III) as an impurity. The reducing agent DHFA itself oxidized in air at room temperature to form TSM, finally get converted to methanol so the possibility of impurity of excess DHFA can be discarded which is also reflected in GC spectrum. It is worth mentioning here gold nanocolloids without PVP is unstable at strongly alkaline condition, because of the stabilizing agent, DHFA, DKSA and TSM are decarboxylated in alkaline condition. After addition of alkali as the stabilzers are decomposed and nanoparticles get agglomerated consequently no catalytic activity was observed whereas PVP stabilized *in situ* generated gold nanocolloids have very high stability and strong catalytic activity towards controlled oxidation of hydroxybenzylalcohols to hydroxybenzaldehydes.

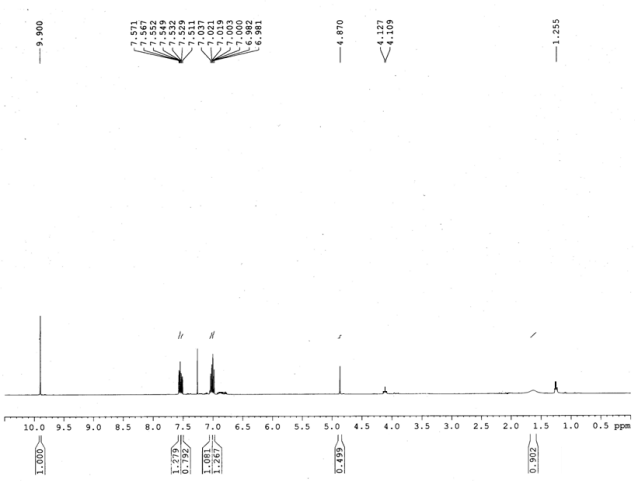

Figure 17. ^{1}H NMR spectrum of 2-hydroxy benzaldehyde obtained after reaction.

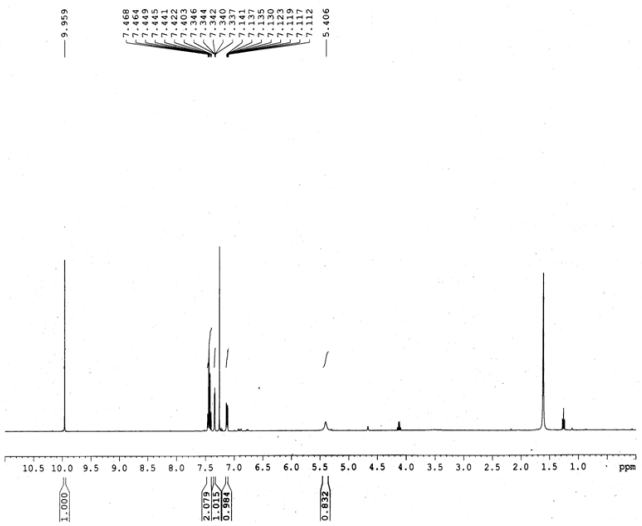

Figure 18. ^{1}H NMR of 3-hydroxy benzaldehyde obtained after reaction.

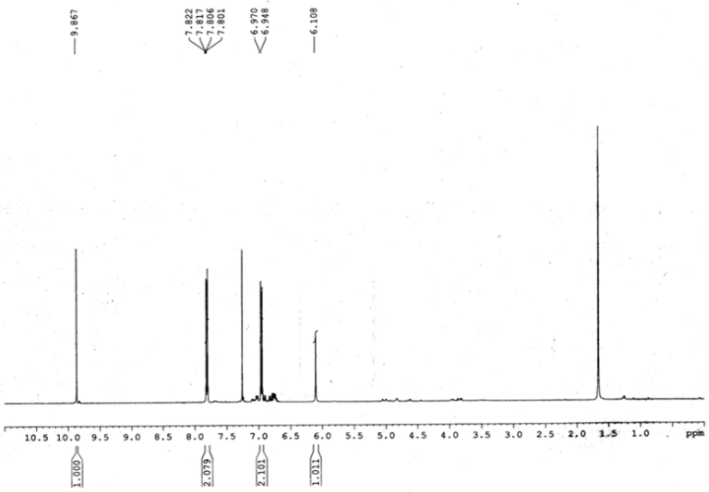

Figure 19. ^{1}H NMR of 4-hydroxy benzaldehyde obtained after reaction.

3.3.6. Magnetic Property of silver and gold nanostructures

Preliminary magnetic studies of the capped silver NRs were found to be ferromagnetic at low temperature (2.5 K) as well as at room temperature (see Figure 20). The field dependent magnetization plot at 2.5 K (black curve in Figure. 20) shows a saturation magnetization of 0.2857 emu g^{-1} with a small hysteresis loop of remanent magnetization 0.004 emu g^{-1} and coercive field 74 O respectively. When the same measurement has been performed at room temperature saturation magnetization value dropped down to 0.224 emu g^{-1} and hysteresis loop became narrower, *i.e* ferromagnetic interaction became weaker.

It is well known fact that silver is diamagnetic in nature even in nanometer scale. As reported earlier, magnetic property in a non magnetic element (Ag, Au) in its nanometer size may arise due to two reasons; either by surface defects due to low coordination number of surface atoms or by generation of unoccupied density of *d* state due to strong charge transfer interaction between surface atom and organic capping agent (mainly sulfur containing).[46, 47] But here the silver NRs capped with oxygen containing organic molecule. To establish the fact that magnetic property of this nanostructure is not arising from inorganic-organic layer due to strong charge transfer, we performed magnetic measurement of the NRs after complete removal of the capping agents. The NRs were found to behave similar to the capped one. The complete removal of the capping agent has been done by heating the NRs at 700 ºC under N_2 atmosphere for 3 hours at a heating rate of 5 ºC/ minute. This is confirmed from the disappearance of Ag…O band in Raman spectra. This observation clearly demonstrates that magnetic property is not chemically induced but is inherent. As has been studied earlier, almost all nanostructure materials with one, two, or three components have deficiencies on the surfaces.[48] This is due to the reduced coordination of the surface atoms of the nanostructure component. In our case, since it is a single component system, the reduced coordination of silver at the surface would give rise to unpaired (non-bonding) electrons which provide ferromagnetic interaction in the Ag-nanorod. Recently Luo *et al*.[49] has established by the First principle DFT spin polarized calculation based on 'superatomic' model that ferromagnetic interaction is possible in the case of silver or gold nanoclusters.

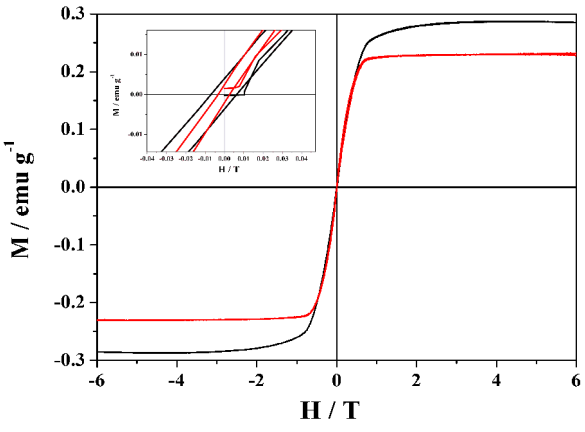

Figure 20. Field dependent magnetization for silver NRs (black at 2.5 K and red at room temperature) (inset: Low field region showing small hysteresis for the NRs (black at 2.5 K and red at room temperature).

There are a large number of reports in the literature where gold nanoparticle shows

ferromagnetic behaviour due to capping agent[51-55] but ferromagnetic behaviour of uncapped nanoparticle yet to be explored. Recent theoretical as well as experimental studies inspired us to study the magnetic properties of the gold nanoparticles. The uncapped gold nanoparticles also show ferromagnetic property as suggested by the field dependent magnetization study at 300 K (Figure 21) and justify the above theoretical finding. The magnetic hysteresis loop shows saturation magnetization of 3 $\times 10^{-3}$ emu g^{-1}, with coercive field 216 G and remanent magnetization 1.1 $\times 10^{-3}$ emu $g^{-1.}$ This results support the theoretical findings.

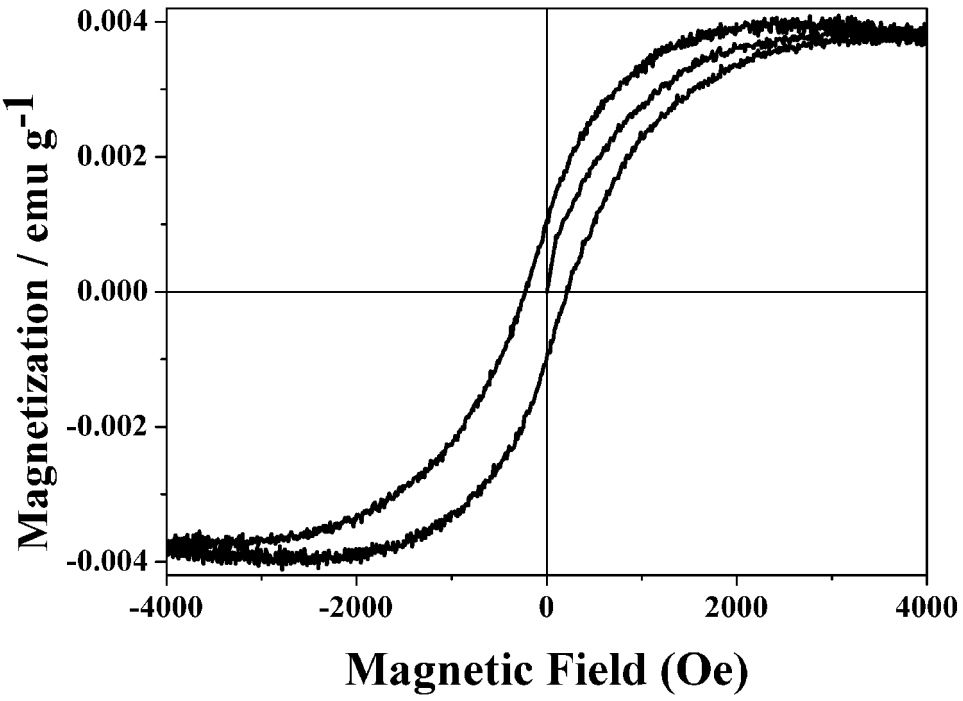

Figure 21. Field dependent magnetization plot of uncapped gold nanoparticle at 300K temperature.

3.4 Summary

We have developed a novel method for the synthesis of silver NRs and gold nanoparticle at room temperature in a facile way by using a new reducing agent. The facile and novel method does not require any toxic chemicals to synthesize the nanostructures. Properties of the NRs were found to be quite exciting compared to others silver nanostructures obtained in other conventional method. NRs were found to exhibit a high SERS sensitivity and trace detection limit towards thiophenol and Rhodamin 6G adsorbates. Ferromagnetic behavior of both gold and silver at it's

nanometer size regime in the absence of any capping agent has been established by using the nanostructures of gold and silver obtained by this method. Therefore this environment benign method is useful for synthesizing coinage metal nanostructure for applications in multiple purposes. The silver NRs with excellent SERS sensitivity may be useful in bio-diagnostics, food and textile application, medical imaging etc. PVP stabilized gold nanoparticle exhibit excellent catalytic activity for controlled and complete aerial oxidation of hydroxybenzyl alcohol to hydroxybenzaldehyde without the formation of any side product.

3.5 References

1. M. A. El-Sayed, *Acc. Chem. Res.,* 2001, **34**, 257.
2. M. A. El-Sayed, *Acc. Chem. Res.,* 2004, **37**, 326.
3. A. P. Alivisatos, *Science,* 1996, **271**, 933.
4. C. Burda, X. Chen, R. Narayanan and M. A. El-Sayed, *Chem. Rev.,* 2005, **105**, 1025.
5. P. Mukherjee and A. K. Nandi, *J. Mat. Chem.,* 2009, **19**, 781.
6. P. V. Kamat, *J Phys. Chem. B.,* 2002, **106**, 7729.
7. J. A. Creighton, C. G. Blatchford and M. G. Albrecht, *J. Chem. Soc., Farad. Trans. 2: Mol. Chem. Phys.,* 1979, **75**, 790.
8. G. D. Scholes, *Adv. Func. Mat.,* 2008, **18**, 1157.
9. N. Zhao, W. Nie, X. Liu, S. Tian, Y. Zhang and X. Ji, *Small,* 2008, **4**, 77.
10. D. L. Leslie-Pelecky and R. D. Rieke, *Chem. Mat.,* 1996, **8**, 1770.
11. R. Narayanan and M. A. El-Sayed, *J. Am. Chem. Soc.,* 2004, **126**, 7194.
12. W. P. Halperin, *Rev. Mod. Phys.,* 1986, **58**, 533.
13. Y. Sun, Y. Xia, *Science,* 2002, **298**, 2176.
14. C. J. Murphy, *Science,* 2002, **298**, 2139.
15. F. W. Brust and B. S. Majumdar, *J. Chem. Soc., Chem. Commun.,*1994, **49**, 801.
16. P. C. Lee and D. Meisel, *J. Phys. Chem.,* 1982, **86**, 3391.
17. Z. L Wang, Y. Liu and Z. Zhang, *A Hand Book of Nanophase and Nanostructured Materials*, Springer Link; **2002**.
18. P. Raveendran, J. Fu and S. L. Wallen, *Green Chem.,* 2006, **8**, 34.
19. S. Mohapatra and T. K Maji, *Dalton Trans.,* 2010**, 39,** 3412.
20. B. F. Abrahams, T. A. Hudson and R. Robson, *Chem. Eur. J.,* 2006, **12**, 7095.
21. D. Sazou, P. Karabinas, D. Jannakoudakis, *J. Electroanal. Chem. Interfacial Electrochem*., 1985**, 185**, 305.

22. U. Heiz and U. Landman, Nanocatalysis, Springer; 2006.
23. K. Yusuf, B. I. Ipe, C. H. Suresh and K. G. Thomas, *J. Phys. Chem C* 2007, **111**, 12839.
24. Y. Yang, L. Xiong, J. Shi and M. Nogami, *Nanotechnology,* 2006, **17**, 2670.
25. H. Z. Yu, H. L. Zhang and Z. F. Liu, *Langmuir,* 1999, **15**, 16.
26. A. D. McFarland, M. A. Young, J. A. Dieringer and R. P. Van, *J. Phys. Chem. B,* 2005, **109**, 11279.
27. J. A. Dieringer, K. L. Wustholz, D. J.Masiello, J. P. Camden, S. L. Kleinman, G. C. Schatz and R. P. Van Duyne, *J. Am. Chem. Soc.,* 2009, **131**, 849.
28. S. Stewart and P. M. Fredericks, *Spectrochim. Acta - Part A.,* 1999, **55**, 1641.
29. M. A. Bryant,S. L. Joa and J. E. Pemberton, *Langmuir,* 1992, **8**, 753.
30. W. Li, Y. Guo and P. Zhang, *J. Phys. Chem. C,* 2010, **114**,7263.
31. L. Sun, Y. Song, L. Wang, C. Guo, Y. Sun, Z. Li and Z. Liu, *J. Phys. Chem. C,* 2008, **112**, 1415.
32. A. Tao, F. kim, C. Hess, J. Goldberger, R. He, Y. sun, Y. Xia and P. Yang, *Nano Lett.,* 2003, **3**, 1229.
33. R. J. Stokes, A. Macaskill, P. J. Lundahl, W. E. Smith, K. Faulds and D. Graham, *Small,* 2007, **3**, 1593.
34. A. D. McFarland, M. A. Young, J. A. dieringer and R. P. V. Duyne, *J. Phys. Chem. B,* 2005, **109**, 11279.
35. J. Gersten, *J. Chem. Phys.,* 1980, **73**, 3023.
36. J-Q. Hu, Q. Chen, Z-X. Xie, G-B. Han, R-H Wang, B. Ren, Y. Zhang, Z-L. Yang and Z-Q.Tian *Adv. Func. Mat*., 2004,**14,** 183.
37. K. T. Carron and L. G. Hurley, *J. Phys. Chem.,* 1991, **95**, 9979.
38. R. Shankar, B. B. Yu and T. P. Bigioni, *J. Phys. Chem. C*, 2010, **114**, 15916.
39. H. Tsunoyama, H. Sakurai, Y. Negishi and T. Tsukuda, *J. Am. Chem. Soc*., 2005 **127**, 9374.
40. H. Tsunoyama, H. Sakurai, Y. Negishi and T. Tsukuda, *J. Am. Chem. Soc*., 2005, **127** 9374.
41. D. Stolcic, M. Fischer, G. Ganteför, Y. D. Kim, Q. Sun and P. Jena, *J. Am. Chem. Soc.,* 2003, **125**, 2848.
42. J. D. Stiehl, T. S. Kim, S. M. McClure and C. B. Mullins, *J. Am. Chem. Soc.*, 2004, **126**, 1606.

43. M. Okumura, Y. Kitagawa, M. Haruta and K. Yamaguchi, *Chem. Phys. Lett.,* 2001, **161**, 163.
44. D. H. Wells, J.W. N. Delgass and K. T. Thomson, *J. Chem. Phy.* 2002, **117**, 10597.
45. T. Ishida, M. Nagaoka, T. Akita and M. Harota, *Chem. Eur. J.,* 2008, **14**, 8456.
46. V. Subramanian, E.E. Wolf and P.V. Kamat, *J. Am. Chem. Soc.,* 2004, **126,** 4943.
47. M. C. Chen, S. D. Tsai, M. R. Chen, S. Y. Ou, W. H. Li and K. C. Lee, *Physic. Rev. B,* 1995, **51**, 4507.
48. B. Pignataro, A. De Bonis, G. Compagnini, P. Sassi and R. S. Cataliotti, *J. Chem. Phys.,* 2000, **113**, 5947.
49. O. K. Song, M. A. Pauley, C. H. Wang, A. K. Y. Jen, *J. Raman Spect.,* 1996, **27**, 685.
50. E. C. Le Ru and P. G .Etchegoin, *Chem Phys. Lett.,* 2004, **396**, 393.
51. J. S. Garitaonandia, M. Insausti, E. Goikolea, M. Suzuki, J. D. Cashion, N. Kawamura, H. Ohsawa, I. G. De, K. Suzuki, F. Plazaola and T. Rojo, *Nano Lett.,* 2008, **8**, 661.
52. M. Suda, N. Kameyama, M. Suzuki, N. Kawamura and Y. Einaga, *Angew. Chem. Int. Ed,* 2008, **47**, 160.
53. A. Sundaresan, R. Bhargavi, N. Rangarajan, U. Siddesh and C. N. R. Rao, *Phys. Rev. B,* 2006, **74**, 161306(4).
54. W. Luo, S. J. Pennycook and S. T. Pantelides, *Nano Lett.,* 2007, **7**, 3134.
55. E. Guerrero, M. A. Muñoz-Márquez, A. Fernández, P. Crespo, A. Hernando, R. Lucena and J. C. Conesa, *J. Appl. Phys.,* 2010**, 107**,064303.

Chapter 4

2,3-dihydroxyfumeric acid (DHFA) as a Precursor for Oxalate & Carbonate in Lanthanide-Organic-Frameworks: Synthesis, Structure, Magnetic and Luminescence Properties

Abstract

A series of lanthanide-organic open framework materials, $\{Ln(CO_3)(C_2O_4)_{0.5}(H_2O)\}_n$ (Ln^{III} = Sm (**1**), Eu (**2**), Gd (**3**), Tb (**4**), Dy (**5**), Ho (**6**)) (CO_3^{2-} = carbonate dianion and $C_2O_4^{2-}$ = oxalate dianion) have been synthesized and structurally characterized. All the compounds obtained from *in situ* synthesis of carbonate and oxalate ligand from 2,3-dihydroxyfumaric acid (DHFA) and lanthanide ions (Ln^{III}) at pH ~ 6 under hydrothermal condition. The probable route to the formation of CO_3^{2-} and $C_2O_4^{2-}$ is the decarboxylation of DHFA and consecutive reductive coupling catalyze by the corresponding Ln^{III} ions. Compound **1** and **2** shows characteristics luminescent properties of Tb^{III} and Eu^{III}, however luminescent intensities significantly quenches upon dehydration which has been correlated to the framework dynamics. The temperature dependent magnetic measurements of compound **3** exhibit interesting ferromagnetic behaviour at low temperature.

Based on this work a paper has been communicated

4.1 Introduction

In recent years, the design and synthesis of novel metal-organic frameworks (MOFs) through coordination of metal ions with variety of carboxylic acid containing organic linkers have received great deal of attention. In particular open framework materials with transition metal ions and di/tri carboxylate organic linkers[1] have become new research field due to the conventional applications in gas storage,[2] size selective catalysis,[3] ion exchange, optical properties and even in drug delivery.[4-6] In this perspective, porous solid containing lanthanide ions are of interest due to their flexible coordination number, high thermal stability and unmatched luminescent, magnetic properties.[7-15] We are currently investigating, Ln-organic frameworks with the goal of harnessing porous properties including gas storage and magnetic properties. The small literature of such materials is associated with the structural break down upon removal of the ancillary coordinated solvent molecules, which fulfill the higher coordination number. The effort to combine porosity with other properties like magnetism or optical properties will lead to finding new phenomena and fabricating new functional materials. However, systematic studies of luminescent properties in Ln-organic porous solid with removal of guest and coordinated solvent molecules are in infancy stage.[16-19] Such materials have potential applications in sensing and molecular recognition properties. Furthermore, little attention has been paid on the magnetic properties of lanthanide frameworks, in particular MOFs based on Gd^{III} ions. The recent reported results suggest the possibility of ferromagnetic interactions between Gd^{III}, however the factors govern such interactions and magnitude has not been well understood. Therefore, the design and construction of efficient Ln-organic framework is extremely important and requires more fundamental research. This chapter deals with synthesis and structural characterization of a series of isomorphous Ln-organic frameworks, $\{Ln(CO_3)(C_2O_4)_{0.5}(H_2O)\}_n$ (Ln^{III} = Sm (**1**), Eu (**2**), Gd (**3**), Tb (**4**), Dy (**5**), Ho (**6**)) (CO_3^{2-} = carbonate dianion and $C_2O_4^{2-}$ = oxalate dianion). In all cases, 2D $\{Ln(CO_3)\}$ layer is alternatively pillared by the $C_4O_4^{2-}$ anions , resulting in a 3D framework. To exploit the dynamic solvent dependent luminescent behavior in porous Ln-organic solid we have exploited Tb and Eu-frameworks, which are the most common lanthanide luminophores and exhibits reversible modulation of luminescent properties upon dehydration and rehydration. Furthermore the temperature dependent magnetic susceptibility measurement of **3** (Gd-analogue) revealed that the ferromagnetic interactions operate between the Gd^{III} centres.

4.2 Experimental section

4.2.1 Materials

$Ln(NO_3)_3 \cdot xH_2O$ (Ln^{III} = Sm, Eu, Gd, Tb, Dy, Ho) and 2,3-dihydroxyfumaric acid were obtained from the Aldrich Chemical Co. All other reagents and solvents employed were commercially available and used as supplied without further purification.

4.2.2 Physical measurement

The elemental analyses were carried out using a Perkin Elmer 2400 CHN analyzer. IR spectra of all the compounds were recorded on a Bruker IFS 66v/S spectrophotometer using the KBr pellets in the region 4000-400 cm^{-1}. Thermogravimetric analyses (TGA) were carried out on METTLER TOLEDO TGA850 instrument under nitrogen atmosphere (flow rate of 50 mL/min) at a heating rate of 3 °C/min. The magnetic measurement were carried out on crystalline sample (~15 mg) of 1 with a quantum design MPMS SQUID magnetometer (applied field 5000G) working in the temperature range 2-300 K. Correction for the sample holder was made by previous calibration and diamagnetic corrections were estimated from Pascal's table. [14]

4.2.3 Synthesis of $\{Ln(CO_3)(C_2O_4)_{0.5}(H_2O)\}_n$ [Ln(III) = Sm (1), Eu (2), Gd (3), Tb (4), Dy (5), Ho (6)]

An aqueous solution (5 mL) of $Ln(NO_3)_3 \cdot xH_2O$ (1 mmol) was added to 5 mL aqueous solution containing (1.5 mmol, 0.276 g) 2,3-dihydroxyfumaricacid dihydrate and 3 mmol of KOH (0.168 g) with constant stirring. The mixture was stirred for 1 hour and then reaction mixture was transferred into a 23 mL teflon-lined stainless steel autoclave and heated at 180 °C for 80 hours. Then cooled down to room temperature for 12 hours and light yellow color needle shaped crystalline products were obtained for b. The crystals were washed several times with water and dried in open atmosphere. (Yield: 79 % relative to $La(NO_3)_3$). IR (KBr cm^{-1}): 3453 br (νOH); 3259 m (νOH); 1664 s (ν_{as} OCO); 1388 s (ν_s OCO); 811 w (ν_{bend} OCO). Yield 45%. Anal calc: H, 2.81; C, 44.98; calcd: H 2.95; C, 44.28.

4.2.4 X-ray crystallography

For all the compounds **1-6**, a suitable single-crystal was mounted on a glass fiber and coated with epoxy resin. X-ray data collection was carried out on a Bruker Smart-CCD diffractometer equipped with normal focus , 2.4 kW sealed tube X-ray source with graphite monochromated Mo-K_α radiation (λ = 0.71073 Å) operating at 50 kV and 30 mA, with ω scan mode and a CCD 2D detector. The size of the unit cell was calculated from the reflections collected on the setting angles of seven frames by changing of 0.5° for each frame. Three different settings were used and were changed by 0.5° per frame and intensity data were collected with a scan width of 0.5°. Empirical absorption correction was performed by using SADABS[15]. The structures were solved by direct methods by using the SIR-92 program and expanded by using Fourier techniques. For all cases (**1-6)**, calculations were carried out using SHELXL 97, SHELXS 97, PLATON and WinGX system, Ver 1.70.01. [16-23]. All the non-hydrogen atoms in both cases were refined anisotropically. Final refinement included atomic positions for all the atoms, anisotropic thermal parameters for all the non-hydrogen atoms, isotropic thermal parameters for the hydrogen atoms. All crystallographic and structure refinements parameters for three complexes are summarized in Table 6. Selected bond lengths, angles for **1-6** are given in Table 2-7 respectively.

Parameters	**1**	**2**	**3**	**4**	**5**	**6**
empirical formula	$C_2H_2O_7Sm$	$C_2H_2O_7Eu$	$C_2H_2O_7Gd$	$C_2H_2O_7Tb$	$C_2H_2O_7Dy$	$C_2H_2O_7Ho$
M_r	288.40	289.98	295.27	296.97	300.54	302.97
Crystal system	orthorhombic	orthorhombic	orthorhombic	orthorhombic	orthorhombic	orthorhombic
Space group	*Cmmm*	*Cmmm*	*Cmmm*	*Cmmm*	*Cmmm*	*Cmmm*
a(Å)	7.8737 (2)	7.9266 (2)	7.8990 (4)	7.8704(1)	7.8495 (4)	7.8067 (13)
b(Å)	15.0581 (4)	15.1789(6)	15.1321 (9)	15.0516(2)	15.0115(8)	14.899 (3)
c(Å)	4.7754 (1)	4.8068 (1)	4.7954 (3)	4.7732 (1)	4.7620(3)	4.7356(10)
V(Å)	566.19	578.34(3)	573.19 (6)	565.44 (2)	561.12 (5)	550.81 (19)
Z	4	4	4	4	4	4
T(K)	293	293	293	293	293	293
λ(Mo K_α)	0.71073	0.71073	0.71073	0.71073	0.71073	0.71073
D_c(g/cm^3)	3.196	3.124	3.213	3.489	3.558	3.654
μ(mm$^{-1)}$	10.328	10.802	11.527	12.487	13.296	14.344
Θ_{max}(deg)	27.1	27.5	19.7	31.5	25.6	27.6
F(000)	496	492	496	540	544	548
Tot.data	3788	3742	1504	1935	2502	843
Unique data ,R_{int}	515, 0.027	727, 0.072	174, 0.026	484, 0.025	337, 0.031	346, 0.045
Data[$I>2\sigma(I)$]	510	619	173	479	328	330
R^a	0.0238	0.0382	0.0221	0.0251	0.0257	0.0453
R_w^b	0.0618	0.0697	0.0714	0.0716	0.0723	0.1185
GOF	1.10	1.19	1.29	1.21	1.25	1.16

Table 1. Crystallographic cell and refinement parameters for **1**-**6**.

4.3 Results and discussion

4.3.1 Structural description of $[Ln(CO_3)(C_2O_4)_{0.5}(H_2O)]_n$

All the compounds **1-6** crystallize in orthorhombic *Cmmm* space group and structural determination reveals a 3D coordination framework composed of mixed CO_3^{2-} (carbonate) and $C_2O_4^{2-}$ (oxalate) ligand. All six compounds are isomorphous, therefore only structural description of **4** has been given in details. Asymmetric unit of **4** with atom numbering scheme is shown in Fig. 1a, where each nine coordinated Tb^{III} ions are chelated to one $C_2O_4^{2-}$, two CO_3^{2-} ligands and two oxygen atoms (μ_2-O) from other two CO_3^{2-} and one water molecule (O1w). The carbon atom (C2) and oxygen atom (O3) of the carbonate anions are in symmetry related disorder state. The Tb-O bond distances are in the range of 2.399(3) – 2.4563(14) Å. Each CO_3^{2-} dianion functions as a tetradentate ligand and chelates to two Tb^{III} ions through (O2, O3 and O2_f, O3) and connect another two Tb^{III} ions through oxo-bridge (μ_2-O2 and μ_2-O2_f) (f = 1-x, -y, z), forming a $[Tb(CO_3)]_n^+$ 2D corrugated sheet in the crystallographic *ac* plane (Fig. 1b).

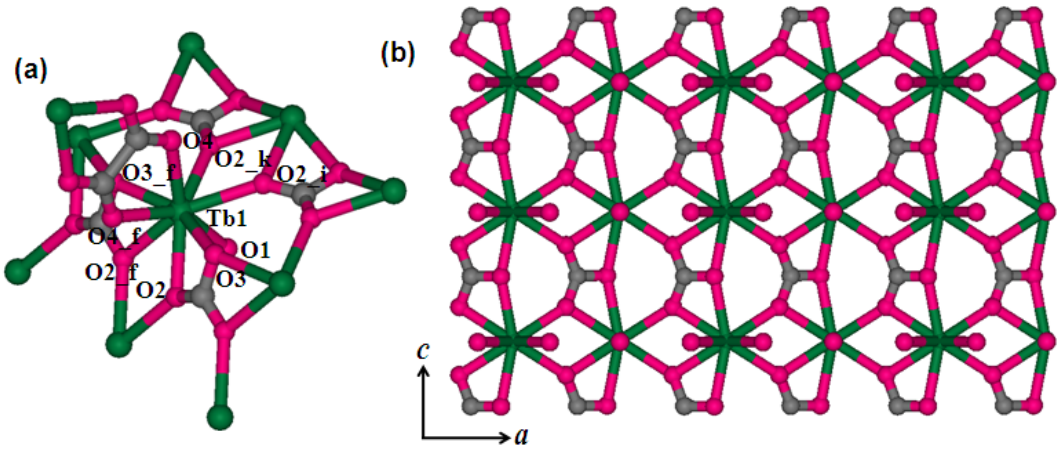

Figure 1. (a) view of the coordination environment of Tb^{III} in compound **1**; (b) View of the $\{Tb(CO_3)\}^+$ 2D sheet formed by carbonate bridging, lying in the *ac* plane.

2D sheets are connected by the $C_2O_4^{2-}$ anions forming a 3D coordination framework with 1D channel along the crystallographic *a*-axis (Fig. 2). The channel is occupied with the two coordinated water molecules (O1w) in face to face to each other. The two water molecules cannot completely occupy the void space in the framework and the remaining square shaped channel dimension is about 2.3 × 2.3 $Å^2$ (Fig. 3a) and after removal of the coordinated water molecules the channel dimension increases to 4.5 × 4.5 $Å^2$ (Fig. 3b). The void space

calculated from the PLATON is about 14.4% to the crystal volume and it has been increased to of 22.1 % after removal the coordinated water molecules. The Tb …Tb separation along the $C_2O_4^{2-}$ bridge is about 6.240 Å. Along the bridging CO_3^{2-} Tb…Tb separations are 4.140 and 4.773 Å for μ_2- O2 and μ_2-O3, respectively. There are several intra-framework H-bonding interactions which provide the extra stability to the 3D framework. All the compounds are isostructural and has similar bond length, bond angles. Selected bond length, bond angles of frameworks **1-6** are given in the Table 2- 7, respectively.

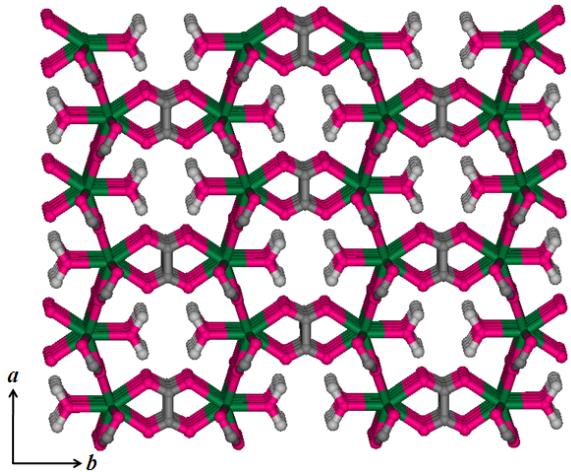

Figure 2. View of the 3D framework of **1** formed by pillaring 2D $\{Tb(CO_3)\}^+$ sheet by oxalate linker.

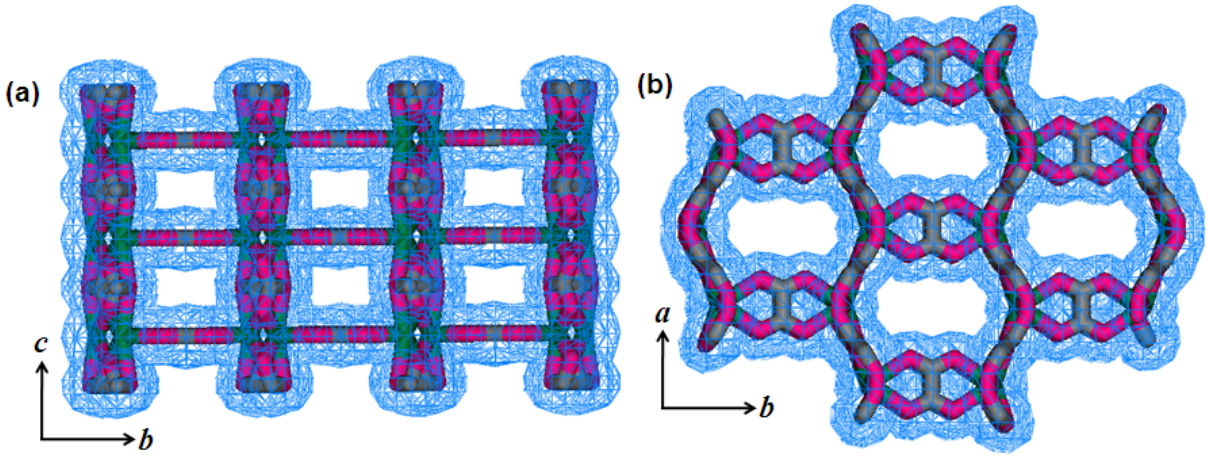

Figure 3. View of the open framework structure of **4** after removal of the metal bound water molecules (a) along the crystallographic *a*-axis; (b) along the crystallographic *c*-axis.

Table 2. Selected bond length (Å) and bond angles (º) for compound **1.**

Sm1 -O1	2.359(8)	Sm1 -O2	2.4190(17)
Sm1-O3	2.423(2)	Sm1-O4	2.402(5)
Sm1-O2_b	2.4190(17)	Sm1-O3_f	2.423(2)
Sm1-O4_f	2.402(5)	Sm1-O3_j	2.423(2)
Sm1-O3_m	2.423(2)		
O1-Sm1-O2	99.2(2)	O3-Sm1-O4_f	132.22(9)
O1-Sm1-O3	74.60(2)	O1-Sm1-O4	146.29(11)
O3-Sm1-O3_j	62.51(12)	O3-Sm1-O3_m	108.69(10)
O1-Sm1-O2_b	99.2(2)	O1-Sm1-O3_f	74.60(2)
O1-Sm1-O4_f	146.29(11)	O2_b-Sm1-O4	82.3(2)
O3_f-Sm1-O4	132.22(9)	O4-Sm1-O4_f	67.43(16)
O1-Sm1-O3_j	74.60(2)	O1-Sm1-O3_m	74.60(2)
O2-Sm1-O3	123.69(10)	O3_j-Sm1-O4	76.70(9)
O2-Sm1-O4	82.3(2)	O3_m-Sm1-O4	132.22(9)
O2-Sm1-O2_b	161.5(3)	O2-Sm1-O3_f	62.00(13)
O2-Sm1-O4_f	82.3(2)	O2-Sm1-O3_j	62.00(13)
O2-Sm1-O3_m	123.69(10)	O3-Sm1-O4	76.70(9)
O2_b-Sm1-O3	62.00(13)	O3-Sm1-O3_f	149.19(2)
O2_b-Sm1-O3_f	123.69(10)	O2_b-Sm1-O4_f	82.3(2)
O2_b-Sm1-O3_j	123.69(10)	O2_b-Sm1-	62.00(13)
O3_f-Sm1-O4_f	76.70(10)	O3_f-Sm1-O3_j	108.69(10)
O3_f-Sm1-O3_m	62.51(12)	O3_j-Sm1-O4_f	132.22(9)
O3_m-Sm1-O4_f	76.70(10)	O3_j-Sm1-O3_m	149.19(2)

Symmetry code: b =x,y,1+z, f=-x,y,1-z, j= x,y,-z, m = -x,y,z

Table 3. Selected bond length (Å) and bond angles (º) for compound **2.**

Eu1-O1	2.396(12)	Eu1-O2_g	2.45(3)
Eu1-O2	2.45(3)	Eu1-O2_i	2.45(3)
Eu1-O3	2.474(3)	Eu1-O4	2.46(4)
Eu1-O5	2.39(4)	Eu1-O3_a	2.474(3)
Eu1-O2_d	2.45(3)		
O1-Eu1-O2	76.6(16)	O1-Eu1-O3	99.1(4)
O3_a-Eu1-O4	76.7(3)	O1-Eu1-O4	146.1(19)
O1-Eu1-O5	147.1(19)	O2_d-Eu1-O4	74.6(10)
O2_g-Eu1-O4	133.8(9)	O1-Eu1-O3_a	99.1(4)
O2_i-Eu1-O4	133.8(9)	O1-Eu1-O2_d	76.6(16)
O3_a-Eu1-O5	87.8(3)	O1-Eu1-O2_g	72.7(16)
O1-Eu1-O2_i	72.7(16)	O2_d-Eu1-O5	129.8(9)
O2-Eu1-O3	52.0(5)	O2_g-Eu1-O5	79.4(10)
O2-Eu1-O4	74.6(10)	O2_i-Eu1-O5	79.4(10)
O2-Eu1-O5	129.8(9)	O2-Eu1-O3_a	113.6(5)
O2-Eu1-O2_d	63.1(6)	O2-Eu1-O2_g	149.3(10)
O2-Eu1-O2_i	108.2(7)	O2_d-Eu1-O3_a	52.0(5)
O3-Eu1-O4	76.7(3)	O2_g-Eu1-O3_a	71.2(5)

O3-Eu1-O5	87.8(3)	O2_i-Eu1-O3_a	134.2(5)
O3-Eu1-O3_a	152.6(4)	O2_d-Eu1-O3	113.6(5)
O2_d-Eu1-O2_g	108.2(7)	O2_g-Eu1-O3	134.2(5)
O2_d-Eu1-O2_i	149.3(10)	O2_i-Eu1-O3	71.2(5)
O2_g-Eu1-O2_i	63.2(6)	O4-Eu1-O5	66.8(12)

Symmetry code: a = x,y,-1+z, d = x,y,2-z, g = -1/2+x,1/2-y,2-z, i= -1/2+x,1/2-y,z

Table 4. Selected bond length (Å) and bond angles (º) for compound **3.**

Gd1-O1	2.412(14)	Gd1-O3_k	2.435(4)
Gd1-O2	2.433(3)	Gd1-O3	2.435(4)
Gd1-O4	2.412(7)	Gd1-O2_b	2.433(3)
Gd1-O3_f	2.435(4)	Gd1-O4_f	2.412(7)
Gd1-O3_i	2.435(4)		
O1-Gd1-O2	99.8(4)	O2_b-Gd1-O3_i	62.1(2)
O1-Gd1-O3	74.55(3)	O2_b-Gd1-O3_k	123.96(16)
O1-Gd1-O4	146.31(17)	O3_f-Gd1-O4_f	132.19(15)
O1-Gd1-O2_b	99.8(4)	O3_f-Gd1-O3_i	108.38(17)
O1-Gd1-O3_f	74.55(3)	O3_f-Gd1-O3_k	62.8(2)
O1-Gd1-O4_f	146.31(17)	O3_i-Gd1-O4_f	76.81(15)
O1-Gd1-O3_i	74.55(3)	O3_k-Gd1-O4_f	132.19(15)
O1-Gd1-O3_k	74.55(3)	O3_i-Gd1-O3_k	149.09(5)
O2-Gd1-O3	62.1(2)	O2-Gd1-O4	81.9(3)
O2-Gd1-O2_b	160.4(5)	O2-Gd1-O3_f	123.96(16)
O2-Gd1-O4_f	81.9(3)	O2-Gd1-O3_i	123.96(16)
O2-Gd-O3_k	62.1(2)	O3-Gd1-O4	132.19(15)
O2_b-Gd1-O3	123.96(16)	O3-Gd1-O3_f	149.09(5)
O3-Gd1-O4_f	76.81(15)	O3-Gd1-O3_i	62.8(2)
O3-Gd1-O3_k	108.38(17)	O2_b-Gd1-O4	81.9(3)
O3_f-Gd1-O4	76.81(15	O4-Gd1-O4_f	67.4(2)
O3_i-Gd1-O4	132.19(15)	O3_k-Gd1-O4	76.81(15)
O2_b-Gd1-O3_f	62.1(2)	O2_b-Gd1-O4_f	81.9(3)

Symmetry code: b = x,y,1+z, f = -x,y,1-z, i = x,y,1-z, k = -x,y,z

Table 2. Selected bond length (Ǻ) and bond angles(º) for compound **4.**

Tb1-O1	2.371(11)	Tb1-O2_k	2.420(2)
Tb1-O2	2.420(2)	Tb1-O3	2.452(2)
Tb1-O4	2.401(6)	Tb1-O3_b	2.452(2
Tb1-O3_e	2.452(2)	Tb1-O2_f	2.420(2)
Tb1-O3_f	2.452(2)	Tb1-O4_f	2.401(6)
Tb1-O2_i	2.420(2)		
O1-Tb1-O2	74.59(2)	O3_e-Tb1-O4	77.5(3)
O1-Tb1-O3	98.0(3)	O2_f-Tb1-O4	76.79(10)
O1-Tb1-O4	146.41(12)	O3_f-Tb1-O4	77.5(3)

O1-Tb1-O3_b	98.0(3)	O4-Tb1-O4_f	67.19(17)
O1-Tb1-O3_e	98.0(3)	O2_i-Tb1-O4	132.16(10)
O1-Tb1-O2_f	74.59(2)	O2_k-Tb1-O4	76.79(10)
O1-Tb1-O3_f	98.0(3)	O3_b-Tb1-O3_e	164.0(4)
O1-Tb1-O4_f	146.41(12)	O2_f-Tb1-O3_b	71.4(2)
O1-Tb1-O2_i	74.59(2)	O3_b-Tb1-O3_f	21.1(3)
O1-Tb1-O2_k	74.59(2)	O3_b-Tb1-O4_f	77.5(3)
O2-Tb1-O3	52.0(2)	O2_i-Tb1-O3_b	52.0(2)
O2-Tb1-O4	132.16(10)	O2_k-Tb1-O3_b	133.6(2)
O2-Tb1-O3_b	113.1(2)	O2_f-Tb1-O3_e	113.1(2)
O2-Tb1-O3_e	71.4(2)	O3_e-Tb1-O3_f	153.4(3)
O2-Tb1-O2_f	149.19(3)	O3_e-Tb1-O4_f	89.2(3)
O2-Tb1-O3_f	133.6(2)	O2_i-Tb1-O3_e	33.6(2)
O2-Tb1-O4_f	76.79(11)	O2_k-Tb1-O3_e	52.0(2)
O2-Tb1-O2_i	62.41(14)	O2_f-Tb1-O3_f	52.0(2)
O2-Tb1-O2_k	108.78(12)	O2_f-Tb1-O4_f	132.16(10)
O3-Tb1-O4	89.2(3)	O2_f-Tb1-O2_i	108.78(12)
O3-Tb1-O3_b	153.4(3)	O2_f-Tb1-O2_k	62.41(14)
O3-Tb1 -O3_e	21.1(3)	O3_f-Tb1-O4_f	89.2(3)
O2_f-Tb1-O3	133.6(2)	O2_i-Tb1-O3_f	71.4(2)
O3-Tb1-O3_f	164.0(4)	O2_k-Tb1-O3_f	113.1(2)
O3-Tb1-O4_f	77.5(3)	O2_i-Tb1-O4_f	76.79(11)
O2_i-Tb1-O3	113.1(2)	O2_k-Tb1-O4_f	132.16(10)
O2_k-Tb1-O3	71.4(2)	O2_i-Tb1-O2_k	149.19(3)
O3_b-Tb1-O4	89.2(3)		

Symmetryb = x, y, 1+z, e = 1-x, y, -z, f = 1-x, y, 1-z, k = 1-x, y, z

Table 6. Selected bond length (Å) and bond angles (º) of compound **5.**

Dy1-O1	2.344(12)	Dy1-O2_k	2.412(3)
Dy1-O2	2.412(3)	Dy1-O3	2.452(3)
Dy1-O4	2.393(6)	Dy1-O3_a	2.452(3)
Dy1-O2_e	2.412(3)	Dy1-O3_e	2.452(3)
Dy1-O4_e	2.393(6)	Dy1-O3_f	2.452(3)
Dy1-O2_h	2.412(3)		
O1-Dy1-O2	74.57(2)	O2_e-Dy1-O4	132.32(13)
O1-Dy1-O3	98.3(3)	O3_e-Dy1-O4	89.2(3)
O1-Dy1-O4	146.24(15)	O4-Dy1-O4_e	67.5(2)
O1-Dy1-O3_a	98.3(3)	O3_f-Dy1-O4	89.2(3)
O1-Dy1-O2_e	74.57(2)	O2_h-Dy1-O4	76.66(13)
O1-Dy1-O3_e	98.3(3)	O2_k-Dy1-O4	132.32(13)
O1-Dy1-O4_e	146.24(15)	O2_e-Dy1-O3_a	72.0(3)
O1-Dy1-O3_f	98.3(3)	O3_a-Dy1-O3_e	21.9(4)
O1-Dy1-O2_h	74.57(2)	O3_a-Dy1-O4_e	89.2(3)
O1-Dy1-O2_k	74.57(2)	O3_a-Dy1-O3_f	163.5(5)
O2-Dy1-O3	51.8(3)	O2_h-Dy1-O3_a	51.8(3)
O2-Dy1-O4	76.66(13)	O2_k-Dy1-O3_a	134.0(3)
O2-Dy1 -O3_a	112.7(3)	O2_e-Dy1-O3_e	51.8(3)
O2-Dy1-O2_e	149.13(4)	O2_e-Dy1-O4_e	76.66(13)

O2-Dy1-O3_e	134.0(3)	O2_e-Dy1-O3_f	112.7(3)
O2-Dy1-O4_e	132.32(13)	O2_e-Dy1-O2_h	108.89(15)
O2-Dy1-O3_f	72.0(3)	O2_e-Dy1-O2_k	62.27(18)
O2-Dy1-O2_h	62.27(18)	O3_e-Dy1-O4_e	77.0(3)
O2-Dy1-O2_k	108.89(15)	O3_e-Dy1-O3_f	152.5(4)
O3-Dy1-O4	77.0(3)	O2_h-Dy1-O3_e	72.0(3)
O3-Dy1-O3_a	152.5(4)	O2_k-Dy1-O3_e	112.7(3)
O2_e-Dy1-O3	134.0(3)	O3_f-Dy1-O4_e	77.0(3)
O3-Dy1-O3_e	163.5(5)	O2_h-Dy1-O4_e	132.32(13)
O3-Dy1-O4_e	89.2(3)	O2_k-Dy1-O4_e	76.66(13)
O3-Dy1-O3_f	21.9(4)	O2_h-Dy1-O3_f	134.0(3)
O2_h-Dy1-O3	112.7(3)	O2_k-Dy1-O3_f	51.8(3)
O2_k-Dy1-O3	72.0(3)	O2_h-Dy1-O2_k	149.13(4)
O3_a-Dy1-O4	77.0(3)		

Symmetry code: a = x, y, -1+z, e =-x, y, -z, f = -x, y, 1-z, h = x, y, -z, k = -x, y, z

Table 7. Selected bond length (Å) and bond angles (º) of compound **6.**

Ho1-O1	2.33(2)	Ho1-O2_k	2.404(7)
Ho1-O2	2.404(7)	Ho1-O3	2.436(6)
Ho1-O4	2.374(13)	Ho1-O3_a	2.436(6)
Ho1-O2_e	2.404(7)	Ho1-O3_e	2.436(6)
Ho1-O4_e	2.374(13)	Ho1-O3_f	2.436(6)
Ho1-O2_h	2.404(7	O1-Ho1-O2	74.62(5)
O2_e-Ho1-O4	132.2(3)	O1-Ho1-O3	98.5(7)
O3_e-Ho1-O4	88.8(7)	O1-Ho1-O4	146.3(3)
O4-Ho1-O4_e	67.5(4)	O1-Ho1-O3_a	98.5(7)
O3_f-Ho1-O4	88.8(7)	O1-Ho1-O2_e	74.62(5)
O2_h-Ho1-O4	76.7(3)	O1-Ho1-O3_e	98.5(7)
O2_k-Ho1-O4	132.2(3)	O1-Ho1-O4_e	146.3(3)
O2_e-Ho1-O3_a	71.5(6)	O1-Ho1-O3_f	98.5(7)
O3_a-Ho1-O3_e	21.1(8)	O1-Ho1-O2_h	74.62(5)
O3_a-Ho1-O4_e	88.8(7)	O1-Ho1-O2_k	74.62(5)
O3_a-Ho1-O3_f	163.0(10)	O2_h-Ho1-O3_a	52.1(6)
O2-Ho1-O3	52.1(6)	O2-Ho1-O4	76.7(3)
O2_k-Ho1-O3_a	133.9(6)	O2-Ho1-O3_a	113.4(6)
O2_e-Ho1-O3_e	52.1(6)	O2-Ho1-O2_e	149.24(8)
O2_e-Ho1-O4_e	76.7(3)	O2-Ho1-O3_e	133.9(6)
O2_e-Ho1-O3_f	113.4(6)	O2-Ho1-O4_e	132.2(3)
O2_e-Ho1-O2_h	108.6(3)	O2_h-Ho1-O2_k	149.24(8)
O2-Ho1-O3_f	71.5(6)	O2_e-Ho1-O2_k	62.7(4)
O2-Ho1-O2_h	62.7(4)	O3_e-Ho1-O4_e	77.0(6)
O2-Ho1-O2_k	108.6(3)	O3_e-Ho1-O3_f	152.8(8)
O3-Ho1-O4	77.0(6)	O2_h-Ho1-O3_e	71.5(6)
O3-Ho1-O3_a	152.8(8)	O2_k-Ho1-O3_e	113.4(6)
O2_e-Ho1-O3	133.9(6)	O3_f-Ho1-O4_e	77.0(6)
O3-Ho1-O3_e	163.0(10)	O2_h-Ho1-O4_e	132.2(3)
O3-Ho1-O4_e	88.8(7)	O2_k-Ho1-O4_e	76.7(3)
O3-Ho1-O3_f	21.1(8)	O2_h-Ho1-O3_f	133.9(6)
O2_-Ho1-O3	113.4(6)	O2_k-Ho1-O3_f	52.1(6)

O2_k -Ho1 -O3	71.5(6)	O3_a-Ho1-O4	77.0(6)

Symmetry code: a = x, y, -1+z, e =-x, y, -z, f = -x, y, 1-z, h = x, y, -z, k = -x, y, z

4.3.2 DHFA as a precursor of oxalate and carbonate linker in 1-6

All the frameworks composed of the Ox^{2-} and CO_3^{2-} ligand, which has never been added to the reaction mixture. Hong *et. al*. reported in situ oxalate ligand synthesis from the hydrothermal reaction of orotic acid, $Sm(NO_3)_3$ and $2CoCO_3.3Co(OH)_2$. They proposed that ox^{2-} ligand was in situ synthesized from oxidation-hydrolysis reaction of orotic acid catalysed by the Sm^{III} ions. They suggested hydrolysis reaction at around C-N bond and oxidation around C=C double bond, although the complete reaction mechanism remains unclear. Later on, Lee *et .al*. and Wang *et. al.* have described synthesis and structures of lanthanide-oxalate coordination polymers with reaction of pyridinedicarboxylate and Ln^{III} ions (Ln = Tb, Eu, Sm, Ho, or Dy). Lee *et. al*. have studied the mechanism of formation of oxalate dianion with the help of GC-MS study and they have concluded that pyridinedicarboxylic acids ($pydcH_2$) can only produce oxalic acids through decarboxylation. Here, in these systems probably similar reaction pathways are following, *i.e*., decarboxylation from the DHFA followed by Ln^{III} ions mediated reductive coupling to the formation of ox^{2-} and CO_3^{2-} dianions, which resulting in situ formation of 3D lanthanide frameworks.

4.3.3 Purity, thermal stability and PXRD patterns

Thermogravimetric analyses (TGA) of all the compound exhibits similar profile. The TGA profile for compound **1** is shown in Figure. 4. The compound does not exhibit any weight loss up to 250˚C. There is a 5.95 % weight loss in the temperature range 250-300 ˚C corresponding to one water molecule per formula unit of **1** (Calcd : 6.01%). The dehydrated framework (**1′**) is stable upto 370˚C without further weight loss. Upon further heating framework decomposed into some unidentified products. In all the cases coordinated water molecules are removed at 300˚C

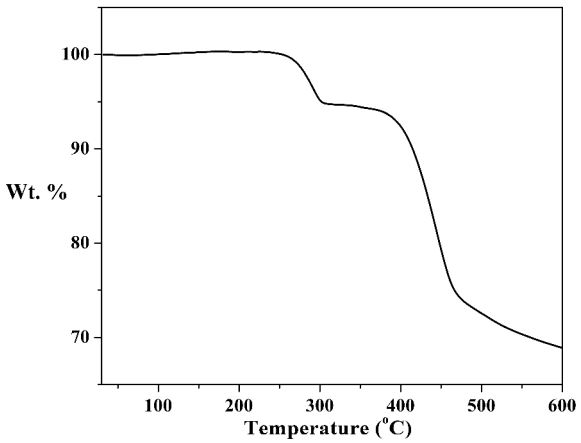

Figure 5. Thermogravimetric analysis of **1** in the temperature range of 27 -600 °C under nitrogen atmosphere with heating rate of 3°C per minute.

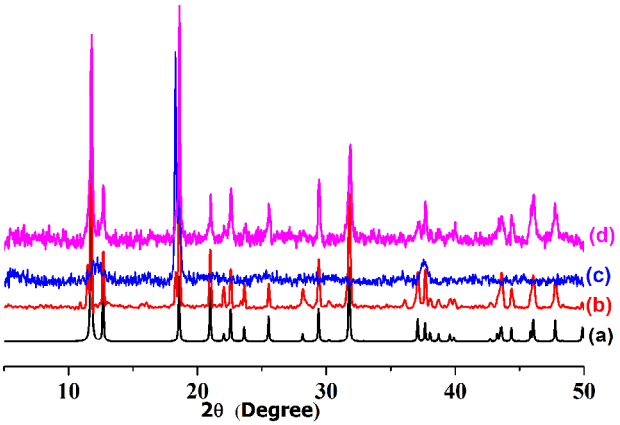

Figure 6. PXRD pattern of compound **1** in different state; (a) simulated; (b) as-synthesized; (c) dehydrated; (d) rehydrated.

As-synthesized compound **1-6** exhibits similar PXRD pattern as of simulated pattern of the structure obtained from single-crystal data suggesting the compound are pure (Figure 6a and 6b). After heating at 290˚C under vacuum the PXRD pattern changes with disappearance of many Bragg's peaks observed in the as-synthesized compound suggesting structural change after removal of the metal coordinated water molecules (Figure 6c). The framework is reversible with respect to the dehydration and rehydration but it requires addition of water drop into the dehydrated compound rather than exposed to water vapour.

4.3.4 Photoluminescence properties of compound 2 and 4

Tb^{III} and Eu^{III} has interesting emission properties. The Laporte rule permits the transition between opposite parity that implies the transition in the single quantum well (e.g f-f transition) is forbidden. Again the spin multiplicity rule forbids the transition between two

state of different multiplicity. As the optical f-f electronic transition in Eu^{III} and Tb^{III} associated with transition from quintet state to septet state are forbidden and named as luminescence rather than fluorescence. Due to the intra configurational f-f electronic transition the extinction coefficient of lanthanides are very weak and direct excitation of Tb^{III} or Eu^{III} do not exhibit any emission. The problem of inefficient absorption can be overcome by indirect excitation of lanthanide via it's coordinated ligand which can act as an 'antenna' molecule. In these compound oxalate and carbonate can act as an antenna, absorb UV light followed by energy transfer to lanthanides emitting state and emission of lanthanide can be observed. Solid state photo luminescent properties of **2** and **4** were investigated. , compound **2** exhibits its characteristics red emission properties when excited at 265 nm. (Figure 6) with emissions corresponds to $^5D_0 \rightarrow ^7F_J$ (J = 0 - 4) transitions of Eu^{III} . The strongest emission is of the $^5D_0 \rightarrow ^7F_2$ transition at 616 nm, followed by $^5D_0 \rightarrow ^7F_1$ at 592 nm. Similarly Compound **4** composed of Tb^{III} emitted green light when excited by ultraviolet light (λ_{ex} = 265 nm). The emission spectrum of **4** was observed in the range of 450 – 700 nm and exhibits four characteristics peaks of Tb^{III} (Figure 7). These peaks are assigned to the $^5D_4 \rightarrow ^7F_J$ (J = 3 - 6) transitions, namely $^5D_4 \rightarrow ^7F_6$ (489 nm) $^5D_4 \rightarrow ^7F_5$ (545 nm) $^5D_4 \rightarrow ^7F_4$ (589 nm) $^5D_4 \rightarrow ^7F_3$(621 nm).

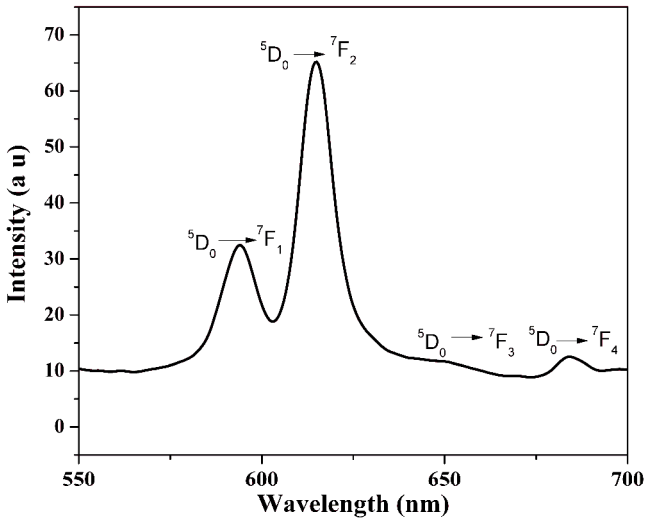

Figure 6. Emission spectrum of $[Eu(CO_3)(C_2O_4)_{0.5}(H_2O)]_n$ (**2**)

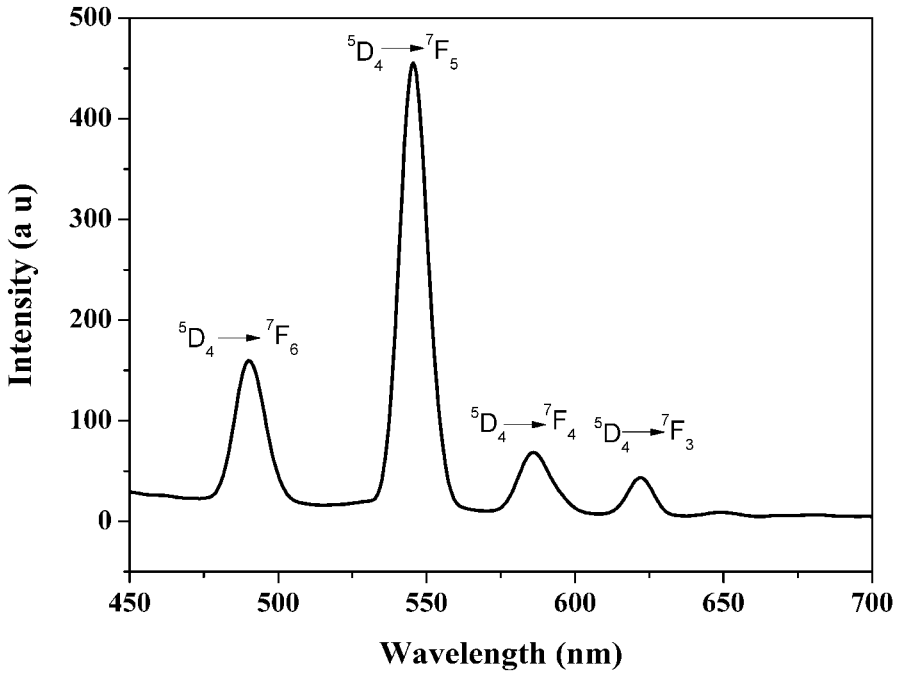

Figure 7. Emission spectrum of $[Tb(CO_3)(C_2O_4)_{0.5}(H_2O)]_n$ (**4**)

4.3.5 Magnetic property of $Gd(CO_3)(C_2O_4)_{0.5}(H_2O)]_n$ (3)

Temperature dependence of molar magnetic susceptibility (χ_M) and $\chi_M T$ product shows a very clear signature of weak but significant ferromagnetic interaction among the gadolinium centers, where χ_M refers to magnetic susceptibility per Gd^{III} center. At room temperature χ_M T (Figure 8) is 7.88 emu K mol^{-1} a value which is expected for a magnetically isolated Gd^{III} atom (S= 7/2) with g = 2.0. This value remains practically constant up to 175 K after that it gradually increases up to 8.19 emu K mol^{-1} at 50K and further it sharply increases up to 10.48 emu K mol^{-1} at 2.62 K. In the χ_M vs T plot there is also the similar behavior like $\chi_M T$ vs T. The χ_M value almost remains constant up to 50 K and further it increases up to 4.0 emu K mol^{-1}.

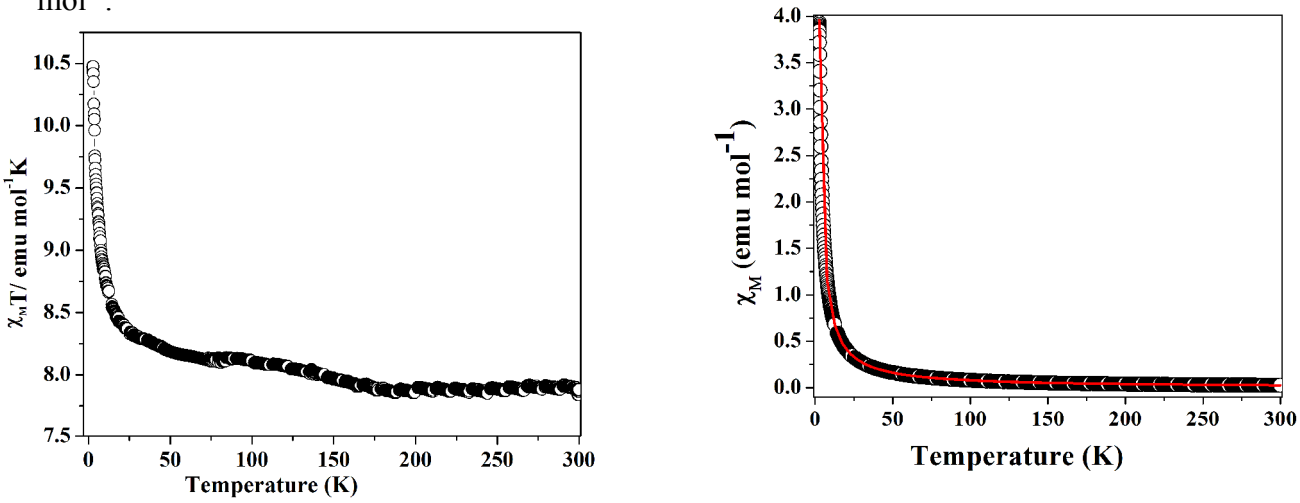

Figure 8. $\chi_M T$ and χ_M vs T for $[Gd(CO_3)(C_2O_4)_{0.5}(H_2O)]_n$ (**3**).

The $1/\chi_M$ vs T plot (Figure 9) shows that experimental data is fitting well with Currie-Weiss equation, with Weiss constant $\theta = 2.49$ K. The positive value of θ is supporting the signature of ferromagnetic interaction. The curries constant C= 7.813 emu K mol^{-1} which is quite closer to the other reported Gd^{III} complexes.

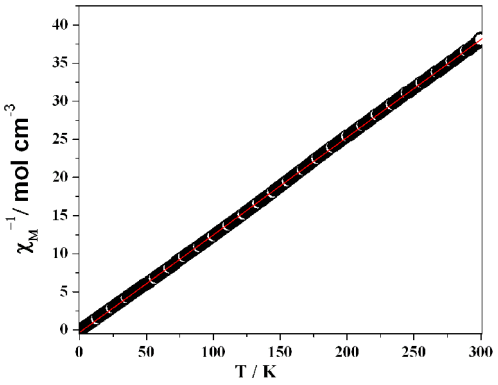

Figure 9. Currie-weiss plot (χ_m^{-1} Vs T) of the gadolinium MOF.

There are two different magnetic exchange pathways possible for this compound; one is oxo bridged and another one is oxalato bridged. Shorter gadolinium (4.16 Å) distance through oxo bridge has higher efficiency towards magnetic exchange compared to oxalate bridged with Gd^{III} …Gd^{III} diustance is about 7.27Å (Figure 10)

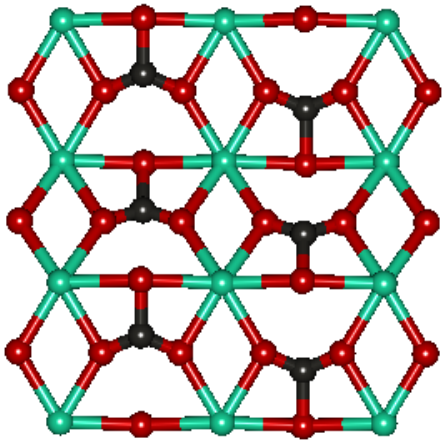

Figure 10. Oxo-bridging in 2D sheet of gadolinium-oxalate-carbonate framework the most effective way of magnetic interaction.

This large distance motivates us to discard the second type of interaction. Consequently we analyze this χ_M vs T plot (figure: 2) by the equation given below using dimmer law

(reference) for the Heisenberg model deduced from the isotropic spin Hamiltonian $\hat{H}= -2J_{ex} S_1S_2$ ($S_1=S_2=7/2$).

$$\chi_M = \frac{N_A\mu_B^2g^2}{K_BT}\left[\frac{e^{2x} + 5e^{6x} + 14\,e^{12x} + 30\,e^{20x} + 55\,e^{30x} + 91\,e^{42x} + 140\,e^{56x}}{1+3\,e^{2x} + 5\,e^{6x} + 7\,e^{12x} + 9\,e^{20x} + 11\,e^{30x} + 13e^{42x} + 15e^{56x}}\right]$$

Where N_A is the Avogadro's number, μ_B is the Bohr's magneton, g is the Lande's factor, k_B is the Boltzman's constant, T is the absolute temperature, J is magnetic exchange parameter. The best least square fittings suggest the parameter J = +0.066 cm^{-1}, g = 2.00. The ferro magnetic interaction is due to the super exchange type of interaction through oxygen bridge among Gd^{III} ions.

4.4 Summary

We have synthesized six different lanthanide-oxalate-carbonate framework using DHFA as a precursor and structurally characterized by x-ray diffraction of the single-crystals. All the frameworks are iso-structural and exhibit high thermal stability. The luminescent property of europium (**2**) and terbium (**4)** and magnetic property of gadolinium (**3)** frameworks were investigated in details. Compound 2 exhibit's characteristic emission peaks of Eu^{III} and appeared red under UV light due to the strongest emission at 615 nm. Compound 4 exhibits characteristic emission peaks of Tb^{III} and appeared green under UV light due to the strongest emission at 545 nm. In both the frameworks carbonate and oxalate plays the role of antenna and exhibit the strong efficiency in the emission property. Compound **3** exhibits ferromagnetic interaction because of super exchange interaction via oxo bridging.

4.5 References

1. J.An, O. K.Farha, J. T. Hupp, E. Pohl, J. I. Yeh, and N. L. Rosi, *Nat. Commun*., 2012, **3**, 604.
2. A. U. Czaja, N. Trukhan and U. Muller, *Chem. Soc. Rev.,*2009**, 38**, 1284.
3. S. Kitagawa, R. Kitaura and S.-i. Noro, *Angew. Chem. Int., Ed.,* 2004**, 43**, 2334.
4. M. D. Allendorf, C. A. Bauer, R. K. Bhakta and R. J. T. Houk, *Chem. Soc. Rev.,* 2009**, 38**, 1330; (e) Y. Cui, Y. Yue, G. Qian and B., Chen, *Chem. Rev*.,2012,**112**, 1126.

5. M.Kurmoo, *Chem. Soc. Rev.* 2009**, 38**, 1353. (g) M. P. Suh, H. J. Park, T. K. Prasad and D.-W. Lim, *Chem. Rev*.,2012, 112, 782.

6. A. Hazra, P. Kanoo and T. K. Maji, *Chem. Commun.* 2011*,* **47**, 538.

7. S. Mohapatra, K. P. S. S. Hembram, U. Waghmare and T. K., Maji, *Chem. Mater.,* 2009, **21**, 5406.

8. D. J. Lun, G. I. N.; Waterhouse and S. G. Telfer, *J. Am. Chem.Soc.,* 2011*,* **133**, 5806.

9. L. E. Kreno, K. Leong, O. K. Farha, M. Allendorf, R. P. Van Duyne and J. T. Hupp, *Chemical Rev.*,2012, **112**, 1105.

10. M. P. Suh, H. J. Park, T. K. Prasad and d. W. Lim, *Chem. Rev.,* 2012,**112**, 782.

11. J. S. Seo, D. Whang, H. Lee, S. I. Jun, J. Oh, Y. J. Jeon, and K. Kim, *Nature*, 2000, **404**, 982.

12. R. J. Kuppler, D. J. Timmons, Q. R. Fang, J. R. Li, T. A. Makal, M. D. Young, D. Yuan, D. Zhao, W. Zhuang and H. C. Zhou, *Coord. Chem. Rev.,* 2009, **253**, 3042.

13. J. Y. Lee, O. K. Farha, J. Roberts, K. A. Scheidt, S. T. Nguyen and J. T. Hupp *Chem. Soc. Rev.,*2009, **38**, 1450.

14. P. Horcajada, R. Gref, T. Baati, P. K. Allan, G. Maurin, P. Cauvreur, G. Ferey, R. E. Morris and C. Serre, *Chem. Rev.*, 2012, **112**, 1232.

15. B.-Q Ma, S. Gao, G. Su, G.-X. Xu, *Angew. Chem. Int. Ed.* 2001, **40,** 434.

16. C. Benneli, D. Gatteschi, *Chem. Rev.,* 2002,**102**, 2369.

17. S. Sivakumar, M. L. P. Reddy, A. H. Cowley and R. R. Butorac, *Inorg. Chem.,* 2011**, 50**, 4882.

18. P. Lama and P. K. Bharadwaj, *Cryst. Growth Des.,*2011, **11**, 5434.

19. K. L. Gurunatha, S. Mohapatra, P. A. Suchetan and T. K. Maji, *Cryst. Growth Des.,*2009*,* **9***,* 3844.

20. J. –C. G. Bünzli, C. Piguet, *Chem. Rev.*, 2002, **102**,1897.

21. A. L. Spek, PLATON, *Molecular Geometry Program, University of Utrecht*, Netherlands, 1999.

22. G. M. Sheldrick, *SADABS, Empirical Absorption Correction Program*, University of Göttingen, Göttingen, Germany, 1997.

23. V.A. Balatov, A. P. Shevchenko, TOPOS, *Program Package for multipurpose crystallochemical analysis*, *Samara state University*, Russia, 1989-2008.

24. Crysfire 2004, *Interactive powder indexing support system*.

25. *SAINT*, 6.02 ed., Bruker AXS, Madison, WI, 1999**.**

26. A. Altomare, G. Cascarano, C. Giacovazzo, A. Gualaradi, *J. Appl. Crystallogr.* 1993, **26**, 343.

27. G. M. Sheldrick, *SHELXL 97*, Program for the Solution of Crystal Structure, University of Göttingen, Germany, 1997.

28. G. M. Sheldrick, *SHELXS 97*, Program for the Solution of Crystal Structure, University of Göttingen, Germany, 1997.

29. Spek, A. L. *J. Appl. Crystallogr.* 2003, **36**, 7.

30. WinGX, A Windows Program for Crystal Structure Analysis: Farrugia, L. J. *J. Appl. Crystallogr.* 1999, **32**, 837.

Chapter 5: Immobilization of Alkali Metal Ions in a 3D Lanthanide-Organic Framework: Hydrogen Storage Characteristics

Abstract

A lanthanide-alkali (Ho^{III}-K^I) bimetallic α-Po type 3D framework $\{KHo(C_2O_4)_2(H_2O)_4\}_n$ (**1**) ($C_2O_4^{2-}$ = oxalate dianion) has been synthesized and structurally characterized. The dehydrated framework, **1′** after removal of the K-bound water molecules found to exhibit permanent porosity with a clear size selective vapor sorption properties and H_2 storage capability. High heat of H_2 sorption (~ -10 kJ/mole) observed in experiment is shown to arise from the preferential interaction of H_2 with unsaturated K^I sites decorated on the pore surfaces, using first-principles density functional theory-based calculations of energetic as well as the detailed structure. Our work shows that a material with better hydrogen storage and release properties can be developed through immobilization of unsaturated reactive alkali metal ions at the pore-surfaces in a metal-organic framework.

A paper related to this chapter has been published, S. Mohapatra, K.P. S. S. Hembram, U. V Wghmare and T. K Maji, ***Chem Mater***., 2009, **21**, 5406.

5.1 Introduction

Recent years, the synthesis and characterization of porous coordination polymers (PCPs) or metal-organic frameworks (MOFs) based on d-block metal ions and versatile organic linkers attracted considerable interest due to its applications in gas storage,[1] selective separation,[2] ion exchange,[3] catalysis,[4] and in molecular recognition properties.[5] In this context, analogous chemistry of MOFs with lanthanide (Ln) ions are attractive because of their versatile coordination geometry,[6] unique luminescent,[7] and magnetic properties,[8] and possible high framework stability.[9] Ln-based MOFs typically contain solvent molecules for the gratification of higher coordination number of Ln and removal of these ancillary solvent molecules from the coordination sphere often results collapse of the framework. Therefore, Ln-frameworks without coordinated solvent molecules may exhibit high thermal stability and framework rigidity, which are essential for porous functionality. To date, only handful examples of Ln-organic frameworks with porous functionality have been reported.[10]

Storage of H_2 in a safe, compact and convenient way represents an important current challenge for its use as an alternative fuel.[11] Nanostructured carbon materials and metal hydrides were extensively studied as potential adsorbents for H_2 storage.[12] Recently, MOFs with tunable pore sizes and chemical environment, have been found to exhibit promising H_2-storage materials.[13] Ideally, for practical use the materials should exhibit quick uptake and release of the H_2 at ambient condition. High H_2-stoarge capacity (7.5 wt%) in MOF at 77 K was recently reported,[13c] but extending the performance to ambient temperature require substantial increase in the heat of adsorption value. One of the strategies is to embed coordinatively unsaturated metal sites on the pore surfaces, which can interact more strongly than that the weak dispersion forces or H-bond interactions. Evidence of stronger binding of H_2 to the Cu^{2+} / Ni^{2+} / Mn^{2+} open metal sites have been reported [14a-f] and theoretical calculations also suggest higher interaction energy of H_2 with the unsaturated sites.[14g-j] Moreover, immobilization of the unsaturated alkali metal cations in the porous framework will exhibit interesting functionality based on strong charge-quadrupole interactions. [14i]

Recently, Shimizu *et. al* reported porous luminescent bimetallic (Ln-alkali)-organic frameworks synthesized in a stepwise manner using the lanthanide-organic metalloligand, which is finally attached to the alkali metal centres.[15] However, bimetallic coordination framework using Ln and alkali metal ions are very few and their porous functionalities are

rarely observed.[16] Moreover, framework decorated with unsaturated alkali metal ions will provide ideal scaffold for more specific and strong binding sites for adsorbates, particularly for H_2.[14i] Hupp *et. al.* recently demonstrated significant high uptake of H_2 by doping alkali metal cations in a redox active porous framework.[17] They observed H_2 uptake increases with dopant cation size, and remarkable 65% increase over uptake in K^I-doped sample compare to the assynthesized framework. In this chapter, I described synthesis, structural characterization and porous functionalities of a 3D bimetallic (Ho^{III}-K^I) framework, $\{KHo(C_2O_4)_2(H_2O)_4\}_n$ (**1**). The dehydrated solid of **1** (**1´**) shows permanent porosity as well as size-selective vapor (H_2O, MeOH, CH_3CN, and EtOH) sorption properties and interesting H_2 storage characteristics with high heat of adsorption value (-9.21 kJ/mol). Using first-principles calculations, we confirm this energy quantitatively, and uncover the nature of H_2-lattice interaction from the detailed structures determined for various sites of interaction. We show that K^I is the favorable site for H_2 adsorption.

5.2 Experimental section

5.2.1 Materials All the reagents were commercially available and used as supplied without further purification. $Ho(NO_3)_3{\cdot}5H_2O$ and oxalic acid dehydrate ($K_2C_2O_4{\cdot}2H_2O$) were obtained from Aldrich Chemical Co.

5.2.2 Synthesis of $\{KHo(C_2O_4)_2(H_2O)_4\}_n$ (1)

A mixture of $Ho(NO_3)_3{\cdot}5H_2O$ (0.220 g, 0.5 mmol), $H_2C_2O_4{\cdot}2H_2O$ (0.111 g, 0.75 mmol), KOH (0.084g, 1.5 mmol) and 10 mL distilled water was placed in a 25 mL beaker and then whole reaction solution was stirred for 1 h. Then reaction mixture was transferred into 23 ml Teflon-lined stainless steel autoclave and heated at 150°C for 120 h. The mixture was allowed to cool to room temperature. Colorless block shaped single crystals suitable for X-ray study was separated manually from the white powder. (Yield 25 %). IR (KBr cm^{-1}); 3526 br (OH); 1621 br s (COO); 1326 s(COO). Anal. calcd. for $C_4H_8HoKO_{12}$: C, 10.61; H, 1.76. Found: C, 10.69; H, 1.54 %. Single phase white crystalline powder of $\{KHo(C_2O_4)_2(H_2O)_4\}$ (**1**) were isolated in hydrothermal reaction by heating a mixture of $Ho(NO_3)_3{\cdot}5H_2O$ (1 mmol, 0.441g), $K_2C_2O_4{\cdot}H_2O$ (0.368g, 2 mmol) at 180°C for 200 h in a 23 ml Teflon-lined stainless

steel autoclave. (Yield 85%). The phase purity was confirmed by the elemental analysis and PXRD measurements.

5.2.3 Physical measurements

The elemental analyses were carried out on a Perkin Elmer 1800 instrument. IR spectra were recorded on a Bruker IFS 66v/S spectrophotometer with samples prepared in KBr pellets in the region 4000-400 cm^{-1}. X-ray powder diffraction (PXRD) pattern were recorded on a Bruker D8 Discover instrument using Mo-Kα radiation.

5.2.4 Adsorption measurements

N_2 (77 K), CO_2 (195 and 298 K) and H_2 (77 K) adsorption study of the dehydrated samples prepared at 493 K under high vacuum, were carried out using QUANTACHROME AUTOSORB-1C analyzer. The adsorption isotherm of different solvents (like H_2O, CH_3CN, EtOH, at 298 K and MeOH at 293 K) were measured in the vapour state by using BELSORP-aqua volumetric adsorption instrument from BEL, Japan. In the sample chamber (~12 mL) maintained at $T \pm 0.03$ K was placed the adsorbent sample (100-150 mg), which had been prepared at 493 K at 10^{-1} Pa for 18 hours prior to measurement of the isotherms. The adsorbate was charged into the sample tube, and then the change of the pressure was monitored and the degree of adsorption was determined by the decrease of the pressure at the equilibrium state. All operations were computer-controlled and automatic. High-pressure hydrogen sorption isotherm measurements at 77 and 195 K and CO_2 sorption isotherm measurement at 298 K were carried out on a fully computer controlled volumetric BELSORP-HP, BEL JAPAN high pressure instrument. The hydrogen and CO_2 used for the high pressure measurements is scientific / research grade with 99.999% purity. For the measurements, approximately 1.00 g sample was taken in a stainless-steel sample holder and degassed at 493 K for a period of 18 hours under 0.1 Pa vacuum. Dead volume of the sample cell was measured with helium gas of 99.999% purity. Non-ideal correction for hydrogen and carbon dioxide gas were made by applying virial coefficients at the respective measurement temperature.

5.2.5 X-ray crystallography

A suitable single-crystal of compound **1** was mounted on a thin glass fiber with commercially available super glue. X-ray single crystal structural data were collected on a Bruker Smart–CCD diffractometer equipped with a normal focus, 2.4 kW sealed tube X-ray source with graphite monochromated Mo-*Kα* radiation (λ = 0.71073 Å) operating at 50 kV and 30 mA, with ω scan mode. The programme SAINT was used for integration of diffraction profiles and absorption correction were made with SADABS programme. All the structures were solved by direct methods using SIR-92 and followed by successive Fourier and difference Fourier Syntheses. All the non-hydrogen atoms were refined anisotropically. All calculations were carried out using SHELXL 97,[18] SHELXS 97,[19] PLATON 99,[20] and WinGX system, ver. 1.70.01.[21] Selected bond distances and angles for **1** is given in Table S1, respectively. The coordinates, anisotropic displacement parameters, and torsion angles for the compound **1** is submitted as supplementary information in CIF format.

5.2.6 Methods of calculation

We use Vienna Ab Initio Simulation Package (VASP) [22a-b] implementation of density functional theory (DFT), with PW91 exchange correlation energy of electrons [22c] to describe ionic potential with augmented wave potentials. [22d] The corresponding plane wave expansion of the Kohn-Sham wave function was cut off at 400 eV in calculation. We sampled, integration over Brillouin zone with a 2 x 2 x 2 uniform mesh of k-points. We use experimental structural parameters of the dehydrated MOF (Figure 1) as an initial host structure and consider several locations and orientations of H_2 molecule interacting at different sites, such those near K and Ho sites on the pore surface till the structures were relaxed to minimize energy (keeping *a*, *b*, *c* fixed) until Hellmann-Feynman forces are less than 0.02 eV / atom. Cation-oxygen bond-lengths in the optimized structure (see supporting information Table S2) are within 2 % (typical of DFT calculations) of the experimental values. Thus our pseudopotentials and other calculation parameters should be reasonably reliable.

5.3 Results and discussion

5.3.1 IR spectroscopy

The IR spectrum of **1** shows bands at 1621 cm^{-1} and 1325 cm^{-1} corresponding to ν_s(COO) and ν_{as}(COO), respectively of the ox^{2-} ligand coordinated to Ho^{III} and K^I atoms.[23] The broad band around 3526 cm^{-1} correspond to the ν(OH) of the water molecules coordinated to K^I atom (Figure 1).

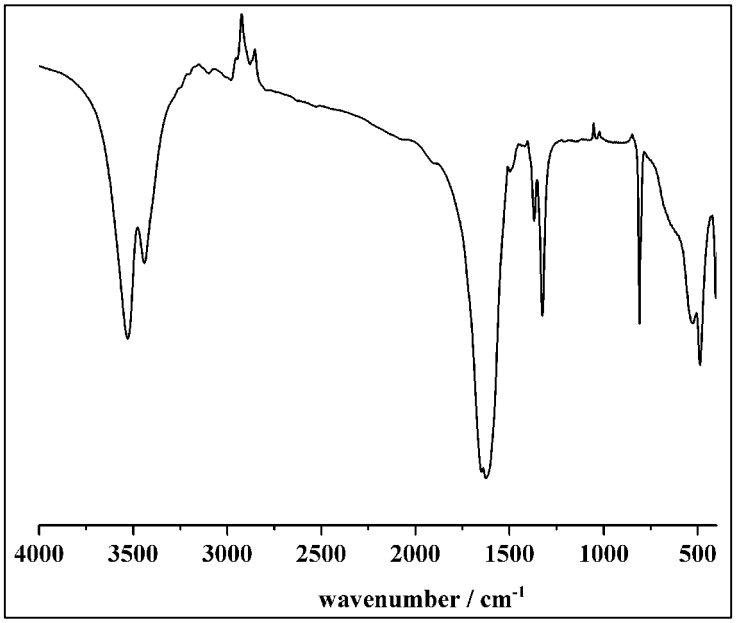

Figure 1: IR spectra for $\{KHo(C_2O_4)_2(H_2O)_4\}_n$ (**1**).

5.3.2 Structural description of $\{KHo(C_2O_4)_2(H_2O)_4\}_n$ (1)

Compound **1** crystallizes in tetragonal $I4_1/amd$ space group and X-ray structural determination[24] reveals that **1** is a neutral 3D bimetallic coordination architecture of Ho^{III} and K^I linked by the oxalate ligand (ox^{2-}), showing the formulation of $\{KHo(C_2O_4)_2(H_2O)_4\}_n$. Each octacoordinated Ho^{III} centre chelated to four different ox^{2-} through the oxygen atoms (O1, O2_c; c = 1/4+y,1/4-x,-1/4+z) forming a distorted square-antiprismatic geometry around Ho^{III} centre with HoO_8 chromophore (Figure 2a). The resulting $Ho(ox)_4^{5-}$ connected to another four Ho^{III} and eight K^I atoms resulting a 3D coordination framework with α-Po type cubic network topology (Figure 2 & 3). Each octacoordinated K^I atom ligated to four oxygen atoms (μ_2-O2) from four different ox^{2-} ligands and rest of the coordination is filled by the four water molecules (O3). Therefore, each ox^{2-} functions as a tetradentate μ_4- bridging

ligand and connected to two Ho^{III} by chelation and two K^I ions through the μ_2-O bridges (Figure 1a). The Ho1-O1 and Ho1-O2 bond distances are 2.339(6) Å and 2.377(5) Å, respectively, whereas K1-O2 bond distance (2.844(5) Å) is slightly smaller than K1-O3 (2.888(14) Å) (Table 2). In the 3D coordination framework along the crystallographic *c*-axis octacoordinated K^I and Ho^{III} atoms are alternatively positioned through μ_2-O bridges, which are further connected by the ox^{2-} ligands forming square shaped channels occupied by the four water molecules coordinated to the K^I atom (Figure3c). Removal of the coordinated water molecules from the K^I centre results bidirectional channels with the dimensions of 3.6 x 3.6 $Å^2$ along the *c*-axis and 2.0 x 1.2 $Å^2$ along perpendicular to the *a*-axis (Figure 2b & 2c and Figure 4) and no additional channels were found along *a* and *b* –axis (Figure 5). The calculation using PLATON suggests that the dehydrated framework contains 30.8% void space to the total crystal volume.[20] The nearest neighbor separations between Ho1 – Ho1 through the ox-bridges and Ho1 – K1 through the μ_2-O-bridges are 6.151 and 4.458 Å, respectively. The compound **1** is one of the very few examples where no additional solvent molecule is coordinated to the Ho-centres to satisfy the high coordination number of the lanthanide ions.

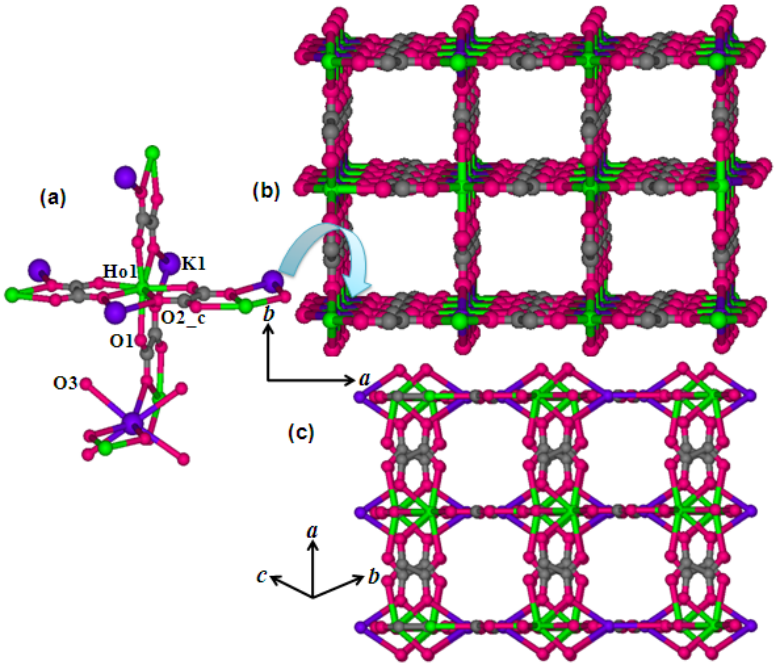

Figure 2. (a) View of the coordination environment of Ho^{III} and K^I in $\{KHo(C_2O_4)_2(H_2O)_4\}_n$ (**1**); (b) View of the 3D framework of **1** showing square shaped channel along the crystallographic *c*-axis; (c)

View of the 3D framework along parallel to *a*-axis showing small channels. K-bound water molecules were removed.

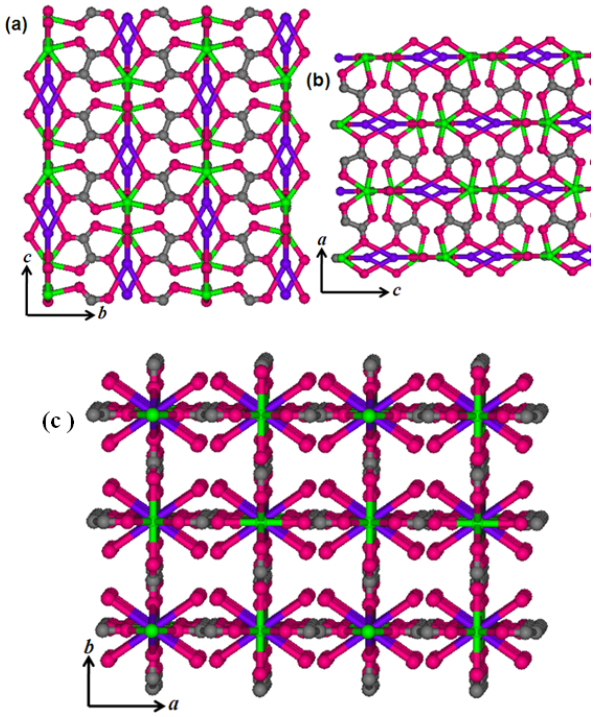

Figure 3: View of the 3D coordination framework of **1** along the crystallographic (a) *a* direction (b) *b* direction (c) *c* direction

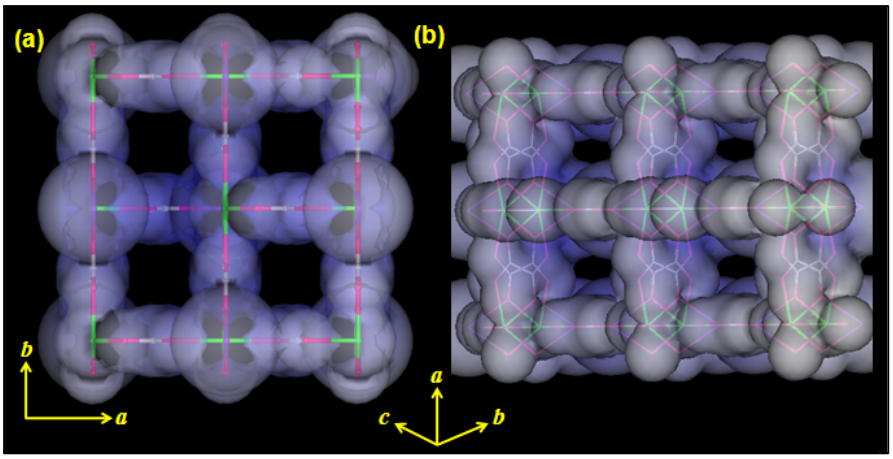

Figure 4. View of the channels: (a) square shaped channels along the crystallographic *c*-axis; (b) oval shaped small channels along parallel to the crystallographic *a*-axis.

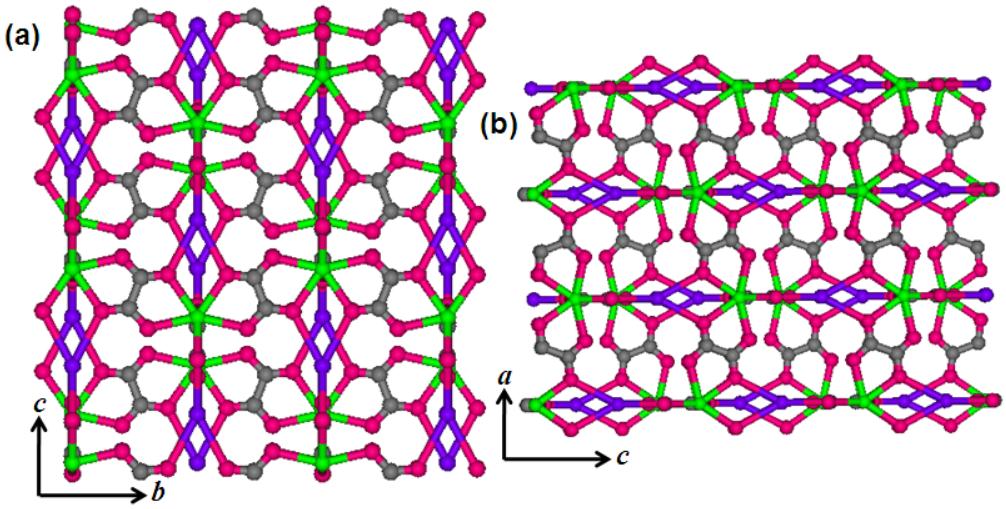

Figure 5. View of the dehydrated framework **1´**. (a) along the crystallographic *a*-axis; and (b) along the crystallographic *b*-axis.

Parameter	
Emperical formula	$H_8DyC_4O_{12}K$
M_w	452.07
Crystal system	Tetragonal
Space group	$I4_1/amd$
a (Å)	11.4651(3)
b (Å)	11.4651(3)
c (Å)	8.9154(3)
α (°)	90
β (°)	90
γ (°)	90
V (Å ^{3})	1171.92(6)
Z	4
T (K)	293
λ (Mo K_α)	0.71069
D_c (g / cm^3)	2.517
μ (mm$^{-1)}$	6.736
$\theta_{max}^{(o)}$	25.7
F(000)	820

Total data	2693
Data [$I>2\sigma(I)$]	524
R^a	0.0175
$R_w{}^b$	0.0490
GOF	1.14

Table 1. Selected bond length and bond angle of the compound

Ho1 -O1	2.339(6)	K1 -O3_i	2.888(14)
Ho1-O2_c	2.377(5)	K1-O2_m	2.844(5)
Ho1-O1_e	2.339(6)	K1-O3_m	2.888(14)
Ho1-O2_f	2.377(5)	K1-O3_t	2.888(14)
Ho1-O2_k	2.377(5)	K1-O2_y	2.844(5)
Ho1-O1_n	2.339(6)	K1-O3_y	2.888(14)
Ho1-O2_s	2.377(5)	K1-O3	2.888(14)
Ho1-O1	2.339(6)	K1-O3	2.888(14)
K1-O2	2.844(5)	K1-O3	2.888(14)
K1-O2_g	2.844(5)	K1-O3_g	2.888(14)

O1-Ho1-O2_c	79.56(13)	O1-Ho1-O1_e	92.78(5)
O1-Ho1-O2_f	68.1(2)	O1-Ho1-O2_k	137.4(2)
O1-Ho1-O1_n	154.6(2)	O1-Ho1-O2_s	79.56(13)
O1-Ho1-O1	92.78(5)	O1_e-Ho1-O2_c	68.1(2)
O2_c-Ho1-O2_f	132.58(12)	O2_c-Ho1-O2_k	132.58(12)
O1_n-Ho1-O2_c	79.56(13)	O2_c-Ho1-O2_s	69.32(19)
O1-Ho1-O2_c	137.4(2)	O1_e-Ho1-O2_f	79.56(13)
O1_e-Ho1-O2_k	79.56(13)	O1_e-Ho1-O1_n	92.78(5)
O1_e-Ho1-O2_s	137.4(2)	O1_e-Ho1-O1	154.6(2)
O2_f-Ho1-O2_k	69.32(19)	O1_n-Ho1-O2_f	137.4(2)
O2_f -Ho1-O2_s	132.58(12)	O1-Ho1-O2_f	79.56(13)
O1_n-Ho1-O2_k	68.1(2)	O2_k -Ho1-O2_s	132.58(12)
O1-Ho1-O2_k	79.56(13)	O1_n-Ho1-O2_s	79.56(13)
O1_n -Ho1-O1	92.78(5)	O1-Ho1-O2_s	68.1(2)
O2-K1-O2_g	140.73(11)	O2-K1-O3_g	67.5(3)
O2-K1 -O3_i	99.2(3)	O2 -K1-O2_m	56.75(16)
O2-K1-O3_m	119.8(3)	O2-K1-O3_t	119.8(3)
O2-K1 -O2_y	140.73(11)	O2-K1-O3_y	99.2(3)
O2_g-K1-O3	67.5(3)	O3-K1-O3_g	24.6(4)
O3-K1-O3_i	90.9(4)	O2_m-K1-O3	119.8(3)
O3-K1-O3_m	108.6(4)	O2 -K1-O3	74.1(3)
O3-K1-O3	69.5(4)	O2_g-K1-O3_g	74.1(3)
O2_g-K1-O3_i	74.1(3)	O2_g -K1 -O2_m	140.73(11)
O2_g-K1-O3_m	67.5(3)	O2_g-K1-O3_t	99.2(3)
O2_g-K1-O2_y	56.75(16)	O3-K1-O3_t	165.4(4)
O2_g-K1-O3	119.8(3)	O3_m-K1-O3_t	69.5(4)
O3-K1-O3_y	160.3(4)	O3-K1-O3	90.9(4)
O2_g-K1-O3	99.2(3)	O2_y -K1-O3_m	99.2(3)
O3_g-K1-O3_i	69.5(4)	O3_m-K1-O3_y	90.9(4)
O2_m-K1-O3_g	99.2(3)	O3_m -K1-O3	160.3(4)

O3_g-K1-O3_m	90.9(4)	O3_m -K1-O3	165.4(4)
O3_g -K1-O3_t	160.3(4)	O2_y-K1-O3_t	67.5(3)
O2_y-K1-O3_g	119.8(3)		
O3_g-K1-O3_y	165.4(4)	O3_t -K1-O3	90.9(4)
O3_g-K1-O3	108.6(4)	O3_t-K1-O3	108.6(4)
O3_g-K1-O3	90.9(4)		
O2_m-K1-O3_i	67.5(3)	O2_y-K1-O3	74.1(3)
		O2_y -K1-O3	67.5(3)
O3_i -K1-O3_t	90.9(4)	O3_y-K1-O3	69.5(4)
O2_y-K1-O3_i	119.8(3)	O3_y-K1-O3	90.9(4)
O3_i-K1-O3_y	108.6(4)		
O3_i -K1-O3	165.4(4)	O3_i -K1-O3	160.3(4)
O2_m-K1-O3_m	74.1(3)		

O2_m -K1-O2_y	140.73(11)	O2_m-K1 -O3_y	67.5(3)
O2_m -K1-O3	99.2(3)	O2_m -K1-O3	119.8(3)
O2-K1-O3	74.1(3)	O2 -K1-O3	67.5(3)

a =1/4-y,-1/4+x,1/4+z; b = 1/2-x,1-y,-1/2+z; c = 1/4+y,1/4-x,-1/4+z; d = x,1-y,1-z; e = 1/4+y,-1/4+x,5/4-z; f = 1/2-x,y,3/2-z;g =1/4-y,1/4-x,3/4-z; h =1-x,1-y,1-z; i =-1/4+y,1/4-x,3/4-z; j =-1/2+x,y,3/2-z; k =1/2+x,y,3/2-z; l =3/4-y,-1/4+x,5/4-z; m =-x,y,z; n = 1-x,y,z; o =3/4-y,1/4-x,-1/4+z; p =1/2+x,1-y,-1/2+z; q =-1/4+y,-1/4+x,1/4+z; r =1/2+x,1/2+y,-1/2+z; s = 3/4-y,1/4+x,-1/4+z; t = -x,1/2-y,z; u =1-x,1/2-y,z; v = -1/4+y,3/4-x,1/4+z; w = -1/2+x,1/2-y,3/2-z; x =1/2+x,1/2-y,3/2-z; y =-1/4+y,1/4+x,3/4-z; z = 1-x,1/2+y,1-z

5.3.3 Framework stability

To study the framework stability of **1** TG analysis and Powder X-ray diffraction (PXRD) pattern at different temperature were performed. TGA study suggests that four K^I bound water molecules are released in the temperature range of 45 - 120 ºC and the dehydrated solid (**1′**) is stable up to 380ºC without further weight loss (Figure 6). The weight loss (obs. 15.01wt %) is consistent with the four water molecules (calc. 14.16 wt %). The PXRD pattern of **1′** shows sharp lines with shifting of some peak positions, like 101 peak shifted 2θ = 12.56 to 12.88 and appearance of some new peak in comparison to the as-synthesised framework **1**, suggesting structural transformation after removal of the K bound water molecules, rather than the collapse of the framework. Indexing of the powder pattern of **1′** by using the TREOR programme [24] suggests monoclinic crystal system with a = 14.690(5) Å, b = 11.428(4) Å, c = 7.879(2) Å, β = 91.50(5)º and V = 1322.39 $Å^3$, which indicates the structural distortion in **1** after removal of the water molecules (see Table2 below). When **1′** is exposed to water vapor for three days, original framework regenerated as suggested by the PXRD pattern (Figure 7). Indexing of the powder pattern of the rehydrated solid indicating the tetragonal crystal system with cell parameters $a = b$ = 11.467(7) Å; c = 8.902(5) Å; V = 1170.75 $Å^3$, which is similar to the synthesized framework **1**.

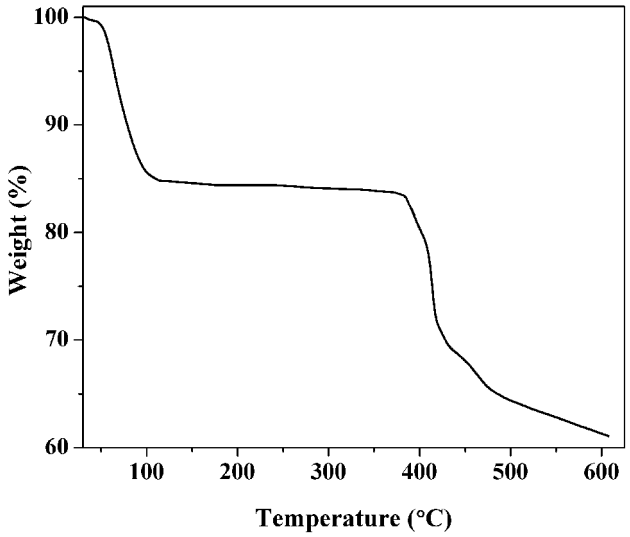

Figure 6. TGA for $\{KHo(C_2O_4)_2(H_2O)_4\}_n$ (**1**) over the temperature range from 25 – 600 °C at a heating rate of 3 °C/ min under the N_2 atmosphere.

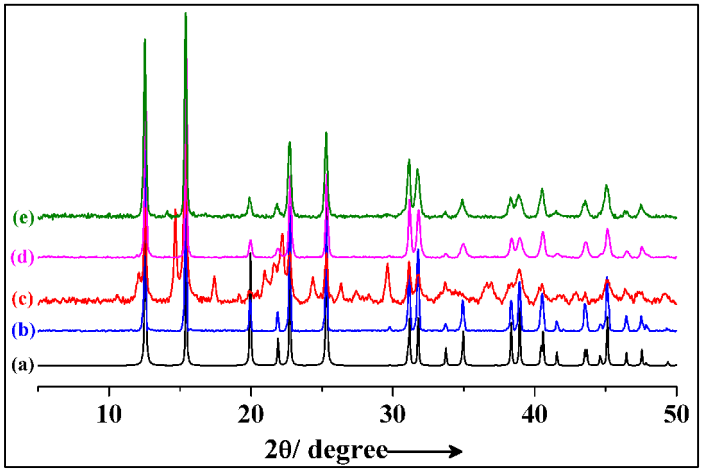

Figure 7. PXRD pattern for $\{KHo(C_2O_4)_2(H_2O)_4\}_n$ (**1**) in different state. (a) simulated from X-ray single crystal data; (b) as-synthesized; (c) at 120°C under vacuum; (d) exposed to the H_2O vapor; and (e) MeCN vapor.

Table2: Indexing results of powder sample of 1´

a = 14.690(5) Å; b = 11.428(4) Å; c = 7.879(2) Å; α = 90.0 °; β = 91.50(5)°; γ = 90.0°

V = 1322.39 Å^3

H	K	L	2θobs	2θcalc
2	0	0	12.052	12.044
1	0	1	12.875	12.882
-1	1	1	14.807	14.800
0	2	0	15.484	15.495
2	2	1	22.835	22.863
-1	0	2	23.231	23.210
4	1	4	25.448	25.463
3	3	0		29.692
-3	1	2	29.763	29.760
-2	2	2		29.855
0	4	0	31.261	31.282
4	2	1		31.315
1	4	0	31.890	31.884
0	1	3	35.047	35.038
-3	0	3	38.435	38.448
-6	1	1	39.030	39.021

NUMBER OF OBS. LINES = 13; NUMBER OF CALC. LINES = 16

M(13)= 9 AV.EPS.= 0.0000450; F 13 = 9.(0.011962, 133)

0 LINES ARE UNINDEXED ; M-TEST= 9 UNINDEXED IN THE TEST= 0

Program used to index TREOR90

5.3.4 Adsorption Property

5.3.4.1 Gas adsorption property

Encouraged by the exceptional high thermal stability of dehydrated compound (**1'**) N_2 (77 K) and CO_2 (195 K) adsorption properties were investigated to establish permanent porosity. As shown in the Figure 8 the framework exhibits a typical type-II isotherm for N_2 (kinetic diameter 3.6 Å) [25-27] and type-I profile for CO_2 (3.4 Å) adsorption. The surface area calculated from the Langmuir equation is about 69.1 m^2 /g and 324.35 m^2 /g for N_2 and CO_2 adsorption profiles, respectively. The steep uptake of CO_2 at low pressure regions suggesting

strong interaction with the pore surfaces, which is also realized by the high isosteric heat of adsorption (-26.3 kJ/mol) obtained from Dubinin-Radushkevich (DR) equation.[27]

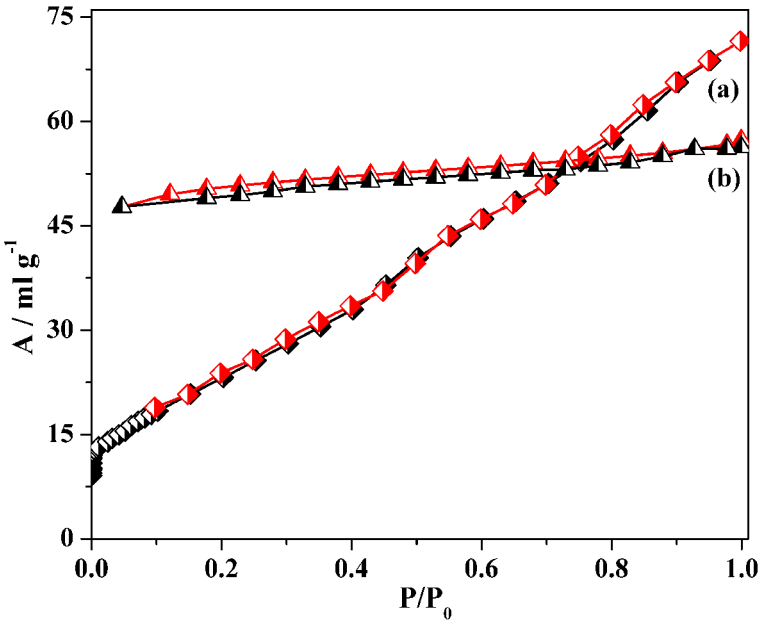

Figure 8. (a) N_2 (at 77 K) and (b) CO_2 (at 195 K) adsorption (black) and desorption (red) isotherms for **1´**. P_o is the saturated vapor pressure of the adsorbates.

Moderate surface area and highly reactive pore surfaces decorated with unsaturated alkali metal ions (K^I) prompted us to measure H_2 storage capacity of the framework **1'**. High pressure hydrogen sorption at 77 K and 195 K exhibit 0.70 wt% and 0.11 wt%, uptake respectively (Figure 9 & 10). Steep uptake of H_2 at low pressure regions at 77 K is consistent with strong interactions between H_2 molecules and pore surfaces, possibly due to the presence of highly reactive unsaturated K-sites. The framework saturated with respect to H_2 at 16 bar and 50 bar at 77 K and 195 K, respectively (Figure 10). The heat of hydrogen adsorption was calculated using Clausius-Clapeyron[13k] equation suggesting ΔH_{ads} = -9.21 kJ/mol at low coverage regions, which is significantly high among the reported porous metal-organic framework systems.[14c] The density of the adsorbed H_2 was calculated with respect to the total pore volume (0.1042 cm^3/g), giving a value of approximately 0.0672 g/cm^3, which is comparable to liquid hydrogen density (0.0708 g/cm^3), indicating that the H_2 molecules are in compressed state in the channels.[13i] We have also measured H_2 sorption at 77 K up to 1 atm (P/P_0 ~ 1), which exhibits steep uptake at very low pressure regions and ended without saturation (Figure 10 right side). The sorption is consistent with high pressure measurement

at low pressure regions. High pressure CO_2 adsorption profile shows 4.7 wt% storage capacities at 298 K and 20 bar (Figure 9 (inset)) and this value is slightly decreases to 3.47 wt % at low pressure measurement (P/P_0 ~ 1) at 298 K (Right side of Figure 9).

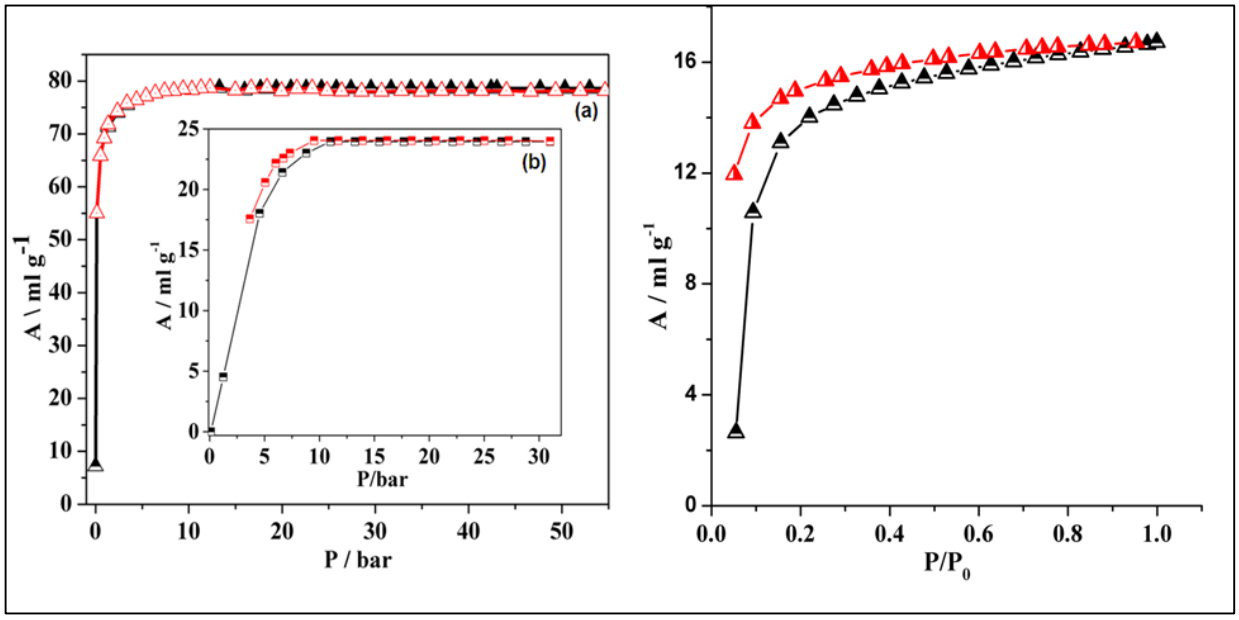

Figure 9. High pressure H_2 and CO_2 sorption isotherm for **1′**. (a) H_2 at 77 K; Figure inset (b) CO_2 at 298 K (left side) CO_2 isotherm upto 1 atm pressure at 298K (right side).

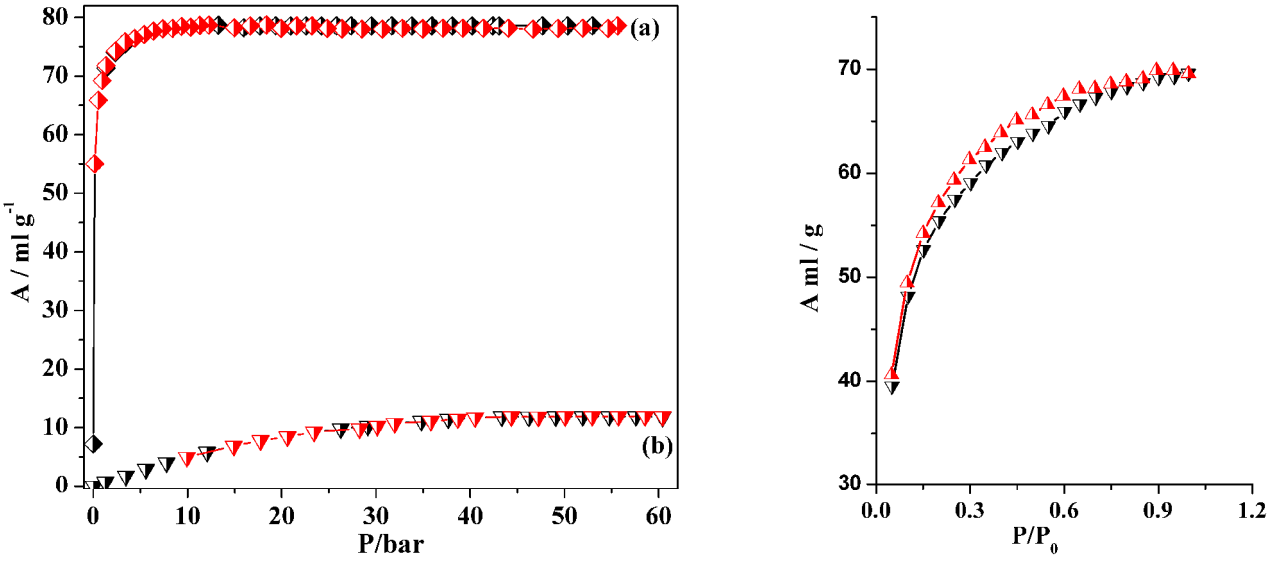

Figure10. H_2 adsorption (black) and desorption (red) isotherm for **1′**. (a) at 77 K; (b) at 195 K.

3.4.2 Vapour adsorption property

Inspired by the squared shaped channel decorated with highly active alkali metal ions, we anticipated that **1'** could selectively adsorb solvent molecules on the basis of size and polarity. H_2O, CH_3CN and EtOH sorption experiments were carried out at 298 K and MeOH sorption was measured at 293 K (Figure 5). H_2O (kinetic diameter 2.65 Å) and CH_3CN (kinetic diameter 4.0 Å) [26-27] sorption profiles exhibit typical type-I curve (Figure 10a & 10c(inset)), whereas MeOH (kinetic diameter 3.8 Å) sorption occurs in two step processes (Figure 10b (inset)). Hysteretic sorption and rapid rise at low pressure region suggesting strong interaction with the pore surfaces. The calculations using saturation sorption amount suggest that framework **1'** uptakes 4 molecules of H_2O, 0.4 molecule of MeOH, 0.7 molecule of MeCN per formula unit. All the profiles were analyzed by DR equation and the values of βE_0 values, which reflect the adsorbate-adsorbent affinity, are 5.8 kJ/mol, 7.72 kJ/mol, 9.99 kJ/mol for H_2O, CH_3CN and MeOH, respectively. CH_3CN loaded samples of **1´** reveals similar PXRD pattern as of as-synthesized framework suggesting structural transformation after accommodation of CH_3CN molecules (Figure 11).

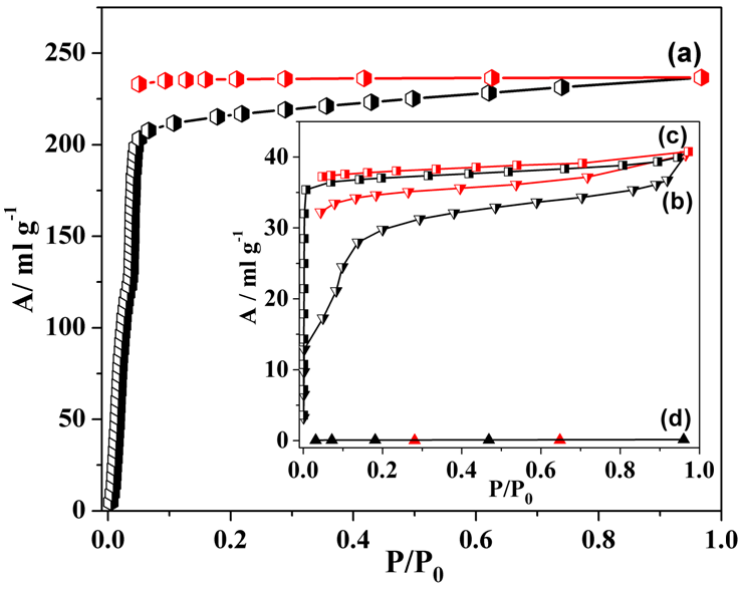

Figure 11. Vapor sorption isotherm for **1´**. (a) H_2O (298 K); Inset figure (b) MeOH (293 K); (c) CH_3CN (298 K) and (d) EtOH (298 K). P_0 is the saturated vapor pressure of the adsorbates at respective temperature.

IR spectrum of CH_3CN adsorbed sample exhibits additional peaks around 2978 cm^{-1} and 2258 cm^{-1}, corresponding to the ν(C-H) and ν(CN), respectively of CH_3CN molecule (Figure 12).[23] The higher ν(CN) stretching frequency compare to the free CH_3CN (ν(CN) = 2231 cm^{-1}) suggests that CH_3CN molecules are strongly embedded in the pores decorated with unsaturated K^I sites. Framework **1´** completely excludes EtOH molecules (kinetic diameter 4.3 Å) [27-28] consistent with the smaller pore size in **1'**. The structural reversibility with dehydration and rehydration can be realized by the similar PXRD pattern and same amount of water adsorption revealed from the sorption profile.

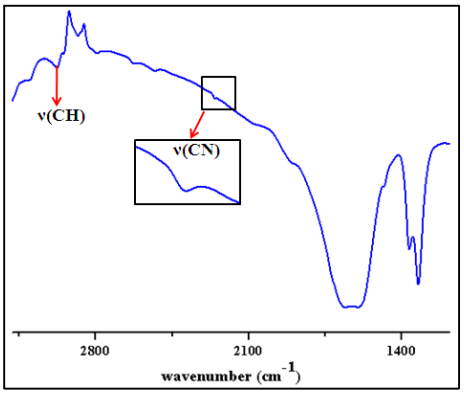

Figure 12. IR spectra for CH_3CN vapor exposed to **1´.**

3.4.3 Theoretical Investigations

We now use first-principles calculations to understand the ability of the framework to store hydrogen at the different lattice sites through determination of the respective adsorption energies and structures. We used the dehydrated (**1´**) structure of the bimetallic MOF as an initial structure in geometry optimization to obtain the bare MOF structure, and its energy (E (Bare MOF)) is used in evaluation of the adsorption energy of hydrogen molecules:

$$\Delta H_{ads} = E\ (MOF\ with\ H_2) - \{E\ (Bare\ MOF) + E\ (H_2)\}$$

Our results for H_2 adsorbed at various sites in the MOF (Table 1) clearly show that the strongest interaction occurs when H_2 is in the small pore and close to K site (Figure 13a) with an adsorption energy of -10.44 kJ / mol. In this configuration K-site lies on the perpendicular bisector of the H_2 bond. In contrast, when K-site lies along the H_2 molecular axis (Figure

12b), we find that the adsorption energy to be positive, showing a strong dependence of ΔH_{ads} on the orientation of H_2 molecule in the small pore. We have also examined H_2 in large pores and respective adsorption energies and structure (Figure 14). When K-site lies on the perpendicular bisector of H_2 bond (Figure 14a), the ΔH_{ads} (-9.03 kJ / mol) is lower than that when K-site lies on the H_2 molecular axis (7.46 kJ / mol) (Figure 14b). When the molecular axis of H_2 in an initial structure is along the line between the center of H_2 and a K-site, the H_2 molecule migrates in relaxation closer to another K-site with its axis perpendicular to the line between its molecular centre and the second K site (Figure 14b). This is consistent with lower energies associated with geometry with perpendicular axis of H_2 and stronger adsorption energies of these two configurations. It is worth mentioning that our theoretically observed ΔH_{ads} values agree well with the experimental finding. Analyses of different inter atomic distances (Table 3) in all the configurations shows that H_2 molecule is always closer to K^I-site than Ho^{III} site. Interestingly, even with the initial configuration of H_2 adsorbed near Ho-site relaxes to a lower energy configuration where H_2 migrates to K-site. This shows that in **1′** K^I is the preferential site of adsorption, and there is no energy barrier for migration of H_2 from Ho^{III} centre to K^I-site.

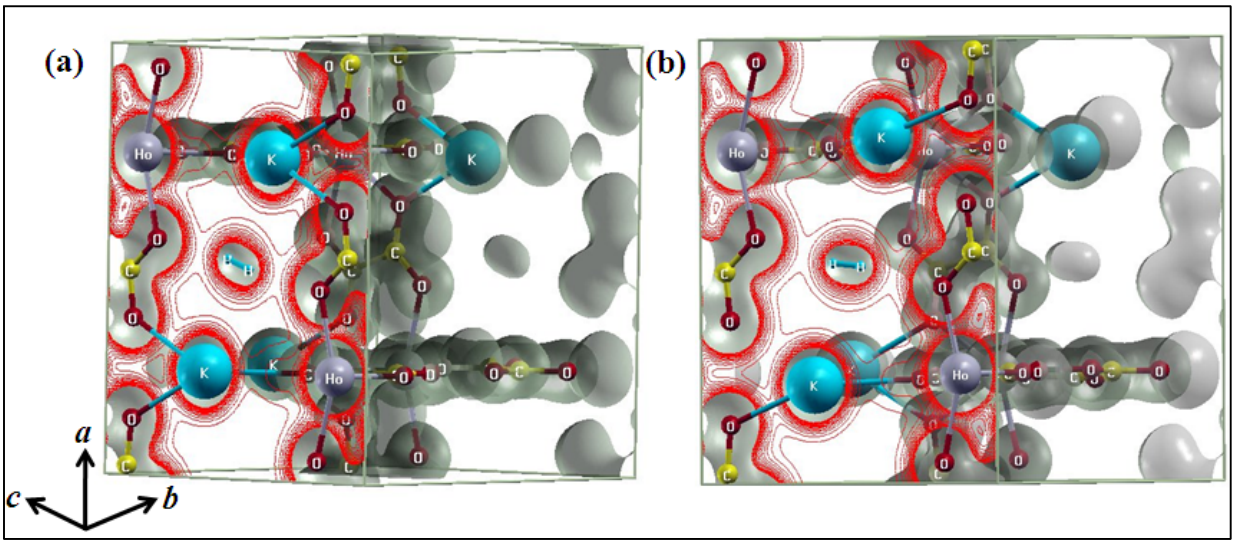

Figure 13. Iso-surfaces of charge density (iso-value = 0.5 a. u) of the optimized structure of an H_2 molecule adsorbed inside a small pore of the **1′** simulated from first-principles: the molecular axis of H_2 is (a) perpendicular and (b) parallel to the line joining the centre of mass of H_2 with K site.

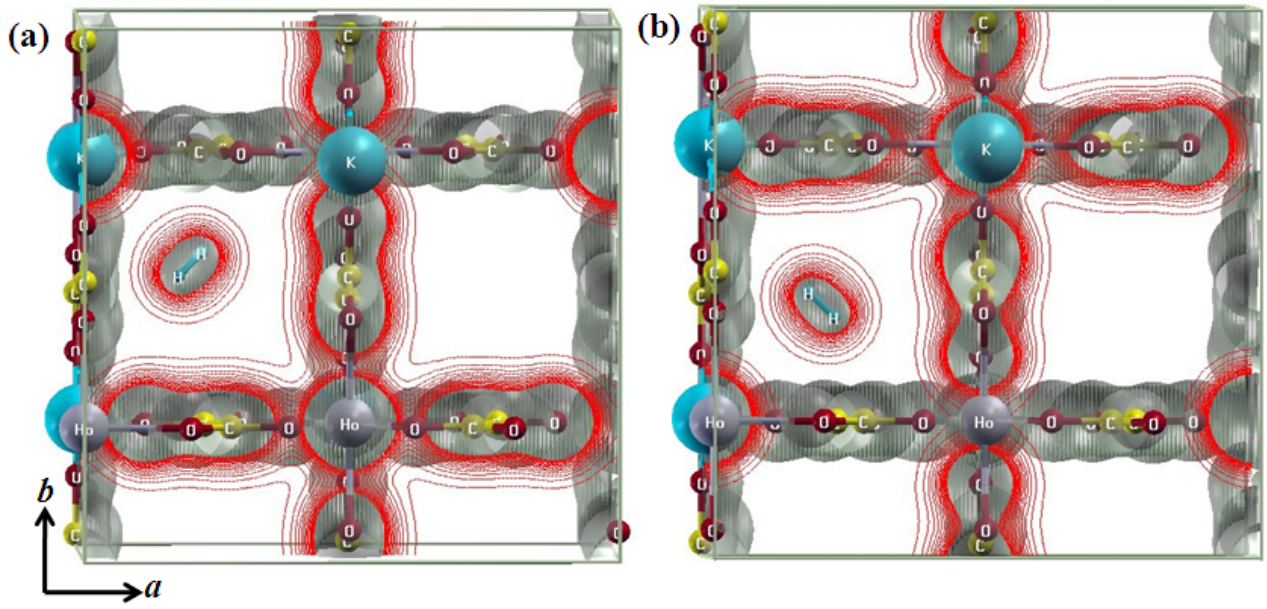

Figure 14. Iso-surfaces of charge density (iso-value = 0.5 a. u) of the optimized structure of an H_2 molecule adsorbed inside a big square pore of the MOF simulated from first-principles: the molecular axis of H_2 is (a) perpendicular and (b) parallel to the line joining the centre of mass of H_2 with K site.

Table 3. Calculated energies and structural parameters of various configurations of H_2 molecules adsorbed in the MOF. Distances are calculated from the centre of mass of H_2 to metal sites.

Structure	ΔH_{ads} (kJ/mole)	H_2– K distance (Å)	H_2 - Ho distance (Å)
H_2 in big pore (K is along the H_2 axis)	-7.46	4.72	4.18
H_2 in small pore (K is along the H_2 axis)	+1.23	3.47	4.39
H_2 in big pore (K is on the perpendicular bisector of H_2 axis)	-9.03	3.27	4.68
H_2 in small pore (K is on the perpendicular bisector of H_2 axis)	-10.45	3.07	4.40

In the optimized structures of H_2 adsorbed in the MOF, our estimate of the H_2 molecular bond-length varies from 0.751 to 0.757 Å. With our theoretical estimate of the bond-length of isolated H_2 molecule of 0.75 Å, it is quite clear that the interaction of H_2 with MOF is not chemisorptive. The interaction between H_2 molecule and the MOF lattice with unsaturated metal (K^I) site is largely electrostatic in nature.[14j] The van der Waals interaction is *not* captured in our theoretical description of the H_2-MOF interaction based on DFT-PW91 approximation, which is expected to be weakly negative at a distance of about 3.8 Å between H_2 molecule and the MOF lattice. However, DFT calculations are known to overestimate the binding energies, hence our estimates of binding energies are close the experimental estimates. We note that our theoretical analysis also ignores thermal contributions to the free energy of binding or its pressure dependence, which could also partly compensate the errors in our estimates of adsorption energies.

5.4 Summary

In conclusion, we have successfully synthesized a new bimetallic (Ho^{III}-K^I) 3D α-Po type framework with bidirectional channels by making use of oxalate as an organic linker. The dehydrated framework (**1´**) shows permanent porosity and good H_2 and CO_2 storage capacity at high pressure and low temperature. The framework **1´** shows high heat of H_2 sorption (~-10 kJ / mole), realized by the interactions with unsaturated K-sites, which is confirmed quantitatively using first-principles calculations. Through first-principles DFT simulations, we show that a hydrogen molecule preferentially adsorbs (a) near a K-site than a Ho-site, and (b) with its axis perpendicular to the line joining K-site and its center. We suggest a recipe to develop better hydrogen storage materials through incorporation of unsaturated and reactive alkali metal ion in the pore-surfaces of metal organic frameworks. The vapor sorption studies which reveal easy uptake of H_2O, MeOH and CH_3CN molecules, but completely excludes EtOH molecules, may find industrial application in discriminating the MeOH molelcule from a mixture of MeOH and its higher homologues.

5.5 References

1. (a) J. L.C. Rowsell and O. M. Yaghi, *Angew. Chem. Int. Ed.,* 2005, **44**, 4670; (b) S. D. Sun, J. M. Simmons, C. D. Collier, D. Yuan and H. –C. Zhou, *J. Am. Chem. Soc.,* 2007, **130**, 1012; (c) G. Férey, *Chem. Soc. Rev.,* 2008, **37,** 191;(d) L. Pan, K. M. Adams, H. E.

Hernandez, X. Wang, C. Zheng, Y. Hattori and K. Kaneko, *J. Am. Chem. Soc.,* 2003**, 125,** 3062.

2. (a) J. S. Seo, D. Whang , H. Lee, S. I. Jun, J. Oh, Y. J. Jeon and K. Kim, *Nature,* 2000, **404**, 982; (b) O. R. Evans, H. L. Ngo and W. Lin, *J. Am. Chem. Soc.,* 2001, **123**, 10395; (c) J. Y. Lee, D. H.Olson, L. Pan, T. J. Emge and J. Li, *Adv. Func. Mater.,* 2007, **17**, 1255; (d) H. L. Ngo and W. Lin, *J. Am. Chem. Soc***.,** 2002, **124**, 14298.

3. (a) T. K. Maji, R. Matsuda and S. Kitagawa, *Nat. Mater.,* 2007**, 6**, 142; (b) K. S. Min and M. P. Suh, *J. Am. Chem. Soc.,* 2000, **122**, 6834; (c) O. M. Yaghi and H. Li, *J. Am. Chem. Soc.,* 1996, **118**, 295.

4. (a) C. D. Wu, A. Hu, L. Zhang and W.Lin, *J. Am. Chem. Soc.,* 2005, **127**, 8940; (b) O. Ohmori and M. Fujita, *Chem. Commun.,* 2004, **10**, 1586; (c) W. Lin, *MRS Bulletin,* 2007, **32**, 544.

5. J. Kido and Y. Okamoto, *Chem. Rev.,* 2002, **102**, 2357.

6. (a) O. Guillou and C. Daiguebonne, *Handbook on the Physics and Chemistry of Rare Earths*; J. -C. G. GschneidnerBünzli, V. K. Pecharsky, Eds.; Elsevier: New York, 2005; Vol. 34, pp 359; (b) C. L. Cahill, D. T. de Lill, M. Frisch, *CrystEngComm*., 2007, **9**, 15.

7. (a) X. Guo, G. Zhu, Q. Fang, M. Xue, G. Tian, J. Sun, X. Li and S. Qiu, *Inorg. Chem.,* 2005, **44**, 3850; (b) E. G. Moore, J. Xu, C. J. Jocher, I. Castro-Rodriguez and K. N. Raymond, *Inorg. Chem.,* 2008, **47**, 3105; (c) J. Y. Wu, T. T. Yeh, Y. S. Wen, J. Twu and K. L. Lu, *Cryst. Growth Des.,* 2006, **6**, 467; (d) A. Fratini, G. Richards, E. Larder and S. Swavey, *Inorg. Chem.,* 2008, **47**, 1030; (e) W. H. Zhu, Z. M. Wang and S. Gao, *Inorg. Chem.,* 2007**, 46,** 1337; (f) A. Thirumurugan and S. Natarajan, *J. Mat. Chem.,* 2005, **15,** 4588.

8. (a) C. Benelli and D. Gatteschi, *Chem. Rev.,* 2002, **102**, 2369; (b) M. Bao-Qing, S. Gao, G. Su and G. X. Xu, *Angew. Chem., Int. Ed*., 2001, **40,** 434; (c) J. P. Costes, J. M. Clemente-Juan, F. Dahan, F. Nicodeme and M. Verelst, *Angew. Chem., Int. Ed.,* 2002, **41**, 323; (d) C. F. Hsu, S. H. Lin and H. H. Wei, *Inorg. Chem. Commun.,* 2005, **8**, 1128; (e) J. P. Costes, J. M. C. Juan, F. Dahan and F. Nicodeme, *Dalton Trans*., 2003, 1272; (f) S.C. Manna, E. Zangrando, A. Bencini, C. Benelli and N. Ray Chaudhuri *Inorg. Chem.,* 2006**, 45**, 9114.

9. (a) F. A. A. Paz and J. Klinowski, *Chem. Commun.,* 2003, **9**, 1484; (b) Z. He, E. Q. Gao, Z. M. Wang, C. H. Yan, M. Kurmoo, *Inorg. Chem*., 2005, **44**, 862; (c) X. Zheng, C. Sun, S. Lu, F. Liao, S. Gao and L. Jin, *Eur. J. Inorg Chem*., 2004, 3262.

10. (a) T. K. Maji, G. Mostafa, H. –C. Chang and S. Kitagawa, *Chem. Commun*., 2005, 2436; (b) L. Pan, K. M. Adams, H. E. Hernandez, X. Wang, C. Zheng, Y. Hattori and K. Kaneko, *J. Am. Chem. Soc.,* 2003**, 125**, 3062; (c) J. Zhao, L. S. Long, R. B. Huang and L. S. Zheng, *Dalton Trans.,* 2008, 4714; (d) A. Dimos, D. Tsaousis, A. Michaelides, S. Skoulika, S. Golhen, L. Ouahab, C. Didierjean and A. Aubry, *Chem. Mater*., 2002, **14**, 2616. (e) C. Serre and G. Ferey, *J. Mat. Chem.,* 2002**, 12**, 3053; (f) T. M. Reineke, M. Eddaoudi, M. O'Keeffe and O. M. Yaghi, *Angew. Chem., Int. Ed.,* 1999**, 38**, 2590; (g) N. L. Rosi, J. Kim, M. Eddaoudi, B. Chen, M. O'Keeffe and O. M. Yaghi, *J. Am. Chem. Soc*., 2005, **127,** 1504; (h) T. Devic, C. Serre, N. Auderbrand, J. Marrot and G. Férey, *J. Am. Chem. Soc.*, 2005, **127**, 12788; (i) J. Luo, H. Xu, Y. Liu, Y. Zhao, L. Daemen, C. Brown, T. V. Timofeeva , S. Ma and H. –C. Zhou, *J. Am. Chem. Soc*., 2008, **130,** 9626; (j) F. Millange, C. Serre, J. Marrot, N. Gardant, F. Pellé and G. Férey, *J. Mater. Chem*., 2004, **14,** 642; (k) Q. Yue, J. Yang, G. –H. Li, G. –D. Li and J. –S. Chen, *Inorg. Chem.,* 2006, **45**, 4431; (l) X. Guo, G. Zhu, Z. Li, F. Sun, Z. Yang and S. Qiu, *Chem. Commun*., 2006, 3172.

11. (a) L. Schlapbach and A. Züttel. *Nature,* 2001, **414**, 353; (b) L. Schlapbach, *MRS Bull.* 2002, 675.

12. (a) C. Liu, Y. Y. Fan, M. Liu and H. T. Cong, *Science,* 1999, **286**, 1127; (b) A. C. Dillon, K. M. Jones, T. A. Bekkedahl, C. H. Kiang, D. S. Bethune, M. J. Heben, 1997, **386**, 377; (c) W. Grochala and P. P. Edwards *Chem. Rev.,* 2004, **104**, 1283.

13. (a) J. L. C. Rowsell and O. M. Yaghi, *Angew. Chem. Int. Ed.,* 2005, **44**, 4670; (b) X. Lin, J. Jia, X. Zhao, K. M. Thomas, A. J. Blake, G. S. Walker, N. R. Champness, P. Hubberstey and M. Schröder, *Angew. Chem. Int. Ed.,* 2006, **45,** 7358; (c) A. G. Wong Foy, A. J. Matzger, O. M. Yaghi, *J. Am. Chem. Soc.,* 2006, **128**, 3494; (d) J. L. C. Rowsell, A. R. Millward, K. S. Park and O. M. Yaghi, *J. Am. Chem. Soc.*, 2004, **126**, 5666; (e) M. Latroche, S. Surblé, C. Serre, C. Mellot-Draznieks, P. L. Llewellyn, J. –H. Lee, and J. S. Chang, S. H. Jhung and G. Férey, *Angew. Chem. Int. Ed.,* 2006, **45**, 8227; (f) B. Panella, M. Hirscher, H.; H. Pütter and U. Müller, *Adv. Funct. Mater*., 2006, **16,** 520; (g) A. Dailly, J. J. Vajo and C. C.

Ahn, *J. Phys. Chem. B,* 2006**, 110**, 1099; (h) L. Pan, M. B. Sander, X. Huang, J. Li, M. Smith, E. Bittner, B. Bockrath and J. K. Johnson, *J. Am. Chem. Soc*., 2004, **126**, 1308; (i) H. Chun, D. N. Dybtsev, H. Kim and K. Kim, *Chem. Eur. J.,* 2005, **11***,* 3521; (j) W. Yang, X. Lin, J. Jia , A. J. Blake, Claire.; Claire. Wilson and P. Hubberstey *Chem. Commun.,* 2008, 359; (k) M. Latroche, S. Surble, C. Serre, C. Mellot-Draznieks, P. L. Llewellyn, J- H. Lee, J-S. Chang, S. H. Jhung and G. Ferey, *Angew. Chem. Int. Ed*., 2006, **45**, 8227 ; (l) M. Dinca, A. Dailly, Y. Liu, C. M. Brown, D. A. Neumann and J. R. Long, *J. Am. Chem. Soc.,* 2006**, 128**, 16876; (m) K. S. Steven and J. R. Long *J. Am. Chem. Soc.,* 2005**, 127**, 6507.

14. (a) B. Chen, N. W. Ockwig, A. R. Milward, D. S. Contreras and O. M. Yaghi, *Angew. Chem. Int. Ed.,* 2005, **44**, 4745; (b) P. M. Forster, J. Eckert, J. S. Chang, S. E. Park, G. Férey and A. K. Cheetham, *J. Am. Chem. Soc*., 2003, **125**, 1309; c) Y. Liu, H. Kabbour, C. M. Brown, D. A. Neumann and C. C. Ahn, *Langmuir,* 2008, **24**, 4772; (d) Q. Yang and C. Zhong, *J. Phys. Chem. B*, 2006, **110**, 655; (e) L. B. Jonathan, C. S. Abraham, M.; Eddaoudi and S. Brian *J. Am. Chem. Soc*., 2007, **129**, 15202.

15. (a) D. Chandler, J. O. Yu, D. T Cramb, G. K. H. Shimizu, *Chem. Mater.,* 2007, **19**, 4467; (b) D.Chandler, D. T. Cramb and G. K. H. Shimizu, *J. Am. Chem. Soc*., 2006, **128**, 10403.

16. (a) X. Zhang, Y. Xing, C. Wang, J. Han, J. Li, M. Ge, X. Zeng and S. Niu, *Inorg. Chim. Acta,* 2009, **362**, 1058; (b) T. Bataille, J. –P. Auffrdic and D. Lour, *Chem. Mater.*, 1999, **11** , 1559.

17. (a) K. L. Mulfort, O. K. Farha, C. L. Stern, A. A. Sarjeant, and J. T. Hupp, *J. Am. Chem. Soc.,* 2009, **131**, 3866 ; (b) K. L. Mulfort and J. T.Hupp, *Inorg. Chem*., 2008, **47**, 7936.

18. G. M. Sheldrick, SHELXL 97, *Program for the Solution of Crystal Structure*, University of Gottingen, Germany, 1997.

19. G. M. Sheldrick, SHELXS 97*, Program for the Solution of Crystal Structure*, University of Gottingen, Germany, 1997.

20. A, L. Spek, *PLATON*, *Molecular Geometry Program,* The University of Utrecht, Utrecht, The Netherlands, 1999.

21. L. J. Farrugia, WinGX - A Windows Program for Crystal Structure Analysis. *J. Appl. Crystallogr*. 1999, **32**, 837.

22. a) G.; Kresse, J. Hafner, *Phys. Rev. B,* 1993, **47**, 558; b) G. Kresse and J. Furthmuller, *Phys. Rev. B,* 1996*,* **54***,* 11169; c) J. P.; Perdew and Y. Wang, *Phys. Rev. B*, 1992,**45**, 13244; d) P. Bloechl, *Phys. Rev. B,* 1994**, 50**, 17953.

23. K. Nakamoto, Infrared and Raman Spectra of Inorganic and Coordination Compounds, 5th ed; John Wiley & Sons; 1997

24. P. –E. Werner, L. Eriksson and M.; Westdahl, *J. Appl. Cryst,* 1985, **18**, 367.

25. M. M.Dubinin, *Chem. Rev,* 1960**, 60,** 235**.**

26. Molecular areas are calculated from liquid density, assuming spherical symmetry and a hexagonal close packing. The equation and values are in ref. 28.

27. C. E. Webster, R. S. Drago, M. C. Zerner, *J. Am. Chem. Soc.,* 1998, **120,** 5509.

Chapter 6

Chapter 6 :Bimodal Magneto-Luminescent Dysprosium(Dy^{III})-Potassium(K^{I})-Oxalate Framework: Magnetic Switchability with High Anisotropic Barrier and Solvent Sensing

Abstract

To incorporate multiple functionalities into a single framework material a lanthanide-alkali (Dy^{III}-K^{I}) bimetallic 3D framework $\{KDy(C_2O_4)_2(H_2O)_4\}_n$ (**1**) ($C_2O_4^{2-}$ = oxalate dianion) has been synthesized and structurally characterized. The framework **1** is isomorphous with $\{KHo(C_2O_4)_2(H_2O)_4\}_n$ reported in previous chapter. Here we have changed Ho^{III} to Dy^{III} to incorporate multiple functionalities like luminescence and magnetism. The dehydrated framework of **1** (**1′**) after removal of the K-bound water molecules found to exhibit permanent porosity with excellent vapor sorption characteristics. The compound **1** shows metal based luminescence property in the visible region and corresponding dehydrated compound **1′** has enhanced emission intensities compared to as-synthesized compound **1**. The H_2O molecules exhibit strong quenching effect compared to other solvents MeOH, MeCN and EtOH, evoking compound **1′** as a potential water sensor material. The ferromagnetic interaction and slow relaxation of magnetization of **1** has been brought out from the ac and dc susceptibility measurements. The compound **1** unveils switching of magnetic properties (ferromagnetic to antiferromagnetic upon dehydration and rehydration) and record anisotropic barrier (418 K) among the other reported lanthanide compounds including single-molecule magnets (SMMs) and single chain magnets (SCMs).

A manuscript related to this chapter has been submitted for publication: S. Mohapatra, R. Bharath, A. Sundaresan, and T. K. Maji (communicated)

6.1 Introduction

During the last two decades the design and synthesis metal-organic hybrid compounds have attracted considerable interest to the chemists, physicists and material scientists due to their fascinating structure and potential application as magnetic, optoelectronic, and porous material.[1-11] Now, one of the most appealing aims is to fabricate multifunctional material which combines a set of well-defined properties (*e.g* porosity and magnetism, porosity and optical) for specific applications.[12] In this context, lanthanide-based metal-organic hybrid compounds are excellent candidates as a multifunctional material because of their interesting magnetic and luminescent properties. Such a synergism, where two or more different functionalities are united would lead to a novel smart material.[13-15] The field of molecular magnetism based on coordination compounds has experienced great deal of attention in the last two decades with the discovery of single molecule magnet (SMM) and single chain magnet (SCM) which exhibit slow relaxation of magnetization and magnetic hysteresis below the blocking temperature (T_B).[16-22] The origin of the SMM behaviour is the existence of an energy barrier (ΔE) that prevents reversal of magnetization which depends on the large ground state spin multiplicity and the easy axis (or Ising type) magnetic anisotropy of the compound ($D < 0$). Lanthanide based mononuclear, polynuclear or extended systems can provide an important platform to explore the SMM or SCM behaviour because of their high spin and large intrinsic magnetic anisotropy based on strong spin –orbit coupling (J = L+S).[22, 23] In this context recent works suggest that dysprosium(III) (Dy^{III}) ions may offer high blocking temperature because of high spin, large magnetic anisotropy and reduced quantum tunnelling of the magnetization (QTM) by using the appropriate ligand system.[24-31] Furthermore, lanthanides have high emission quantum yields under ambient condition; therefore lanthanide organic frameworks would open up the new possibilities for low cost sensor.[12,32] We envisioned that the presence of porosity in such lanthanide-organic frameworks provides the opportunities to study gas storage, sensing for small molecules and guest dependent magnetic and luminescent properties which are of particular interest for applications as magnetic device and sensors. Some elegant examples of porous magnet based on transition metal ions with reversible solvent induced change in the magnetic ordering have been recently documented.[33-36] It has been observed that slight change around the metal coordination environment have significant influence on the magnetic exchange coupling. Very few porous magnetic coordination framework are known to exhibits reversible ferromagnetic to antiferromagnetic phase transition through

desolvation and resolvation,[33] to the best of our knowledge such phenomenon in lanthanide-organic systems yet to be reported. In this chapter we have exploited the large intrinsic magnetic anisotropy, high ground state spin and luminescence property of Dy^{III} to fabricate a multifunctional compound, $\{KDy(C_2O_4)_2(H_2O)_4\}_n$ (**1**). Moreover the magnetically innocent K^I ion is an integral part of the framework and acts as a potentate of the structure. Dehydrated compound **1′** exhibits permanent porosity and interesting vapour (H_2O, MeOH, MeCN, EtOH) sorption properties. The temperature dependence magnetic measurement of **1** reveals ferromagnetic interaction through oxalate linker. Interestingly this unique bimetallic MOF **1** exhibits slow magnetic relaxation, very high (record breaking) anisotropic barrier (418 K), and switching of magnetic property from ferromagnetic to antiferromagnetic *via* dehydration and rehydration, hitherto unknown in any lanthanide-organic framework materials. The compound **1** has well characterized emissions at visible region based on Dy^{III} and shows change in emission intensities after removal and reintroduction of guest molecules like H_2O, MeOH, MeCN and EtOH, which has been exploited for selective sensing for solvent molecules based on quenching of the emission intensities. To the best of our knowledge this is the first report in the literature of lanthanide MOFs where three interesting properties like porosity; solvent induced modulation in magnetic and luminescent properties has been unveiled in a single framework material (Scheme 1).

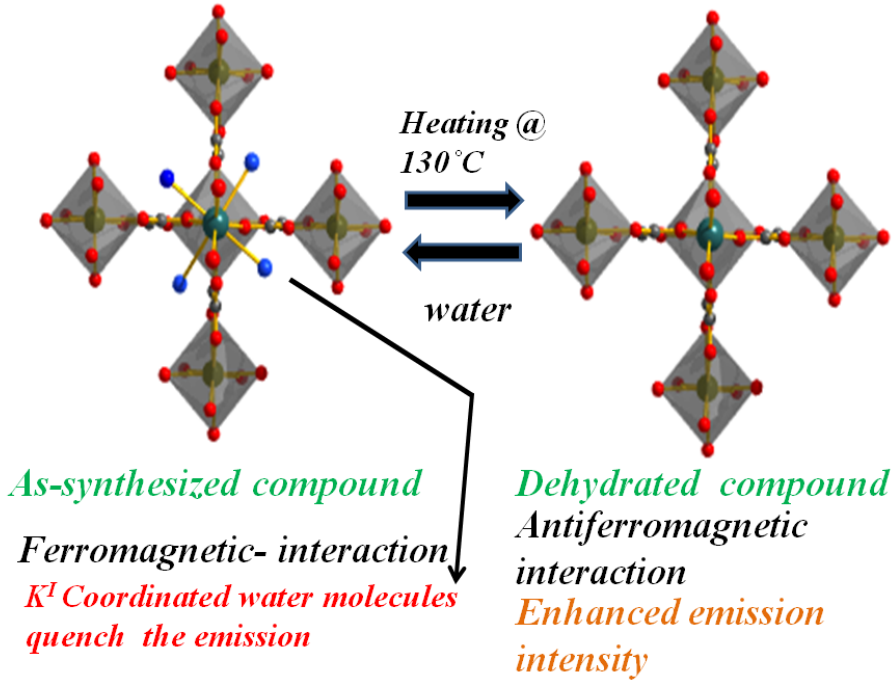

Scheme 1: Water induced change in magnetic and luminescent properties in **1**.

6.2 Experimental section

6.2.1 Materials

All the reagents were commercially available and used as supplied without further purification. $Dy(NO_3)_3 \cdot 5H_2O$ and potassium oxalate ($K_2C_2O_4 \cdot 2H_2O$) were obtained from Aldrich Chemical Co.

6.2.2 Synthesis of $\{KDy(C_2O_4)_2(H_2O)_4\}_n$ (1)

$Dy(NO_3)_3 \cdot 5H_2O$ (0.145 g, 0.33 mmol), $K_2C_2O_4$, 2 H_2O (0.121 g, 0.66 mmol), and 10 mL of distilled water were placed in a 25 mL beaker, and the whole reaction mixture was vigorously stirred for 1 hour. The white colour reaction mixture was then transferred into a 23 mL Teflon-lined stainless steel autoclave and the system was kept in the oven at 180 ^oC for 8 days. The autoclave was kept out and slowly allowed to cool to room temperature. White colour crystalline solid was obtained. The white colour solid was filtered and washed several times with water to remove unreacted starting materials and then dried under vacuum. Yield 72.5 % (relative to Dy^{III}). Anal. Calcd. for $KDyH_8C_4O_{12}$: C, 10.68; H, 1.78. Found: C, 10.71; H, 1.75. IR (KBr cm^{-1}); 3530 br (OH); 1623 br s (COO); 1329 s(COO).

6.2.3 Physical measurements

The elemental analyses were carried out on a Perkin Elmer 1800 instrument. IR spectra were recorded on a Bruker IFS 66v/S spectrophotometer with samples prepared in KBr pellets in the region 4000-400 cm^{-1}. X-ray powder diffraction (PXRD) pattern were recorded on a Bruker D8 Discover instrument using Cu-Kα radiation. Magnetic measurements were carried out with vibrating sample magnetometer in Physical Properties Measurement Systems (PPMS, Quantum Design, USA). UV-vis and fluorescence spectra were recorded on a perkin elmer model Lambda 900 spectrophotometer and perkin Elmer model LS 55 spectrophotometer, respectively. Lifetime measurements were carried out at room temperature using Edinburgh Instrument FLSP 920 spectrometer.

6.2.4 Adsorption measurements

The adsorption isotherm of different solvents (H_2O, CH_3CN, EtOH, at 298 K and MeOH at 293 K) were measured in the vapour state by using BELSORP-aqua volumetric adsorption instrument from BEL, Japan. In the sample chamber (~12 mL) maintained at T ± 0.03 K was placed the adsorbent sample (100-150 mg), which had been prepared at 433 K at 10^{-1} Pa for 18 hours prior to measurement of the isotherms. The adsorbate was

charged into the sample tube, and then the change of pressure was monitored and the degree of adsorption was determined by the decrease of pressure at the equilibrium state. All operations were computer-controlled and automatic.

6.2.5 X-ray crystallography

A suitable single-crystal of compound **1** was mounted on a thin glass fibre with commercially available super glue. X-ray single-crystal structural data were collected on a Bruker Smart–CCD diffractometer equipped with a normal focus, 2.4 kW sealed tube X-ray source with graphite monochromated Mo-*Kα* radiation (λ = 0.71073 Å) operating at 50 kV and 30 mA, with ω scan mode. The programme SAINT [38] was used for integration of diffraction profiles and absorption correction were made with SADABS programme.[39] All the structures were solved by direct methods using SIR-92 [40] and followed by successive Fourier and difference Fourier Syntheses. All the non-hydrogen atoms were refined anisotropically. All calculations were carried out using SHELXL 97,[41] SHELXS 97,[42] PLATON 99,[43] and WinGX system, ver. 1.70.01.[44] Crystal data and structure refinement parameters for **1** is given in Table 1 and selected bond distances and angles for **1** is given in Table 2.

6.3 Results and discussion

6.3.1 Structural description of $\{KDy(C_2O_4)_2(H_2O)_4\}_n$ (1)

Compound **1** crystallizes in tetragonal space group $I4_1/a$. Single-crystal X-ray structural determination reveals that **1** is a neutral 3D bimetallic coordination architecture of Dy^{III} and K^{I} bridged by the oxalate linkers (ox^{2-}) (Figure 1, left). The compound **1** isomorphous to $\{KHo(C_2O_4)_2(H_2O)_4\}_n$ reported in previous chapter. Similarly here each octacoordinated Dy^{III} center chelated to four different ox^{2-} through the oxygen atoms (O1 and O2) forming a distorted square-antiprismatic coordination geometry. It is worth mentioning here that the coordination number eight of Dy^{III} is satisfied without any ancillary solvent molecule (Figure 1). Each octacoordinated K^{I} center are connected to four oxygen atom (μ_2-O1) of ox^{2-} and rest of the four coordination numbers were satisfied by four solvent water molecules (O1w). Oxalate is acting as linker along crystallographic *a*, *b* and *c* direction to form a 3D architecture (Figure 1). Dy^{III}-O1/O2 bond distances are 2.390(3) and 2.351(2) Å and K(I)-O1/O1w bond distances are 2.849(3) and 2.908(4) Å which are similar to the distances in $\{KHo(C_2O_4)_2(H_2O)_4\}_n$. After removal of water molecules, square shaped channels with the dimensions of 3.54 ×

3.54 Å^2 along perpendicular to the *a*-axis has been generated (Figure 1 right). The distance between two oxalate bridged Dy^{III} centers are 6.172 Å.

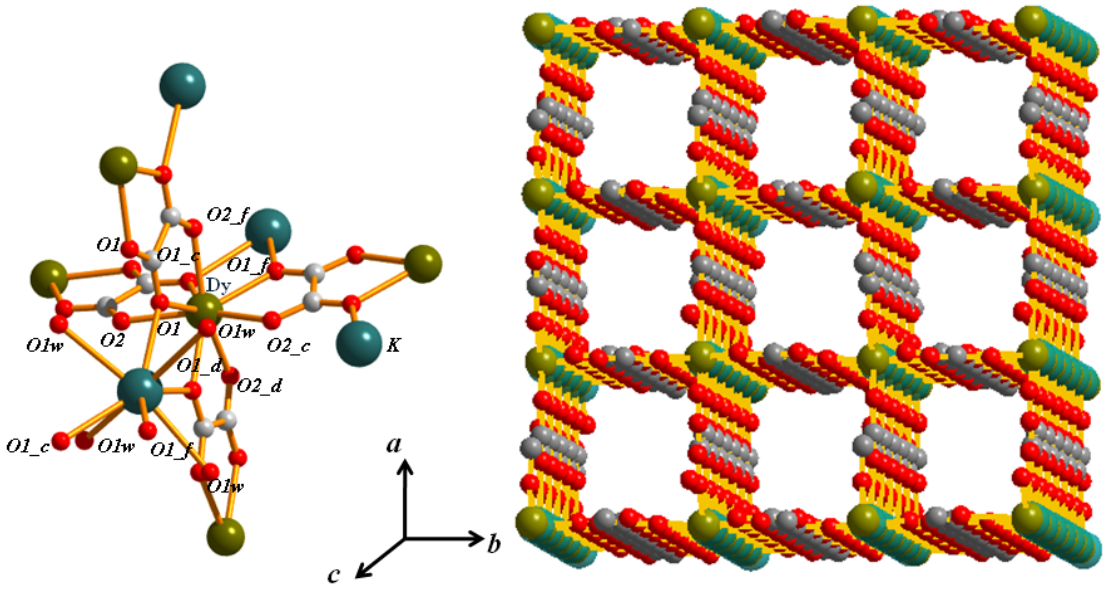

Figure 1. (Left) Coordination environment of Dy^{III} and K^{I} copnnected via ox^{2-} linker (left), and (right) extended 3D structure viewing along crystallographic *c* axis and water molecules are removed for showing the channels.

Table1. Crystal data and structure refinement parameters for $\{KDy(C_2O_4)_2(H_2O)_4\}_n$ **(1)**.

Empirical formula	Dy $KH_8C_4O_{12}$
M_r	449.5
Crystal system	Tetragonal
Space group	$I4_1/a$
a (Å)	11.5128(2)
b (Å)	11.5128(2)
c (Å)	8.9087(2)
α (°)	90
β (°)	90
γ (°)	90
V (Å ^{3})	1180.80(4)
Z	4
T (K)	293
λ (Mo $K_α$)	0.71069
D_c (g / cm^3)	2.484
μ (mm$^{-1)}$	6.736
$θ_{max}$(degree)	25.7
F(000)	820
Total data	2693
Data [*I*>2σ(*I*)]	524
R^a	0.0175
R_w ^{b}	0.0490
GOF	1.14

$R_a = \Sigma||Fo|-|Fc||/\Sigma|Fo|$; $^b R_w = [\Sigma\{w(Fo^2-Fc^2)^2\}/\Sigma\{w(Fo^2)^2\}]^{1/2}$

Table 2. Selected bond lengths (Å) and bond angles (˚) for $\{KDy(C_2O_4)_2(H_2O)_4\}_n$ (**1**).

Bond distances (Å)			
Dy-O1	2.390(3)	Dy -O1_c	2.390(3)
Dy-O1_f	2.390(3)	Dy –O2_c	2.351(2)
Dy-O2	2.351(2)	Dy -O1_d	2.390(3)
Dy –O2_f	2.351(2)	K-O1	2.849(3)
Dy –O2_d	2.351(2)	K-O1W	2.908(4)

Bond angles(˚)			
O1-Dy -O3	75.70(8)	O1_c -Dy -O3_d	137.59(9)
O1_c -Dy-O3_f	83.18(8)	O1_c -Dy-O3_d	137.59(9)
O1-Dy -O1_c	132.14(8)	O1_c -Dy-O1_d	132.14(8)
O1_d -Dy-O3_c	68.12(9)	O1_c -Dy-O3_c	75.70(8)
O1-Dy-O3_c	137.59(9)	O3-Dy-O3_f	92.86(8)
O3_c-Dy-O3_d	92.86(8)	O1_f -Dy-O3	37.59(9)
O1-Dy-O1_d	70.01(8)	O1_f -Dy-O3	37.59(9)
O1_f -Dy-O3_c	83.18(8)	O1_f -Dy-O3_f	75.70(8)
O1-Dy -O3_d	83.18(8)	O3-Dy -O3_d	154.20(9)
O3_c -Dy-O3_f	154.20(9)	O3_d -Dy-O3_f	92.86(8)
O1-Dy-O1_f	132.14(8)	O1_d -Dy -O3	83.18(8)
O1_d -Dy-O3_d	75.70(8)	O1_f -Dy-O3_d	68.12(9)
O1-Dy-O3_f	68.12(9)	O3-Dy-O3_c	92.86(8)
O1_d-Dy-O1_f	32.14(8)	O1_d -Dy -O3_f	137.59(9)
O1_c -Dy -O3	68.12(9)		

Symmetry code: a = 7/4-y,-3/4+x,1/4+z, b = 3/4+y,7/4-x,-1/4+z,c = 5/4-y,-3/4+x,1/4-z, d = 2-x,1/2-y,z, e = 5/2-x,1/2-y,1/2-z, f = 3/4+y,5/4-x,1/4-z

6.3.2 Thermal stability and structural reversibility

Powder X-ray diffraction (PXRD) patterns of the bulk as-synthesized compound **1** is similar to the simulated pattern calculated from CIF file suggesting compound is pure (Figure 3a and 3b)**.** To study the framework stability of **1** TGA and PXRD study at different states were performed. TGA suggest that four K^I bound water molecules are released in the temperature range of 45 - 120 ºC and the dehydrated solid **(1′)** is stable up to 380 ºC without further weight loss (Figure 2). The weight loss (obs. 15.01wt %) is consistent with the four water molecules (calc. 14.16 wt %). The PXRD pattern of **1′**

shows sharp lines with shifting of some peak positions, and appearance of some new peaks compared to the as-synthesized framework **1**, suggesting structural transformation to lower symmetry after the removal of the K^I bound water molecules. Indexing of the powder pattern of **1′** by using the Treor 90 programme [37] suggests triclinic crystal system with a = 9.079(9) Å, b = 12.201(2) Å, c = 13.990(7) Å, α= 60.473(3) º β = 84.824(2) º, γ = 68.854(8) º and V = 1250.35 $Å^3$, which indicates the structural transformation in **1** after removal of the water molecules (see Table 3). When **1′** is exposed to water vapour for three days, as-synthesized framework regenerated as suggested by the PXRD pattern. Indexing of the powder pattern of the rehydrated solid indicating the tetragonal crystal system with cell parameters a = b = 11.467(7) Å; c = 8.902(5) Å; V = 1170.75 $Å^3$, which is similar to the as-synthesized framework **1**.

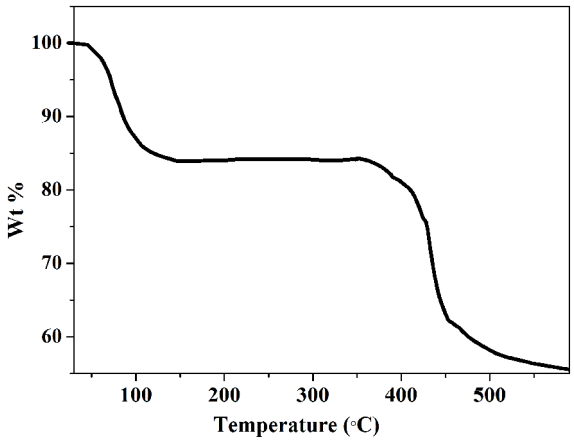

Figure 2. TGA profile for compound **1** in the temperature range of 28-600 °C with a heating rate 3 °C per minute.

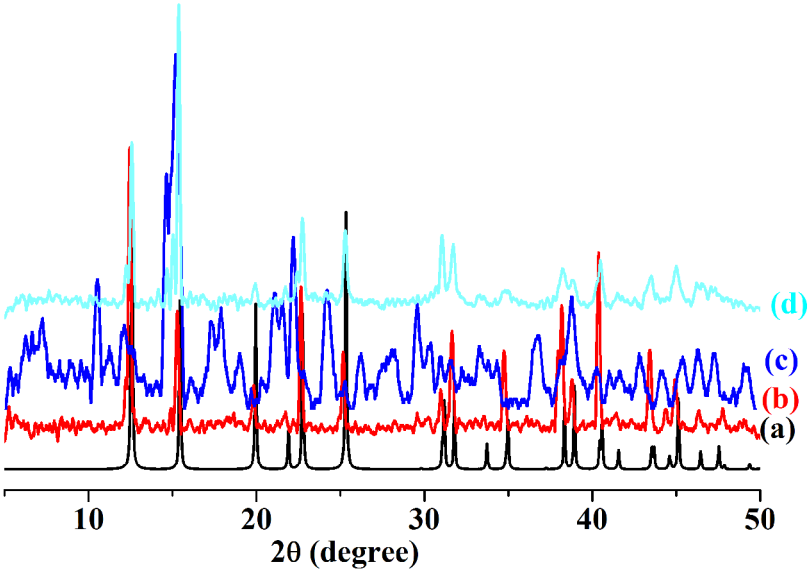

Figure 3. PXRD patterns of **1** in different state. (a) simulated, (b) as-synthesized, (c) dehydrated (**1′**) and (d) rehydrated (**1″**).

Table 3. Indexing result for the dehydrated framework **(1′).**

$2\theta_{OBS}$	$2\theta_{calc}$	D_{obs}
7.258	7.299	12.1697
8.290	8.277	10.6572
8.926	8.940	9.8993
10.495	10.500	8.4224
11.249	11.265	7.8597
12.105	12.132	7.3054
14.669	14.627	6.0338
15.200	15.217	5.8241
16.135	16.117	5.4889
17.906	17.934	4.9496
18.977	18.947	4.6727
19.678	19.662	4.5079
20.379	20.367	4.3544
21.079	21.090	4.2112
21.566	21.574	4.1173
22.208	22.212	3.9996
24.213	24.207	3.6728
25.265		3.5223
	26.163	
	26.187	
26.219	26.226	3.3962
28.204	28.218	3.1615
	29.499	
29.586	29.533	3.0169

6.3.3 Vapour adsorption studies

The detailed gas storage (H_2 and CO_2) characteristics of the isostructural Ho^{III}-K^{I} framework has been reported in the previous chapter and hence I have focused only the vapour sorption properties. Inspired by the squared shaped channels decorated with unsaturated alkali metal ions, we anticipated that **1'** would show interesting vapour sorption properties on the basis of size and polarity of the pore surface. H_2O (kinetic diameter = 2.8 Å), MeOH (4.0 Å), MeCN (4.3 Å) and EtOH (4.8 Å) sorption experiments were carried out using BELSORP aqua-3 sorption instrument (Figure 4). The dehydrated framework (**1'**) unveils double step H_2O adsorption profile and final uptake amount is about 220 mL g^{-1} at P/P_0 ~0.9 which corresponds to 3.7 water molecules per formula unit

of **1′** (Figure 4a). The two step adsorption profile of H_2O argues guest induced structural transformation during the adsorption based on different sorption sites in the framework. However, MeOH, MeCN and EtOH show one step typical type I adsorption profile (Figure 4 (inset)). The calculations using final saturation amount of MeOH (35 mL g^{-1}), MeCN (44 mL g^{-1}) and EtOH (22 mL g^{-1}) indicate that 0.58, 0.74 and 0.37 molecule of MeOH, MeCN and EtOH occluded per formula unit of **1′**. In all cases the rapid uptake at low pressure region and incomplete hysteretic sorption profile signifying strong interaction of the solvent molecules with the pore surfaces which is decorated with the unsaturated K^I site. All the profiles were analyzed by Dubinin-Radushkevich (DR) equation[45] and the values of βE_0, which reflect the adsorabate-adsorbent interaction, are 7.21 kJ mol^{-1}, 7.03 kJ mol^{-1}, 9.75 kJ mol^{-1} and 15.30 kJ mol^{-1} for H_2O, MeCN, MeOH and EtOH respectively further reflecting the strong adsorbate-adsorbent interaction. The sorption amount of the different solvent vapors depends not only to their size but also to their polarity, coordination ability with the framework structure having unsaturated K^I sites. The structural reversibility with respect to dehydration and rehydration can be realized by the similar PXRD pattern and almost same amount of water adsorption revealed from the sorption profile (Figures 3 and 4a).

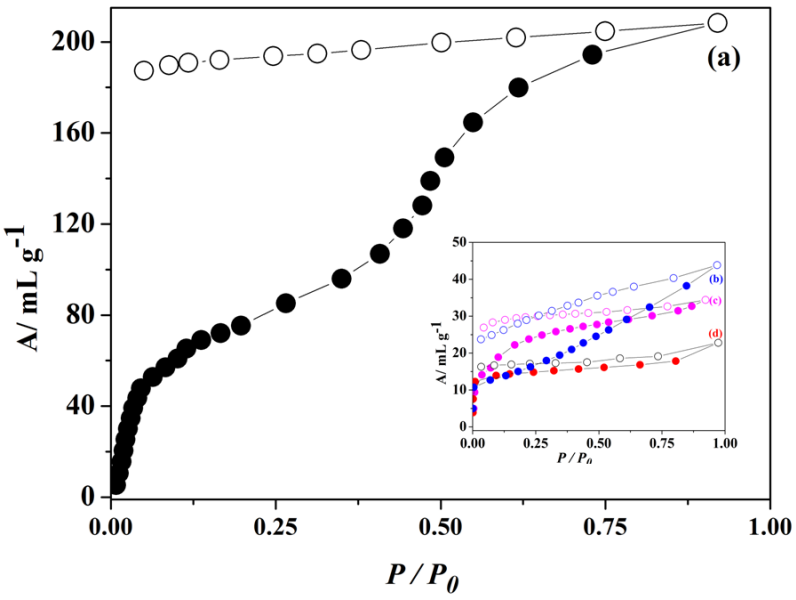

Figure 4. (a) H_2O (298 K) sorption profile for **1′**. Inset: solvent sorption isotherms for (b) MeCN (298 K), (c) MeOH (293 K) and (d) EtOH (298 K). P_0 is the saturated vapour pressure of the respective solvent molecules at that temperature.

6.3.4 Photoluminescence property

The luminescent properties of as-synthesized, dehydrated and rehydrated compound of **1** were investigated in the solid state. As shown in Figure 5a, the emission spectrum of assynthesized compound **1** was recorded in the range 450 to 700 nm using the excited wavelength (λ_{ex}) of 365 nm. The luminescent spectra exhibit two characteristics peaks of Dy^{III} at 485 nm and 576 nm, which corresponds to $^4F_{9/2} \rightarrow {}^6H_{15/2}$, $^4F_{9/2} \rightarrow {}^6H_{13/2}$ transitions respectively.[13-15] To realize the effect of K^I bound water molecule on the luminescence intensity, the emission spectrum has been recorded for the dehydrated compound (heating at 130º C for 6 hours under vacuum) under same experimental condition. We observed the luminescent intensity increased to almost double and the emission peak is little blue shifted compared to the as-synthesized compound (Figure 5b). This study clearly demonstrates that water molecules acts as a quencher although they are not directly coordinated to Dy^{III} ion. The slight blue shifted emission can be correlated to the structural change after removal of water molecules which we observed from the PXRD pattern. It is worth noting that water exposed dehydrated compound shows decrease in emission intensity consistent with the quenching effect of the water molecules (Figure 5c). We did not observe the same emission intensity as of as-synthesized compound which can be corroborated to the incomplete rehydration.

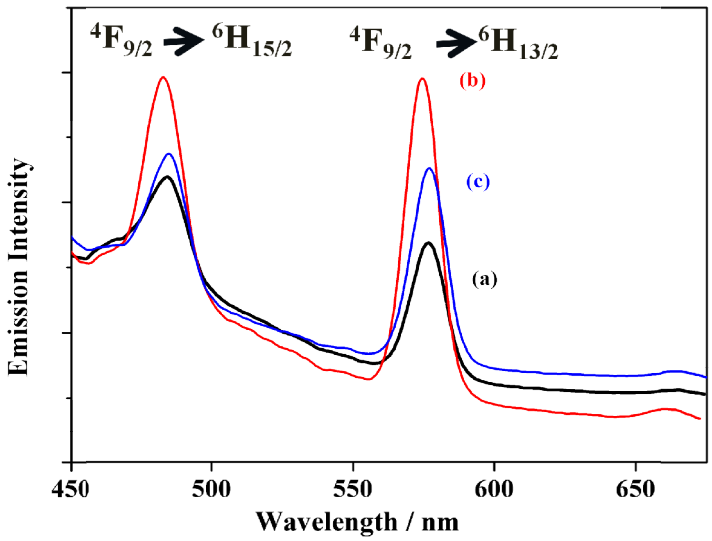

Figure 5. Luminescence spectra of **1** in different state; (a) as-synthesized **1**,(b) dehydrated **1′**, (c) rehydrated **1″** excited at 365 nm.

As the dehydrated compound **1′** uptakes different solvent vapors (vide supra) into the framework structure, we have studied the effect of emission intensities after exposing

different solvent vapors. Time dependent measurement has been carried out by keeping a glass slide containing thin layer of dehydrated compound inside a quartz cuvoid having solvent molecule to study the quenching effect. The emission intensity at 576 nm was studied after exciting at 365nm with a certain time interval. The extent of intensity change at different time interval with different solvent vapors has been shown in Figure 6 which suggest the quenching is highly efficient in case of H_2O compared MeCN, MeOH and EtOH.

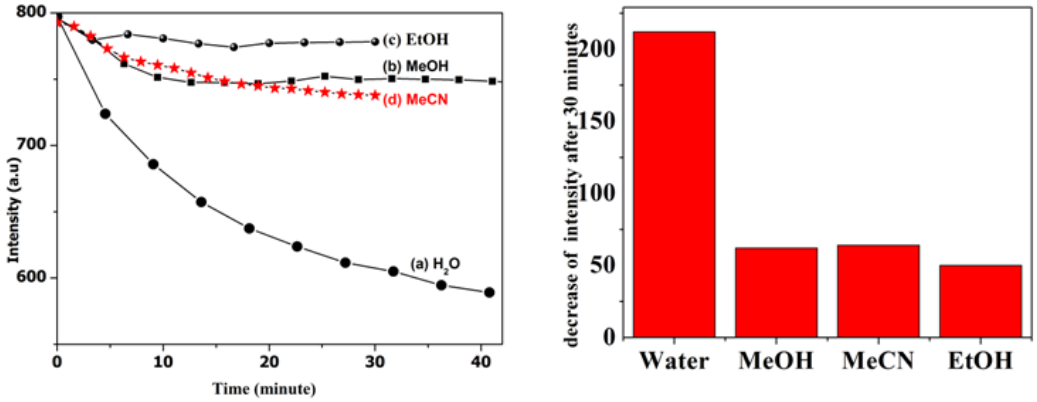

Figure 6. Left: Change of luminescence intensity of **1′** with time; (a) H_2O, (b) MeOH, (c) EtOH, and (d) MeCN; and Right: the corresponding histogram showing the same.

Indeed, the extent of quenching is depend on the amount of solvent included into the framework. In the vapour sorption isotherms the adsorption amount is decreasing in the order, H_2O> MeCN > MeOH> EtOH and the extent of quenching by the solvent also follow the same order. The high quenching effect of water compared to other solvents (MeOH, EtOH, MeCN) may find application of compound **1′** as a water sensor. Surprisingly here in **1** water molecules are not directly coordinated to the Dy^{III} center, although its significant quenching effect has been observed. Significantly high enhancement of intensity after dehydration is due to the inhibition of nonradiative decay process. The quantum yield depends on the energy gap between emissive state and highest sublevel of the ground state multiplet. The smaller the energy gap easier will be the nonradiative decay through the vibration of O-H group of ligand, guest or coordinated solvent molecules which are in sufficiently close proximity to the emissive lanthanide ion. Furthermore, to support the quenching effect of water, we have performed the lifetime measurements of the $^4F_{9/2}$ state of Dy^{III} for **1** and **1′** (Figure 7). The significant increase in the lifetime of $^4F_{9/2}$ in **1′** (τ_1 = 10.258 μs, τ_2 = 2.063 μs) from **1** (τ_1 = 7.894 μs,

τ_2=1.558 μs) suggesting indeed water molecules act as an effective quencher in this system.

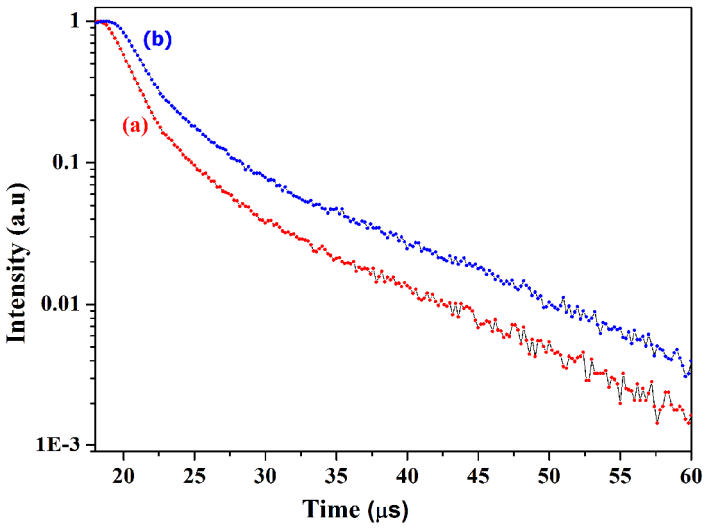

Figure 7. Lifetime measurements for **1** and **1′.** (a) Decay profile for **1** and (b) decay profile of **1′** for $^4F_{9/2}$ state of Dy(III), showing longer lifetime of $^4F_{9/2}$ in **1'** compared to **1** (The deay profiles were fitted with bi-exponential behaviour).

6.3.5 Magnetic properties

6.3.5.1. Static magnetic property

The temperature dependence zero field cooled dc magnetic susceptibility measurement of **1** was performed in the temperature range of 3 – 300 K. The plots of temperature dependence of molar magnetic susceptibility χ_M and $\chi_M T$ of **1** show a very clear signature of weak but significant ferromagnetic interaction among the Dy^{III} centers (Figure 8a). At room temperature $\chi_M T$ value is 14.25 emu K mol^{-1}, close to the value expected for a magnetically isolated Dy^{III} centre (g = 4/3, J = 15/2). $\chi_M T$ value gradually increases upon decreasing the temperature and reaches maximum of 16.68 emu K mol^{-1} at 50 K and then $\chi_M T$ value remain constant up to 32 K. Further cooling $\chi_M T$ rapidly decreases to 14.95 emu mol^{-1} K at 3 K and this is due to the depopulation of the excited state Stark levels. The increase of $\chi_M T$ up to 50 K from 300 K clearly suggests the presence of the ferromagnetic interaction in the system. The linear fitting of χ_M^{-1} vs T plot for **1** gives the Weiss constant (θ) = 11.3 K which further confirms the ferromagnetic interaction operating between the Dy^{III} centres at a distance of 6.17Å connected by the ox^{2-} linker (Figure 8b). The ox^{2-} is a small linker simultaneously can offer both σ and π electronic pathways for magnetic super-exchange between the Dy^{III} centres. To study effect of

dehydration on the magnetic properties, we have also measured the magnetic susceptibility of the dehydrated compound **1′** in the temperature range of 3 – 300 K and shows different $\chi_M T$ vs T profile (Figure 9a). The $\chi_M T$ value continuously decreases from 14.23 emu K mol^{-1} at 300 K and reaches minimum at 3 K suggesting antiferromagnetic interaction operating in the system (Figure 9). Currie-Weiss fitting of χ_M^{-1} vs T data for **1'** shows Weiss constant (θ) is -3.88 K confirming antiferromagnetic interaction in **1'** (Figure 9b). To understand the effect of rehydration in magnetic properties, **1'** was exposed to water vapor for three days and then rehydrated framework **1''** was subjected for magnetic measurement which shows similar $\chi_M T$ vs T profile as of compound **1.** The $\chi_M T$ value gradually increases from 300 K upon cooling and reaches maximum at 50 K and again decreases on further cooling due to the depopulation of excited state Starks level (Figure 10A). Linear fitting of χ_M^{-1} vs T deduced positive θ value of 3.65 K suggesting reappearance of ferromagnetic interaction and the smaller θ value compared to the as-synthesized compound evoking rehydration is not complete (Figure 10B). This result indicates that reversible ferromagnetic to antiferromagnetic phase transition based on dehydration and rehydration in the framework which is unprecedented in the lanthanide-organic framework systems.

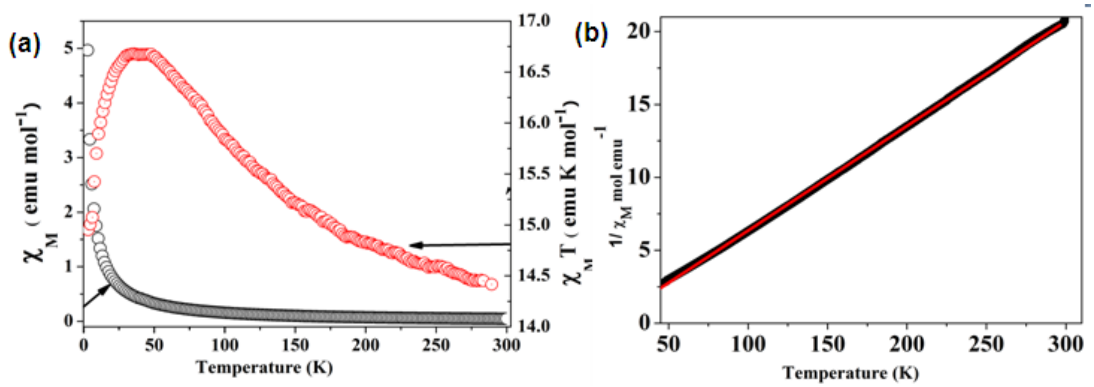

Figure 8. (a) Plot of χ_M and $\chi_M T$ as a function of temperature for as-synthesized compound **1**, (b) χ_M^{-1}vs T plot, in the temperature range of 3 to 300 K.

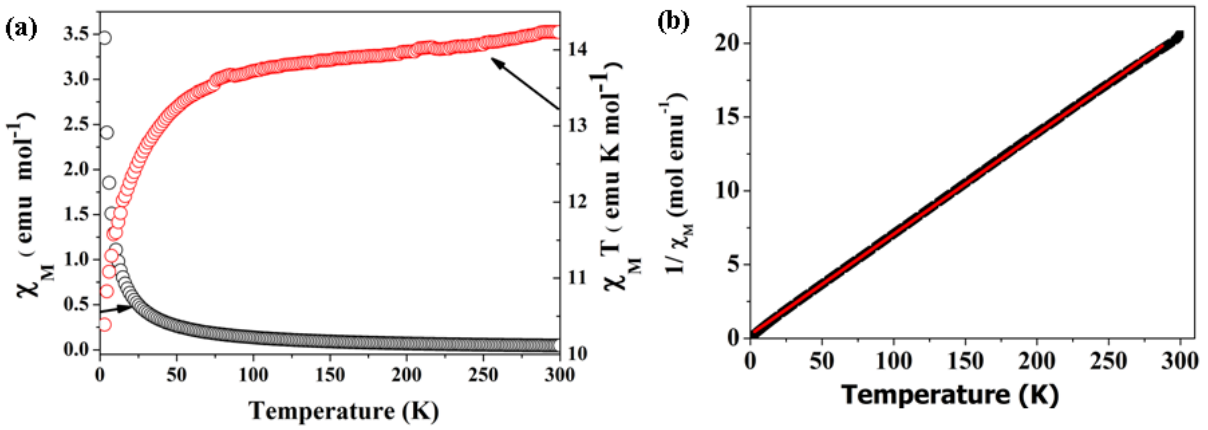

Figure 9. (a) Plot of χ_M and χ_MT as a function of temperature for dehydrated compound **1′**, (b) χ_M^{-1}vs T plot, in the temperature range of 3 to 300 K.

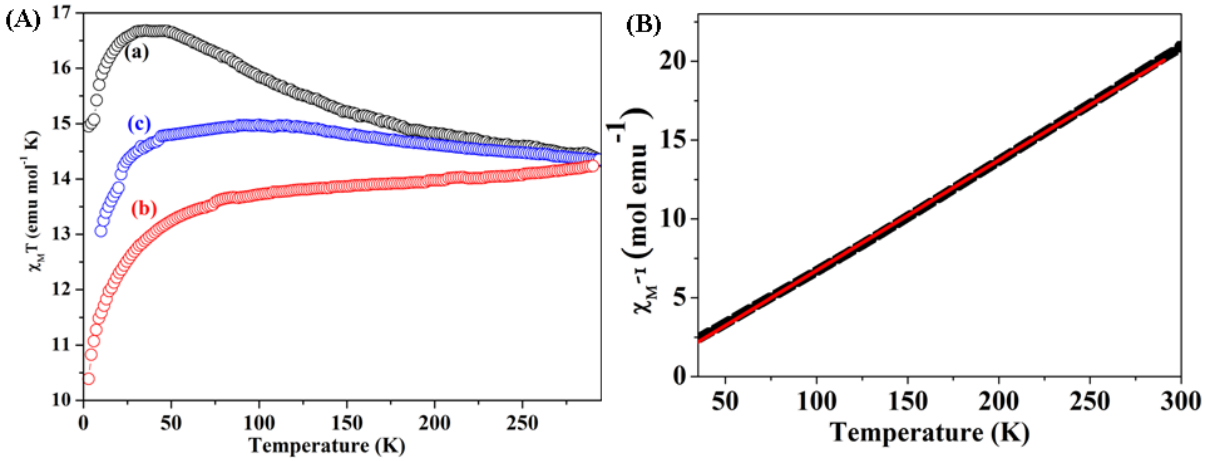

Figure 10. (A) Plot χ_MT as a function of temperature, (a) as-synthesized **1**, (b) dehydrated **1'**, (c) rehydrated **1''** in the temperature range 3K to 300 K, (B) χ_M^{-1}vs T plot for rehydrated **1''**, in the temperature range of 3 to 300 K.

6.3.5.2 Dynamics of magnetization

To understand the dynamic of magnetization we performed alternating current (ac) magnetic measurement of compound **1** under H_{DC} = 0 and H_{ac} = 10 Oe in the temperature range of 80 to 5 K. Both the real χ_M' and imaginary χ_M'' vs T part of the ac susceptibilities show strong frequency dependence below 53 K and peaks are more prominently observed in the imaginary χ_M'' vs T profile (Figure 11 and 12). The peaks are observed above 1000 Hz and shift to higher temperature with increasing frequencies which is corroborating the slow relaxation of the magnetization. Dehydrated framework obtained after heating at 130˚C for 6 hours also shows similar frequency dependence (Figure 13). Furthermore both the χ_M' and χ_M'' value increases with decreasing

temperature below about 30 K which is similar to behaviour of superparamagnism plus paramagnetism. Superparamagnetic property of the compound also confirmed from the field dependent isothermal magnetization measurements at 3 K (Figure15). The saturation magnetization value of 6.05 μ_B without any hysteresis is a signature of superparamagnetic behaviour of the compound. The peak temperature T_p obtained from the plots of χ_M'' vs T after Gaussian fitting deduce a linear plot of 1/Tp vs lnτ and obey the Arrhenius law $\tau = \tau_0 \exp(\Delta E/K_BT)$ (Figure 12). The best fitting yields the energy barrier, $\Delta E/K_B$ = 418 K and relaxation time $\tau_0 = 1.23 \times 10^{-09}$ S. To the best of our knowledge, this is the highest anisotropic relaxation barrier among lanthanides compounds including single molecule magnets (SMMs) and single chain magnet (SCMs). On the other hand to obtain dynamical exponent, zv, frequency dependence of ac χ_M'' was fitted by conventional critical scaling law of spin dynamics as described by $\boldsymbol{\tau} = \boldsymbol{\tau}_0 [(T_p-T_f/T_f)]^{-zv}$, where $\boldsymbol{\tau} = 1/2\pi f$ providing zv = 2.58 (Figure 14, left). The zv value for spin glasses is in the range of 4-12 and this result suggests that the interesting magnetic behaviour is not originated from spin glass rather than it is a conventional magnetic phase transition. We have repeated all the measurements several times to confirm and the reproducibility of this unprecedented results. The dehydrated compound was also subjected for the ac susceptibility measurement and shows the similar behaviour with $\Delta E/K_B$, $\boldsymbol{\tau}_0$ and zv values of 382 K, 3.0×10^{-09} S and 2.24 respectively (Figure 13, Figure 14 right). Similar value of relaxation barrier in **1** and **1′** and the dynamics of the magnetization is independent of the nature of magnetic interaction between two neighbouring Dy^{III} center. This observation clearly demonstrates that the slow relaxation of magnetization is due to the single-ion magnetic anisotropy of the Dy^{III} centre and similar results also observed in other sandwitched organometallic Dy^{III} complexes reported by Murugesu *et. al*.[46]

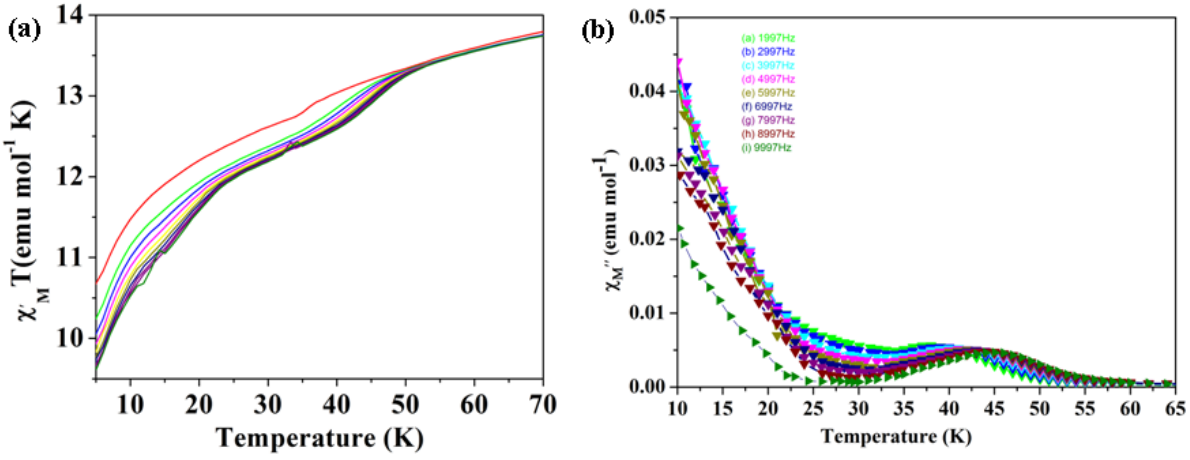

Figure 11. (a) Frequency dependence of χ_M'**T** and (b) χ_M'' for as-synthesized compound **1**.

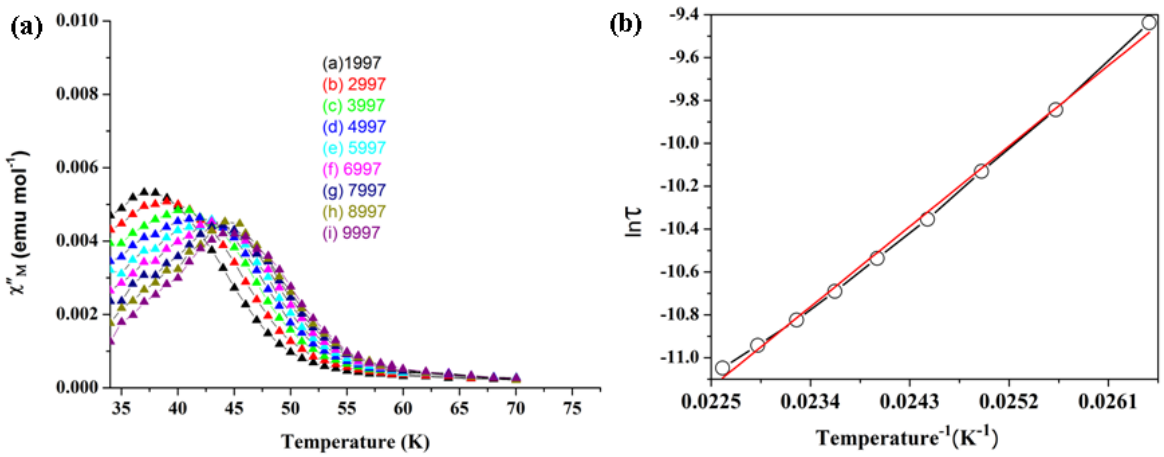

Figure 12. (a) Frequency dependence of χ_M'' of as-synthesized compound in temperature range 35-65 K and (b) the corresponding Arrhenius plot. (frequency in Hz are given in the inset of the figure)

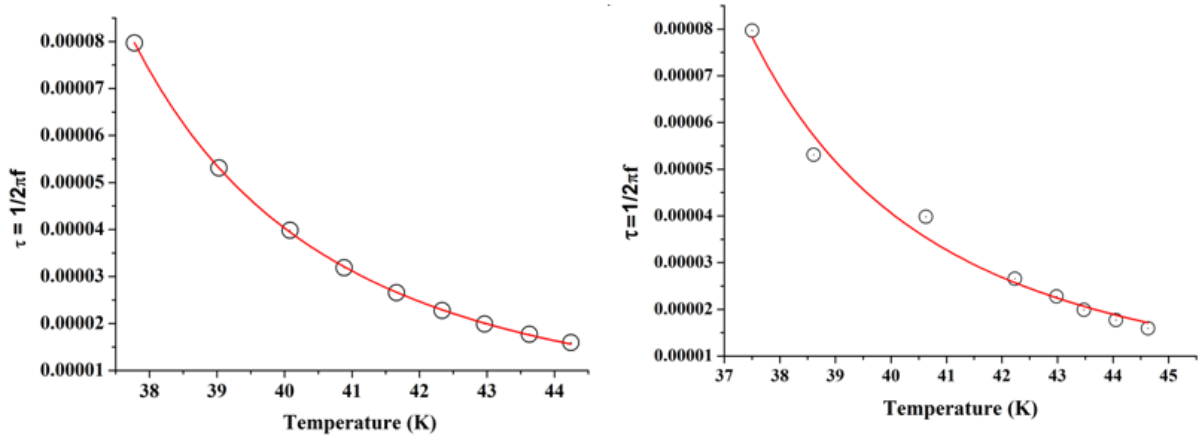

Figure 13. Frequency dependence of χ_M'' of dehydrated compound (**1′**) in temperature range 35-65 K and Arrhenius plot.

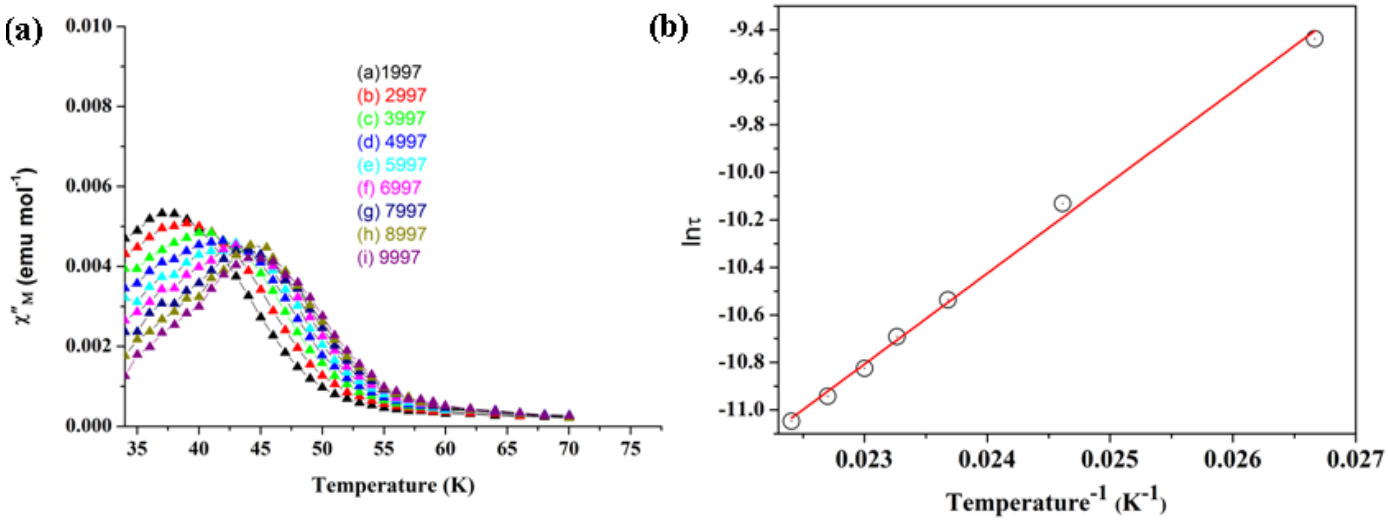

Figure 14. Frequency dependence of χ_M'' of as-synthesized compound **1** (left) and dehydrated compound **1′** (right) was fitted by conventional critical scaling law of the spin dynamics as described by $\tau = \tau_0 [(Tp-T_f/T_f)]^{-zv}$.

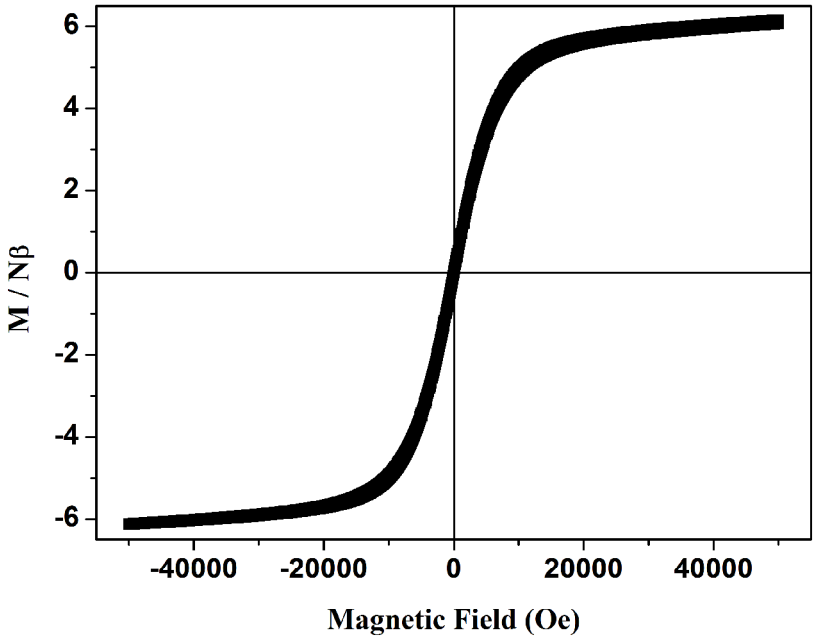

Figure 15. Isothermal field dependent magnetization for as-synthesized compound **1.**

6.4 Summary

A bimetallic (Dy^{III}-K^{I}) 3D framework with bidirectional channel structure decorated with unsaturated K^{I} sites has been successfully synthesized using oxalate as a linker. The as-synthesized compound **1** shows ferromagnetic behaviour and metal based luminescence properties. The vapor sorption studies reveal two step uptake for H_2O molecules and single step type I profile for MeOH, MeCN and EtOH molecules. The compound found to exhibit reversible water responsive change in magnetic and luminescent properties. The framework demands it's high impact in the field of molecular magnetism and posseses highest ever reported anisotropic barrier of 418 K among lanthanide MOFs including single molecular magnet, single ion magnet and single chain magnet. We could able to incorporate multiple functionalities into a single framework compound by choosing Dy^{III} as a metal ion.

6.5 References

1. M. Kurmoo, *Chem. Soc. Rev.* 2009**, 38**, 1353.

2. J. An, O. K.Farha, J. T. Hupp, E. Pohl, J. I. Yeh, and N. L. Rosi, *Nat. Commun*., 2012, **3**, 604

3. A. U. Czaja, N. Trukhan and U. Muller, *Chem. Soc. Rev.,*2009**, 38**, 1284.

4. S. Kitagawa, R. Kitaura and S.-i. Noro, *Angew. Chem. Int., Ed.,* 2004**, 43**, 2334.

5. M. D. Allendorf, C. A. Bauer, R. K. Bhakta and R. J. T. Houk, *Chem. Soc. Rev.,* 2009**,** **38**, 1330.

6. Y. Cui, Y. Yue, G. Qian and B., Chen, *Chem. Rev*., 2012,**112**, 1126.

7. M. P. Suh, H. J. Park, T. K. Prasad and D.-W. Lim, *Chem. Rev*., 2012, **112**, 782.

8. A. Hazra, P. Kanoo and T. K. Maji, *Chem. Commun.,* 2011*,* **47**, 538.

9. H. L. Sun, Z. M. Wang and S. Gao, *Coord. Chem. Rev.,* 2010, **254**, 1081.

10. D. J. Lun, G. I. N. Waterhouse and S. G. Telfer, *J. Am. Chem. Soc.,* 2011*,* **133**, 5806.

11 L. E. Kreno, K. Leong, O. K. Farha, M. Allendorf, R. P. Van Duyne and J. T. Hupp, *Chem. Rev.*, 2012, **112**, 1105.

12. J. Rocha, L. D. Carlos, F. A. A. Paz and D. Ananias, *Chem. Soc. Rev.,* 2011**,** **40**, 926.

13. B. Zhao, H. L. Gao, X. Y. Chen, P. Cheng, W. Shi, D. Z. Liao, S. P. Yan, and Z. H. Jiang, *Chem- Eur. J.*, 2006, **12**, 149.

14. E. Chelebaeva, J. Larionova, Y. Guari, R. A. Sá Ferrieira, L. D. Carlos, F. A. A. Paz, A. Trifonov, and C. Guérnin, *Inorg. Chem*., 2009, **48**, 11048.

15. X. Q. Zhao, B. Zhao, S. Wei, and P. Cheng, *Inorg. Chem*., 2009, **48**, 11057.

16. D. Gatteschi, R. Sessoli and J. Villain, *Molecular Nanomagnets*, Oxford University Press, 2006.

17. J. Vallezo, J. Cano, I. Castro, M. Julve, F. Lioret, O. Fabelo, L. Cañadillas-Delgado and E. Pardo, *Chem Commun.,* 2012, **48**, 7726.

18. I. J. Hewitt, I. Lan, C. E. Anson, J. Luzon, R. Sessoli and A. K. Powell, *Chem Commun.,* 2009, 6765.

19. Z. Chen, B. Zhao, P. Cheng, X. Q. Zhao, W. Shi and Y. Song, *Inorg. Chem.,* 2009, **48**, 3493.

20. D. Tanaka, T. Inose, H. Tanaka, S. Lee, N. Ishikawa and T. Ogawa, *Chem Commun.,* 2012, **48**, 7796.

21. M. J. Martinéz-Pérez, S. Cardona-Serra, C. Schlegel, F. Moro, P. J. Alonso, H. Prima-García, J. M. Clemente-Juan, M. Evangelisti, A. Gaita-Ariño, J. Sesé, J. V. Slageren, E. Coronado and F. Luis, *Phys. Rev. Lett.,*2012, **108**, 247213.

22. H. L. Sun, Z. M. Wang and S. Gao, *Coord. Chem. Rev.,* 2010, **254**, 1081.

23. C. Benelli and D. Gatteschi, *Chem. Rev.,* 2002, **102**, 2369.

24. S. D. Jiang, B-W. Wang, H-L Sun, Z-M Wang and S. Gao, *J. Am. Chem. Soc.,* 2011, **133**, 4730.

25. S. D. Jiang, S. S. Liu, L- N Zhou, B-W Wang, Z-M Wang and S. Gao, *Inorg.Chem.,* 2012, **51**, 3079.
26. C-S. Liu, M. Du, E. C. Sañudo, J. Echeiverria, M. Hu, Q. Zhang, L-M. Zhou and S. M. Fang, *Dalton. Trans.,*2011, **40**, 9366.
27. A. Bhunia, M. T. Gamer, L. Ungur, L. F. Chibotaru, A. K. Powell, Y. Lan, P. W. Rowesky, F. Menges, C. Riehn and G. N. Schatteburg, *Inorg.Chem.,* 2012, DOI**:** 10.1021/ic300065x.
28. P. H. Lin, T. J. Burchell, R. Clérac and M. Murugesu, *Angew. Chem. Int., Ed.,* 2008**,** **120**, 8980.
29. P. H. Lin, T. J. Burchell, L. Ungur, L. F. Chibotaru, W. Wernsdorfer and M. Murugesu, *Angew. Chem. Int., Ed.,* 2009, **48**, 9849.
30. F. Tuna, C. A. Smith, M. Bodensteiner, L. Ungur, L. F. Chibotaru, E. J. L. McInnes, R. E. P. Winpenny, D. Collison and R. A. Layfield, *Angew. Chem. Int., Ed.,* 2012**, 51**, 6976.
31. Y. Wang, X.-L. Li, T. –W. Wang, Y. Song and X. -Z. You, *Inorg. Chem.,* 2010, **49**, 969.
32. Z. Lu, X. Wang, Z. Liu, F. Liao, S. Gao, R. Xiong, H. Ma, D. Zhang and D. Zhu, *Inorg. Chem.,* 2006, **45**, 999.
33. N. Sabbatini and M. Guardigli, *Coord. Chem. Rev.,*1993, **123**, 201.
34. M. Kurmoo, H. Kumagai, K. W. Chapman and C. J. Kepert, *Chem. Commun.* 2005, 3012.
35. N. Motokawa, S. Matsunaga, S. Takaishi, H. Miyasaka, M. Yamashita and K. R. Dunbar, *J. Am. Chem. Soc.,* 2010, **132**, 11943.
36. X. N. Cheng, W-X Zhang, Y-Y Lin, Y-Z. Zheng and X- M. Chen, *Adv. Mater.*, 2007, **19**, 1494.
37. P. –E. Werner, L. Eriksson and M.; Westdahl, *J. Appl. Cryst.* 1985, **18**, 367.
38. SMART (V 5.628), SAINT (V 6.45a), XPREP, SHELXTL; Bruker AXS Inc. Madison, Wisconsin, USA, 2004.
39. G. M. Sheldrick, *Siemens Area Detector Absorption Correction Program*, University of Göttingen, Göttingen, Germany, 1994.
40. A. Altomare, G. Cascarano, C. Giacovazzo and A. Gualaradi, *J. Appl. Cryst.*, **1993**, *26*, 343.
41. G. M. Sheldrick, SHELXL 97, *Program for the Solution of Crystal Structure*, University of Gottingen, Germany, 1997.

42. G. M. Sheldrick, SHELXS 97*, Program for the Solution of Crystal Structure*, University of Gottingen, Germany, 1997.

43. A. L. Spek, *PLATON*, *Molecular Geometry Program,* The University of Utrecht, Utrecht, The Netherlands, 1999.

44. L. J. Farrugia, WinGX - A Windows Program for Crystal Structure Analysis. *J. Appl. Crystallogr*., 1999, **32**, 837.

45. M. M. Dubinin and L.V. Radushkevich, *Dokl. Akad. Nauk. SSSR*.,1947**, 55,** 331**.**

46. M. Jeletic, P-H Lin, J. J. Leroy, I. Korovkov, S. I. Gorelsky and M. Murugesu, *J. Am. Chem. Soc.,* 2011, **133**, 19286.

Lanthanide-Mucicate Frameworks: Hydrophilicity, Color Tunability, Metal ion Sensing and Magnetic Properties

Chapter 7: Lanthanide Mucicate Frameworks

Abstract:

Two 3D porous Tb^{III}-mucicate frameworks, $\{[Tb_2(Mu^{2-})_3(H_2O)_2]\cdot 4H_2O\}_n$ **(1)** and $\{[Tb(Mu^{2-})(Ox^{2-})_{0.5}(H_2O)]\cdot H_2O\}_n$ **(2)** have been synthesized under hydrothermal condition by changing the pH of the reaction medium. Both the structures are chararacterized by single-crystal X-ray diffraction study, powder X-ray diffraction and elemental analyses. Isostructural Eu^{III} framework of **1** and seven mixed Tb^{III}-Eu^{III}–mucicates were synthesized by doping different % of Eu^{III} under similar reaction conditions and unveil different emission color ranging from green to red when excited with the light of same wavelength. Lifetime measurements of pure and doped compounds suggest energy transfer from Tb^{III} (donor) to Eu^{III} (acceptor). Both the dehydrated Tb^{III}-MOFs exhibit selective water vapor sorption over other solvent molecules (MeOH, MeCN and EtOH) of less polarity and bigger size and has been correlated to the highly hydrophilic pore surfaces decorated with -OH groups and oxygen atoms from the carboxyl ($-COO^-$)groups of mucicate. Compounds **1** and **2** are magnetically similar and show antiferromagnetic interaction at low temperature. Furthermore framework **1** has been exploited for sensing of different metal ions based on Lewis acid-base interaction between pendant oxygen of hydroxo and carboxylate groups of mucicate (Mu^{2-}). The framework exhibits highly specific and selective sensing of Cu^{II} ions based on luminescence quenching.

(1) A paper related to this chapter has been published, S. Mohapatra, S. Adhikari, H. Riju and T. K. Maji, ***Inorg.Chem***, 2012, **51**, 4891.
(2) A paper related to this chapter has been submitted for publication.

Chapter 7: Lanthanide Mucicate Frameworks

7 .1 Introduction

Metal-organic frameworks (MOFs) with open structure have attracted considerable interest due to their promising applications in gas storage, catalysis, sensing, magnetism and luminescence.[1] Majority of research on MOFs has been focused on the transition metal ions.[1a-c,g.h] Recently, lanthanides (Ln^{III}) containing MOFs have attracted substantial interest due to their structural versatility (based on different coordination number) with interesting photoluminescence, magnetic and electronic properties resulting from the 4f electronic shell.[1d,e,2] In general, (Eu^{III}, Pr^{III}, sm^{III}), (Tb^{III}, Er^{III}), and (Tm^{III}, Ce^{III}) lanthanide ions show red, green and blue emission respectively and multiple emission colors can be achieved by adjusting the relative amounts of red, green and blue component in a host lanthanide compound.[3] Moreover, materials emitting multiple colours under single wavelength excitation are of paramount importance in the field of light display, lasers and optoelectronic devices. The emsisson properties of the different individual lanthanide compounds are well documentend,[1d-e,2a] however, colour modulation in lanthanide based MOFs by varying dopant concentration is yet to be properly explored.[3a,d,f] Furthermore, to date, a few lanthanide-organic frameworks with porous functinalities have been reported.[1i, 2b,c] Among the different organic linkers, 2,3,4,5-tetrahydroxyhexanedioic acid (mucic acid) is a rarely used naturally occuring organic linker and based on four hydroxy and two carboxy groups it can provide pH dependent flexible binding modes.[4] Moreover long alkyl chain with four hydroxy groups can be useful for generating flexible and porous structure. Systematic study on the effect of pH on framework structure[5] and overall network topology in metal-mucicate system yet to be reported. In this chapter we have used mucic acid as an organic linker for the synthesis of lanthanide (Tb^{III} and Eu^{III}) -based frameworks having flexible coordination geometry. We have isolated two Tb^{III}-muciate frameworks, $\{[Tb_2(Mu^{2-})_3(H_2O)_2]\cdot 4H_2O\}_n$**(1)** and $\{[Tb(Mu^{2-})(Ox^{2-})_{0.5}(H_2O)]\cdot H_2O\}_n$ **(2)** by changing the pH of the reaction media (Scheme 1). At pH ≈ 2 mucic acid acts both as a ligand and prcursor of oxalate whereas at pH≈ 4 it acts as a linker only. Eu^{III}-mucicate $\{[Eu_2(Mu^{2-})_3(H_2O)_2]\cdot 4H_2O\}_n$ **(3)** framework, and a series of Eu^{III}-doped frameworks (different atom %), isomorph of **1,** have been synthesised and luminescence colour of the compounds, $\{[Tb_{2-2x}\ Eu_{2x}(Mu^{2-})_3(H_2O)_2]\cdot 4H_2O\}_n$ were easily tuned from green, green-yellow, yellow, orange and red-orange by changing the doping concentration of Eu^{III} ion. To the best of our knowledge, this is a first report of color tunability and pH controlled synthesis of lanthanide-mucicate frameworks. The temperature dependent magnetic susceptibility stydy of **1** and **2** suggests both the frameworks are antiferromagnetic in nature. Furthermore because of the presence of pendant oxygens of carboxylate and hydroxo group of mucicate on the pore surface, compound **1** has been exploited for the sensing of metal ions and suggest highly specific sensing for Cu^{II} ions.

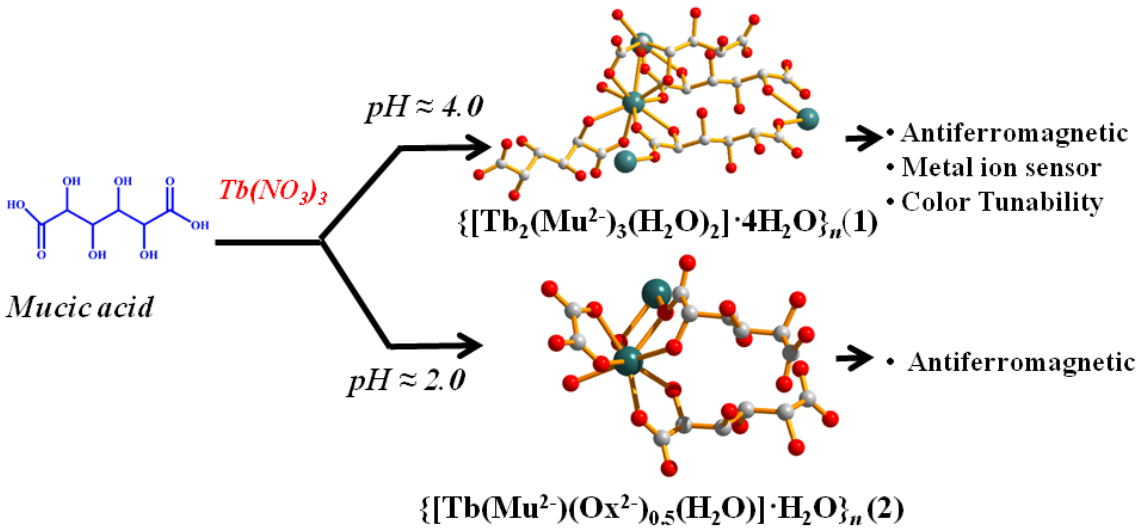

Scheme 1. pH controlled synthesis of Tb^{III}-mucicate (**1**) and Tb^{III}-mucicate-oxalate (**2**) frameworks.

7.2 Experimental section

7.2.1 Materials All the reagents were commercially available and used as supplied without further purification. $Tb(NO_3)_3{\cdot}5H_2O$, $Eu(NO_3)_3{\cdot}5H_2O$ and mucic acid were obtained from Aldrich Chemical Co.

7.2.2 Synthesis of $\{Tb_2(Mu^{2-})_3(H_2O)_2]{\cdot}4H_2O\}_n$ (1) and $\{[Tb(Mu^{2-})(Ox^{2-})0.5(H_2O)]{\cdot}H_2O\}_n$ (2)

Mucic acid, (0.079 g, 0.375 mmol) was dissolved in 10 mL water by using KOH (0.042 g, 0.75 mmol). To the above clear solution $Tb(NO_3)_3{\cdot}5H_2O$ (0.109 g, 0.25 mmol) was added and vigorously stirred for 1 h. A white colour reaction mixture of pH ≈ 4.0 was obtained. Then reaction mixture was transferred into a 23 mL Teflon-lined stainless steel autoclave and then kept in a oven at 120^o C for 72 hour. Then the autoclave was kept out and allowed to cool to room temperature. White colour crystalline solid of compound **1** was obtained and filtered and washed several times with water to remove unreacted starting materials and subsequently dried under vacuum. Yield 72.5 % (relative to Tb^{III}). Anal. Calcd. for $C_{18}H_{36}Tb_2O_{30}$ (**1**): C 20.57, H 3.43.Found: C 20.59, H 3.31, IR (KBr pellet, cm^{-1}): 3427s ν(O-H); 1653s $\nu_a(COO_{unidentate})$, 1596s $\nu_a(COO_{bridging})$, 1314m $\nu_s(COO)$.

Compound **2** was synthesized adopting similar reaction condition as of **1** except pH, the reaction was carried out at pH ≈ 2.0. Yield 30% Anal. Calcd. for $C_7H_{12}TbO_{12}$ (**2**): C 18.79, H 2.68 Found: C 18.85, H 2.75, IR (KBr pellet, cm^{-1}): 3427s ν(O-H); 1656s $\nu_a(COO_{unidentate})$, 1596s $\nu_a(COO_{bridging})$, 1314m $\nu_s(COO)$

7.2.3 Synthesis of $\{Eu_2(Mu^{2-})_3(H_2O)_2].4H_2O\}_n$ (3)

Compound **3** was synthesized adopting the similar procedure as of **1**. Yield 68%. Anal Calcd for $C_{18}H_{36}Eu_2O_{30}$ (**1**): C 20.84, H 3.47.Found: C 20.79, H 3.39, IR (KBr pellet, cm^{-1}): 3429 s ν(O-H); 1657s $\nu_a(COO_{unidentate})$, 1594s $\nu_a(COO_{bridging})$, 1318m $\nu_s(COO)$.

7.2.4 Synthesis of $\{[Tb_{2x}Eu_{2(1-x)}(Mu^{2-})_3(H_2O)_2]\cdot 4H_2O\}_n$

A requisite amount (see Table 1 below) of $Eu(NO_3)_3\cdot 5H_2O$ &$Tb(NO_3)_3\cdot 5H_2O$ were dissolved in 5 ml water in a 10 mL beaker. In a another 10 mL beaker mucic acid (0.375 mmol, 0.079 g) and KOH (0.75 mmol, 0.042 g) were dissolved in 5 ml distilled water and two aqueous solutions were mixed in a 23 mL teflon container and a white color mixture was obtained. The mixture solution was vigorously stirred for 1 h and fitted into an autoclave. Then the whole system was kept in an oven at 120 ^oC for 72 hours. After 72 hours the autoclave was kept out and allowed to cool to room temperature. The white colored crystalline solid was filtered and washed with water several times to remove unreacted starting materials and dried under vacuum. All the powder samples have been characterized by the IR, CHN, PXRD and EDAX analyses.

Table1: Synthetic conditions for different % of Eu^{III} doped compounds.

Sl. No	Reaction Stoichimetry	% of Eu^{III} used in compound 1	% of Eu^{III} obtained from EDX data
1	$Eu(NO_3)_3$ (0.00125 mmol, 0.005g) + $Tb(NO_3)_3$ (0.24875 mmol, 0.108 g) + Mucic acid (0.375 mmol, 0.079 g + KOH (0.75 mmol, 0.42 g) + 7 ml H_2O	**0.5**	**0.6**
2	$Eu(NO_3)_3$ (0.005 mmol, 0.002 g) + $Tb(NO_3)_3$ (0.245 mmol, 0.107g) + Mucic acid (0.375 mmol, 0.079g + KOH (0.75 mmol, 0.42 g)+7 ml H_2O	**1.25**	**1.24**
3	$Eu(NO_3)_3$ (0.011 mmol, 0.005 g) + $Tb(NO_3)_3$ (0.238 mmol, 0.104 g)+ Mucic acid (0.375 mmol, 0.079 g + KOH (0.75 mmol, 0.42g)+7ml H_2O	**5**	**4.33**

4	$Eu(NO_3)_3$ (0.025mmol, 0.010g) + $Tb(NO_3)_3$ (0.225 mmol, 0.097g) + Mucic acid (0.375mmol, 0.079g + KOH (0.75mmol, 0.42g) + 7 ml H_2O	**10**	**7.03**
5	$Eu(NO_3)_3$ (0.0375mmol, 0.016g) + $Tb(NO_3)_3$ (0.2125mmol, 0.0924g) + Mucic acid (0.375mmol, 0.079g + KOH (0.75mmol, 0.42g) + 7ml H_2O	**15**	**15.3**
6	$Eu(NO_3)_3$ (0.0625 mmol, 0.0265 g)+$Tb(NO_3)_3$(0.1875 mmol, 0.082 g) + Mucic acid (0.375 mmol, 0.079g + KOH (0.75 mmol, 0.42g) + 7ml H_2O	**25**	**24**
7	$Eu(NO_3)_3$ (0.125 mmol, 0.0535g) + $Tb(NO_3)_3$ (0.125 mmol, 0.054 g) + Mucic acid (0.375 mmol, 0.079g + KOH (0.75 mmol, 0.42 g) + 7 ml H_2O	**50**	**49.69**

7.2.5 Physical measurements

The elemental analyses were carried out on a Perkin Elmer 2400 CHN analyzer. IR spectra were recorded on a Bruker IFS 66v/S spectrophotometer with samples prepared in KBr pellets in the region 4000-400 cm^{-1}. Thermogravimetric analysis (TGA) were carried out on METTLER TOLEDO TGA850 instrument in the temperature range of 25 - 650 °C under nitrogen atmosphere (flow rate of 50 mL min^{-1}) at a heating rate of 5 °C/min. X-ray powder diffraction (PXRD) patterns were recorded on a Bruker D8 Discover instrument using Cu-Kα radiation. UV-Vis absorption measurements were recorded on a Perkin-Elmer Lambda 900 UV/Vis/NIR spectrometer. Fluorescence spectra were recorded on a Perkin Elmer model LS 55 spectrophotometer. Lifetime measurements were carried out at room temperature using Edinburgh Instrument FLSP 920 spectrometer.

7. 2.6 Adsorption measurements

7.2.6.1 Gas adsorption

N_2 at 77 K and CO_2 at 195 K adsorption studies with the dehydrated sample of **1** (*i.e* **1′)** and **2 (***i.e* **2′)** were carried out using QUANTACHROME QUADRASORB-*SI* analyzer. In the sample tube about 100 -120 mg sample was placed which had been prepared at 413 K under a dynamic vacuum (10^{-1} pa) for about 12 h prior to the measurement of the isotherms. Helium gas (99.999% purity) at a certain pressure was introduced in the gas chamber and allowed to diffuse into the sample chamber by opening the valve. The

amount of gas adsorbed was readily calculated from the pressure difference (P_{cal}-P_e), where P_{calc} is the calculated pressure with no gas adsorption and P_e is the observed equilibrium pressure. All operations were computer controlled and automatic.

7.2.6.2 Vapour adsorption

The adsorption isotherms of different solvents (H_2O, CH_3CN, EtOH, at 298 K and MeOH at 293 K) were measured in the vapor state by using BELSORP-aqua-3 volumetric adsorption instrument from BEL, Japan. In the sample chamber (~12 mL) maintained at T ± 0.03 K was placed the adsorbent sample (~100 mg), which had been pre-treated at 413 K with vacuum level of 10^{-1} Pa for about 12 hours prior to measurement of the isotherms. The adsorbate was charged into the sample tube, and then the change in pressure was monitored and the degree of adsorption was determined by the decrease in pressure at the equilibrium state. All operations were computer-controlled and automatic.

7.2.7 X-ray crystallography

Suitable single-crystals of **1** and **2** were mounted on a thin glass fiber with commercially available super glue. X-ray single-crystal structure data were collected on a Bruker Smart–CCD diffractometer equipped with a normal focus, 2.4 kW sealed tube X-ray source with graphite monochromated Mo-$K\alpha$ radiation (λ = 0.71073 Å) operating at 50 kV and 30 mA, with ω scan mode. The programme SAINT [7a] was used for integration of diffraction profiles and absorption corrections were made with SADABS programme.[7b] Both the structures were solved by direct methods using SIR-92 [7c] and followed by successive fourier and difference fourier syntheses. All the non-hydrogen atoms were refined anisotropically. All calculations were carried out using SHELXL 97,[7d] SHELXS 97, [7e] PLATON,[7f] and WinGX system, ver. 1.70.01.[7g] Crystal data, Structure refinement parameters and selected bond distances and angles for **1** and **2** are given in table 2 - 4.

7.3 Result and discussion

7.3.1 Structural description of $\{Tb_2(Mu^{2-})_3(H_2O)_2]\cdot 4H_2O\}_n$ (1) and $\{[Tb(Mu^{2-})(Ox^{2-})_{0.5}(H_2O)]\cdot H_2O\}_n$ (2)

The Tb^{III}-mucicate frameworks have been synthesized hydrothermally at 120˚C at pH ≈ 4.0 (for **1**) and 2.0 (for **2)** . Various coordination modes of mucicate (Mu^{2-}) to Tb^{III} are shown in Figure 1. $\{[Tb_2(Mu^{2-})_3(H_2O)_2]\cdot 4H_2O\}_n$(**1**) and $\{[Tb(Mu^{2-})(Ox^{2-})_{0.5}(H_2O)]\cdot H_2O\}_n$ (**2**) crystallizes in triclinic space group $P\bar{1}$ (Table 2) and structure determination of both **1** and **2** reveal 3D coordination framework of Tb^{III} bridged by Mu^{2-} (dianionic form of mucic acid) in **1** and Mu^{2-} and oxalate (Ox^{2-}) in **2**. There are four different types of binding mode of Mu^{2-} viz *Mu^{2-}_a, Mu^{2-}_b* and *Mu^{2-}_c* and *Mu^{2-}_d* in compounds **1** and **2** (Figures **1 & 2**).

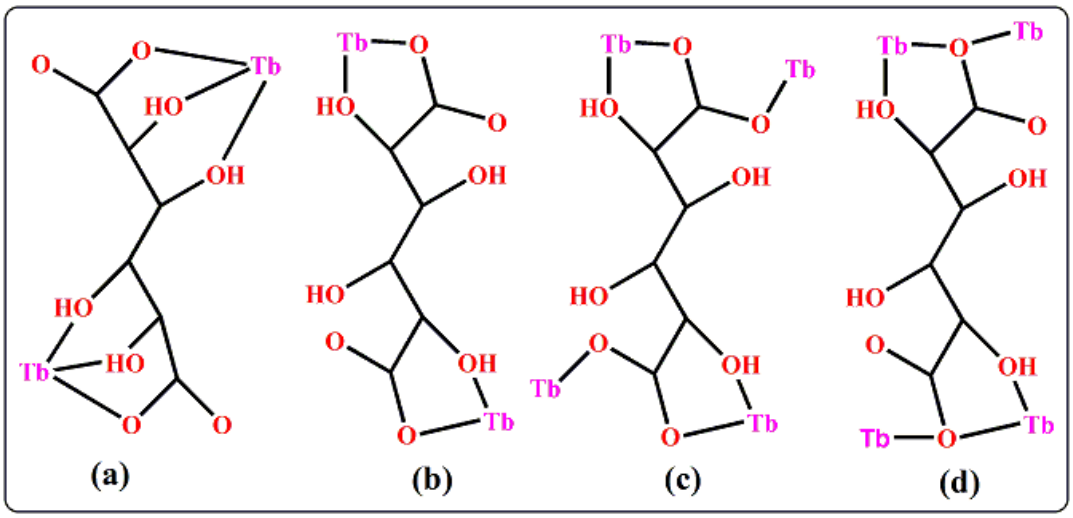

Figure 1. Schematic of different binding modes of mucicate observed in compound **1** and **2**.

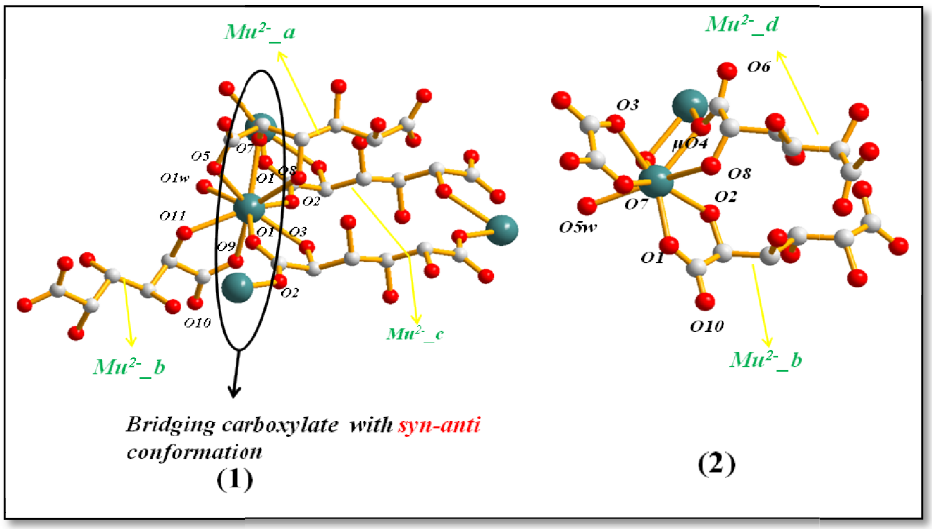

Figure 2. View of the coordination environment of Tb^{III} in **1** and **2** , showing four different binding modes of mucicate (*Mu^{2-}_a* to *Mu^{2-}_d*).

In **1**, nine coordinated Tb1 center connected to three different Mu^{2-} (*Mu^{2-}_a, Mu^{2-}_b* and *Mu^{2-}_c*) to satisfy coordination number eight, whereas in **2**, Tb1 centre is coordinated to two Mu^{2-} (*Mu^{2-}_b*, *Mu^{2-}_d*) and one Ox^{2-} to satisfy coordination number seven (Figure 2).

Ninth and eighth coordination of Tb1 in **1** and **2** are occupied by water molecule, respectively.In **1**, Mu^{2-}_*a* and Mu^{2-}_*b* are chelated to a Tb^{III} center in tridentate (O5, O7, O8) and bidentate (O9, O11) fashion, respectively to build a 1D zigzag chain along the crystallographic *c*-direction (Figure 3a). The chains are lying on the *ac* plane (Figure 3b) which are diagonally pillared by the Mu^{2-}_*c* where *syn-anti* bridged carboxylate oxygens (O1, O2) and O3 from OH coordinated to Tb^{III} centres resulting in a 3D structure (Figure 4a). In compound **2,** each octa-coordinated Tb1 centre chelated to Ox^{2-} through the oxygen atoms (O3, O7) and two Mu^{2-} , (Mu^{2-}_*b* and Mu^{2-}_*d*) through oxygens (O1, O2, and μ2-O4, O8). A 2D sheet is formed by the coordination of Mu^{2-}_*b* and Mu^{2-}_*d* in crystallographic *bc* plane (Figure 3) which is further connected by Ox^{2-} along crystallographic *a* direction to form a 3D coordination framework (Figure 4b).

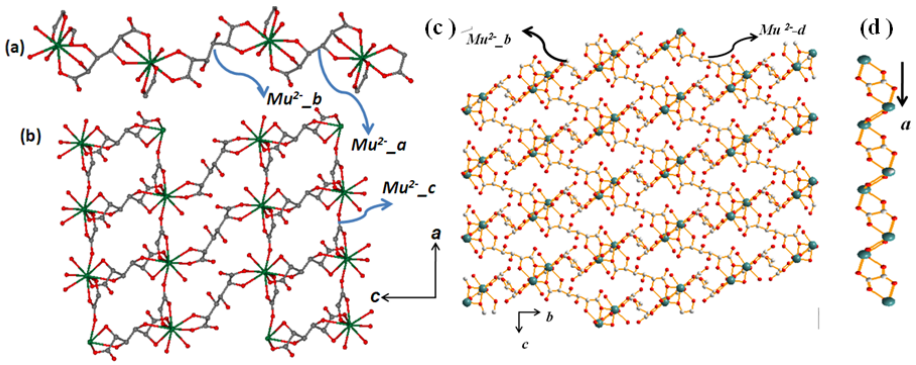

Figure 3. (a) 1D chains of Tb^{III} alternatively connected by the mucicates (Mu^{2-}_*a* and Mu^{2-}_*b*); (b) View of 2D sheet in the *ac* plane; **(c)** 1D chains of Tb^{III} is formed by the mucicate (Mu^{2-}_*d)* which are connected by the another mucicate (Mu^{2-}_*b*) to form 2D sheet like structure in the *bc* plane in **2** (d) 2D sheets are further connected by the oxalates (Ox^{2-}) along crystallographic *a* direction to form 3D structure in **2** (Figure 4).

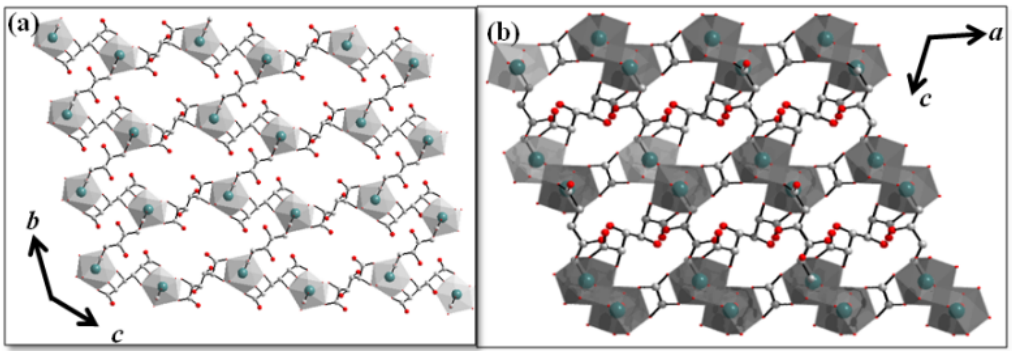

Figure 4. (a) 3D structure of 1 viewing along a-axis formed by the three different binding types of Mu^{2-} (b) 3D structure of 2 viewing along b-axis formed by the two different Mu^{2-} and one Ox^{2-}.

Topological analysis suggests both the frameworks have 7-c uninodal structure with point symbol $\{3^6;4^8;5^6;6\}$ and type of topology is svi-x/I 4/m c m->I b a m, Bond sets: 1,4,5,6: svi-x; obtained from Topos Topological Database (TTD)[6b] (Figure 5). Tb1–O bond distances are in the range of 2.315(5) – 2.574(4) Å and 2.288(8) – 2.444(4) Å for **1** and **2,** respectively (Table 3 & 4). 3D framework of **1** contains dumbbell shaped channel (4.9×6.9Å^2) along *a* axis and rectangular shaped channels (2.8×1.7Å^2) along *b* axis occupied by the guest water molecules (Figures 6a-b, 7a). Compound **2** contains hexagonal shaped channels along *c* axis with a smaller pore aperture (3.85×2.31 Å^2) (Figure 6c & 7b). Compound **1** and **2** contains four and one guest water molecules per formula unit, respectively. The effective pore dimension of the dumbbell shaped channels in **1** is less due to the presence of hanging hydroxyl groups on the pore walls (Figure 7a). Calculation using PLATON[6a] suggest that the dehydrated framework of **1** and **2** contains 23.7% and 17% void space to the total crystal volume.

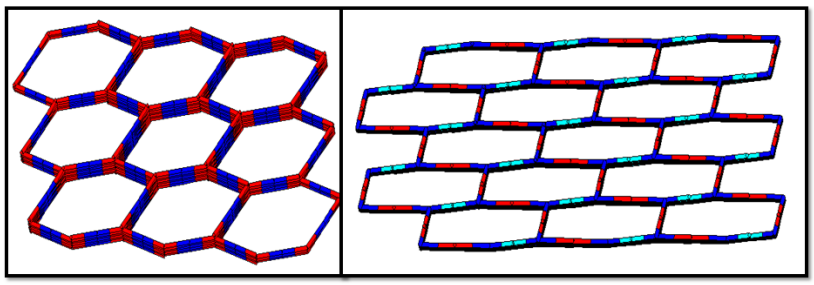

(1) **(2)**

Figure 5. Simplified topological diagram for compound **1** (left side) and compound **2** (right side).

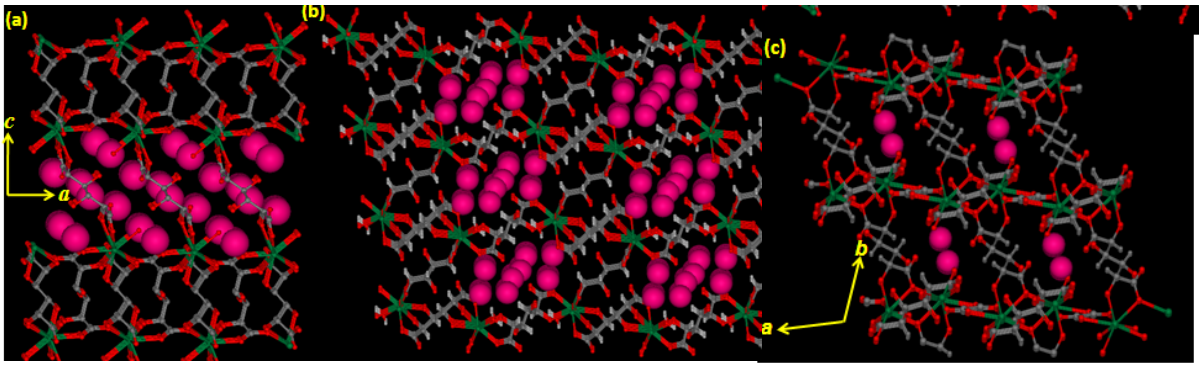

Figure 6. (a) and (b) showing water filled channels in framework **1** along the crystallographic *b* and *a*-axis, and (c) showing water filled channels in framework **2** along the crystallographic *c*-axis.

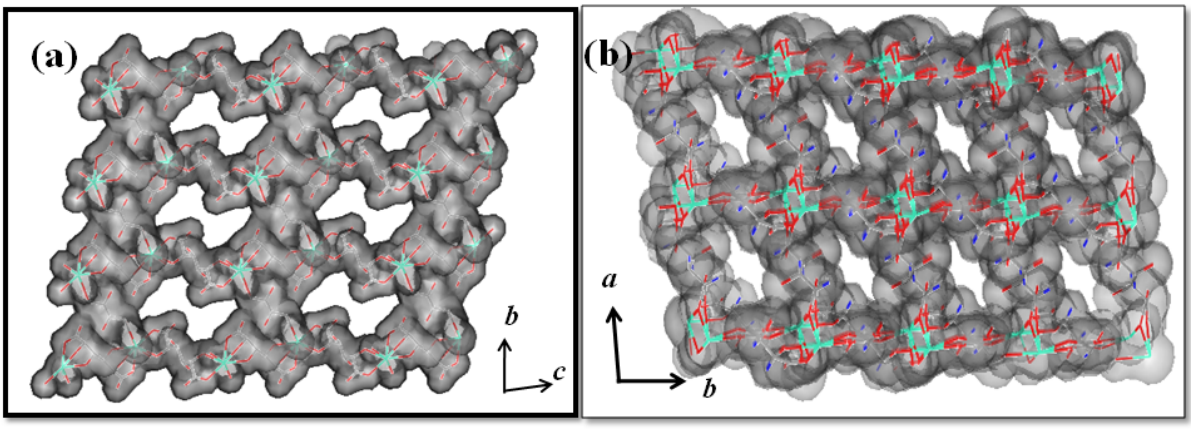

Figure 7. View of the pores. (a) dumbbell shaped pores in **1** along the crystallographic *a*-axis; (b) hexagonal shaped pores in **2** along the crystallographic *c*-axis.

Table 2: Crystal data and structure refinement parameters for **1** and **2.**

parameters	**1**	**2**
Empirical formula	$C_{18}H_{36}Tb_2O_{30}$	$C_7H_{12}TbO_{12}$
Formula weight	1050.31	447.03
Crystal system	Triclinic	Triclinic
Space group	*P*ī (No. 2)	*P*ī (No. 2)
a, Å	6.0783(2)	8.5574(8)
b, Å	8.6457(2)	8.8061(8)
c, Å	16.1954(5)	9.8454(9)
α, deg	77.801(2)	98.523(4)
β, deg	88.351(2)	112.604(4)
γ, deg	83.637(1)	108.548(4)
V, Å^3	826.73(4)	443.04(1)
Z	1	1
T, K	293	293
μ, mm^{-1}	4.365	5.788
D_{calcd}, g/cm^3	2.166	2.361
λ (Mo-Kα) (Å)	0.71073	0.71073
θ max (°)	25.7	23.9
Total data	11282	4837
Unique data	3146	1897

Data [$I>2\sigma(I)$]	2834	1664
R_{int}	0.060	0.046
GOF on F^2	1.10	1.07
$R_1[I>2\sigma(I)]$[a]	0.0322	0.0439
$R_w[I>2\sigma(I)]$[b]	0.0858	0.1173

[a] $R = \sum||Fo|-|Fc||/\sum|Fo|$; [b] $R_w = [\sum\{w(Fo^2-Fc^2)^2\}/\sum\{w(Fo^2)^2\}]^{1/2}$

Table 3. Selected bond lengths (Å) and angles (°) for $\{Tb_2(Mu^{2-})_3(H_2O)_2].4H_2O\}_n$ **(1)**

Tb1-O1	2.369(4)	Tb1-O1W	2.429(5)
Tb1-O3	2.474(4)	Tb1-O5	2.412(4)
Tb1-O7	2.574(4)	Tb1-O8	2.466(3)
Tb1-O9	2.315(5)	Tb1-O11	2.494(4)
Tb1-O2_b	2.378(4)		
O1-Tb1-O1W	142.64(14)	O1-Tb1-O3	63.95(14)
O1-Tb1-O5	79.63(16)	O1-Tb1-O7	128.05(13)
O1-Tb1-O8	74.08(14)	O1-Tb1-O9	89.12(15)
O1-Tb1-O11	71.84(13)	O1-Tb1-O2_b	133.10(14)
O1W-Tb1-O3	141.01(14)	O1W-Tb1-O5	85.04(15)
O1W-Tb1-O7	71.57(14)	O1W-Tb1-O8	133.77(15)
O1W-Tb1-O9	78.09(16)	O1W-Tb1-O11	70.88(16)
O1W-Tb1-O2_b	79.48(16)	O3-Tb1-O5	133.85(13)
O3-Tb1-O7	118.45(11)	O3-Tb1-O8	68.96(13)
O3-Tb1-O9	74.26(14)	O3-Tb1-O11	119.77(14)
O2_b-Tb1-O3	69.19(14)	O5-Tb1-O7	63.46(14)
O5-Tb1-O8	74.68(13)	O5-Tb1-O9	135.08(14)
O5-Tb1-O11	69.11(13)	O2_b-Tb1-O5	137.16(15)
O7-Tb1-O8	62.20(13)	O7-Tb1-O9	142.83(15)

Symmetry code: b = 1+x, y, z

Table 4. Selected bond lengths (Å) and angles (°) for $\{[Tb(Mu^{2-})(Ox^{2-})_{0.5}(H_2O)].H_2O\}_n$ **(2)**

Tb1-O1	2.394(9)	Tb1-O2	2.288(8)
Tb1-O3	2.397(9)	Tb1-O4	2.381(8)
Tb1-O5w	2.348(10)	Tb1-O7_a	2.444(9)
Tb1-O4_c	2.406(8)	Tb1-O8_c	2.386(7)
O1-Tb1-O2	65.9(3)	O3-Tb1-O5W	79.4(3)
O1-Tb1-O3	150.4(3)	O3 -Tb1-O7_a	67.0(3)
O1-Tb1-O4	74.1(3)	O3-Tb1-O4_c	75.6(3)
O1-Tb1-O5W	115.7(3)	O2-Tb1-O5W	82.2(3)
O1-Tb1-O7_a	140.1(2)	O2-Tb1-O7_a	77.6(3)
O1-Tb1-O4_c	77.8(3)	O2-Tb1-O4_c	133.6(3)
O1-Tb1-O8_c	86.2(3)	O2-Tb1-O8_c	84.1(3)
O2-Tb1-O3	143.6(3)	O3-Tb1-O4	83.7(3)

Symmetry code: a = -1+x, y, z; c =1-x, -y, 1-z

Table 5: Result of indexing of powder pattern.

	D-OBS	Q-OBS	QO-QC	H	K	L
1	15.825	.00399	.00000	-1	0	0
2	8.403	.01416	.00001	0	1	0
3	8.170	.01498	.00004	1	1	0
4	7.922	.01593	.00002	-2	0	0
5	6.846	.02133	.00003	-1	1	0
6	6.477	.02383	.00001	2	1	0
7	6.038	.02743	.00002	0	0	1
8	5.654	.03128	.00001	1	0	1
9	5.273	.03597	.00007	-3	0	0
10	5.128	.03803	.00005	1	1	1
11	4.962	.04061	.00003	3	1	0
12	4.792	.04355	.00006	-2	0	1
13	4.672	.04581	.00001	0	-1	1
14	4.619	.04687	.00008	2	1	1
15	4.350	.05285	.00001	1	-1	1
16	4.287	.05440	.00000	1	2	0
17	4.088	.05983	.00000	-2	1	1
18	3.987	.06291	.00006	3	0	1
19	3.911	.06539	.00003	4	1	0
20	3.864	.06699	.00002	-1	2	0
21	3.708	.07273	.00009	-3	-1	1
22	3.684	.07369	.00005	3	2	0
23	3.636	.07563	.00001	0	2	1
24	3.562	.07882	.00003	2	2	1
25	3.472	.08297	.00005	-3	1	1
26	3.409	.08606	.00003	-1	2	1
27	3.368	.08814	.00000	4	1	1
28	3.319	.09078	.00000	4	0	1
29	3.238	.09535	.00002	4	2	0
30	3.191	.09822	.00004	5	1	0

7.3.2 Characterization of isostructural Eu^{III} and mixed Tb^{III}/Eu^{III} frameworks of 1

PXRD pattern of $\{[Eu_2(Mu^{2-})_3(H_2O)_2]\cdot 4H_2O\}_n$ (**3**) and other compounds with different ratios of Tb^{III}/Eu^{III} are similar to **1** and indexing of the pattern for **3** using Crysfire 2004 program[6c] suggest the identical cell parameter to **1** (Table 5) confirming **1** , **3** and different Eu^{III} doped Tb^{III} compounds are isomorphous (Figure 8).

Cell parameters: a = 16.19805 Å, b = 8.64270 Å, c =6.07702 Å, α = 83.62°, β = 88.35°, γ = 77.83°, V = 826.47 Å^3

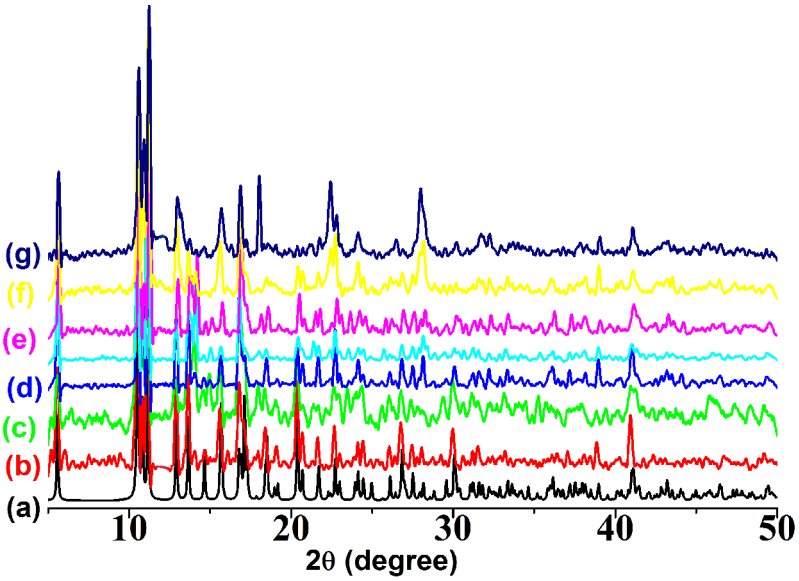

Figure 8. PXRD patterns: (a) simulated pattern of $\{[Tb_2(Mu^{2-})_3(H_2O)_2]\cdot 4H_2O\}_n$ (**1**), (b) as-synthesized pattern of $\{[Eu_2(Mu^{2-})_3(H_2O)_2]\cdot 4H_2O\}_n$ (**3**), (c)-(g) powder patterns of mixed Tb^{III}-Eu^{III} compound by dopings different % of Eu^{III} in compound **1** (c) 50 atom % Eu, (d) 25 atom % Eu^{III}, (e) 15 atom% , (f) 7.03 atom% Eu^{III}, (g) 5 atom% Eu^{III}

7.3.3 Thermal stability

Thermogravimetric analysis (TGA) suggests the concomitant release of both coordinated and crystalline water molecules in compound **1** and stepwise release of crystalline and coordinated water molecules in compound **2** (Figure 8a). Both the dehydrated frameworks (**1′** and **2′**) are stable up to 230˚C. Powder X–ray diffraction (PXRD) study of both dehydrated frameworks show significant change indicating structural transformation after removal of the guest and coordinated water molecules rather than collapse of the framework (Figure 10).

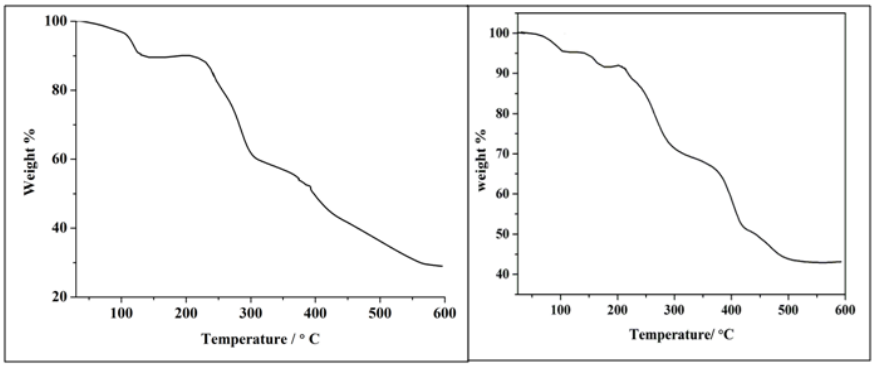

Figure 9. TGA profiles (left side for compound **1** and right side for compound **2)** in the temperature range of 28-600°C under the N_2 atmosphere (flow rate 50 mL/min).

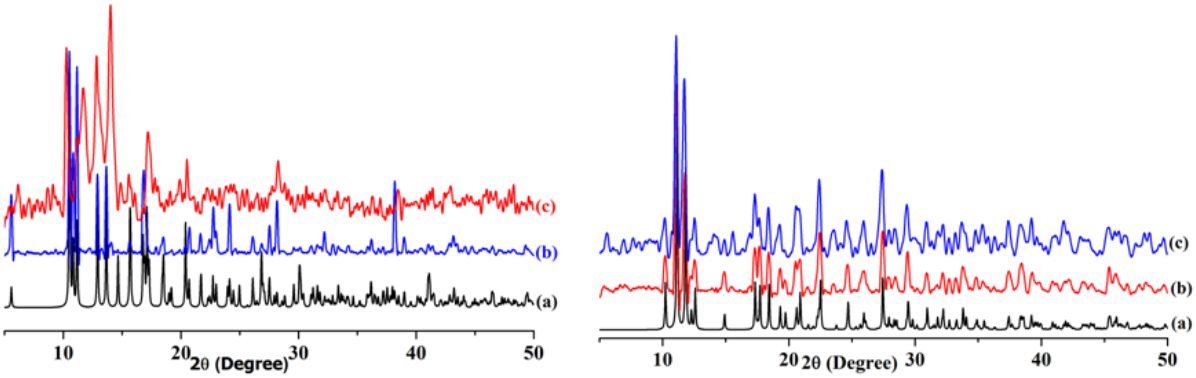

Figure 10. PXRD patterns of **1** (left side) and **2** (right side); (a) simulated from X-ray single-crystal data; (b) as-synthesized compound; (c) dehydrated at 120˚C.

7.3.4 Adsorption property

To examine the permanent porosity, the dehydrated framework **1′**and **2′** were subjected to adsorption studies with N_2 (kinetic diameter 3.6 Å) and CO_2 (kinetic diameter 3.3 Å) at 77 K and 195 K, respectively. Both the isotherms show typical type-II profile with small uptake up to P/P_0 =**1,** indicating only surface adsorption (Figure 11). These results can be correlated to the smaller effective pore size of **1′** and **2′** compared to the kinetic diameter of N_2 and CO_2. In case of **1′**, effective pore size is smaller due to blocking by pendent hydroxyl groups. Water (kinetic diameter 2.65 Å), MeOH (4.0 Å), MeCN (4.3 Å) and EtOH (4.5 Å) vapor sorption isotherms were measured at ambient condition to study the selectivity based on polarity and pore size of the framework. As shown in Figure 12, the sorption profile of H_2O shows typical type-I curve with steep uptake at low pressure region whereas other solvents are not adsorbed by none of the compounds suggesting the strong hydrophilic nature of the pore surface. The amount of final uptake are about 160 and 40 mL g^{-1} at P/P_0 ~1, which corresponds about 7 and 1 molecule of H_2O per formula unit of **1′** and **2′,** respectively. The values of βE_o which reflect the adsorbate-adsorbent affinity are significantly high (9.7 kJ mol^{-1}(**1′**) and 8.99 kJ mol^{-1}(**2′**)) also suggesting strong hydrophilic nature of the framework which can be attributed to the presence of pendent oxygen (carboxyl group) and hydroxyl group on the pore surface. The effective pore dimensions in **1′** and **2′** are also not sufficient for the inclusion of larger guest molecules like MeOH, MeCN and EtOH.

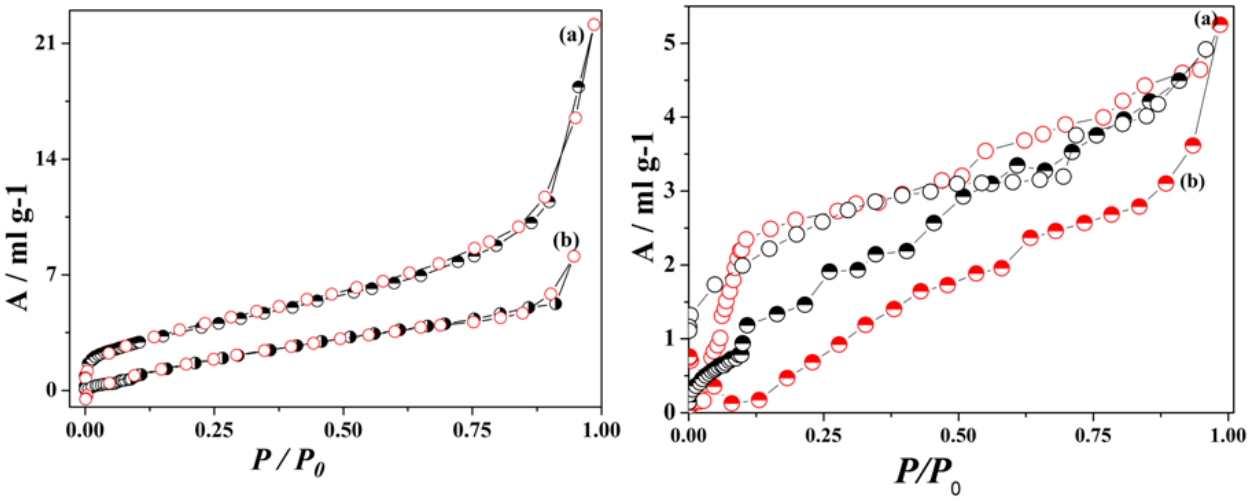

Figure 11. (a) N_2 and (b) CO_2 gas sorption isotherms at 77 K and 195 K respectively; (left side for compound **1′** and right side for **2′).**

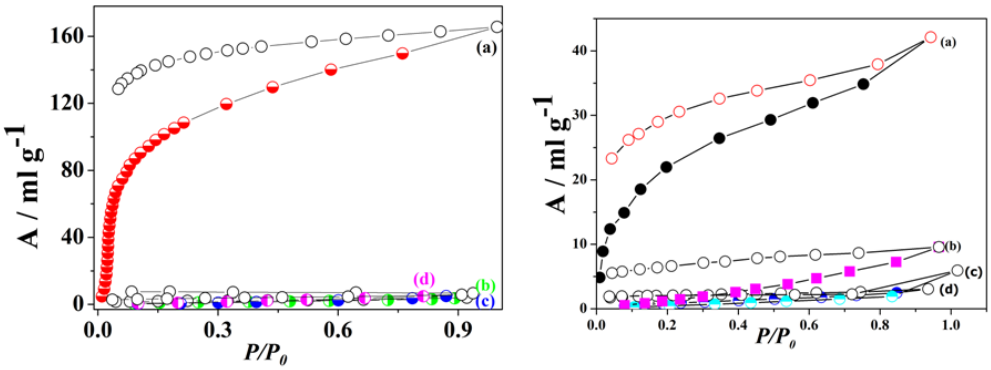

Figure 12. Solvent vapor sorption isotherms for dehydrated compound of **1′** (left) and **2′** (right); (a) H_2O (298 K), (b) MeOH (293 K), (c) EtOH (298 K), (d) MeCN (298 K). P_0 is the saturated vapour pressure of the solvent at the respective temperature.

7.3.5 Photoluminescence property and tuneable emission colour

The typical emission spectrum of **1** and its Eu^{III}-analogue, **3** show their respective characteristics peaks when excited at 315 nm. Compound **1** shows emission peaks at 485, 545, 585 and 620 nm corresponds to transitions from $^5D_4$ to ^7F_J (where J = 6, 5, 4, 3) for Tb^{III} (Figure 13) whereas compound **3** exhibits emission at 590, 615, 650 and 693 nm related to $^5D_0$ to ^7F_J transitions where J =1, 2, 3, 4 respectively (Figure 14). The red color emission of the pure Eu^{III} compound (**3**) is due to the most intense peak at 615 nm for $^5D_0$ to $^7F_2$ transition and green color of the pure Tb^{III} compound is due to the most intense peak at 545 nm for $^5D_4$ to $^7F_6$ transition.

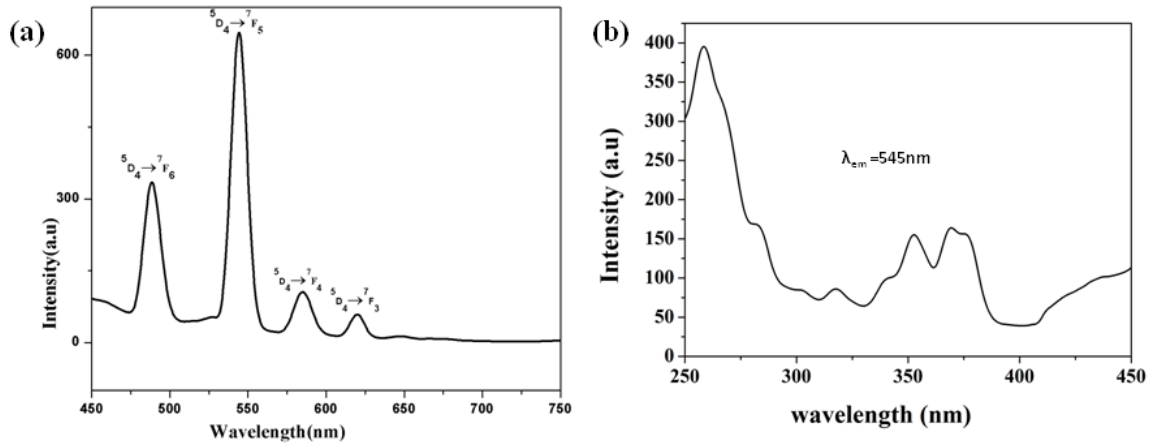

Figure 13. (a) Emission spectrum of as-synthesized compound $\{[Tb_2(Mu^{2-})_3(H_2O)_2].4H_2O\}_n$ (**1**) and (b) corresponding excitation spectrum of 1 with λ_{em}= 545 nm

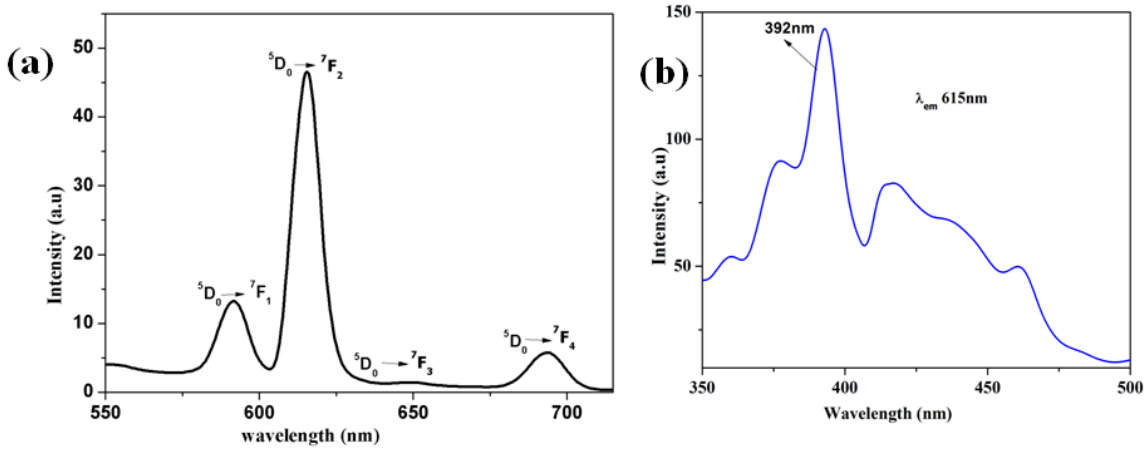

Figure 14. (a) Emission spectrum of as-synthesized compound $\{[Eu_2(Mu^{2-})_3(H_2O)_2]\cdot 4H_2O\}_n$ (**3**) and (b) corresponding excitation spectrum of **3** with λ_{em}= 615 nm.

Furthermore, Tb^{III} and Eu^{III} are well known donor acceptor pair where Tb^{III} acts as a donor and Eu^{III} acts as an acceptor and they have green and red emission respectively as described previously. Eu^{III} and Tb^{III} has similar charge and ionic radii, therefore Eu^{III} can be doped easily in Tb^{III} compound and corresponding emission colour can be tuned based on concentration of the acceptor Eu^{III} through energy transfer process. Thus, to obtain color tunability based on compound **1**, we varied the doping amount of Eu^{III} in **1** and isolated seven mixed Tb^{III}-Eu^{III} compounds of Eu^{III} contents 50, 24, 15, 7, 5, 1.25 and 0.6 atom%. The composition of the compounds were confirmed from energy dispersive X-ray (EDX) analysis. By increasing Eu^{III} content in the compound, we observed that the emission color changes from green, to red gradually (Inset of Figure 15). As we know lanthanide ion possesses very low extinction coefficient due to the intra configurational f–f transition and have very weak emission when

directly excited. The problem of inefficient emission can be overcome via the indirect excitation of coordinated organic ligand and this phenomenon is generally known as sensitization or antenna effect. In all the compounds mucic acid is acting as an antenna. In order to understand the energy transfer phenomena we have excited different Eu-doped Tb- compound at 315 nm. The emission spectrum and decay profiles for different compounds are shown in the Figure 15 and Figure 16. The spectrum of $Tb_{2-2x}Eu_{2x}$ compound shows peak at 482, 545, 589, 615 nm among them the most intense peaks are at 545 nm and 615 nm for green and red emission respectively. The intensity of the peaks at 545 nm and 615 nm decreases and increases, respectively with increasing % of Eu^{III} in $\{[Tb_{2-2x}Eu_{2x}(Mu^{2-})_3(H_2O)_2]\cdot 4H_2O\}_n$. The lifetime of $^5D_0$ (Eu^{III}) and $^5D_4$ (Tb^{III}) state increases and decreases in the doped sample from the pure compound implies the presence of Förster resonance energy transfer (FRET) from Tb^{III} to Eu^{III}.[3j,3k] The efficiency of energy transfer between single donor–acceptor pair at distance r is $E = R_0^6/(R_0^6 + r^6)$, where R_0 is Förster distance. Due to the longer distance (6Å) between Tb^{III} and Eu^{III} centers the FRET would be weak in doped compounds, with very low concentration of acceptor (Eu^{III}) (Table 6).

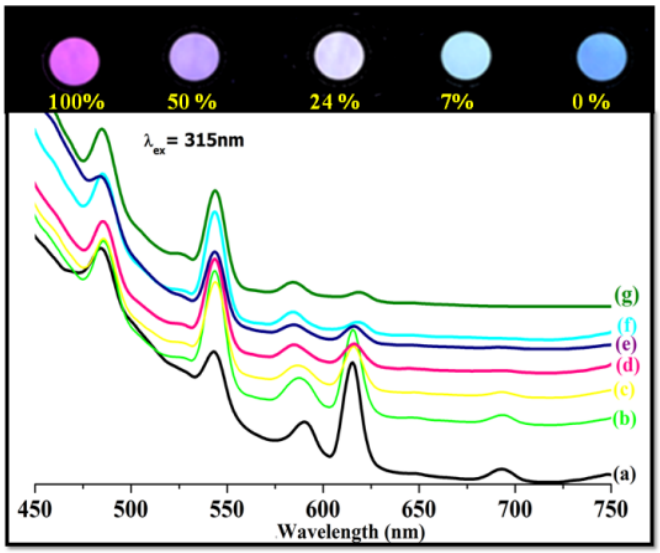

Figure 15. Top: Colour of different sample of different Eu^{III} content in **1** under UV light and Down: Emission spectra of mixed Tb^{III}-Eu^{III} compounds with different % of Eu-doping (a) 50%, (b) 24%, (c) 15%, (d) 7%, (e) 4%, (f) 1.24%, (g) 0.6% (λ_{ex}=315 nm).

7.3.6 Interpretation of energy transfer from lifetime measurement

The decay profile of the lifetime measurement for $^5D_4$ (Tb^{III}) and $^5D_0$ (Eu^{III}) states are shown below. The emissions at 545 nm and 625 nm are monitored for $^5D_4$ (Tb^{III}) and $^5D_0$ (Eu^{III}) state respectively. The τ values were obtained by fitting the line with single-exponential decay function. The lifetime $^5D_0$ state of Eu^{III} increased from 353 μs in pure Eu^{III} compound (**3**) to 497 μs in 7.03% Eu^{III} doped compound suggesting the presence of energy transfer.

$I=I_0 \exp(-T/\tau)$; where T = time, τ = lifetime and I = Intensity

The probability of energy transfer ($P_{Tb\rightarrow Eu}$)= $(1/\tau)-(1/\tau_0)$

Energy transfer efficiency ($E_{Tb\rightarrow Eu}$) = $1-(\tau/\tau_0)$

where τ_0 = lifetime of $Tb^{III}(^5D_4)$ in absence of Eu^{III}

τ = lifetime of Tb^{III} ($^5D_4$) in presence of Eu^{III}

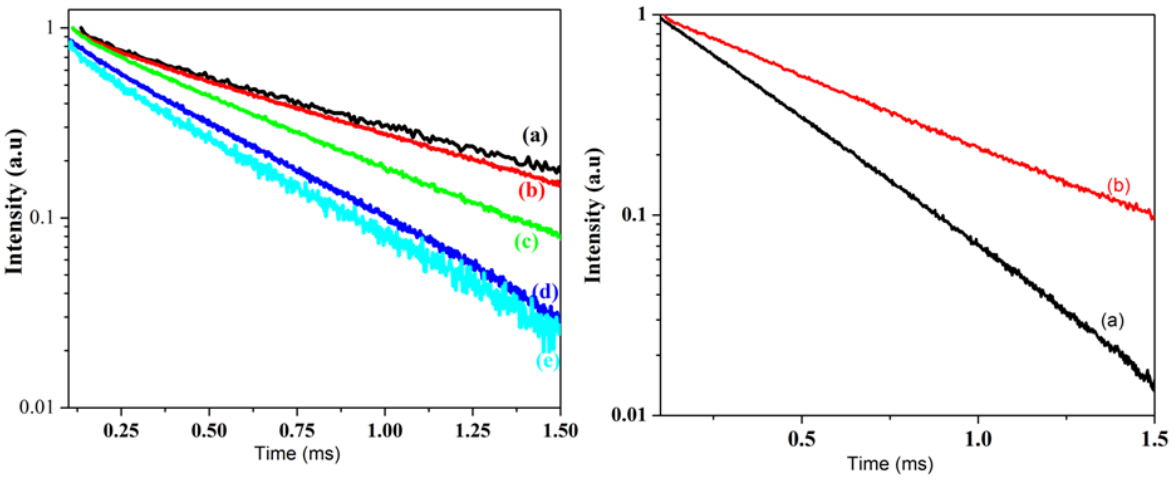

Figure 16. (Right side) Decay profile for $^5D_4$ state of Tb^{III} excited at 315 nm: (a) pure Tb^{III} (**1**); (b) 1.24% Eu^{III} ; (c) 7.03% Eu^{III} ; (d) 25% Eu^{III} ; (e) 50% Eu^{III} (left). (Left side) Decay profile for $^5D_0$ state of Eu^{III}: (a) pure Eu^{III} (**3**); (b) 7.03% Eu^{III}.

Compound	$\tau(^5D_4)(\mu s)$	$P_{Tb\rightarrow Eu}(ms^{-1})$	$E_{Tb\rightarrow Eu}(\%)$
100% Tb^{III}	825		
1.24% Eu^{III}	773	0.082	6.3
7.03% Eu^{III}	550	0.606	33.3
25% Eu^{III}	453	1.086	45.1
50% Eu^{III}	400	1.288	51.5
100% Eu^{III}	353 ($^5D_0$)		
7.03% Eu^{III}	497 ($^5D_0$)		

Table 6: Life time and composition dependent change in the probability ($P_{Tb\rightarrow Eu}$) and efficiency of energy transfer ($E_{Tb\rightarrow Eu}$).

7.3.7 Sensing of metal ions by $\{[Tb_2(Mu^{2-})_3(H_2O)_2]\cdot 4H_2O\}_n$ (1)

The porosity, flexibility and the presence of pendant hydroxo group or carboxylate oxygen at the pore surface motivated us to employ compound **1** as a metal ion sensor. As mentioned in the previous section that the emission property of **1** arises due to the presence of Tb^{III} and the emission intensity of Tb^{III} depends on the antenna effect of the mucicate ligand. Here in compound **4**, pendent hydroxo group can act as a Lewis basic site which can interact with the different guest cations (Lewis acid). As the metal ion may bind to pendant hydroxo group the antenna effect will be inhibited and the emission intensity will be reduced. We have employed various metal ions (Na^+, Mg^{2+}, Ca^{2+}, Co^{2+}, Ni^{2+}, Cu^{2+}, Zn^{2+}, Cd^{2+}, and Pb^{2+}) to understand this indirect quenching effect. To neglect the effect of anion on the quenching effect we employed all the nitrate salt of the respective cation. We performed the reaction after removing the guest water molecules at 100˚C and the dehydrated framework was used for the experiment. For each experiment 7 mg of the dehydrated framework was added into the 3 mL of 10^{-2}(M), 10^{-3}(M) and 10^{-4}(M) aqueous solution of nitrate salts of corresponding cation and vigorously stirred for 24 hours. After stirring the metal ion incorporated MOF was extracted from the solution and dried under vacuum at 100˚C. The dried samples were used for the emission property study. The dehydrated sample was used as a reference sample. The quenching effect of different metal ions were calculated from the most intensed emission peak at 545 nm ($^5D_4$ to $^7F_5$) with λ_{ex} of 220 nm (Figure15). The intensity change has been represented diagrammatically at 10^{-2} (M) concentration of different metal ions and dehydrated MOF (Figure 16). The emission intensity of Cu^{2+} incorporated MOF exhibits minimum intensity, suggesting maximum quenching effect

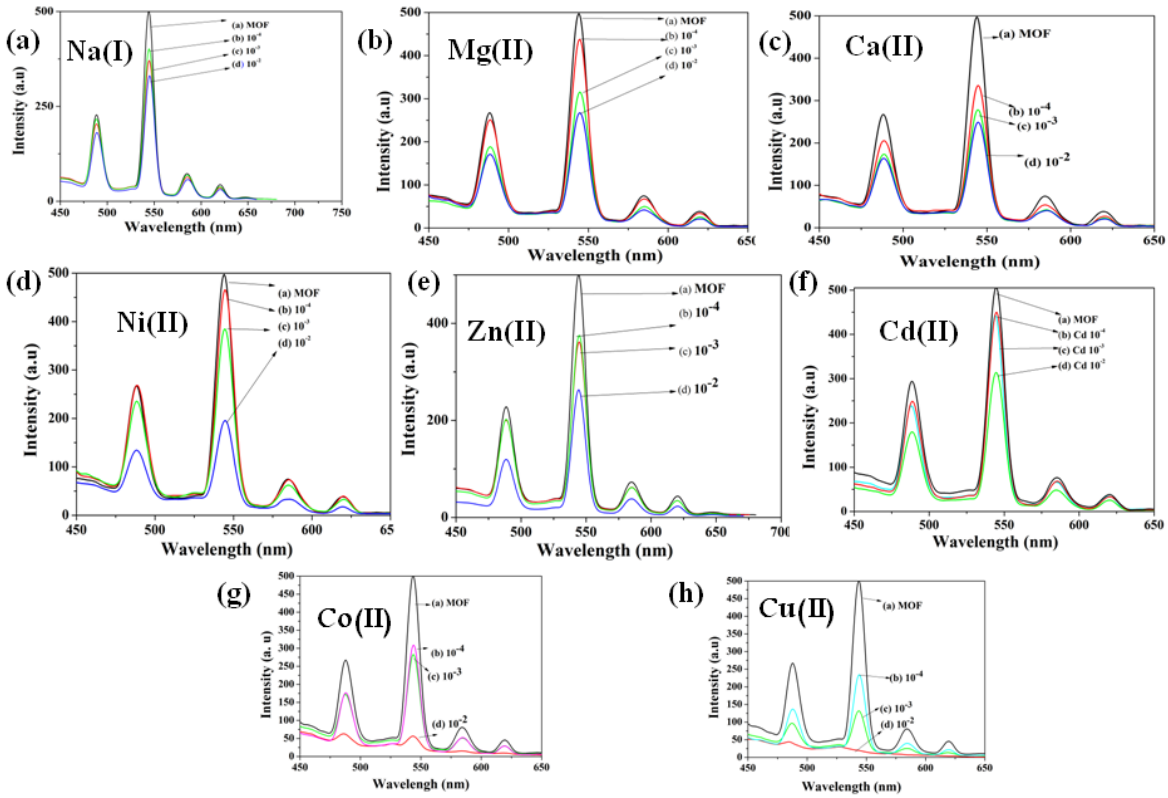

Figure 15. Quenching effect of different metal ions at different molar concentrations of (a) $NaNO_3$ (b) $Mg(NO_3)_2$, (c) $Ca(NO_3)_2$, (d) $Ni(NO_3)_2$ (e) $Zn(NO_3)_2$, (f) $Cd(NO_3)_2$, (g) $Co(NO_3)_2$ and (h) $Cu(NO_3)_2$

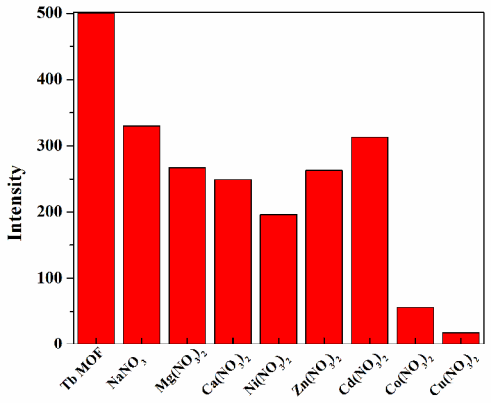

Figure 16. Comparison of luminescence intensity at 545 nm of dehydrated terbium MOF (**1′**) and metal ion @ MOF at 10^{-2} M concentration.

The quenching effect of various metal ion has been rationalized by the stern-Volmer equation: $I_0 / I = 1 + K_{sv}[M]$ where I_0 is the luminescent intensity of free MOF , I is the luminescent intensity of the metal ion incorporated MOF and K_{sv} is quenching effect coefficient. The K_{sv} value has been calculated from the Stern-Volmer equation for different metal ions and shown below in Table 7. The very high *Ksv* value in case of Cu^{II} suggest strong sensitivity and apecific sensing properties by MOF1

Table7: Quenching effect coefficient calculated for different metal ions based on Stern-Volmer equation.

Metal ion	$K_{sv}[M^{-1}]$
Na^{+}	49.4
Mg^{2+}	15.7
Ca^{2+}	84.9
Co^{2+}	769.5
Ni^{2+}	16.9
Cu^{2+}	2454.3
Zn^{2+}	43.6
Cd^{2+}	34.3

To further examine the quenching effect of Cu^{II} on luminescence intensity, lifetime studies of Tb^{III} ($^5D_4$) were carried out. Cu^{2+} incorporated MOF shows faster decay profile with smaller lifetime for $^5D_4$ state compared to the dehydrated mof **1** (Figure 17). Decay profiles were best fitted with single-exponential behaviour and calculated lifetimes for dehydrated and Cu(II) (10^{-3} M) incorporated MOFs are 996 μs and 781 μs respectively.The decrease lifetime of $^5D_4$ state in presence of Cu^{2+} also suggesting the quenching effect of Cu^{II} ions.

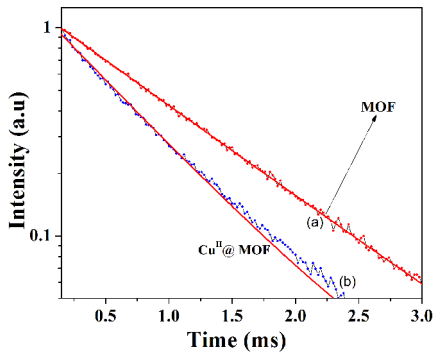

Figure 17: Decay profile for $^5D_4$ state of Tb^{III} excited at 220 nm: (a) dehydrated Tb^{III} MOF(**1**); (b) Cu^{2+} (10^{-3} incorporated Tb^{III} MOF (Red lines are best fitted with single exponential behaviour (r^2 =0.99)).

The strongest quenching effect exhibited by Cu^{II} followed by Co^{2+}.To explain the possible mechanism of differential quenching effect by different metal ion, X-ray photoelectron spectroscopic studies were carried on pure MOF and Co(II) and Cu(II) incorporated MOF. The binding energy of O1s peak from pendant hydroxo group and carboxylate group at 530.9eV

shifted to 531.15 and 531.1 eV for Cu^{2+} and Co^{2+} incorporated MOFs respectively (Figure 18). This observation clearly demonstrates that the binding of pendant carboxylate and hydroxo oxygens to the metal ions (Cu^{2+} and Co^{2+}). Such binding reduces the antenna effect efficiency of mucicate resulting in a quenching of the luminescence. Chen *et al.* has reported similar kind of phenomena in a Eu^{III} MOF where pyridyl nitrogen acts as Lewis basic site to interact with metal ions.[8]

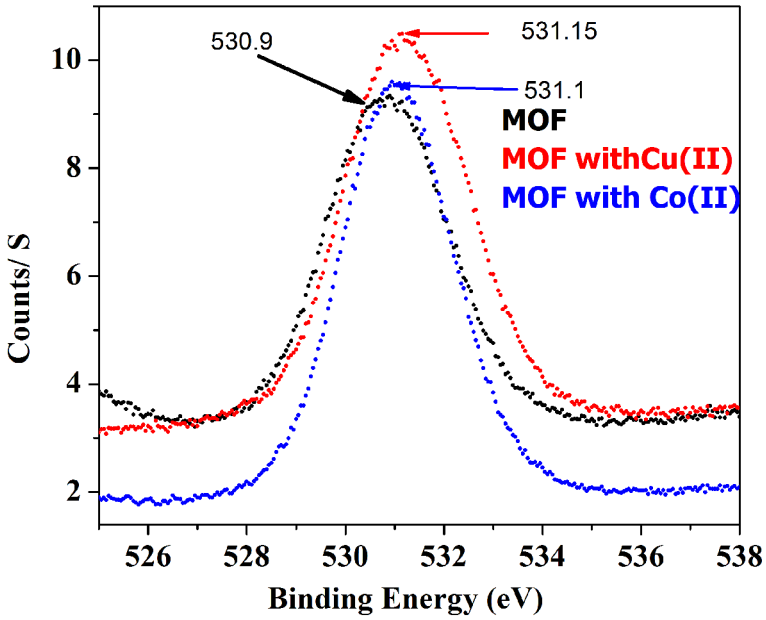

Figure 18. XPS spectra of pure MOF (black), Cu^{2+}@MOF (red) and Co^{2+}@MOF(blue)

7.3.8 Magneto-structural correlations

Temperature dependent susceptibility data (χ_M vs T and χ_MT vs T) in the temperature range of 300-2 K are shown in Figure 19a for **1** and Figure 20a for **2**. Both the compounds show similar temperature dependent χ_MT profile suggesting similar magnetic interaction present in both cases. At room temperature χ_MT values are 23.80 emu mol^{-1} K (for two Tb^{III} ions) and 11.54 emu mol^{-1} K for **1** and **2** respectively. The χ_MT values are very closed to the values expected for isolated Tb^{III} center (J =6, g_J= 1.5, χ_MT= 11.81 emu mol^{-1} K). In compound **1** χ_MT slightly increases from 23.80 emu mol^{-1} K at 300 K to 24.01 emu mol^{-1} K at 230 K and then decreases to 19.63 emu mol^{-1} K at 2 K. Compound **2** behave similarly as of compound **1** without any anamoly at high temperature. The χ_MT value decreases from 11.63 emu mol^{-1} K at 300K to 9.45 emu mol^{-1} K at 2.5 K . The occurrence of anti ferromagnetic interaction in compound **2** is mediated by the oxalate and oxo bridges. Both the χ_MT profiles suggest the presence of weak anti-ferromagnetic interaction between Tb^{III} centers. 3D structure of compound **1** has been built via *syn-anti* bridging carboxylate for **1** and oxalate for **2** which is responsible for the weak antiferromagnetic interaction in **1** and **2**, respectively (Figure 21). Linear fitting of χ_M^{-1} vs T plot of **1** and **2** suggests

Curie constant, C= 24.13 and 11.63 emu mol^{-1} K and Weiss constant, θ =-2.2 K and -2.39 K for **1** and **2** respectively (Figure 19b and 20b). The negative Weiss constants supports presence of weak anti-ferromagnetic interaction in both the compounds. Field dependent magnetization study at 2.5 K exhibit no hysterisis also suggesting antiferromagnetic interaction in the system (Figure 22).

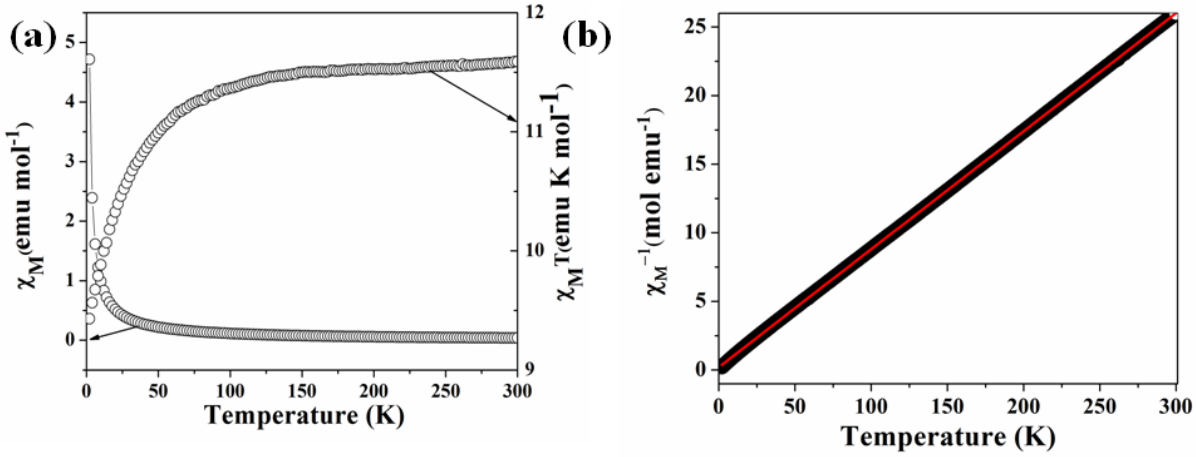

Figure 19. (a) variation of χ_M and χ_MT plot as a function of temperature of compound**1** (b) variation of χ_M^{-1} plot as a function of temparature.

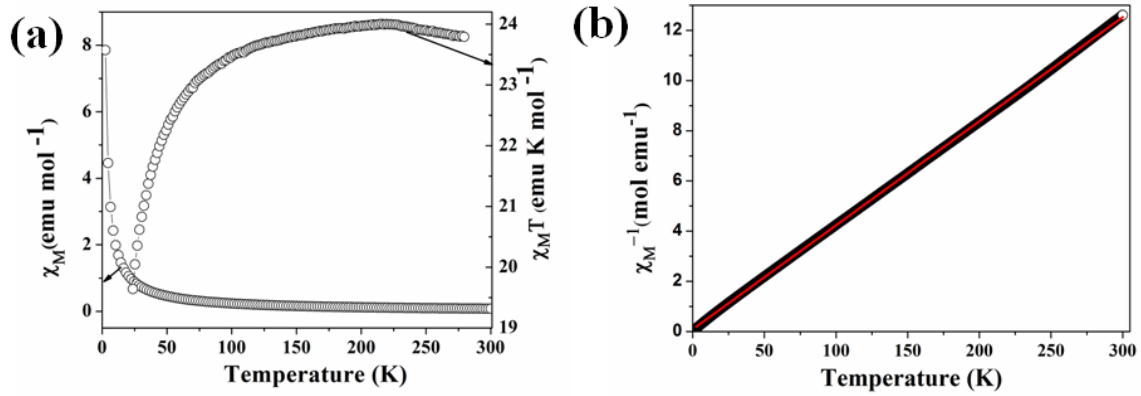

Figure 20. (a)Variation of χ_M and χ_MT as a function of temperature of compound **2** (b) variation χ_M^{-1} as a function of temperature.

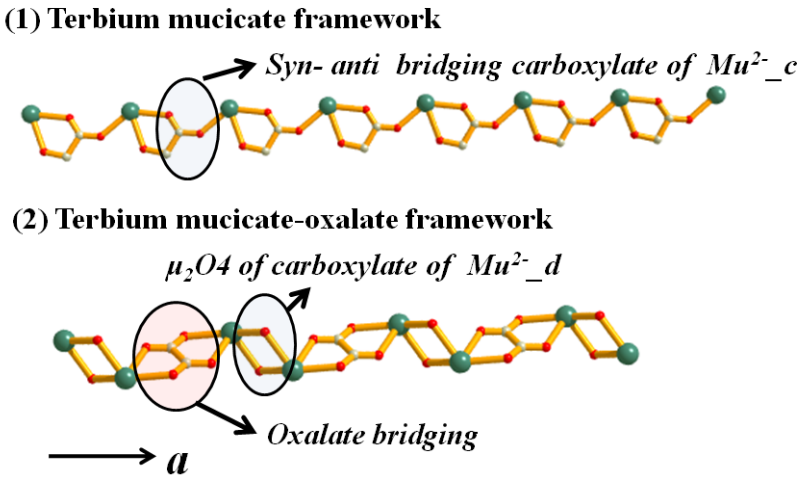

Figure 21. Possible magnetic interaction pathways in **1** and **2**.

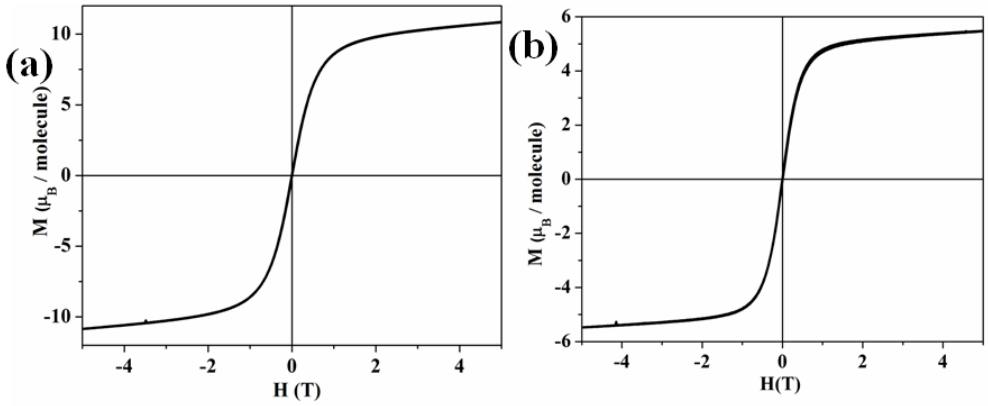

Figure 22. Field dependent magnetization plot of (a)**1** (b) **2**.

7.4 Summary

We have synthesized two different Tb^{III}-mucicate and one isostructural Eu^{III}-mucicate frameworks at two different pH and structurally characterized. High temperature acidic condition produces oxalate by decomposition of the ligand. This is the first report of synthesis of two different mucicate MOFs by varying the pH of the medium. All the frameworks are hydrophillic in nature. Mixed lanthanide Tb_xEu_{1-x} compounds are synthesized by dopping different % of Eu^{III} into the framework of 1 and composition dependent emission color and energy transfer efficiency has been demonstrated. Temperature dependent dc magnetic susceptibility study shows that both the compounds are anti-ferromagnetic in nature. Compound 1 has been exploited for sensing applications for different metal ions and suggest highly slective sensing for Cu^{II} ions. The K_{sv} values suggests that quenching effect of Cu^{2+} is maximum compared to other metal ions (Na^{+}, Mg^{2+}, Ca^{2+}, Ni^{2+},Co^{2+}, Zn^{2+}, Cd^{2+}). The quenching effects by different metal ions were correlated to the inhibition of antenna effect efficiency of mucicate after binding with metal ions.

7.5 References

(1) (a) J. An, O. K. Farha, J. T. Hupp, E. Pohl, J. I. Yeh, and N. L. Rosi, *Nat. Commun*., 2012, **3**, 604; (b) A. U. Czaja, N. Trukhan and U. Muller, *Chem. Soc. Rev.,*2009**, 38**, 1284; (c) S. Kitagawa, R. Kitaura and S.-I. Noro, *Angew. Chem. Int., Ed.,* 2004**, 43**, 2334; (d) M. D. Allendorf, C. A. Bauer, R. K. Bhakta and R. J. T. Houk, *Chem. Soc. Rev.,* 2009**, 38**, 1330; (e) Y. Cui, Y. Yue, G. Qian and B., Chen, *Chem. Rev*.,2012,**112**, 1126; (f) M. Kurmoo, *Chem. Soc. Rev.* 2009**, 38**, 1353. (g) M. P. Suh, H. J. Park, T. K. Prasad and D.-W. Lim, *Chem. Rev*., 2012, **112**, 782; (h) A. Hazra, P. Kanoo and T. K. Maji, *Chem. Commun.* 2011*,* **47**, 538. (i) S. Mohapatra, K. P. S. S. Hembram, U. Waghmare and T. K., Maji, *Chem. Mater.,* 2009**, 21**, 5406; (j) D. J. Lun, G. I. N.; Waterhouse and S. G. Telfer, *J. Am. Chem.Soc.,* 2011*,* **133**, 5806; (k) L. E. Kreno, K. Leong, O. K. Farha, M. Allendorf, R. P. Van Duyne and J. T. Hupp, *Chem.Rev.*,2012, **112**, 1105.

(2) (a) S. Sivakumar, M. L. P. Reddy, A. H. Cowley and R. R. Butorac, *Inorg. Chem.,* 2011**, 50**, 4882; (b) P. Lama and P. K. Bharadwaj, *Cryst. Growth Des.,*2011, **11**, 5434; (c) K. L. Gurunatha, S. Mohapatra, P. A. Suchetan and T. K. Maji, *Cryst. Growth Des.,*2009*,* **9***,* 3844.

(3) (a) R. C. Evans, L. D. Carlos, P. Douglas and J. Rocha, *J. Mater.Chem.,* 2008**, 18**, 1100; (b) G. He, D. Guo, C. He, X. Zhang, X. Zhao and C. Duan, *Angew. Chem. Int., Ed.,* 2009**, 48**, 6132; (c) G. Li, Z. Hou, C. Peng, W. Wang, Z. Cheng, C. Li, H. Lian and J. Lin, *Adv. Funct. Mater.,* 2010, **20**, 3446; (d) K. Liu, H. You, Y. Zheng, G. Jia, Y. Song, Y. Huang, M.Yang, J. Jia, N. Guo and H. Zhang, *J. Mater.Chem.,* 2010, **20** , 3272; (e) X.Zhang, M. A. Ballem, Z.-J. Hu, P. Bergman, K. Uvdal, , *Angew. Chem. Int., Ed.* **2011**, *50*, 5729. (f) H. Guo, Y. Zhu, S. Qiu, J. A. Lercher and H. Zhang, *Adv. Mater.* 2010, **22**, 4190; (g) T. Yamase and H. Naruke, *J. Phys. Chem. B.,* 1999**, 103**, 8850; (h) H. Li, H. K. Yang, B. K. Moon, B. C. Choi, J. H. Jeong, K. Jang, H. S. Lee and S. S. Yi, *Inorg. Chem.,* 2012*,* **50**, 12522; (i) C.-L. Choi, Y.-F.Yen, H. H. Y. Sung, A. W. H. Siu, S. T. Jayarathne, K. S. Wong and I. D., Williams, *J. Mat. Chem.,* 2011, **21**, 8547; (j) S. Biju, D. B. Ambili Raj, M. L. P. Reddy, C. K. Jayasankar, A. H. Cowley and M. Findlater, *J. Mater. Chem*., 2009, **19**, 1425; (k) D. T. DeLill, A. de Bettencourt-Dias, C. L. Cahill, *Inorg. Chem.,* 2007, **46**, , 3960.

(4) (a) K. L. Wong, G. L. Law, Y. Y. Yang and W. T. Wong, *Adv. Mater,* 2006**, 18**, 1051; (b) A. Lakatos, R. Bertani, T. Kiss, A. Venzo, M. Casarin, F. Benetollo, P.

Ganis, D. Favretto, *Chem.Eur. J.,* 2004**, 10**, 1281; (c) A. Dornyei, E. Garribba, T. Jakusch, P. Forgo, G. Micera and T. Kiss, *Dalton Trans.,* 2004, 1882.

(5) (a) N. A. Khan, J. W. Jun and S. H. Jhung, *Eur. J. Inorg.Chem.,* 2010, 1043. (b) P. M. Forster, A. R. Burbank, C. Livage, G. Ferey and A. K., Cheetham, *Chem. Commun.,* 2004, 368; (c) P. M. Forster, N. Stock and A. K.,Cheetham, *Angew. Chem. Int., Ed.,* 2005**, 44**, 7608;(d) P. Mahata, M. Prabu and S. Natarajan, *Inorg. Chem.,* 2008, **47**, 8451.

(6) (a) A. L. Spek, PLATON, *Molecular Geometry Program, University of Utrecht*, Netherlands, 1999; (b) V. A. Balatov, A. P. Shevchenko, TOPOS, *Program Package for multipurpose crystallochemical analysis*, *Samara state University*, Russia, 1989-2008; (c) Crysfire 2004, *Interactive powder indexing support system*.

(7) (a) *SAINT*, 6.02 ed., Bruker AXS, Madison, WI, 1999**;** (b) G. M. Sheldrick, *SADABS, Empirical Absorption Correction Program*, University of Göttingen, Göttingen, Germany, 1997 (c) A. Altomare, G. Cascarano, C. Giacovazzo, A. Gualaradi, *J. Appl. Crystallogr.* 1993, **26**, 343; (d) G. M. Sheldrick, *SHELXL 97*, Program for the Solution of Crystal Structure, University of Göttingen, Germany, 1997;(e) G. M. Sheldrick, *SHELXS 97*, Program for the Solution of Crystal Structure, University of Göttingen, Germany, 1997;(f) Spek, A. L. *J. Appl. Crystallogr.* 2003, **36**, 7; (g) WinGX, A Windows Program for Crystal Structure Analysis: Farrugia, L. J. *J. Appl. Crystallogr.* 1999, **32**, 837.

(8) B. Chen, L. Wang, Y. Xiao, F. R. Fronczek, M. Xue, Y. Cui and G. Qian, *Angew. Chem. Int., Ed.* 2009**, 48**, 500.

Chapter 8

Synthesis of Lanthanide Frameworks Derived from 2,5-dihydroxyterephthalate: Structural Characterization, Adsorption and Ligand Based Emission Properties

Abstract: Five novel metal-organic frameworks, $\{La(H_2dhta)_{1.5}(H_2O)_2\}_n$ **(1)**, $\{La(H_2dhta)(ox)_{0.5}(H_2O)_3\}_n$ **(2)**, $\{[La(H_2dhta)_{1.5}(H_2O)_6]\cdot 3H_2O\}_n$ **(3)** and $\{[Gd_2(dhta)(dhtaH_2)(H_2O)_5]\cdot 2H_2O)\}_n$ **(4)** $\{La(ox)_{0.5}(\mu\text{-}OH)_2(\mu\text{-}H_2O)(H_2O)_2\}_n$ **(5)**(H_4dhta= 2,5-dihydroxyterephthalic acid, ox = oxalate dianion), of various dimensionality have been synthesized hydrothermally from single precursor H_4dhta ligand and structurally characterized. In these compounds H_4dhta acts as linker as well as precursor for oxalate depending on the reaction conditions. Coordination mode of H_4dhta linker strongly depends on the synthesis conditions and forms various structures with lanthanides with different network topology. Furthermore H_4dhta is an excited state intramolecular proton transfer (ESIPT) responsive linker and based on this compound **1** exhibit tunable ligand based emission properties in different solvent with different polarity. Compound **1** and **4** exhibit selective water vapor sorption over other solvents. Reversible single-crystal-to-single-crystal structural transformation upon dehydration and rehydration has been observed in compound **4.**

(1) Paper related to this chapter has been published, K. L. Gurunatha, S. Mohapatra, Suchetan P. A and T. K. Maji, ***Cryst. Growth Des.***, 2009, **9**, 3844.
(2) A Paper related to this chapter has been published **S. Mohapatra,** S. Y. Vyasamudri, G. Mostafa and T. K. Maji ***J. Mol. Str.***, 2009, **932**, 123.
(3) Manuscript of a Paper related to this chapter is under preparation, S. Mohapatra and T. K Maji

8.1 Introduction

Recent years porous coordination polymers (PCPs) or metal-organic frameworks (MOFs) materials has developed into a significant area of research due to its promising applications in gas storage (like H_2, CH_4, and CO_2 storage),[1] separations,[2] catalysis,[3] sensing[4] and ion exchange processes.[5] PCPs or MOFs are highly crystalline materials constructed through highly directional covalent bonding between metal centers and organic linkers containing a varieties of functional groups. In this context, MOFs containing lanthanide (Ln) ions are attractive because of their versatile coordination geometry (with the coordination number ranging from the 7-12),[6] unique luminescent[7] and magnetic properties,[8] and possible high framework stability.[9] Moreover lanthanides have stronger coordinating ability to oxygen donor ligands and always contains solvent molecules for the gratification of higher coordination number. After removal of the coordinated water molecules from the MOF structure resulted a compound containing coordinatively unsaturated metal ion as a Lewis acidic site to exhibit catalytic[10] and interesting adsorption properties.[11] However, to date, few examples of lanthanide-organic frameworks with porous functionality have been reported.[12] Among the different organic linkers, 2,5-dihydroxyterephthalic acid (H_4dhta), is an exciting linker due to the two hydroxyl groups at 2,5–positions along with the two carboxylic groups at 1,4 positions, which has been recently used for the construction of porous MOFs with transition metal ions.[13] Furthermore H_4dhta is a bifunctional salicylic acid derivative and excited state intramolecular proton transfer responsive linker and have ligand based tunable emission colour. Therefore H_4dhta linker yet to be explored for the synthesis of lanthanide-organic framework. Because of the presence of two different functional groups (–OH, –COOH) versatile framework structures is expected based on the synthetic conditions (pH, temperature and stoichiometry). With the aim to synthesize different kind of open framework porous materials, we exploited the versatile binding ability of the 2,5-dihydroxyterepthalic acid and the flexible coordination geometry of the Ln^{III} ions (scheme1). Here we report synthesis of five different lanthanide-organic frameworks by changing the reaction parameters using the same ligand (H_4dhta). We characterize all the five lanthanide organic frameworks $\{La(H_2dhta)_{1.5}(H_2O)_2\}_n$ (**1**), $\{La(H_2dhta)(ox)_{0.5}(H_2O)_3\}_n$ (**2**), $\{[La(H_2dhta)_{1.5}(H_2O)_6]\cdot 3H_2O\}_n$ **(3)**, $\{[Gd_2(dhta)(H_2dhta)(H_2O)_5]\cdot 2H_2O)\}_n$ **(4)**, and $\{La(ox)_{0.5}(\mu\text{-}OH)_2(\mu\text{-}H_2O)(H_2O)_2\}_n$ **(5)** by single-crystal structural characterization. We unveiled the solvent dependent ligand based emission property of **1,** single-crystal-to-single-crystal structural transformation upon

dehydration and rehydration in **4** and selective water vapor sorption property of both **1** and **4.**

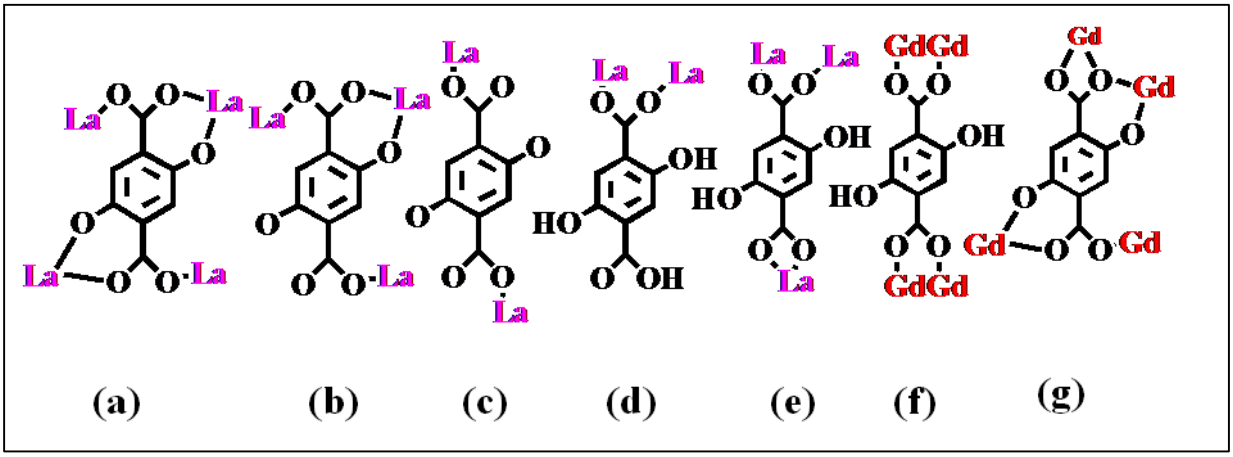

Scheme 1. Various binding modes of dhta to lanthanides in lanthanide-dhta frameworks.

8.2. Experimental section

8.2.1 Materials

All the reagents and solvents employed were commercially available and used as supplied without further purification. $La(NO_3)_3 \cdot 6H_2O$, $Gd(NO_3)_2 \cdot 6H_2O$, $Ho(NO_3)_3 \cdot 5H_2O$ and 2,5-dihydroxyterephthalic acid were obtained from Aldrich chemical co.

8.2.2 Physical measurements

The elemental analyses were carried out using a Perkin Elmer 2400 CHN analyzer. IR spectra of all the compounds in different state were recorded on a Bruker IFS 66v/S spectrophotometer using the KBr pellets in the region 4000-400 cm^{-1}. The UV-Vis spectra (Perkin-Elmer, lambda-900) and the photoluminescence studies (PL, Perkin-Elmer, LS-55) were carried out on powdered samples in the solid state at room temperature. Thermogravimetric analysis (TGA) were carried out on METTLER TOLEDO TGA850 instrument in the temperature range of 25-600 °C under nitrogen atmosphere (flow rate of 50 mL/min) at a heating rate of 3 °C /min. X-ray powder diffraction (PXRD) pattern in different state of the samples were recorded on a Bruker D8 Discover instrument using Cu-$K\alpha$ radiation.

8.2.3 Adsorption measurements

N_2 and CO_2 adsorption studies were carried out using QUANTACHROME AUTOSORB-1C analyzer at 77 K and 195 K, respectively. The adsorption isotherm of different solvents (like H_2O, CH_3CN, EtOH at 298 K and MeOH at 293 K) were measured in the gaseous state by using BELSORP-aqua volumetric adsorption instrument from BEL, Osaka, Japan. In the sample chamber (~12 mL) maintained at $T \pm 0.03$ K was placed the adsorbent sample (100-150 mg), which had been prepared at 473 K for **1**, **2** and 453 K for **3**, **5** at 10^{-1} Pa for about 6 hours prior to measurement of the isotherms. The adsorbate was charged into the sample tube, and then the change of the pressure was monitored and the degree of adsorption was determined by the decrease of the pressure at the equilibrium state. All operations were computer-controlled and automatic.

8.2.4 Synthesis of $\{La(H_2dhta)_{1.5}(H_2O)_2\}_n$ (1)

$La(NO_3)_3 \cdot 6H_2O$ (0.5 mmol, 0.217 g) with 2,5-dihydroxyterephthalic acid (0.75 mmol, 0.099 g) and KOH (1.5 mmol, 0.084 g) were mixed well in 10 mL water and stirred for 30 min in open atmosphere. Then reaction mixture was transferred to a 25 mL Teflon-lined hydrothermal vessel and heated for three days at 165 ˚C and then hydrothermal vessel was cooled down to room temperature for 12 h. Yellow crystals were obtained as a single phase product which was filtered and washed with water. IR (KBr cm^{-1}): 3496 br (νOH); 3390 m (νOH); 1552 s (ν_{as} OCO); 1347 s (ν_s OCO); 830 w (ν_{bend} OCO).[14] (Yield: 0.165g 80%,). Anal. calc. for $C_{16}H_{20}Gd_2O_{19}$ C, 23.11; H, 2.40; Found: C, 23.23; H, 2.28.

8.2.5 Synthesis of $\{La(H_2dhta)(ox)_{0.5}(H_2O)_3\}_n$ (2)

Hydrothermal reaction of $La(NO_3)_3 \cdot 6H_2O$ (0.5 mmol, 0.217 g) with 2,5-dihydroxyterphthalic acid (0.5mmol, 0.149 g) and KOH (1 mmol, 0.56 g) and in 6 mL water at 180 ˚C for 3 days resulted in yellow crystalline material.

8.2.6 Synthesis of $\{[La(H_2dhta)_{1.5}(H_2O)_6]\cdot 3H_2O\}_n$ (3)

Compound **3** has been synthesized adopting similar reaction stoichiometry and hydrothermal condition as of compound **2**. Here the reaction temperature has been decreased 150 ˚C . Yellow crystalline solids obtained after three days, which was filtered and washed with water

8.2.7 Synthesis of $\{[Gd_2(dhta)(H_2dhta)(H_2O)_5]\cdot 2H_2O)\}_n$ (4)

$Gd(NO_3)_3\cdot 6H_2O$ (0.5 mmol, 0.225 g) with 2,5-dihydroxyterephthalic acid (0.5 mmol, 0.099 g) and KOH (1 mmol, 0.056 g) were mixed well in 8 mL water and stirred for 30 min in open atmosphere. Then reaction mixture was transferred to a 25 mL Teflon-lined hydrothermal vessel and heated for three days at 180 ˚C and then hydrothermal vessel was cooled down to room temperature for 12 h. Greenish yellow crystals were obtained as a single phase product which was filtered and washed with water. (Yield: 80% corresponds to 0.165 g in this synthetic condition). IR (KBr cm^{-1}): 3496 br (ν_{OH}); 3390 m (ν_{OH}); 1552 s (ν_{as} OCO); 1347 s (ν_s OCO); 830 w (ν_{bend} OCO). Anal. calc. for $C_{16}H_{20}Gd_2O_{19}$ C, 23.11; H, 2.40; Found: C, 23.23; H, 2.28.

8.2.8 Synthesis of $\{La(ox)_{0.5}(\mu\text{-}OH)_2(\mu\text{-}H_2O)(H_2O)_2\}_n$ (5)

$La(NO_3)_3\cdot xH_2O$ (1 mmol, 0.325 g), 2,5-dihydroxyterephthalic acid (0.5 mmol, 0.099 g) and KOH (1 mmol, 0.056 g) were mixed in 7 mL water and stirred for 30 min. Then the reaction mixture was transferred to a 25 mL Teflon-lined hydrothermal vessel and heated for three days at 180 ºC and then cooled down to room temperature for 12 h. The colorless square block type crystals were separated along with the white powder as impurity. IR (KBr cm^{-1}): 3453 br (ν OH); 3259 m (ν OH); 1664 s (ν_{as} OCO); 1388 s (ν_s OCO); 811 w (ν_{bend} OCO). Yield 45%. Anal found: H, 2.81; C, 44.98; calcd: H 2.95; C, 44.28.

8.2.9 Single-crystal X-ray diffraction

Suitable single-crystals of compounds **1-5** were mounted on a thin glass fiber with commercially available super glue. X-ray single-crystal structural data were collected on a Bruker Smart–CCD diffractometer equipped with a normal focus, 2.4 kW sealed tube X-ray source with graphite monochromated Mo-*Kα* radiation (λ = 0.71073 Å) operating at 50 kV and 30 mA. The programme *SAINT* was used for integration of diffraction profiles and absorption correction was made with *SADABS* programme.[17a,b] All the structures were solved by SIR 92 and refined by full matrix least square method using SHELXL.[17d] For all the compounds the non-hydrogen atoms were refined anisotropically. All hydrogen atoms were fixed by HFIX and placed in ideal positions. For the final refinement the hydrogen atoms of the ligand were placed geometrically and held on the riding mode. Potential solvent accessible area or void space was calculated using the *PLATON*-99.[16] The coordinates, anisotropic displacement parameters, and torsion angles for all the compounds are submitted as supplementary information in CIF format. All crystallographic and structure refinement data of the compounds are summarized in Table

1. All calculations were carried out using SHELXL 97, PLATON 99, SHELXS 97 and WinGX system, Ver 1.70.01. [17] Selected bond length and bond angles and hydrogen bonding parameters are given in table 2-13 for compound **1-5.**

Table 1. Crystallographic Cell and Structure Refinement Data for **1 -5**

	1	**2**	**3**	**4**	**4′**	**4a**	**5**
Empirical formula	$C_{12}H_9LaO_{11}$	$C_9H_{10}LaO_{11}$	$C_{12}H_{12}LaO_{18}$	$C_{16}H_{16}Gd_2O_{19}$	$C_{16}H_{14}Gd_2O_{17}$	$C_{16}H_{16}Gd_2O_{19}$	CH_8LaO_7
M_r	468.10	433.08	583.08	826.77	792.77	826.77	270.97
Crystal System	Monoclinic	Triclinic	Triclinic	Monoclinic	Monoclinic	Monoclinic	Monoclinic
space group	*C*2/*c*	*P*$\bar{1}$	*P*$\bar{1}$	*P*2/*c*	*P*2/*c*	*P*2/*c*	$P2_1/c$
a (Å)	29.8921(8)	6.9027(1)	6.9633(2)	8.9065(2)	8.8975(5)	8.9160(7)	4.8599(3)
b (Å)	13.2062(4)	9.1857(2)	11.8791(4)	15.0925(3)	15.1126(11)	15.1027(14)	8.9770(5)
c (Å)	6.7368(2)	10.7359(2)	13.3164(4)	8.5028(2)	8.4960(6)	8.5126(8)	14.3882(9)
α (deg)	90.00	69.471(1)	70.327(2)	90	90	90	90.00
β (deg)	101.015(1)	83.507(1)	78.025(2)	96.260(1)	96.210(5)	96.304(5)	94.418(3)
γ (deg)	90.00	86.916(1)	78.556(2)	90	90	90	90
V (Å^3)	2610.43(13)	633.33(2)	1004.71(6)	1136.14(4)	1135.71(13)	1139.34(18)	625.85(7)
Z	8	2	2	2	2	2	4
T (K)	293	293	293	293	293	293	293
D_c (g cm^{-3})	2.382	2.271	1.908	2.411	2.318	2.375	2.855
μ (mm^{-1})	3.341	3.432	2.215	5.881	5.872	5.864	6.802
F (000)	1808	418	558	780	748	760	500
θ_{max} (deg)	25.7	27.8	29.0	31.9	25.8	26.9	31.7
λ (Mo Kα)(Å)	0.71073	0.71073	0.71073	0.71073	0.71073	0.71073	0.71073
Tot. data	8299	6948	20004	9892	8401	7380	6445
unique data, R_{int}	2422, 0.027	2955,0.030	5357, 0.101	3609, 0.030	2119, 0.111	2347, 0.118	1987, 0.018
data [$I > 2\sigma(I)$]	2250	2705	3738	3187	1401	1466	1397
R^a,	0.0290	0.0244	0.0531	0.0285	0.0689	0.0756	0.0604
$R_w{}^b$	0.0762	0.0577	0.1268	0.0783	0.1737	0.1649	0.1384
S	1.17	1.04	0.99	1.05	1.07	1.05	1.22

$^a R = \sum||Fo|-|Fc||/\sum|Fo|$. $^b R_w = [\sum\{w(Fo^2-Fc^2)^2\}/\sum\{w(Fo^2)^2\}]^{1/2}$

8.3 Results and discussion

8.3.1 Structural description of $\{La(H_4dhta)_{1.5}(H_2O)_2\}_n$ (1)

Compound **1** crystallizes in monoclinic *C*2/*c* space group and X-ray structure determination reveals that it is a neutral 3D coordination framework of La^{III}. There are two different types of binding modes of H_2dhta in compound **1** *viz dhta_a* and *dhta_b* (Figure 1). Coordination number seven of the nine coordinated La^{III} ion has been satisfied with oxygen atoms of five different dhta linker, two of which has dhta_*a* type binding mode (sky blue color portion) and remaining three has dhta_*b* type binding mode (red color portion). dhta_a implies the H_2dhta linker coordinated to four Ln^{III} ion as a hexadentate ligand whereas dhta_*b* involved in coordination to three different La^{III} center as a tetradentate ligand with one hydroxo and one carboxylate oxygen atoms remain pendant (O6 and O8). Eighth and ninth coordination sites are occupied by the water molecules (O1 and O2) and tricapped-trigonal-prismatic coordination geometry of La^{III} is completed. La1-O bond distances are in the range of 2.463(4) - 2.664(4) Å and La1-O-La1 bond angles are in the range of 61.84(12) – 146.69(12) ˚ reflecting the distortion from ideal tricapped, trigonal-prismatic geometry (see Table2). La^{III} ions are connected by two different type of H_2dhta linker through *syn-anti* carboxylate bridging oxygens(O4, O5) , chelating carboxylate and hydroxo oxygens (O3, O4, O10, O11) and monodentate carboxylate oxygens (O7) to form a 3D structure (Figure 2a). 3D structure of the framework contains coordinated water filled channel along crystallographic *c* direction (figure 2a). After removal of the coordinated water molecules, the framework provides a pore along the *c*-axis with the dimension of 3.99 × 3.04 $Å^2$, which correlates 6.1 % void space to the total crystal volume as suggested by the PLATON (Figure 2b).[16] Both the H_2dhta ligands undergoes π-π stacking interactions (cg···cg distances are in the range of 3.368(4) – 3.458(3) Å). All these non-covalent interactions provide overall topology and extra stability to the 3D framework. In the 3D framework nearest neighbor separation between the two La^{III} ions along the two different H_2dhta ligands are 9.054 and 10.064 Å, respectively.

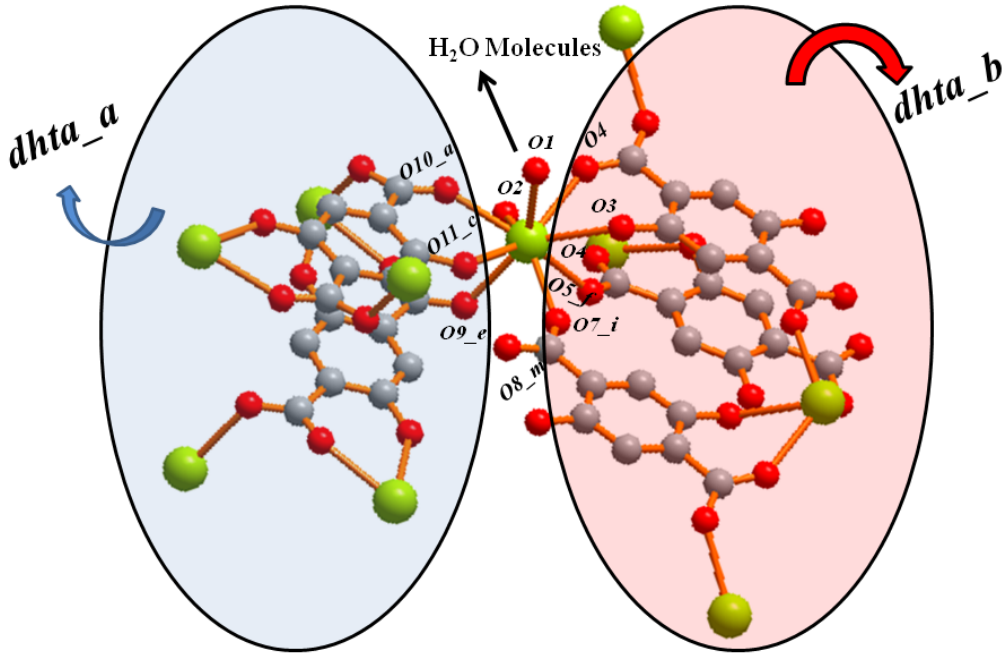

Figure 1. Coordination geometry of La^{III} in compound **3** with two different type of binding mode of H_2dhta.

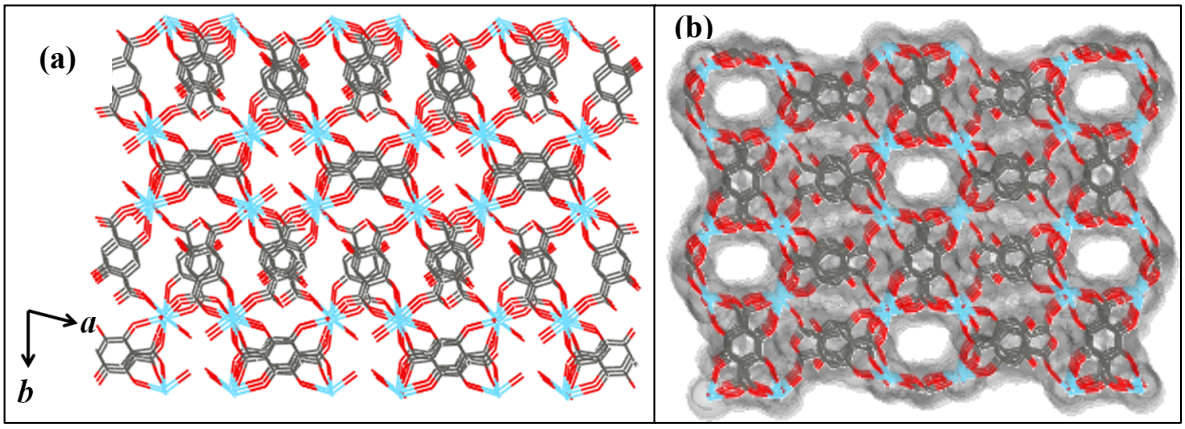

Figure 2. (a) 3D structure of compound **3** view along crystallographic *c* axis showing coordinated water molecules exposed in the pore (b) view of space pore along *c* direction after removal of the coordinated water molecules.

Table 2. Selected bond lengths (Å) and angles (°) for **1**.

La1 -O1	2.606(11)	La1 -O2	2.619(15)
La1 -O3	2.674(12)	La1 -O4	2.494(13)
La1 -O9	2.461(12)	La1 -O10_a	2.529(12)
La1 -O11_b	2.583(12)	La1 -O7_f	2.506(12)

O1 -La1-O2	120.6(4)	O1 -La1 -O4	71.1(5)
O1 -La1-O3	61.4(4)	O1-La1 -O10_a	143.2(4)
O1 -La1-O9	72.2(4)	O1 -La1 -O7_f	100.3(4)
O1-La1- O11_b	72.2(4)	O2-La1 -O3	125.0(4)
O2 -La1-O4	67.8(4)	O2 -La1-O9	72.1(4)
O2 -La1-O10_a	68.3(4)	O2 -La1 -O11_b	128.5(4)
O2 -La1-O7_f	138.5(4)	O3-La1-O4	62.0(4)
O3 -La1-O9	132.8(4)	O3-La1 -O10_a	147.0(4)
O3 –La1 -O11_b	105.3(4)	O3 -La1-O7_f	67.7(4)
O4 -La1 -O9	96.5(4)	O4 -La1-O10_a	135.1(4)
O4 -La1-O11_b	142.6(4)	O4 -La1-O7_f	126.4(4)
O9 -La1-O10_a	78.5(4)	O9 -La1-O11_b	65.4(4)
O7_f -La1 -O9	132.2(4)	O10_a -La1-O11_b	75.7(4)
O7_f -La1 -O10_a	83.2(4)	O7_f -La1 -11_b	67.4(4)

Symmetry code: a = -x, y, 3/2-z, b =-x, 1-y, 1-z, f =1/2-x, 1/2-y, 2-z

8.3.2 Structural description of $\{La(H_2dhta)(ox)_{0.5}(H_2O)_3\}_n$ (2)

Compound **2** crystallizes in triclinic space group $P\bar{1}$ and structural determination from X-ray diffraction of single-crystal reveals that a neutral 2D bi-layered coordination framework of La^{III} composed of mixed H_2dhta and ox ($C_2O_4^{2-}$) ligands. Each nine coordinated La^{III} ions chelated to one H_2dhta (O6, O7), one ox^{2-} ligand (O4, O5) and another two H_2dhta ligand through monodentate carboxylate oxygen atoms (O8 and O9) (Figure 3). Rest of the sites is occupied by the three water molecules (O1, O2 and O3) which are acting as hydrogen bond donor to form a 3D structure. A 1D bilayer chain has been formed by the coordination of dhta_*e* ligand and these chains are further connected by the ox^{2-} linkers forming 2D corrugated sheet in the crystallographic *bc* plane (Figure 4). In the 2D network La1-O bond distances are in the range of 2.427(3) – 2.712(3) Å (table 3). The 2D sheets are further connected to each other through hydrogen bonding interaction to form 3D supramolecular structure (Figure 5). Oxygens (O1, O2, O3) of coordinated water molecules acts as hydrogen bond donor and ligand oxygens (O4, O5, O6, O10. O11) are hydrogen bond acceptor. The donor acceptor O···O distances are in the range of 2.504(3) - 2.879(4) Å) (table 4).

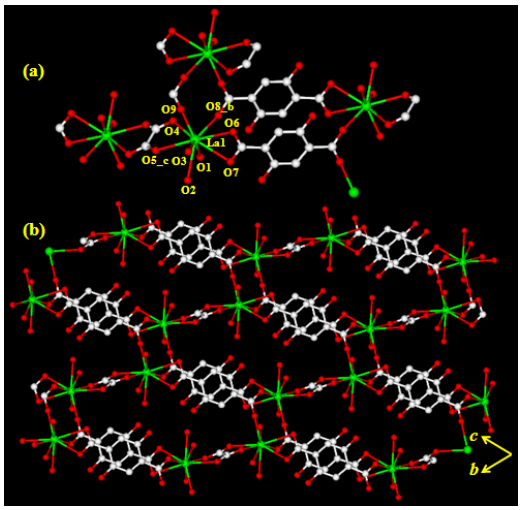

Figure 3. Coordination geometry of La^{III} in compound **2**.

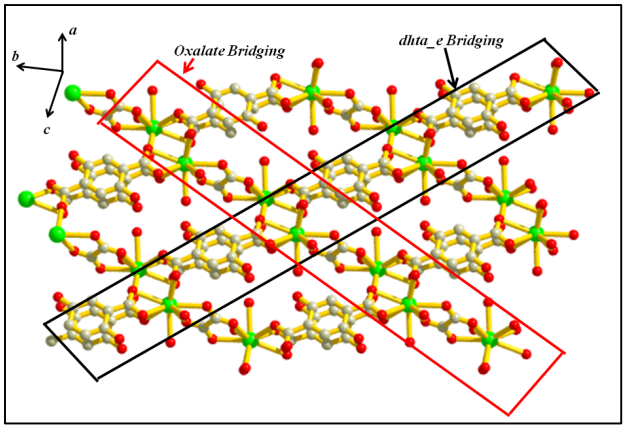

Figure 4. Formation of 2D sheet via coordination of oxalate and dhta_e.

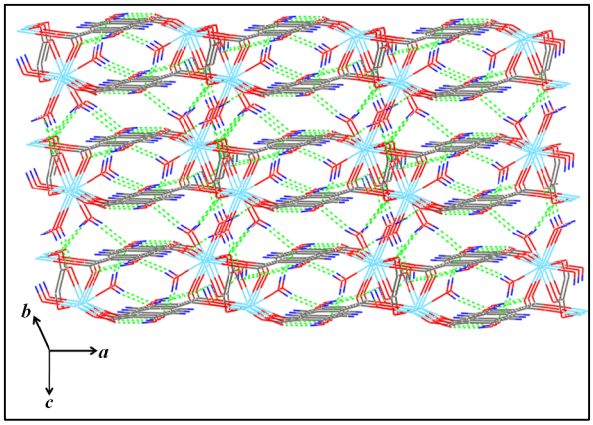

Figure 5. Formation of 3D supramolecular structure via hydrogen bonding interaction (green color) between the 2D sheets.

Table 3. Selected bond lengths (Å) and angles (°) for **2**.

La1-O1	2.558(3)	La1-O2	2.573(3)
La1-O3	2.499(3)	La1-O4	2.577(2)
La1-O6	2.712(3)	La1-O7	2.588(2)
La1-O8_b	2.515(2)	La1-O5_c	2.555(3)
O1-La1-O2	68.09(10)	O1-La1-O3	137.71(10)
O1-La1-O4	67.87(10)	O1-La1-O6	111.77(8)
O1-La1-O7	72.14(9)	O1-La1-O8_b	71.93(9)
O1-La1-O5_c	86.22(8)	O2-La1-O3	70.02(9)
O2-La1-O4	111.69(9)	O2-La1-O6	109.05(9)
O2-La1-O7	68.43(9)	O2-La1-O8_b	135.21(8)
O2-La1-O5_c	64.80(8)	O3-La1-O4	135.75(9)
O3-La1-O6	76.93(9)	O3-La1-O7	87.58(9)
O3-La1-O8_b	142.18(9)	O3-La1-O5_c	81.19(8)
O4-La1-O6	134.75(9)	O4-La1-O7	135.58(9)
O4-La1-O8_b	69.13(8)	O4-La1-O5_c	62.78(8)
O6-La1-O7	48.90(8)	O6-La1-O8_b	68.35(8)
O5_c-La1-O6	157.98(7)	O7-La1-O8_b	80.93(8)
O5_c-La1-O7	132.98(8)	O5_c-La1-O8_b	131.73(7)

a =2-x,1-y,1-z, *b*=x,1+y,z, *c* =-1+x,y,z, *d*=1-x,1-y,1-z, *e*=1-x,-y,2-z

Table 4. Hydrogen bonding interactions

D --- H....A	D – H	H...A	D...A	D - H...A
O1 --H1 ..O11	0.86(5)	2.00(5)	2.807(4)	158(4)
O1 --H2 ..O10	0.78(6)	2.01(6)	2.782(4)	170(6)
O2 --H3..O5	0.75(5)	2.14(5)	2.879(4)	169(6)
O2 --H4..O11	0.79(5)	2.07(5)	2.819(4)	160(5)
O3 --H5..O6	0.93(6)	1.82(6)	2.737(4)	168(6)
O3 --H6..O4	0.73(4)	2.07(4)	2.784(4)	169(4)

8.3.3 Structural description of $\{[La(H_2dhta)_{1.5}(H_2O)_6].3H_2O\}_n$ (3)

Compound **3** crystallizes triclinic $P\bar{1}$ space group and structural determination reveals that a neutral 1D chain of La^{III} composed of H_2dhta linkers in two different type of binding mode viz H_2dhta_c and H_2dhta_d (see Scheme 1 and Figure 6a). Each nine coordinated La^{III} centers are connected to three different dhta linkers (O2, O8, O9) to satisfy coordination number three and remaining six coordination numbers are satisfied with six O atoms of coordinated water molecules (O1-O6). In the 1D chain La1-O bond distances are in the range of 2.635(4) – 2.502(5) Å (table 5). 1D chains are further connected to each other via supramolecular π···π stacking interactions between the phenyl rings of H_2 dhta to form a 2D sheet like structure. (cg···cg distance 3.652(4) Å, α (dihedral angle) =0, $\beta = \gamma = 22.36^{\circ}$, slippage =1.389Å) (Figure 6b). The 2D supramolecular structure has no further non covalent interaction to form 3D structure due to the longer distance. The

distance between nearest neighbor La^{III} centers in 1D chain and sheets are 5.564(5) and 6.963(4) Å respectively.

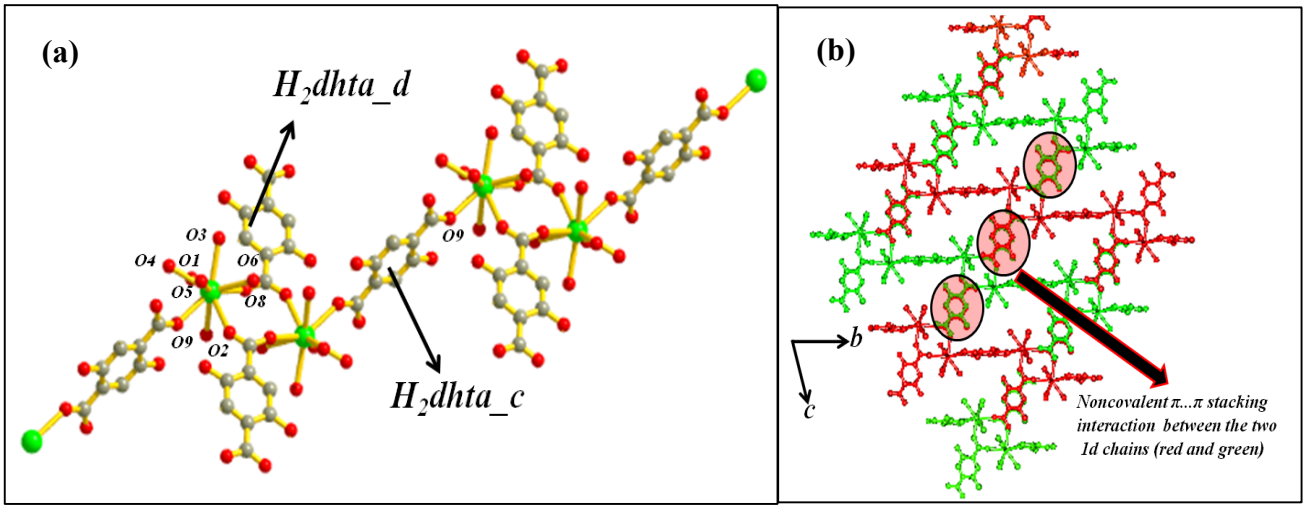

Figure 6. (a) coordination environment and 1D chain of compound **3** **(b)** Formation of 2D supramolecular sheet via π···π stacking interaction between 1D chains

Table 5. Selected bond lengths (Å) and angles (°) for **3**.

La1-O1	2.576(5)	La1-O2	2.516(4)
La1-O3	2.596(5)	La1-O4	2.635(4)
La1-O5	2.598(5)	La1-O6	2.564(5)
La1-O7	2.559(5)	La1-O8	2.502(5)
La1-O9	2.548(4)		

O1-La1-O2	72.16(14)	O5 -La1-O8	78.11(16)
O1-La1-O3	80.63(15)	O5-La1-O9	69.57(15)
O1-La1-O4	134.14(15)	O6-La1-O7	110.84(16)
O1-La1-O5	136.82(16)	O6-La1-O8	134.22(16)
O1-La1-O6	67.05(16)	O6-La1-O9	68.80(14)

O1-La1-O7	69.24(15)	O7-La1-O8	69.91(16)
O1-La1-O8	138.88(16)	O7-La1-O9	68.73(14)
O1-La1-O9	99.36(15)	O8-La1-O9	69.66(15)
O2-La1-O3	80.97(14)	O2-La1-O4	69.45(13)
O2-La1-O5	141.48(15)	O2-La1-O6	133.45(14)
O2-La1-O7	72.89(15)	O2-La1-O8	91.64(14)
O2-La1-O9	141.10(13)	O3-La1-O4	69.54(15)
O3-La1-O5	80.83(16)	O3-La1-O6	71.32(16)
O3-La1-O7	144.76(16)	O3-La1-O8	135.14(16)
O3-La1-O9	136.31(14)	O4-La1-O5	72.44(14)
O4-La1-O6	128.98(14)	O4-La1-O7	120.06(14)
O4-La1-O8	66.49(15)	O4-La1-O9	126.32(14)
O5-La1-O6	70.14(16)	O5-La1-O7	133.97(16)

8.3.4 Structural description of $\{[Gd_2(dhta)(H_2dhta)(H_2O)_5]\cdot 2H_2O)\}_n$ (4)

The greenish-yellow single-crystals of **4** was synthesized under hydrothermal condition using $Gd(NO_3)_3$. Single-crystal X-ray diffraction study reveals that compound **4** crystallizes in monoclinic space group *P*2/*c*. There are two crystallographically independent Gd^{III} atoms (Gd1 and Gd2) in the asymmetric unit connected by two different binding modes of H_4dhta *viz* dhta_f and dhta_g (Scheme 1 and Figure7a). Each nine coordinated Gd1 atom is chelated to two different dhta linkers of binding mode dhta_g through carboxylate oxygen atoms (O3, O4 and O3_c, O4_c, *c* = -x, y, 1/2-z) and attached to two other oxygen atoms (O8, O8_c) from dhta_f . The rest of the coordination sites around Gd1 are occupied by the three water molecules (O1, O1_c and O2). Whereas Gd2 is octa-coordinated and surrounded by two chelated dhta through carboxylate and hydroxyl oxygen atoms (O4, O5 and O4_b, O5_b; b = -1-x,y,1/2-z), another two oxygen atoms (O7, O7_b) from two H_2dhta linkers and rest of the coordination sites are occupied by two water molecules (O6, O6_b). Therefore, each tetraanionic dhta chelated to two Gd1 and two Gd2 centres, whereas dianionic H_2dhta linker are connected to two Gd1 and Gd2 centres through *syn-syn* carboxylate bridging (Figure 7a). Gd1 – O and Gd2 – O bond distances are in the range of 2.362(3) – 2.645(3) Å and 2.242(3) – 2.486(3) Å, respectively (Table 6). Each Gd1 is connected to two nearest neighbors Gd2 through μ_2-O4, forming a 1D Gd-O4-Gd chain and further connection of the chains by dhta resulting a 2D corrugated sheet lying in the crystallographic *ac* plane (Figure 8). The 2D sheet further pillared by the dhtaH_2 through *syn-syn* bridging between Gd1 and Gd2 forming a novel 2D pillared-bilayer network with 2D water filled channels along crystallographic *c* and *a*-axis (Figure 7b & 8a). The pillar H_2 dhta linkers are alternating positioned in parallel to the direction of the side channels and the thickness of the bilayer galleries is 17.17 Å (Figure 1b). Each 2D pillared-bilayer networks further interdigitated with the coordinated water (O2) molecules through H-bonding interactions (Table 9) forming a 3D supramoleculer network with 1D water filled channels along the crystallographic *c*-axis (Figure 7a & 9b). The dimensions of the rectangular and supramolecular oval shaped channels along the crystallographic *c*-axis are 4.43 x 3.32 $Å^2$ and 4.43 x 1.94 $Å^2$, respectively (Figure 9b).[16] The dimension of the triangular channels along the crystallographic *a*-axis is about 4.48 × 1.40 $Å^2$.

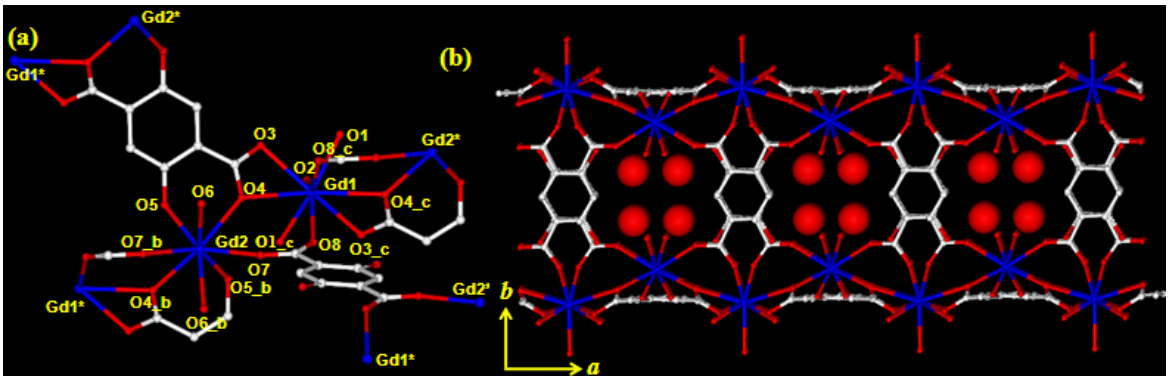

Figure 7. (a) View of the coordination environments of two Gd^{III} centres in **4**; (b) View of the 2D pillared-bilayer framework of **4** showing water filled channels along the crystallographic *c*-axis.

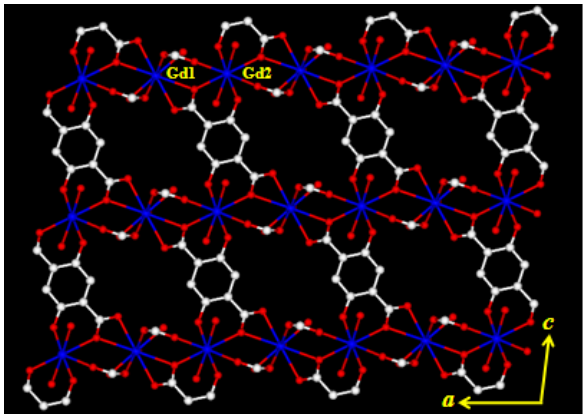

Figure 8. View of the 2D sheet of alternating Gd1 and Gd2 centres connected by the dhta linker lying in the crystallographic *ac* plane.

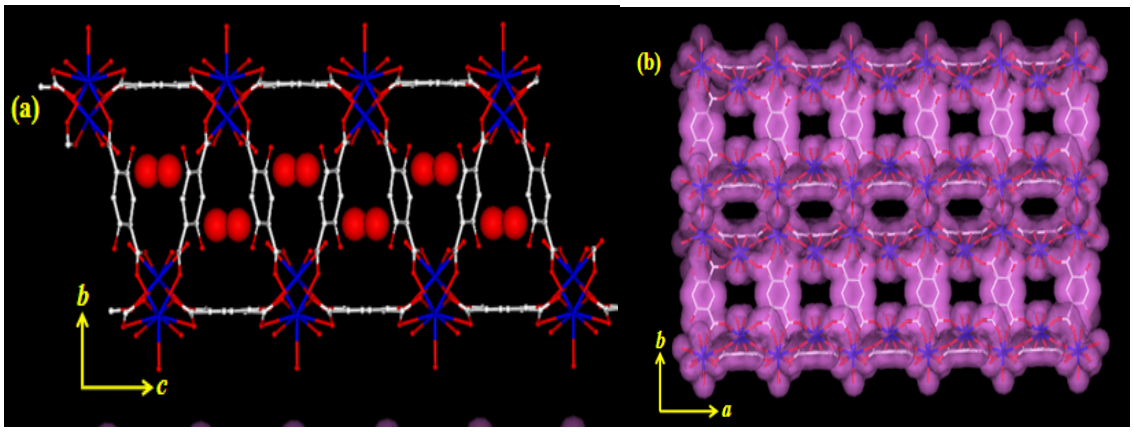

Figure 9. (a) View of the pillared-bilayer network along the crystallographic *a*-axis showing triangular channels filled with the water molecules; (b) View of the two different pores in 3D supramolecular framework.

The calculations using PLATON suggest 3.2 and 21.3% void space of **4** to the total crystal volume after removal of guest and coordinated water molecules, respectively.[17] The Gd1···Gd2 separation along the Gd-O-Gd chain is 4.771 Å and Gd1···Gd1, Gd1···Gd2 and Gd1···Gd2 separation are 11.624, 8.503 and 9.317 Å, respectively in the 2D sheet lying in the *ac* plane. The separation of the Gd1···Gd2 in the bilayer is 10.870 Å.

Table 6. Selected bond lengths (Å) and angles(°) for $\{[Gd_2(dhta)(H_2dhta)(H_2O)_5]\cdot 2H_2O)\}_n$ (**4**)

Gd1-O1	2.362(3)	Gd1-O2	2.479(5)
Gd1-O3	2.457(3)	Gd1-O4	2.645(3)
Gd1-O8	2.392(3)	Gd1-O1_c	2.362(3)
Gd1-O3_c	2.457(3)	Gd1-O4_c	2.645(3)
Gd1-O8_c	2.392(3)	Gd2-O4	2.486(3)
Gd2 -O5	2.242(3)	Gd2-O6	2.457(5)
Gd2-O7	2.412(3)	Gd2-O4_b	2.486(3)
Gd2-O5_b	2.242(3)	Gd2-O6_b	2.457(5)
Gd2-O7_b	2.412(3)		

O1-Gd1 -O2	67.40(7)	O4_c-Gd1-O8	80.04(10)
O1 -Gd1-O3	73.64(10)	O8-Gd1-O8_c	74.95(11)
O1-Gd1 -O4	123.12(9)	O1_c-Gd1-O3_c	73.64(10)
O1-Gd1 -O8	144.38(11)	O1_c-Gd1-O4_c	123.12(9)
O1-Gd1-O1_c	134.81(10)	O1_c-Gd1-O8_c	144.38(11)
O1-Gd1-O3_c	97.26(10)	O3_c-Gd1-O4_c	50.58(9)
O1-Gd1 -O4_c	70.45(9)	O3_c-Gd1-O8_c	121.99(11)
O1-Gd1-O8_c	78.29(11)	O4_c-Gd1-O8_c	74.66(10)
O2-Gd1 -O3	78.33(7)	O4-Gd2-O5	71.30(9)
O2-Gd1-O4	106.00(6)	O4-Gd2-O6	138.43(12)
O2-Gd1 -O8	142.53(8)	O4-Gd2-O7	70.24(10)
O1_c-Gd1-O2	67.40(7)	O4-Gd2-O4_b	133.37(9)
O2 -Gd1-O3_c	78.33(7)	O4-Gd2-O5_b	79.86(9)
O2-Gd1-O4_c	106.00(6)	O4-Gd2-O6_b	76.25(12)
O2-Gd1-O8_c	142.53(8)	O4-Gd2-O7_b	137.49(11)
O3-Gd1-O4	50.58(9)	O5-Gd2-O6	150.27(13)
O3-Gd1-O8	121.99(11)	O5-Gd2-O7	139.65(11)
O1_c-Gd1-O3	97.26(10)	O4_b-Gd2-O5	79.86(9)
O3-Gd1-O3_c	156.67(10)	O5-Gd2-O5_b	102.26(10)
O3-Gd1-O4_c	138.28(8)	O5-Gd2-O6_b	86.62(14)
O3-Gd1-O8_c	77.94(11)	O5-Gd2-O7_b	82.58(11)
O4-Gd1-O8	74.66(10)	O6-Gd2-O7	69.12(13)
O1_c-Gd1-O4	70.45(9)	O4_b-Gd2-O6	76.25(12)
O3_c-Gd1 -O4	138.28(8)	O5_b-Gd2-O6	86.62(14)
O4-Gd1-O4_c	148.00(9)	O6-Gd2-O6_b	99.68(17)
O4-Gd1-O8_c	80.04(10)	O6-Gd2-O7_b	72.90(15)
O1_c-Gd1-O8	78.29(11)	O4_b-Gd2-O7	137.49(11)
O3_c-Gd1-O8	77.94(11)	O5_b-Gd2-O7	82.58(11)
O6_b-Gd2-O7	72.90(15)	O7-Gd2-O7_b	119.44(10)
O4_b-Gd2-O5_b	71.30(9)	O4_b-Gd2-O6_b	138.43(12)
O4_b-Gd2-O7_b	70.24(10)	O5_b-Gd2-O6_b	150.27(13)
O5_b-Gd2-O7_b	139.65(11)	O6_b-Gd2-O7_b	69.12(13)
Gd1-O4 -Gd2	136.84(11)		

Symmetry code: b = -1-x,y,1/2-z; c = -x,y,1/2-z

Table 7. Selected bond lengths (Å) and angles (°) for $\{[Gd_2(dhta)(dhtaH_2)(H_2O)_5]\}_n$ (**4′**)

Gd1 -O1	2.356(12)	Gd1-O2	2.461(17)
Gd1-O3	2.458(12)	Gd1-O4	2.650(11)
Gd1 -O8	2.395(12)	Gd1-O1_a	2.356(12)
Gd1 -O3_a	2.458(12)	Gd1-O4_a	2.650(11)
Gd1 -O8_a	2.395(12)	Gd2-O4	2.468(11)
Gd2 -O5	2.229(11)	Gd2-O6	2.441(16)
Gd2 -O7	2.400(13)	Gd2-O4_b	2.468(11)
Gd2 -O5_b	2.229(11)	Gd2-O6_b	2.441(16)
Gd2 -O7_b	2.400(13)		
O1-Gd1-O2	67.5(3)	O4_a-Gd1-O8	79.8(4)
O1-Gd1-O3	97.0(4)	O8-Gd1-O8_a	74.3(4)
O1-Gd1-O4	70.1(4)	O1_a-Gd1-O3_a	97.0(4)
O1-Gd1-O8	78.6(4)	O1_a-Gd1-O4_a	70.1(4)
O1-Gd1-O1_a	135.0(4)	O1_a-Gd1-O8_a	78.6(4)
O1-Gd1-O3_a	74.0(4)	O3_a-Gd1-O4_a	50.8(4)
O1-Gd1-O4_a	123.7(4)	O3_a-Gd1-O8_a	121.8(4)
O1-Gd1-O8_a	143.9(4)	O4_a-Gd1-O8_a	74.3(4)
O2-Gd1-O3	78.5(3)	O4-Gd2-O5	71.9(4)
O2-Gd1-O4	106.3(3)	O4-Gd2-O6	138.2(4)
O2-Gd1-O8	142.9(3)	O4-Gd2-O7	70.3(4)
O1_a-Gd1-O2	67.5(3)	O4-Gd2-O4_b	133.5(4)
O2-Gd1-O3_a	78.5(3)	O4-Gd2-O5_b	79.4(4)
O2-Gd1-O4_a	106.3(3)	O4-Gd2-O6_b	76.7(4)
O2-Gd1-O8_a	142.9(3)	O4-Gd2-O7_b	137.8(4)
O3-Gd1-O4	50.8(4)	O5-Gd2-O6	150.0(5)
O3-Gd1-O8	121.8(4)	O5-Gd2-O7	140.1(4)
O1_a -Gd1-O3	74.0(4)	O4_b-Gd2-O5	79.4(4)
O3-Gd1-O3_a	156.9(4)	O5-Gd2-O5_b	102.4(4)
O3-Gd1-O4_a	138.1(3)	O5-Gd2-O6_b	87.2(5)
O3-Gd1-O8_a	78.0(4)	O5-Gd2-O7_b	82.6(4)
O4-Gd1-O8	74.3(4)	O6-Gd2-O7	68.8(5)
O1_a-Gd1-O4	123.7(4)	O4_b-Gd2-O6	76.7(4)
O3_a-Gd1-O4	138.1(3)	O5_b-Gd2-O6	87.2(5)
O4-Gd1-O4_a	147.4(4)	O6-Gd2-O6_b	98.6(5)
O4-Gd1-O8_a	79.8(4)	O6-Gd2-O7_b	72.4(5)
O1_a-Gd1-O8	143.9(4)	O4_b-Gd2-O7	137.8(4)
O3_a-Gd1-O8	78.0(4)	O5_b-Gd2-O7	82.6(4)
O6_b-Gd2-O7	72.4(5)	O7-Gd2-O7_b	118.7(5)
O4_b-Gd2-O5_b	71.9(4)	O4_b-Gd2-O6_b	138.2(4)
O4_b-Gd2-O7_b	70.3(4)	O5_b-Gd2-O6_b	150.0(5)
O5_b-Gd2-O7_b	140.1(4)	O6_b-Gd2 -O7_b	68.8(5)

Symmetry code: a = -x,y,1/2-z; b = 1-x,y,1/2-z

Table 8. Selected bond lengths (Å) and angles (°) for $\{[Gd_2(dhta)(H_2dhta)(H_2O)_5]\cdot 2H_2O)\}_n$ (**4a**).

Gd1 -O1	2.376(12)	Gd1-O2	2.510(18)
Gd1-O3	2.447(12)	Gd1-O4	2.645(11)
Gd1-O8	2.386(12)	Gd1-O1_c	2.376(12)
Gd1-O3_c	2.447(12)	Gd1-O4_c	2.645(11)
Gd1-O8_c	2.386(12)	Gd2-O4	2.492(11)
Gd2-O6	2.480(16)	Gd2-O7	2.424(13)
Gd2-O5_a	2.238(11)	Gd2-O4_d	2.492(11)
Gd2-O6_d	2.480(16)	Gd2-O7_d	2.424(13)
Gd2-O5_e	2.238(11)		
O1-Gd1-O2	67.2(3)	O4_c-Gd1-O8	79.9(4)
O1-Gd1-O3	97.0(4)	O8-Gd1-O8_c	74.6(4)
O1-Gd1-O4	70.6(4)	O1_c-Gd1-O3_c	97.0(4)

O1-Gd1-O8	78.8(4)	O1_c-Gd1-O4_c	70.6(4)
O1-Gd1-O1_c	134.3(4)	O1_c-Gd1-O8_c	78.8(4)
O1-Gd1-O3_c	73.5(4)	O3_c-Gd1-O4_c	50.5(4)
O1-Gd1-O4_c	122.9(4)	O3_c-Gd1-O8_c	122.3(4)
O1-Gd1-O8_c	144.4(4)	O4_c-Gd1-O8_c	75.0(4)
O2-Gd1-O3	77.9(3)	O4-Gd2-O6	138.2(4)
O2-Gd1-O4	105.8(2)	O4-Gd2-O7	70.7(4)
O2-Gd1-O8	142.7(3)	O4-Gd2-O5_a	79.8(4)
O1_c-Gd1-O2	67.2(3)	O4-Gd2-O4_d	133.3(3)
O2-Gd1-O3_c	77.9(3)	O4-Gd2-O6_d	76.3(4)
O2-Gd1-O4_c	105.8(2)	O4-Gd2-O7_d	137.3(4)
O2-Gd1-O8_c	142.7(3)	O4-Gd2-O5_e	71.4(4)
O3-Gd1-O4	50.5(4)	O6-Gd2-O7	68.6(5)
O3-Gd1-O8	122.3(4)	O5_a-Gd2-O6	86.3(5)
O1_c-Gd1-O3	73.5(4)	O4_d-Gd2-O6	76.3(4)
O3-Gd1-O3_c	155.8(4)	O6-Gd2-O6_d	100.2(5)
O3-Gd1-O4_c	138.6(4)	O6-Gd2-O7_d	73.2(5)
O3-Gd1-O8_c	78.4(4)	O5_e-Gd2-O6	150.4(4)
O4-Gd1-O8	75.0(4)	O5_a-Gd2-O7	82.7(4)
O1_c-Gd1-O4	122.9(4)	O4_d-Gd2-O7	137.3(4)
O3_c-Gd1-O4	138.6(4)	O6_d-Gd2-O7	73.2(5)
O4-Gd1-O4_c	148.4(3)	O7-Gd2-O7_d	118.7(4)
O4-Gd1-O8_c	79.9(4)	O5_e-Gd2-O7	140.1(4)
O1_c-Gd1-O8	144.4(4)	O4_d-Gd2-O5_a	71.4(4)
O3_c-Gd1-O8	78.4(4)	O5_a-Gd2-O6_d	150.4(4)
O5_a-Gd2-O7_d	140.1(4)	O5_a-Gd2-O5_e	102.4(4)
O4_d-Gd2-O6_d	138.2(4)	O4_d-Gd2-O7_d	70.7(4)
O4_d-Gd2-O5_e	79.8(4)	O6_d-Gd2-O7_d	68.6(5)
O5_e-Gd2-O6_d	86.3(5)	O5_e-Gd2-O7_d	82.7(4)

Symmetry code: a = x,y,-1+z; c = -x,y,-1/2-z; d = 1-x,y,-1/2-z; e = 1-x,y,1/2-z

Table 9. Hydrogen bonding table (Å, °) in **4**

Symmetry Code: i = 1+x,y,z; ii = -x,-y,-z; iii = x,-y,1/2+z, v= -1+x, y, z

D-H…A	D-H	H…A	D….A	<D-H…A
O1-H1…O5^{i}	0.8500	1.7000	2.539(4)	170.00
O1- H2…O3^{ii}	0.9400	2.0000	2.880(4)	155.00
O2- H3…O3^{iii}	0.8300	2.0600	2.830(3)	155.00
O6-H6...O10^{iv}	0.7900	1.8000	2.59(5)	175
O6-H7...O9^{v}	0.8700	2.5200	2.810(7)	100.00

8.3.5 Structural description of $\{La(ox)_{0.5}(\mu\text{-}OH)_2(\mu\text{-}H_2O)(H_2O)_2\}_n$ (5)

Compound **5** crystallizes in monoclinic $P2_1/c$ space group and structural determination suggests a 3D neutral coordination framework of La^{III} bridged by the oxalate ligand (ox^{2-}), hydroxo (OH^-) and aqua (H_2O) ligand (Figure 10). Each ten

coordinated La^{III} ions connected to an one chelated ox^{2-} ligand (O1, O2), four bridging μ-OH groups (O3, O4 and O3_c and O4_c; c = 2–x, –1/2+y, 3/2–z), two bridging μ-OH_2 (O3w, O3w_b; b = 1+ x, y,z) and other two coordinated water molecules (O1w, O2w). The La1–O bond distances are in the range of 2.478(7) - 2.798(7) Å. La1-O (μ–OH / μ-OH_2) bond distances related to the bridging hydroxo or aqua ligands are smaller compare to free coordinated water molecules La1-O(OH_2) (Table 9). The La1–O(μ-OH_2)-La1 bond angles is higher compare to the La1–O(μ-OH)-La1 bond angles (Table 2). Each La^{III} ions connected to the five different La^{III} ions through μ-OH, μ-OH_2 and μ-ox bridges resulting a 3D neutral coordination framework (Figure 10). In the 3D coordinated framework there is a small channel (2.48 × 1.98 $Å^2$) along the crystallographic b-axis (Figure 10c), however, upon removal of the coordinated water molecules (O1w and O2w) this increases to large rectangular channels with the dimension of 4.29 ×1.98 $Å^2$ (Figure 10b) and large rhombus type channels generate along the crystallographic a-axis (Figure 10b).[16,18,19] These bi-directional channels correspond to the 23.4% void space to the total crystal volume as calculated by the PLATON-99.[16] In the 3D framework, La···La separation along the ox bridge, hydroxo (OH^-) bridge and aqua bridge are 6.653, 4.521 and 4.860 Å, respectively. There are several intramolecular O-H···O H-bonding interactions between coordinated water molecules and ox^{2-} ligand, which stabilizes the overall 3D framework (Table 10).

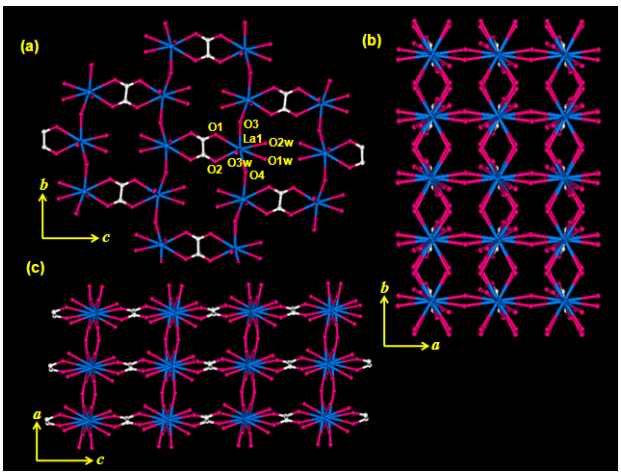

Figure10. Perspective view of the 3D coordination framework of **5** (a) along the crystallographic *a*-axis; (b) along the crystallographic *b*-axis; (c) along the crystallographic *c*-axis.

Table 9. Bond distances (Å) and angles (º) for $\{La(ox)_{0.5}(\mu\text{-}OH)_2(\mu\text{-}H_2O)(H_2O)_2\}_n$ **(5)**

La1-O1	2.567(7)	La1-O1W	2.710(9)
La1-O2	2.567(7)	La1-O2W	2.613(10)
La1-O3	2.478(7)	La1-O3W	2.481(9)
La1-O4	2.504(7)	La1-O3W_b	2.500(9)
La1-O3_c	2.798(7)	La1-O4_c	2.765(7)
O1-La1-O1W	163.7(3)	O2W -La1-O3_c	69.1(3)
O1-La1-O2	61.3(2)	O2W-La1-O4_c	90.1(3)
O1-La1 -O2W	125.4(3)	O3-La1-O3W	53.6(3)
O1-La1-O3	135.2(2)	O3-La1-O4	62.3(2)
O1-La1-O3W	97.5(3)	O3-La1-O3W_b	113.5(3)
O1-La1-O4	119.9(2)	O3-La1-O3_c	166.3(2)
O1 -La1-O3W_b	77.2(3)	O3-La1-O4_c	119.9(2)
O1-La1-O3_c	57.5(2)	O3W-La1-O4	114.3(3)
O1-La1-O4_c	69.3(2)	O3W-La1-O3W_b	154.7(3)
O1W-La1-O2	118.8(3)	O3_c-La1-O3W	126.6(3)
O1W-La1-O2W	59.5(3)	O3W-La1-O4_c	72.4(3)
O1W-La1-O3	45.6(3)	O3W_b-La1-O4	52.2(3)
O1W -La1-O3W	70.2(3)	O3_c-La1-O4	119.1(2)
O1W-La1-O4	75.8(3)	O4-La1-O4_c	166.2(2)
O1W-La1-O3W_b	118.4(3)	O3_c-La1-O3W_b	71.7(3)
O1W-La1-O3_c	120.8(2)	O3W_b-La1-O4_c	126.3(3)
O1W-La1-O4_c	96.2(2)	O3_c-La1-O4_c	55.2(2)
O2-La1-O2W	164.0(3)	O2-La1-O3	74.5(2)
O2-La1-O3W	64.0(3)	La1-O3-La1_d	117.8(3)
O2-La1-O4	87.9(2)	La1-O3W-La1_a	154.7(4)
O2-La1-O3W_b	92.4(3)	La1-O4-La1_d	118.1(3)
O2-La1-O3_c	118.7(2)	O2-La1 -O4_c	105.9(2)
O2W-La1-O3	99.2(3)	O2W-La1-O3W	124.3(3)
O2W-La1-O4	76.1(3)	O2W-La1-O3W_b	76.4(3)

Symmetry Code: a = -1+x,y,z; b = 1+x,y,z; c = 2-x,-1/2+y,3/2-z; d = 2-x,1/2+y,3/2-z

Table 10. Table of hydrogen bonding

D-H···A	D-H	H…A	D….A	<D-H…A
O1W -- H1W1 .. O1 [i]	0.9500	1.8700	2.625(12)	135.00
O2W -- H1W2 .. O1W [ii]	0.9500	2.3600	3.036(14)	127.00
O2W -- H2W2 .. O2 [iii]	0.9500	1.8400	2.713(12)	151.00

Symmetry code: i = 2-x,1/2+y,3/2-z; ii = 1+x,y,z; iii = 2-x,-1/2+y,3/2-z

8.3.6 Framework stability

To examine the framework stability of **1** and **4**, thermogravimetric (TG) analyses (Figure 11) and powder X-ray diffraction (PXRD) measurements (Figure 12) at different temperature were carried out. TGA curve of **1** shows (Figure 11a) that the framework is

stable up to 170 ˚C without any weight loss, and 6.8 % wt. loss in the temperature range of 170 – 240 ˚C suggesting the removal of two coordinated water molecules (calculated 6.9 wt %). The dehydrated framework (**1′**) is stable up to 300 ˚C and further heating decomposes the framework into unidentified products. PXRD pattern of **1** after removal of the coordinated water molecule has been changed indicating the compound has structural transformation after removal of the metal coordinated water molecules (Figure 12a). Compound **4** shows stepwise release of guest and coordinated water molecules as expected. The release of the guest water molecules occurs at ~65 ˚C to form $\{[Gd_2(H_2dhta)_2(H_2O)_5)]\}_n$ (**4′**) (wt. loss observed 3.9 % and calculated 4.34 %), which is stable up to ~175˚C. Upon further heating one coordinated water molecule is released at ~210 ˚C, resulting dehydrated framework, $\{[Gd_2(H_2dhta)_2(H_2O)_4)]\}_n$ (**4′′**). Remaining four coordinated water molecules are released in the temperature range of ~320–480 ˚C to form completely dehydrated framework, $\{[Gd_2(H_2dhta)_2)]\}_n$ and further heating decomposes the compound into unidentified products. Figure 14b shows PXRD patterns of simulated, as-synthesized **4**, **4′** and **4′′** and the rehydrated form of **4′**. PXRD pattern of **4′** is similar to **4,** suggesting the porous framework remains unchanged after guest water molecule removal. However in case of **4′′** there is a significant shifting of the **(**010) peak to the higher angle (5.67 to 6.76 ˚) suggesting the decrease of separation between 2D pillared bilayer framework. This structural contraction can be realized by the release of

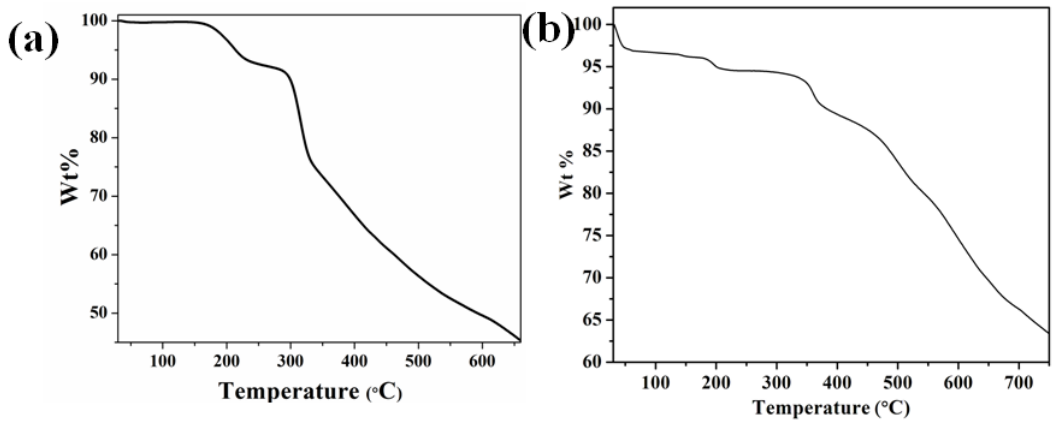

water molecules coordinated to Gd1, which are located in

Figure 11. TGA of $\{La(H_4dhta)_{1.5}(H_2O)_2\}_n$ **(a)** and $\{[Gd_2(dhta)(H_2dhta)(H_2O)_5]\cdot 2H_2O)\}_n$ (**b**) in the temperature range of 25 – 750 °C at a heating rate of 3 °C/min under the N_2 atmosphere.

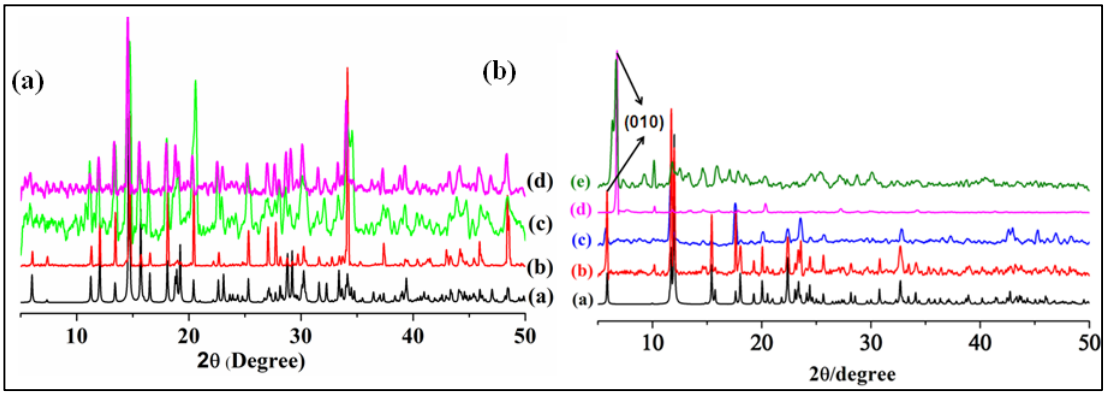

Figure 12. PXRD patterns of 1 (a) and **4** (b) in different state: (a) simulated from X-ray single-crystal data; (b) as-synthesized; (c) heated at 200 ˚C for **1** 120 ˚C for **4 (4′)** (d) rehydrated form of compound **1** and compound **4** heated at 200 ˚C compound (**4″**); (e) Rehydrated compound **4** (for 7 days) compound of **4″.**

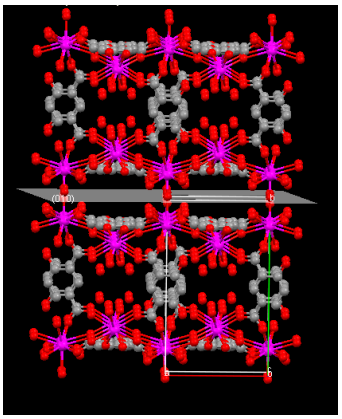

Figure 13. View 3D supramolecular framework showing (010) plane passing between the 2D pillared-bilayer framework.

(010) plane in between 2D pillared bilayer networks (Figure 13). High temperature release of the other four water molecules (O1, O1_c, O6, O6_b) can be correlated to the involvement of multiple H-bonding interactions compare to the O2.

8.3.7 Single-crystal-to-single-crystal structural transformation in 4

Stepwise release of the guest and coordinated water molecules and high thermal stability of the framework **4** inspired us to determine the crystal structures after removing guest as well as coordinated water molecules. The as-synthesized crystals were heated at 110 ºC for three hours under the N_2 atmosphere to remove guest water molecules. The

change in color and morphology of the crystals were monitored by a microscope which suggests greenish yellow color of the crystals remain unchanged after heating (Figure 14).

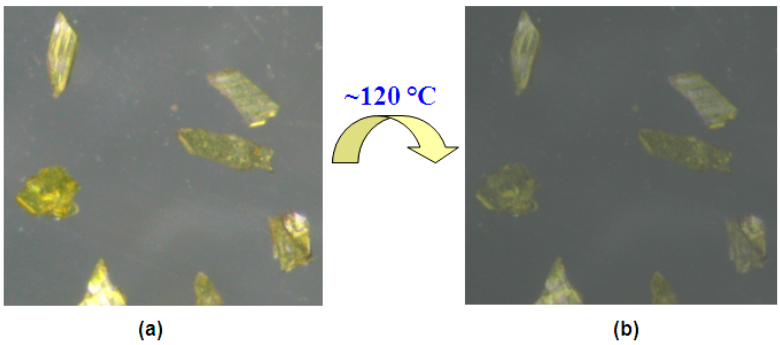

Figure 14. Color of the crystals of **4** in different state: (a) as-synthesized (b) crystals heated at 120 °C.

The guest water free crystal (**4′**) shows similar crystal system and space group as of compound **4**. (Table 7) Structural determination of **4′** reveals complete removal of the guest water molecule with formula $\{[Gd_2(dhta)(H_2dhta)(H_2O)_5]\}_n$ with similar cell parameter as of **4** (Figure 14b) and 2D pillared-bilayer network is retained, suggesting the rigidity of the framework **4** (Figure 15b). There are no significant changes in the channel sizes after removal of the guest water molecules (Figure 15b). In **4′,** the Gd-O bond distances are comparable to **4** and negligible changes were observed in the bond angles (Table 6 and 7). We could not determine the structure after removal of the coordinated water molecules at 220 ˚C because removal of the coordinated water molecule destroys the single crystallinity of the crystals and breaks into the several pieces. The dehydrated crystal **4′** exposed to the water vapor for three days to understand the reversibility which produces 4a. Structure determination of **4a** reveals that **4′** returned to **4** with the formulation of $\{[Gd_2(dhta)(dhtaH_2)(H_2O)_5]\cdot 2H_2O)\}_n$ (**4**), (Figure 15c). Cell parameters of the rehydrated compound **4a** are almost similar to that of **4**, suggesting complete reversibility of the structure (Table1). The bond lengths and angles are also comparable to that of compound **4** (Table 6 and 8)). Such single-crystal-to-single-crystal structural transformation in flexible porous Ln-organic frameworks is scanty in the literature compared to transition metal-organic frameworks.

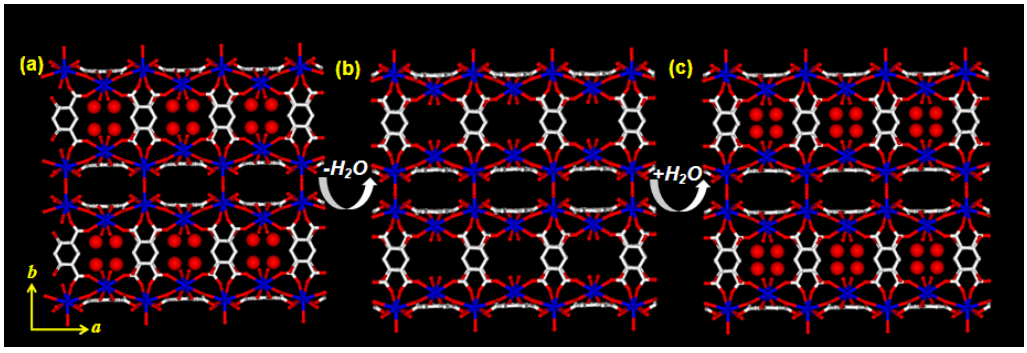

Figure 15. (a) View of the interdigitated 3D supramolecular framework of **1** formed by the 2D pillared-bilayer framework showing two different channels along the *c*-axis; (b) View of the 3D framework of **1′**; (c) View of the 3D rehydrated framework of **1a** showing structural reversibility**.**

8.3.8 Porous functionality of 1 and 4

Framework **1** does not contain any regular channels however after removal of the coordinated water molecules 3D framework shows 1D pore decorated with unsaturated La^{III} sites on the pore surface. To unveil permanent porosity **1′** (dehydrated form of **1**) was subjected for gas (N_2 at 77 K and CO_2 at 195K) sorption study and found neither of the gases are adsorbed by the framework. Due to the presence of unsaturated La^{III} center in **1′** it shows very strong affinity to water. Water sorption isotherm (Figure 18b) showing the steep uptake at very low pressure region, high βE_0 value of 18.5 kJ mol^{-1} calculated from DR equation and hysteresis in water vapor sorption profile unequivocally suggests the dehydrated framework has very strong affinity to water. The amount of uptake at P/P_0 ~ 1.0 is 120 mL g^{-1} corresponds to 2.31 molecule of water per formula unit of **1′.** Slightly higher amount of uptake compared to the number of coordinated water molecule is attributed to the adsorbate-adsorbate interaction. Framework **4** contains regular channels and dehydrated phase **4′** does not exhibit any structural transformation, which inspired us for the gas as well as different solvent sorption studies. N_2 (kinetic diameter = 3.6 Å) [18-19] sorption for **4′** at 77K exhibit small steep uptake at low pressure region and then monotonous increases with increasing pressure and ended with the value of 78 mL/g at P/P_0 = 1. Such type of N_2 sorption curve was recently reported by Chen *et al* in Cu^I flexible coordination framework with small window.[20] Even they have able determine the N_2 molecules in a loaded framework. Moreover, we have also studied N_2 sorption isotherm for **4″** at 77 K shows almost linear increase with increasing pressure and sorption amount is 48 mL/g at P/P_0 = 1 without saturation. The value is quite smaller than the corresponding value of **4′**, also corroborating interlayer structural contraction after removal of the coordinated water molecules (O3) which observed in the PXRD pattern. The size of the channels between two pillared layer frameworks is about 3.4 × 3.4 $Å^2$, which is removed in **4″**.

We have also studied the adsorption properties for **4′** and **4″** with the different solvent molecules (H_2O, MeOH, EtOH and CH_3CN) to study the effect of the channels size and interaction with the coordinatively unsaturated Gd ^{III} sites. H_2O (kinetic diameter = 2.68

Å) sorption study with **4′** shows that with increasing pressure amount of sorption increases, and final amount is 45 mL/g at P/P_0 =1, agreeing with two guest water molecules occupied the channels in the as-synthesized framework. This curve is characteristics for H_2O sorption in a porous solid where adsorbate-adsorbate interaction is also play important role along with the adsorbate-adsorbent interactions. Hysteresis adsorption can be correlated to the H-bonding interactions of the water molecules with the pore surfaces. We have also performed H_2O sorption with the dehydrated phase **1′′**, which indicates steep uptake at low pressure regions suggesting strong sorption affinity of H_2O to the surfaces of **4′′**. The amount of sorption is about 2.80 molecules of H_2O per formula unit, correlates to the two guest and one coordinated H_2O molecules. The strong affinity of **4′′** to H_2O compare to **4′** is due to the one Gd^{III} is coordinatively unsaturated in **4′′**, which provide high interaction sites to the H_2O molecules. Both the profiles were analyzed by the Dubinin-Radushkevich equation[21] and the corresponding βE_0 values, which reflect the adsorbate-adsorbent affinity, are 3.40 and 4.26 kJ/mol, for **4′** and **4′′**, respectively, indicating the stronger affinity of the H_2O molecules to**4″**. However both the frameworks **4′** and **4′′** do not adsorb other organic solvents, like MeOH (kinetic diameter 4.0 Å), EtOH (4.8 Å) and MeCN (4.2 Å), this may be due to larger size and weaker coordinating ability compared to H_2O.[18-19]

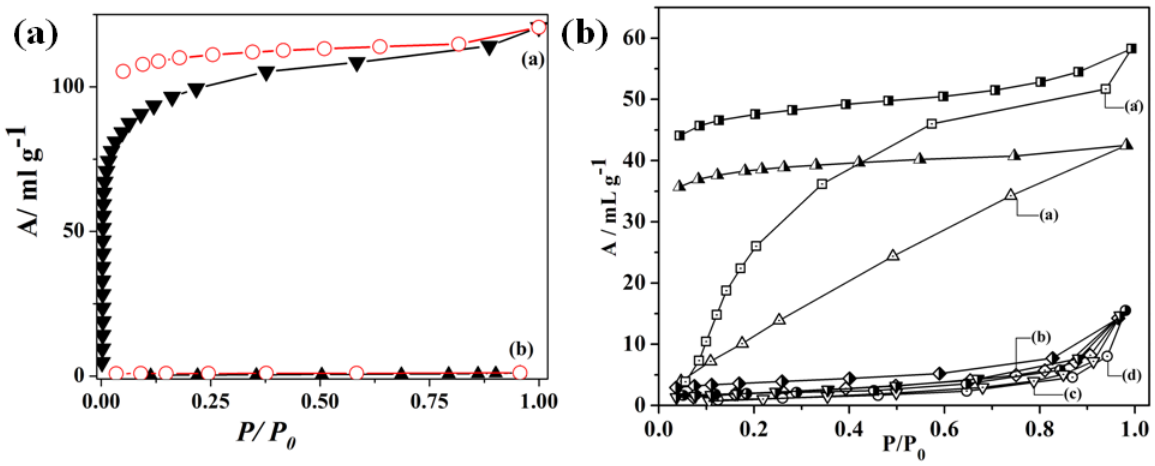

Figure 16. Sorption isotherm for **1′** and **4′**: (a) H_2O; (b) MeOH; (c) MeCN, and (d) EtOH. sorption profile (a′) showing H_2O for **4′′**. P_0 is the saturated vapor pressure of the respective adsorbate at corresponding temperature.

8.3.9 Photoluminescence property of 1

Recently Maji *et. al*. reported for the first time a novel molecular design concept to control the emission of a metal-organic framework {$Mg(H_2dhta)(DMF)_2$}, based on excited state intramolecular proton transfer (ESIPT) of the linker H_2dhta (2,5-dihydroxyterephthalate).[22] Compound $\{La(H_2dhta)_{1.5}(H_2O)_2\}_n$ (**1**) is a three dimensional framework, composed of two different kind of H_2dhta linkers with different binding mode (see details structure description part). In one H_2dhta linker both carboxylate and -OH groups are involve in bridging whereas in other one –OH groups remain pendent which can take part in the excited state proton transfer process. We have done detailed fluorescence spectroscopic studies of compound **1** to investigate tunable emission properties based on ESIPT process. Compound **1** shows broad absorption spectrum in the UV region with maxima of 390 nm. Compound **1** reveals wide range of emission when dispersed in different solvent system having different polarity. Acetic acid (CH_3COOH) or formic acid (HCOOH) dispersed state of **1** shows a blue emission with maxima at 454 and 461 nm respectively, whereas significantly red shifted green emission (λ_{max} = 510 nm) was observed in DMSO when excited at 505 nm in all solvent systems. The large Stokes shifted green emission in DMSO presumably attributed to the ESIPT process in the compound. The ESIPT process is prevented in CH_3COOH or HCOOH solvent system due to the adduct formation through the intermolecular hydrogen bonding with the ligand. Surprisingly, in water, a highly polar protic solvent, intense yellow emission (λ_{max} = 538 nm) was observed which could be due to the additional intermolecular proton transfer with the solvent. However, in solvent like MeOH, or DMF broad emission ranging from blue to yellow range with different spectral features was observed suggesting involvement of the various excited state processes. Therefore compound **1** shows multi-color ligand based emission in different solvent systems with different polarity through the proper control of the ESIPT process.

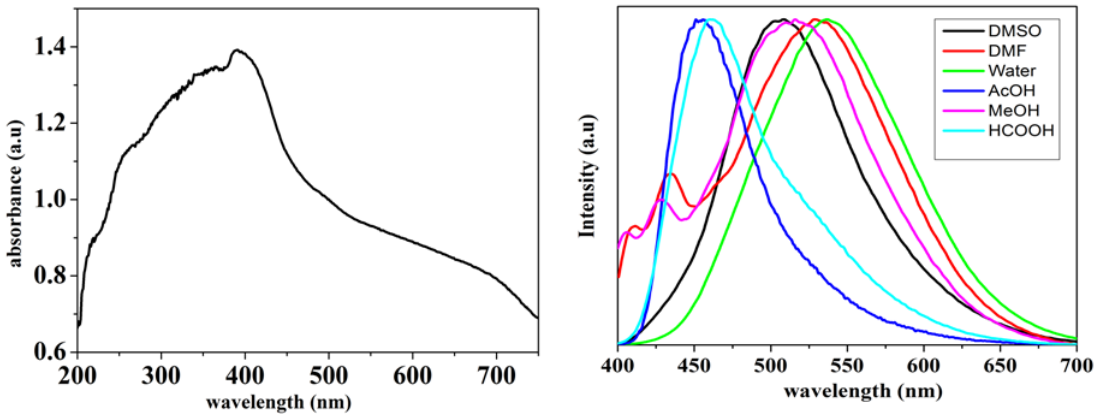

Figure 17. Left: UV-vis spectrum of **1** in solid state. Right: Solvent dependent ligand based (ESIPT responsive) emission Property of **1′**.

8.4 Summary

In conclusion, we have synthesized and structurally characterized five novel lanthanide-organic coordination framework using 2,5-dhta as a linker and precursor of oxalate. Framework **1** and **4** shows porosity and strong affinity towards the H_2O molecules compared to the other organic solvents. Compound **2** is a 3D coordination framework without any regular channels; however, after removal of the coordinated H_2O molecules exhibit 1D channel type structure. Compound **3** is a 2D coordination sheet formed by the mixed ligand, 2,5dhta and ox^{2-} linkers, although we have never used the ox ligand in the reaction. The formation of oxalate ligand occurred by the decarboxylation of the 2,5dhta and consecutive oxidative coupling of CO_2 catalyzed by the Ln^{III} ions. Thus controlled stoichiometry, pH, temperature as well different Ln^{III} ions play the driving role for the synthesis of different kind of coordination architectures. Different binding mode in a same reaction condition with Gd^{III}, and La^{III} may be due to the different size of the Ln^{III} ions. Framework **1** exhibit interesting solvent responsive ligand based emission property via ESIPT process.

8.5 References

1. (a) O. M. Yaghi, M. O'Keeffe, N. W. Ockwig and H. K. Chae, *Nature,* 2003, **11**, 705; (b) S. Kitagawa, R. Kitaura and S. I. Noro, *Angew. Chem., Int. Ed.* 2004, **43**, 2334; (c) S. L. James, *Chem. Soc. Rev.,* 2003, **32**, 276; (d) D. Maspoch, D. Ruiz-Molina, J. Veciana, *J. Mater. Chem.,* 2004, **14**, 2713; (e) G. Férey, C. Mellot-Draznieks, C. Serre and F. Millange, *Acc. Chem. Res.,* 2005**, 38**, 217; (f) G. Férey, *Chem. Soc. Rev.,* 2008, **37**, 191; (g) J. L. C. Rowsell and O. M. Yaghi, *Angew. Chem., Int. Ed.,* 2005, **44**, 4670; (h) X. Lin, J. Jia, X. Zhao, K. M. Thomas, A. J. Blake, G. S. Walker, N. R. Champness, P. Hubberstey and M. Schröder, *Angew. Chem., Int. Ed.*, 2006**, 45**, 7358; (i) M. Dinca, A. F. Yu and J. R. Long, *J. Am. Chem. Soc.*, 2006, **128**, 8904; (j) S. Ma, D. Sun, J. M. Simmons, C. D. Collier, D. Yuan and H. C. Zhou, *J. Am. Chem. Soc.,* 2008, **130**, 1012.

2. (a) J. S. Seo, D. Whang, H. Lee, S. I. Jun, J. Oh, Y. J. Jeon and K. Kim, *Nature,* 2000, **404**, 982; (b) O. R. Evans, H. L. Ngo and W. Lin, *J. Am. Chem. Soc.* 2001, **123**, 10395; (c) J. Y. Lee, D. H. Olson, L. Pan, T. J. Emge and J. Li, *Adv. Func. Mater.,* 2007, **17**, 1255; (d) H. L. Ngo and W. Lin, *J. Am. Chem. Soc.,* 2002, **124,** 14298.

3. (a) C. D. Wu, A. Hu, L. Zhang and W. Lin, *J. Am. Chem. Soc.,* 2005, **127**, 8940; (b) O. Ohmori and M. Fujita, *Chem. Commun.,* 2004, **10**, 1586; (c) W. Lin, *MRS Bulletin* 2007, **32,** 544.

4. (a) B. Chen, L. Wang, Y. Xiao, F. R. Fronczek, M. Xue, Y. Cui and G. A. Qian, *Angew. Chem., Int. Ed.,* 2009, **48**, 500; (b) K. L.Wong, G. L. Law, Y. Y. Yang and W. T. Wong, *Adv. Mater.,* 2006, **18**, 1051; (c) D. T. De Lill, A. De Bettencourt-Dias and C. L. Cahill, *Inorg. Chem.,* 2007, **46**, 3960.

5. (a) T. K. Maji, R. Matsuda and S. Kitagawa, *Nat. Mater.* 2007, **6**, 142; (b) K. S. Min and M. P. Suh, *J. Am. Chem. Soc.*, 2000, **122**, 6834; c) O. M. Yaghi and H. Li, *J. Am. Chem. Soc.,* 1996, **118**, 295.

6. (a) O. Guillou and C. Daiguebonne, *Handbook on the Physics and Chemistry of Rare Earths*; (b) K A. Gschneidner, J. -C. G. Bu¨nzli, V. K. Pecharsky, Elsevier Eds. New York, 2005, **34**, 359-404; (c) C. L.; Cahill, D. T. de Lill and M.Frisch, *CrystEngComm*., 2007, **9**, 15.

7. (a) X. Guo, G. Zhu, Q. Fang, M. Xue, G. Tian, J. Sun, X. Li and S. Qiu, *Inorg. Chem.* 2005**, 44**, 3850; (b) E. G. Moore, J. Xu, C. J. Jocher, I. Castro-Rodriguez and K. N. Raymond, *Inorg. Chem.* 2008, **47**, 3105; (c) J. Y. Wu, T. T. Yeh, Y. S. Wen, J. Twu, and K. L. Lu, *Cryst. Growth Des.* 2006, **6**, 467; (d) A. Fratini, G. Richards, E. Larder and S. Swavey, *Inorg. Chem.,* 2008**, 47**, 1030; (e) W. H. Zhu, Z. M. Wang and S. Gao, *Inorg. Chem.,* 2007, **46**, 1337; (f) A. Thirumurugan and S. Natarajan, *J. Mat. Chem.*, 2005, **15**, 4588.

8. C. Benelli and D.Gatteschi, *Chem. Rev.,* 2002, **102**, 2369; (b) M. Bao-Qing, S. Gao, G. Su and G. X. Xu, *Angew. Chem., Int. Ed.,* 2001, **40**, 434; (c) J. P. Costes, J. M.Clemente-Juan, F. Dahan, F. Nicodeme and M. Verelst, *Angew. Chem., Int. Ed.,* 2002, **41**, 323; (d) C. F. Hsu, S. H. Lin and H. H. Wei, *Inorg. Chem. Commun.,* 2005, **8,** 1128; (e) J. P. Costes, J. M. C. Juan, F. Dahan and F. Nicodeme, *Dalton Trans.* 2003, 1272.

9. (a) F. A. A. Paz and J. Klinowski, *Chem. Commun.,* 2003, **9**, 1484; (b) Z. He, E. Q. Gao, Z. M. Wang, C. H. Yan and M. Kurmoo, *Inorg. Chem.,* 2005, **44**, 862; (c) X. Zheng, C. Sun, S. Lu, F. Liao, S. Gao and L. Jin, *Eur. J. Inorg Chem.* 2004, 3262.

10. (a) M. Shibasaki and N. Yoshikawa, *Chem. Rev.,* 2002, **102**, 2187; (b) G. A. Molander, *Chem. Rev.,* 1992, **92**, 29; (c) O. R. Evans, H. L. Ngo and W. Lin, *J. Am. Chem. Soc*., 2001, **123**, 10395.

11. (a) T. K.; Maji, G. Mostafa, H. –C. Chang and S. Kitagawa, *Chem. Commun*., 2005, 2436; (b) L. Pan, K. M. Adams, H. E. Hernandez, X. Wang, C. Zheng, Y. Hattori and K. Kaneko, *J. Am. Chem. Soc.*, 2003, **125**, 3062; (c) J. Zhao, L. S. Long, R. B. Huang and L. S. Zheng, *Dalton Trans.* 2008, 4714; (d) A. Dimos, D. Tsaousis, A. Michaelides, S. Skoulika, S. Golhen, L. Ouahab, C. Didierjean and A. Aubry, *Chem. Mater*., 2002, **14**, 2616.

12. (a) C. Serre and G. Ferey, *J. Mat. Chem.*, 2002, **12**, 3053; (b) T. M. Reineke, M. Eddaoudi, M. O'Keeffe and O. M. Yaghi, *Angew. Chem., Int. Ed.*, 1999, **38**, 2590; (c) N. L. Rosi, J. Kim, M. Eddaoudi, B. Chen, M. O'Keeffe and O. M. Yaghi, *J. Am. Chem. Soc*., 2005, **127**, 1504; (d) T. Devic, C. Serre, N. Auderbrand, J. Marrot and G. Férey, *J. Am. Chem. Soc.*, 2005, **127**, 12788; (e) J. Luo, H. Xu, Y. Liu, Y. Zhao, L. Daemen, C. Brown, T. V. Timofeeva, S. Ma and H. –C. Zhou, *J. Am. Chem. Soc*., 2008, **130**, 9626; (f) F.; Millange, C. Serre, J. Marrot, N. Gardant, F. Pellé and G.Férey, *J. Mater. Chem*., 2004, **14**, 642; (g) Q. Yue, J. Yang, G. –H. Li, G. –D. Li and J. –S. Chen, *Inorg. Chem.*, 2006, **45**, 4431; (h) X. Guo, G. Zhu, Z. Li, F. Sun, Z. Yang and S. Qiu, *Chem. Commun*., 2006, 3172.

13. (a) C. D. Ene, F. Tuna, O. Fabelo, C. Ruiz-Perez, A. M. Madalan, H. W. Roesky and M. Andruh, *Polyhedron*, 2008**, 27**, 574; (b) M. Eddaoudi, J. Kim, N. Rosi, D. Vodak, J. Wachter, M. O'Keeffe and O. M. Yaghi, *Science,* 2002, **295**, 469; (c) N. L. Rosi, J. Kim, M. Eddaoudi, B. Chen, M. O'Keeffe and O. M. Yaghi, *J. Am. Chem. Soc.,* 2005, **127**, 1504; (d) P. D. C. Dietzel, R. Blom and H. Fjellvag, *Dalton Trans.* 2006, 2055; (e) P. D. C. Dietzel, B. Panella, M. Hirscher, R. Blom and H. Fjellvag, *Chem. Commun.*, 2006, 959; (f) P. D. C. Dietzel, Y. Morita, R. Blom and H. Fjellvag, *Angew. Chem., Int. Ed.,* 2005, **44**, 6354; (g) P. D. C. Dietzel, R. E. Johnsen, R. Blom and H. Fjellvag, *Chem. Eur. J.* 2008, **14**, 2389; (h) N. E. Ghermani, G. Morgant, J. d'Angelo, D. Desmaele, B. Fraisse, F. Bonhomme, E. Dichi and M. Sgahier, *Polyhedron,* 2007, **26**, 2880; (i) J. F. Bickley, R. P. Bonar-Law, C. Femoni, E. J. MacLean, A. Steinera and S. J. Teat, *J. Chem. Soc., Dalton Trans.*, 2000, 4025.

14. Nakamoto, K. *Infrared and Raman Spectra of Inorganic and Coordination compounds*, 5th ed; John Wiley & Sons; 1997

15. The size is measured by considering van der Waals radii for constituting atoms. Hereafter, all the size-estimation of pore is made in this way.

16. A. L. Spek, PLATON, *Molecular Geometry Program, University of Utrecht*,Netherlands, 1999

(17) (a) *SAINT*, 6.02 ed., Bruker AXS, Madison, WI, 1999**;** (b) G. M. Sheldrick, *SADABS, Empirical Absorption Correction Program*, University of Göttingen, Göttingen, Germany, 1997 (c) A. Altomare, G. Cascarano, C. Giacovazzo and A. Gualaradi, *J. Appl. Crystallogr.* 1993, **26**, 343; (d) G. M. Sheldrick, *SHELXL 97*, Program for the Solution of Crystal Structure, University of Göttingen, Germany, 1997;(e) G. M. Sheldrick, *SHELXS 97*, Program for the Solution of Crystal Structure, University of Göttingen, Germany, 1997;(f) Spek, A. L. *J. Appl. Crystallogr.* 2003, **36**, 7; (g) WinGX, A Windows Program for Crystal Structure Analysis: Farrugia, L. J. *J. Appl. Crystallogr.* 1999, **32**, 837.

(18) Molecular area is calculated from liquid density, assuming spherical symmetry and a hexagonal close packing. The equation and values are in ref. 19.

(19) C. E. Webster, R. S. Drago, M. C. Zerner, *J. Am. Chem. Soc.*, 1998, **120**, 5509.

(20) Z. P. Zhang, X. –M. Chen, *J. Am. Chem. Soc*., 2008, **130**, 6010.

(21) M. M.Dubinin, *Chem. Rev.*, 1960**, 60,** 235**.**

(22) K. Jayaramulu, P. Kanoo, S. J. George and T. K. Maji, *Chem. Commun.*, 2010, **46**, 7906.

General Conclusions:

My thesis deals with the syntheses and diverse properties of metal-organic frameworks and nanomaterials. Hydroxy acid can play versatile role viz a redox active reagent, linker and precursor of oxalate and carbonate for the syntheses of metal-organic framework and nanomaterials depending on it's structure and reaction conditions. All the three different types of hydroxy acids were converted to oxalate at high temperature in presence of lanthanide ions. The reaction occurs because of the catalytic activity of metal ions. An aliphatic unsaturated hydroxyacid, DHFA plays the role of reducing agent and it can form other ligands at room temperature as well as higher temperature. At room temperature and alkaline condition it forms trisubstituted methanol and high temperature it breaks into oxalate and carbonate, which act as linkers to form 3D metal-organic hybrid framework materials. DHFA serves as a reducing agent and capping agent for the synthesis of silver and gold nanostructures. Biocompatibility as well as reducing and capping capability of this reagent implies it's future application for the synthesis of nanomaterials under biological condition. An aliphatic saturated long chain hydroxy acid, mucic acid can act as a precursor and linker for the synthesis of different metal organic frameworks. A highly stable aromatic hydroxyacid, 2,5-dihydroxyterephthalic acid can exhibits interesting ligand based tunable emission properties based on excited state intramolecular proton transfer process. Using different hydroxy acids and various nitrogen containing rigid linkers it is possible to design materials of desired functionality. In this thesis I could able to establish that rationally designing of a material is possible through the proper choice of organic linkers and inorganic metal ions. A modestly explored area of research is lanthanide based metal-organic framework and mixed metal-organic framework of variety of metal ions in terms of charge ionic radii and functionalities ($\{K\ Ln(C_2O_4)_2(H_2O)_4\}_n$: gas storage, magnetic luminescent properties). A Dysprosium (III) based 3D extended solid exhibit very high anisotropic barrier

and the magnetic interaction could be modulated through dehydration and rehydration is a very interesting observation. The effect of solvent like water has significant contribution to the structure and functionality of the frameworks. A porous host with guest or coordinated water molecules can serves as a key to exhibit different response in terms of magnetic and luminescence properties. Furthermore hydroxo group present beyond the coordination sphere of the metal ions of the framework can act as an active site to act as a host for specific species and help towards separation and sensing of solvents and metal ions depending upon their interaction to these specific sites

9. List of Publications:

From Thesis:

- **S. Mohapatra**, S. Adhikari, H. Riju and T. K. Maji, Tb^{III}, Eu^{III} and mixed Tb^{III}-Eu^{III}-mucicate frameworks: hydrophilicity and composition dependent colour tunability ***Inorg. Chem.***, **51,** 4891 (2012).
- **S. Mohapatra**, H. Sato, R. Matsuda, S. Kitagawa and T. K. Maji, Highly rigid and stable porous Cu^{I} metal- organic framework with reversible single-crystal-to-single-crystal structural transformation ***CrystEngComm***, **14**, 4153 (2012)
- **S. Mohapatra**, R. K. Kumar and T. K. Maji, Green synthesis of catalytic and ferromagnetic gold nanoparticles ***Chem. Phys. Lett.***, **508**, 76 (2011).
- **S. Mohapatra**, S. Siddhanta, D. Ravinder Kumar, C. Narayana and T. K. Maji, Facile and green synthesis of SERS active and ferromagnetic silver nanorods ***Eur. J. Inorg. Chem.***, 4969 (2010).
- **S. Mohapatra** and T. K. Maji, Facile synthesis of anion dependent versatile Cu^{I} and mixed-valent porous Cu^{I}/Cu^{II} frameworks in aqueous solution and aerobic condition, ***Dalton Trans.***, **39**, 3412 (2010).
- **S. Mohapatra**, K. P. S. S. Hembram, U. Waghmare and T. K. Maji, Immobilization of alkali metal ions in a 3D lanthanide-organic framework: Selective sorption and hydrogen storage characteristics ***Chem. Mater.***, **21**, 5406 (2009).
- **S. Mohapatra,** S. Y. Vyasamudri, G. Mostafa and T. K. Maji, Lanthanide (La^{III}/Ho^{III})-oxalate open framework materials formed by In situ ligand synthesis ***J. Mol. Str.***, 932, 123 (2009).
- K. L. Gurunatha, **S. Mohapatra**, Suchetan P. A. and T. K. Maji, Single-crystal-to-single-crystal structural transformation in a flexible porous gadolinium-organic framework with selective and controlled sorption properties ***Cryst. Growth Des.***, **9**, 3844 (2009).

Miscellaneous:

- K. V. Rao, **S. Mohapatra**, T. K. Maji and S. J. George, Guest-Responsive Reversible Swelling and Fluorescence Response in a Super-Absorbent, Dynamic Microporous Polymer ***Chem. Eur. J.***, **18**, 4505, (2012).
- A. Hazra, P. Kanoo, **S. Mohapatra**, G. Mostafa and T. K. Maji, A flexible supramolecular host with a crowned chair octameric water cluster and highly selective adsorption properties ***CrystEnggComm***, 12, 2775 (2010).
- K. V. Rao**, S. Mohapatra**, C. Kulkarni, T. K. Maji and S. J. George, Extended phenylene based microporous organic polymers with selective carbon dioxide adsorption ***J. Mater. Chem.***, **21**, 12958 (2011).